

**Two Iron-Sulfur Proteins Involved in Isoprenoid Biosynthesis
with New Catalytic Roles**

by

Weiya Xu

A dissertation submitted to the Graduate Faculty of
Auburn University
in partial fulfillment of the
requirements for the Degree of
Doctor of Philosophy

Auburn, Alabama
August 9, 2010

Keywords: Isoprenoid Biosynthesis, iron-sulfur cluster, GcpE, LytB, EPR spectroscopy

Copyright 2010 by Weiya Xu

Approved by

E. C. Duin, Chair, Associate Professor of Chemistry and Biochemistry
D. Goodwin, Associate Professor of Chemistry and Biochemistry
H. Ellis, Associate Professor of Chemistry and Biochemistry
A. Gorden, Assistant Professor of Chemistry and Biochemistry
Sang-Jin Suh, Associate Professor of Biological Sciences

Abstract

(E)-4-hydroxy-3-methylbut-2-enyl diphosphate synthase (GcpE or IspG) and (E)-4-hydroxy-3-methylbut-2-enyl diphosphate reductase (LytB or IspH) are involved in the last two steps of the DOXP pathway for isoprenoid biosynthesis. GcpE converts 2-C-methyl-D-erythritol-2,4-cyclodiphosphate (MEcPP) into (E)-4-hydroxy-3-methylbut-2-enyl diphosphate (HMBPP) in the penultimate step of the DOXP pathway. LytB catalyzes the conversion of (E)-4-hydroxy-3-methyl-but-2-enyl diphosphate (HMBPP) into two products: isopentenyl diphosphate (IPP) and dimethylallyl diphosphate (DMAPP) in the terminal step of the DOXP pathway.

GcpE and LytB are iron-sulfur proteins containing a [4Fe-4S] cluster at the active site. The spectroscopic characterizations of the [4Fe-4S] cluster have been studied. In order to develop potential inhibitors for drugs, the catalytic mechanisms of GcpE and LytB have been investigated.

For GcpE, two individual electron transfer steps have different midpoint potentials. The reaction intermediate species have been trapped and studied with titration experiments. The EPR properties of species FeS_A are similar to that detected in ferredoxin:thioredoxin reductase (FTR), indicating the direct binding from substrate or the reaction intermediate. The characterization of FeS_A species has been performed with ^{57}Fe -EPR and ENDOR spectroscopy. The diphosphate group does not directly bind to iron-sulfur cluster based on the distance calculated from the ^{31}P superhyperfine coupling.

The FeS_B species has been identified as the product binding to the 4Fe cluster. Based on these information, a new mechanism has been proposed for GcpE.

For LytB, it is determined that the active form is a [4Fe-4S] cluster and the enzyme activity is related to the cluster content of [4Fe-4S] clusters. A similar transient paramagnetic species FeS_I to FeS_A species in case of GcpE has been detected after incubation of one-electron-reduced enzyme with substrate. The characterization of FeS_I species has been carried out with ⁵⁷Fe-EPR and ENDOR spectroscopy. It is implied that the diphosphate group does not bind to the iron-sulfur cluster, but the hydroxyl group might be the binding group. The preliminary data from site-directed mutagenesis of LytB (including H42A, H42F, H124A, H124F, E126A and E126Q) identified several mutations that have different effects on iron-sulfur cluster or reaction intermediate. The further exploration will be executed to achieve more details and information about catalytic mechanism.

A [4Fe-4S] cluster is discovered at the active site of both GcpE and LytB. After incubation with reductant and substrate, new paramagnetic species are detected during the reaction. Our data indicate that these new paramagnetic species are iron-sulfur based and might be bound by substrate through the hydroxyl group. The mutant studies on LytB suggest that His42, His124 and Glu126 play important roles in the catalysis. The mechanisms for GcpE and LytB are proposed, however, further investigation is necessary for full understanding of them.

Acknowledgments

This dissertation could not have been written without the great help of the people I would like to thank.

I highly acknowledge my profound gratitude to my advisor: Dr. Evert C. Duin, for his invaluable guidance, support, encouragement, persistence, and supervision throughout the entire period of my graduate study and research work at Auburn University.

I am greatly thankful to my committee members: Dr. H. Ellis, Dr. A. Gorden, Dr. D. Goodwin, and Dr. Sang-Jin Suh, for their valuable comments and instructive suggestions to my research and dissertation.

I also appreciate the following: Dr. H. Jomma for providing the plasmids of GcpE and LytB, MEcPP and HMBPP; Dr. B. Hoffman and Dr. N. Lees for ENDOR measurements; Dr. E. Oldfield for providing the plasmids of mutant LytB enzymes and D-HMBPP.

I would like to thank my lovely lab colleagues: Na Yang, Dolapo Adedeji, Mi Wang, Dhanushi Welideniya, Divya Prakash, Dominique Hall, Bryant Goodridge, Reema Bashir, Frank Crisona, for their generous support and help. Also I thank all my friends for their kindly help.

I am also grateful to the Department of Chemistry and Biochemistry at Auburn University and NSF for their financial support during the course of this work.

Finally, special thanks are given to my family for always being there to be supportive. I am indebted to my parents for their continuous love, understanding, endurance and encouragement through my life.

Table of Contents

Abstract	ii
Acknowledgments	iv
List of Tables	xi
List of Figures	xii
List of Abbreviations	xvii
Chapter 1 Literature Review	1
1.1 Isoprenoid Biosynthesis	1
1.2 The DOXP Pathway	6
1.3 Iron-Sulfur Proteins	10
1.3.1 The Basic Structures of Iron-Sulfur Clusters.....	11
1.3.2 The Biological Functions of Iron-Sulfur Clusters	13
1.3.3 Magnetic and Electronic Properties of Iron-Sulfur Proteins.....	16
1.3.4 Classes of [4Fe-4S] Clusters Involved in Catalysis.....	19
1.3.4.1 Hydrolyases.....	19
1.3.4.2 The Class of Radical SAM Proteins	20
1.3.4.3 Ferredoxin:thioredoxin Reductase (FTR) and Heterodisulfide Reductase (HDR)	24
1.4 Physical Methods for Studying Metal Centers in Metalloproteins	27
1.4.1 Electron Paramagnetic Resonance Spectroscopy (EPR)	31

1.4.1.1 The Basic Principles of EPR.....	32
1.4.1.2 g-factor.....	35
1.4.1.3 The Magnetic Interactions.....	37
1.4.1.4 Frequency.....	44
1.4.2 Electron-Nuclear Double Resonance (ENDOR).....	44
1.5 Significance of Research.....	47
Chapter 2 (E)-4-Hydroxy-3-methylbut-2-enyl Diphosphate Synthase.....	54
2.1 Introduction.....	54
2.1.1 Statement of Research.....	64
2.2 Experiments and Materials.....	65
2.2.1 Expression and Purification.....	66
2.2.2 Protein Determination.....	68
2.2.3 Iron Determination.....	68
2.2.4 Sulfur Determination.....	69
2.2.5 Kinetic Studies.....	69
2.2.6 Electronic and Magnetic Characterizations.....	70
2.3 Results.....	72
2.3.1 Expression and Purification.....	72
2.3.2 Basic Absorption and EPR Spectroscopy.....	72
2.3.3 The FeS _A Species and FeS _B Species are Iron-Sulfur Based.....	76
2.3.4 Kinetic Studies.....	76
2.3.4.1 Effect of MEcPP on the Signal Intensity of the FeS _A Species.....	83
2.3.4.2 Detection of the FeS _A and FeS _B Species in Single-Turnover Experiments.....	86

2.3.4.3 Effect of Methyl Viologen on the Signal Intensity of the FeS _A Species	86
2.3.4.4 Effect of Titanium(III) Citrate on the Signal Intensity of the FeS _A Species	89
2.3.5 Spectroscopic Properties of the FeS _A Species	94
2.3.6 Reduction of the [4Fe-4S] Cluster	96
2.3.7 Origin of the FeS _B Species.....	103
2.3.7.1 Spectroscopic properties of the FeS _B Species.....	110
2.4 Discussion and Conclusion	115
2.4.1 Reduction of the [4Fe-4S] Cluster in GcpE.....	115
2.4.2 The FeS _A Species	116
2.4.3 The FeS _B Species	118
2.4.4 Reaction Conditions: Temperature, Substrate Concentration, Reduction System	120
2.4.5 Proposed Mechanisms	121
Chapter 3 (E)-4-Hydroxy-3-methylbut-2-enyl Diphosphate Reductase.....	128
3.1 Introduction	128
3.1.1 Function of LytB in the Cell	128
3.1.2 Characterization of the Iron-Sulfur Cluster of LytB.....	129
3.1.3 Crystal Structure of LytB.....	131
3.1.4 Proposed Reaction Mechanism.....	133
3.1.5 Statement of Research on LytB	138
3.2 Experiments and Materials	139
3.2.1 Expression Vectors for Wild-Type LytB and Mutants	139

3.2.2 Expression and Purification	139
3.2.3 Characterization of the Purified Enzymes	140
3.2.4 Reconstitution	141
3.2.5 Enzyme Activity Assay.....	141
3.2.6 Circular Dichroism (CD) Spectroscopy.....	142
3.2.7 EPR Spectroscopy.....	142
3.3 Results	143
3.3.1 Expression and Purification	143
3.3.2 Wild-Type Enzyme.....	144
3.3.2.1 Cluster Type Present in Wild-Type LytB Enzymes	144
3.3.2.2 Cluster Content Related to Activity.....	153
3.3.2.3 Kinetic Studies	153
3.3.2.4 Characterization of the HMBPP Induced Signal, FeS ₁	158
3.3.2.5 ENDOR Spectroscopy	163
3.3.2.6 CD Spectroscopy	169
3.3.3 Mutated Enzymes	169
3.3.3.1 Mutants Characterization.....	171
3.3.3.2 Activity	177
3.3.3.3 Incubation of One-Electron-Reduced Mutant LytB with HMBPP	177
3.4 Discussion and Conclusion	184
3.4.1 Type of Cluster Present at Active Site.....	184
3.4.2 Reduction of the [4Fe-4S] Cluster.....	186
3.4.3 Substrate Binding.....	186

3.4.4 Mutants Studies.....	188
3.4.5 Proposed Mechanism.....	193
Chapter 4 Conclusions and Future Work.....	199
4.1 GcpE	199
4.2 LytB	202
References	205

List of Tables

Table 1.1 Biological functions and types of iron-sulfur clusters	14
Table 1.2 The advantages and properties of different techniques	30
Table 1.3 Ligand atom nuclear spins and their EPR superhyperfine patterns	42
Table 1.4 Transition metal nuclear spins	43
Table 1.5 Human bacterial pathogens that use the DOXP pathway	48-49
Table 3.1 V_{\max} , cluster content and corrected specific activity for the LytB samples from <i>A. aeolicus</i>	155
Table 3.2 Enzymatic activity of WT and mutants from <i>A. aeolicus</i>	179

List of Figures

Figure 1.1 Examples of Isoprenoids	2
Figure 1.2 Isoprenic units	4
Figure 1.3 The mevalonate pathway for isoprenoid biosynthesis.....	5
Figure 1.4 The DOXP pathway for isoprenoid biosynthesis	8
Figure 1.5 Basic types of iron-sulfur clusters	12
Figure 1.6 Magnetic properties of iron-sulfur clusters	17
Figure 1.7 Reaction catalyzed by Aconitase.....	21
Figure 1.8 Binding of S-adenosyl methionone and reaction catalyzed by Radical SAM enzymes	23
Figure 1.9 Proposed mechanism for FTR.....	26
Figure 1.10 Proposed mechanism I for HDR.....	28
Figure 1.11 Proposed mechanism II for HDR	29
Figure 1.12 EPR spectra of iron-sulfur clusters.....	33
Figure 1.13 Zeeman effect	34
Figure 1.14 1 st Derivative	36
Figure 1.15 g-anisotropy.....	38
Figure 1.16 Interactions: electron-nuclear & electron-electron spin interactions.....	39
Figure 1.17 Hyperfine interaction.....	40
Figure 1.18 Fosmidomycin	51

Figure 2.1 The alignment of GcpE sequences	56
Figure 2.2 Absorption spectra for GcpE	57
Figure 2.3 Electron paramagnetic resonance data for samples obtained with the freeze-quench technique in the presence of dithionite	58
Figure 2.4 Overview of paramagnetic species detected in GcpE during turn-over experiments	60
Figure 2.5 Electron paramagnetic resonance data for samples which were hand-mixed and flash frozen in the presence of dithionite.....	61
Figure 2.6 Temperature behavior for the different paramagnetic species detected in a GcpE sample that was hand-mixed with dithionite and MEcPP and flash frozen at 4 min and 20 s	63
Figure 2.7 FPLC profile of DEAE sepharose column	73
Figure 2.8 FPLC profile of Mono Q column	74
Figure 2.9 SDS-PAGE showing the progress in the purification of GcpE.....	75
Figure 2.10 Overlay of the spectra from Figure 2.4 (black lines) with similar samples prepared with ⁵⁷ Fe-enriched enzyme (gray lines).....	77
Figure 2.11 Michaelis-Menten and Lineweaver-Burk plots for GcpE	78
Figure 2.12 Time dependency of the development of the FeS _A and FeS _B species in GcpE	80
Figure 2.13 Dependency of the FeS _A EPR signal intensity on the concentration of dithionite	81
Figure 2.14 FeS _A EPR signal intensity as a function of the concentration of MEcPP and as a function of time	84
Figure 2.15 Dependency of FeS _A EPR signal intensity on the concentration of MEcPP..	85
Figure 2.16 Signal turn-over experiment	87
Figure 2.17 Electron paramagnetic resonance spectrum for a 10 s sample that was prepared in the presence of methyl viologen	88
Figure 2.18 FeS _A EPR signal intensity as a function of the concentration of titanium(III) citrate and as a function of time	90

Figure 2.19 FeS _A EPR signal intensity as a function of the concentration of titanium(III) citrate and as a function of time	92
Figure 2.20 FeS _A EPR signal intensity as a function of the concentration of titanium(III) citrate and as a function of time	93
Figure 2.21 Curie Plot of the FeS _A EPR signal	95
Figure 2.22 35 GHz CW EPR and pulsed ENDOR spectra of the FeS _A species.....	97
Figure 2.23 35 GHz pulsed ³¹ P ENDOR spectra (black line) and spectral simulations (blue line)	98
Figure 2.24 Incubation of as-isolated GcpE with dithionite-reduced methyl viologen ...	100
Figure 2.25 Electron paramagnetic resonance data for reduced GcpE samples	101
Figure 2.26 UV-visible absorption of GcpE treated with titanium(III) citrate	102
Figure 2.27 Electron transfer from reduced GcpE to MEcPP	104
Figure 2.28 FeS _B species from reduced GcpE with HMBPP bound	106
Figure 2.29 EPR signals of GcpE samples that were tested for activity.....	108
Figure 2.30 Addition of MEcPP to the FeS _B form.....	109
Figure 2.31 Comparison of the ‘0 min’ and the ‘0.5 min’ traces from Figure 2.30, panel B	111
Figure 2.32 35 GHz pulsed ³¹ P ENDOR spectra of a GcpE sample flash frozen after 5 min (blue line) incubation time (the FeS _A species).....	112
Figure 2.33 Hypothetical mechanism I.....	122
Figure 2.34 Hypothetical mechanism II.....	124
Figure 2.35 Hypothetical mechanism III	125
Figure 2.36 Hypothetical mechanism IV	126
Figure 3.1 Amino acid sequence alignment of LytB proteins showing conserved residues of interest.....	130
Figure 3.2 Structure of LytB from <i>A. aeolicus</i>	132

Figure 3.3 Proposed ligand docking to LytB	134
Figure 3.4 Hypothetical mechanism I.....	136
Figure 3.5 Hypothetical mechanism II.....	137
Figure 3.6 FPLC profile for purification of the <i>Plasmodium falciparum</i> enzyme on an immobilized nickel affinity chromatography column	145
Figure 3.7 SDS-PAGE showing the progress in the purification of the <i>P. falciparum</i> enzyme.....	146
Figure 3.8 UV-visible absorption of as-isolated (—) and dithionite-reduced (--) LytB protein from <i>P. falciparum</i>	147
Figure 3.9 UV-visible absorption of as-isolated (—) and dithionite-reduced (--) LytB protein from <i>A. aeolicus</i>	148
Figure 3.10 EPR spectra of LytB protein from <i>A. aeolicus</i>	149
Figure 3.11 EPR spectra of LytB protein from <i>P. falciparum</i>	151
Figure 3.12 Curie plots for the EPR signal in LytB from <i>A. aeolicus</i>	152
Figure 3.13 Absorption spectra of LytB protein from <i>A. aeolicus</i> before the treatment with Chelex Resin (—) and after the treatment with Chelex Resin (--).....	154
Figure 3.14 Relationship of enzyme activity on cluster content.....	156
Figure 3.15 Michaelis-Menten and Lineweaver-Burk plots	157
Figure 3.16 EPR spectra of the LytB protein from <i>P. falciparum</i> before and after addition of HMBPP.....	159
Figure 3.17 The effect of reduction of the cluster with dithionite and subsequent application to a PD 10 desalting column, on the absorption spectra of the LytB enzyme from <i>P. falciparum</i>	160
Figure 3.18 EPR spectra of LytB protein from <i>P. falciparum</i>	162
Figure 3.19 Comparison of EPR signal of the ‘intermediate’ species obtained with <i>A. aeolicus</i> enzyme from cell grown on natural abundance iron containing medium (--) and from cell grown on ⁵⁷ Fe-enriched medium (—).....	164
Figure 3.20 35 GHz CW EPR and pulsed ENDOR spectra of the FeS _I species.....	165

Figure 3.21 EPR data showing the absorption spectra for the samples used in Figure 3.20.....	167
Figure 3.22 Pulsed ¹ H-ENDOR spectra of the FeS _I species.....	168
Figure 3.23 Circular dichroism spectra of reconstituted LytB from <i>A. aeolicus</i>	170
Figure 3.24 Absorption spectra for WT and mutant LytB proteins from <i>A. aeolicus</i>	172
Figure 3.25 Absorption spectra for WT and mutant LytB proteins from <i>A. aeolicus</i> after Chelex treatment.....	173
Figure 3.26 EPR spectra of WT and mutant LytB proteins from <i>A. aeolicus</i>	174
Figure 3.27 EPR spectra of reduced WT and mutant LytB proteins from <i>A. aeolicus</i> after cluster reconstitution.....	176
Figure 3.28 Circular dichroism spectra of WT and mutant LytB proteins from <i>A. aeolicus</i>	178
Figure 3.29 ‘FeS _I ’ EPR signals detected in WT and mutant enzymes from <i>A. aeolicus</i>	180
Figure 3.30 Temperature behavior studies of FeS _I with reconstituted mutant enzymes from <i>A. aeolicus</i>	182
Figure 3.31 Overview of the signals detected in one-electron-reduced WT and mutant enzymes after incubation with HMBPP for 30 s.....	185
Figure 3.32 Detail of the active site of LytB protein crystallized in the presence of HMBPP	187
Figure 3.33 Overlay of the open form detected in LytB from <i>A. aeolicus</i> (blue - PDB ID 3DNF) and the closed form detected in LytB from <i>E. coli</i> (green – PDB ID 3KE8).....	189
Figure 3.34 Hypothetical Mechanism I	194
Figure 3.35 Hypothetical Mechanism II.....	195
Figure 3.36 Hypothetical Mechanism III.....	197

List of Abbreviations

IPP	Isopentenyl pyrophosphate
DMAPP	Dimethylallyl diphosphate
MVA	Mevalonate
HMGCoA	Hydroxymethylglutaryl-CoA
DOXP	1-deoxy-D-xylulose-5-phosphate
MEP	2-C-methyl-D-erythritol 4-phosphate
MEOP	2-C-methylerythrose 4-phosphate
CDP-ME	4-(cytidine 5'-diphospho)-2-C-methyl-D-erythritol
CDP-MEP	2-phospho-4-(cytidine 5'-diphospho)-2-C-methyl-D-erythritol
MEcPP	2-C-methyl-D-erythritol 2,4-cyclodiphosphate
HMBPP	1-hydroxy-2-methyl-2-(E)-butenyl-4-diphosphate
GcpE/IspG	1-hydroxy-2-methyl-2-(E)-butenyl-4-diphosphate synthase
LytB/IspH	(E)-4-hydroxy-3-methyl-2-butenyl diphosphate reductase
IUB	International Union of Biochemistry
HiPIPs	High potential Iron-Sulfur proteins
SAM	S-adenosyl-methionine
FNR	Fumarate and nitrate reduction regulatory protein
PFL	Pyruvate formate lyase
LAM	Lysine 2,3-aminomutase

FTR	Feredoxin:thioredoxin reductase
HDR	Heterodisulfide reductase
CoM-SH	Coenzyme M
CoB-SH	Coenzyme B
EPR	Electron paramagnetic resonance spectroscopy
ENDOR	Electron-nuclear double resonance
CD	Circular dichroism
MCD	Magnetic Circular dichroism
CW	Continuous wave
IPTG	Isopropyl- β -D-thiogalactoside
DEAE	Diethylaminoethyl
SDS-PAGE	Sodium dodecyl sulfate-polyacrylamide gel electrophoresis
<i>E. coli</i>	<i>Escherichia coli</i>
<i>A. aeolicus</i>	<i>Aquifex aeolicus</i>
<i>P. falciparum</i>	<i>Plasmodium falciparum</i>
WT	Wild-Type

Chapter 1: Literature Review

“GOLD is for the mistress – silver for the maid – copper for the craftsman cunning at his trade.” “Good!” said the Baron, sitting in his hall, “But Iron – Cold Iron – is master of them all.”

Rudyard Kipling “Cold Iron”

1.1 Isoprenoid Biosynthesis

Isoprenoids form one of the largest and most structurally diverse groups of essential metabolites present in all living organisms (Fig. 1.1). They are involved in myriads of bio-processes. Ubiquinone, plastoquinone, menaquinone, and phyloquinone function in redox reactions. Sterols and hopanoids are involved in membrane structure. Carotenoids and chlorophylls are important for light harvesting and photo protection. Steroid hormones, cytokinins, gibberellins, and abscisic acids play an important role in the regulation of growth and development. Isoprenoids also function as secondary metabolites in plants to protect them against herbivores and pathogens and to attract pollinators and seed-dispersing animals (1-3).

All isoprenoids are derived from the branched C₅ carbon skeleton of isoprene. The

enormous diversity of the structures is achieved by the number of repetitions of the branched C₅ carbon skeleton motif. The structures are further modified through cyclization reactions, rearrangements and oxidation of the carbon skeleton. Isopentenyl pyrophosphate (IPP) is the biological equivalent of isoprene and possesses the basic branched C₅ skeleton of the isoprenic unit (Fig. 1.2). The biosynthesis of isoprenoids starts with consecutive condensations of a unit of IPP to its isomer dimethylallyl diphosphate (DMAPP).

The mevalonate pathway was first revealed by incorporation experiments with isotopically labeled precursors for biosynthesis of cholesterol in liver tissues and ergosterol in yeast. This pathway (Fig. 1.3) starts from acetate, activated as acetyl coenzyme A, and yields IPP. It was widely accepted as the only pathway for all organisms since its discovery, and was the subject of intensive study (4-6).

However, labeling studies with certain bacteria and plants were inconsistent with the above conclusion. For instance, isotopically labeled mevalonate (MVA) and acetate in plant systems were not converted into carotenoids, monoterpenes or diterpenes (7-11). In contrast, efficient incorporation into sterols, triterpenoids and sesquiterpenoids was observed.

Another interesting example is mevinolin, a specific inhibitor of hydroxymethylglutaryl-CoA (HMGCoA) reductase, catalyzing the committed step of the MVA pathway (Fig. 1.3). Mevinolin strongly inhibits sterol biosynthesis in plants, but

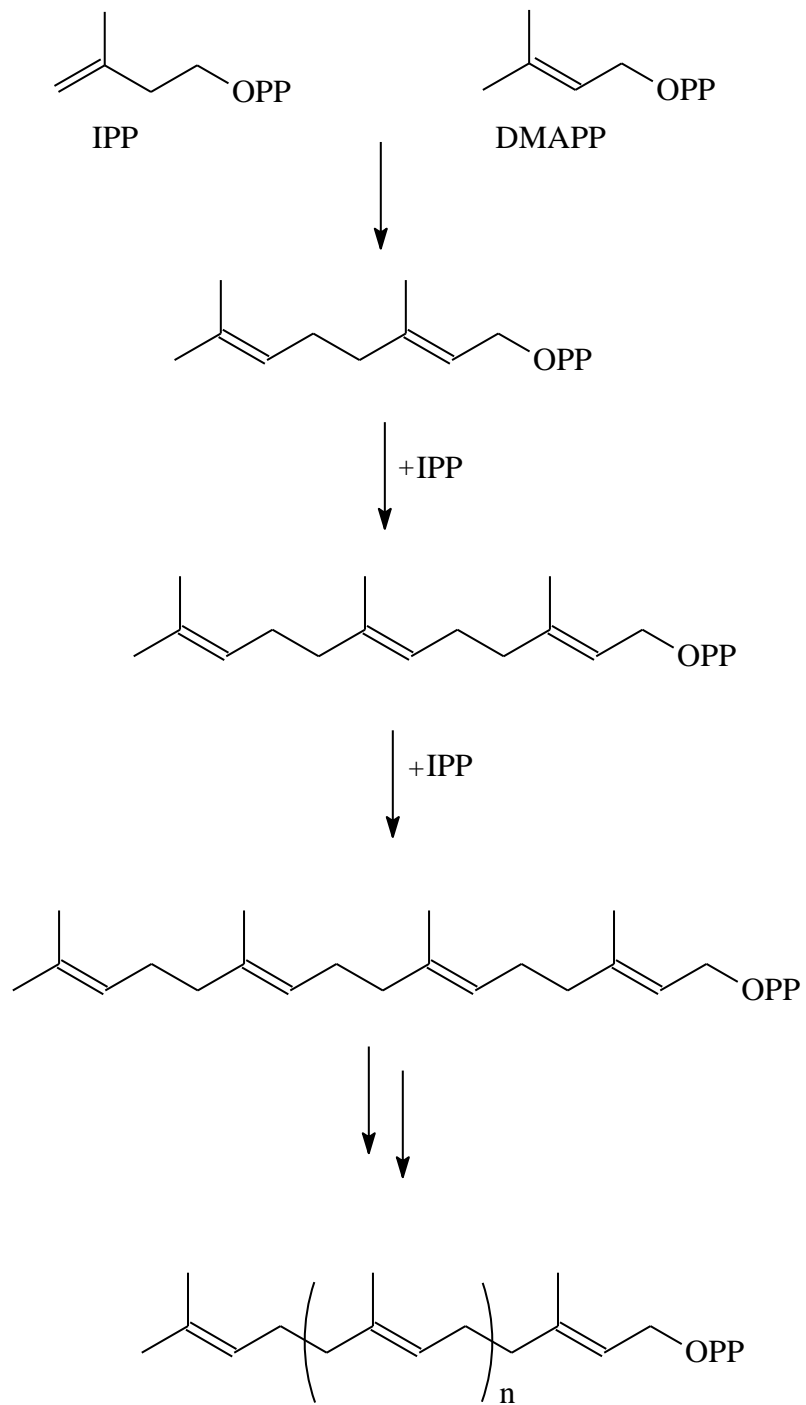


Figure 1.2 Isoprenic units

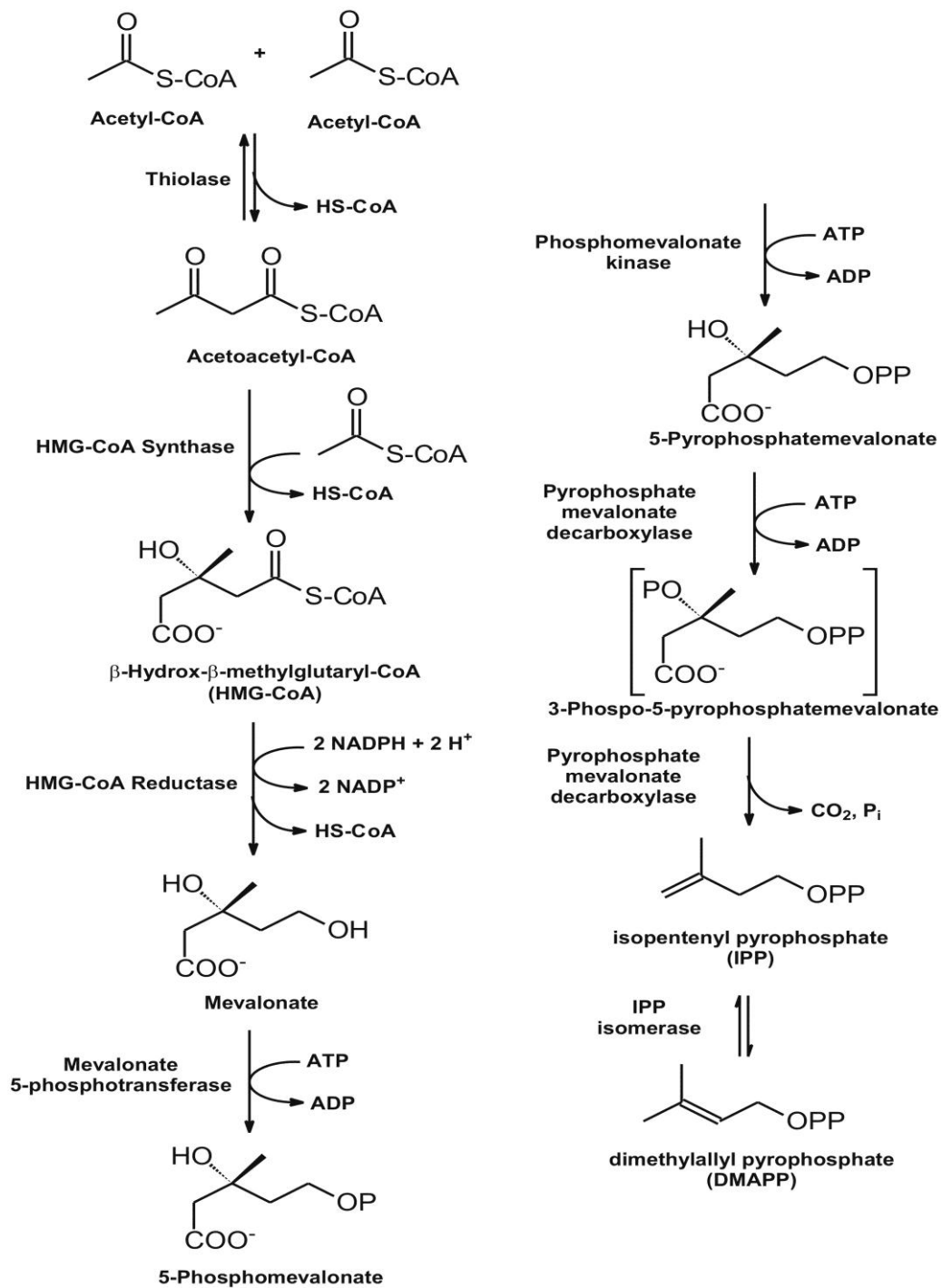


Figure 1.3 The mevalonate pathway for isoprenoid biosynthesis

it did not affect the formation of chloroplast pigments such as the carotenoids and chlorophylls containing the terpenic phytyl side-chain (12-14).

Furthermore, incorporation of MVA, MVA phosphate or MVA diphosphate into isoprenoids was not observed in a purified fraction of spinach chloroplasts or daffodil chromoplasts. Although, the key enzymes of the MVA pathway could not be characterized in these plant systems (15;16), it was unquestionable that IPP functions as the isoprenoid precursor in the chloroplast (17).

Based on these contradictory results, it was proposed that a second metabolic route or an alternative pathway existed for isoprenoid biosynthesis other than the mevalonate pathway. As a matter of fact, it was present but not yet discovered or identified at that time.

1.2 The DOXP Pathway

In 1996, the first reaction step of the alternative mevalonate-independent pathway for the formation of IPP and DMAPP was discovered in *Escherichia coli* by Rohmer in France (18). Since then the mevalonate-independent pathway for isoprenoid biosynthesis has been found to be widespread amongst phototrophic eukaryotes. This pathway is now known as the alternative pathway, the non-mevalonate pathway, the DOXP pathway (1-deoxy-D-xylulose-5-phosphate (DOXP) being the first intermediate) or the MEP pathway (2-c-methyl-D-erythritol 4-phosphate). Here we will refer to the pathway as the DOXP pathway. The DOXP pathway is utilized by several Gram-positive bacteria, most

of the Gram-negative bacteria, and apicomplexan parasites to synthesize isoprene precursors. In contrast, the mevalonate pathway is used by mammals (including humans), Gram-positive bacteria and archaea.

Figure 1.4 shows all reaction steps of the DOXP pathway.

- i. The first step is the condensation of pyruvate and D-glyceraldehyde 3-phosphate to generate DOXP. This reaction is catalyzed by DOXP synthase (EC 4.1.3.37). Studies have shown that the biosynthetic intermediate DOXP serves as a precursor not only for isoprenoid biosynthesis, but also for thiamine and pyridoxol biosynthesis. Thus, it is suggested that DOXP synthase is a key enzyme for both the DOXP pathway and biosynthesis of vitamins B₁ and B₆ (19-21).
- ii. The second step is the intramolecular acyloin rearrangement of DOXP to form a branched polyol derivative — 2-C-methylerythrose 4-phosphate (MEOP). It is followed by a reduction step to yield 2-C-methyl-D-erythritol 4-phosphate (MEP) catalyzed by DOXP reductoisomerase (also named IspC, EC 1.1.1.267). This step is the first of the more specific steps in the DOXP pathway, and Fosmidomycin was designated and synthesized as an antibiotic in 1980 (22) based on the studies of the reaction mechanism of this step.
- iii. The third step is the conversion of MEP into a diphosphocytidyl derivative — 4-(cytidine 5'-diphospho)-2-C-methyl-D-erythritol (CDP-ME) in the presence

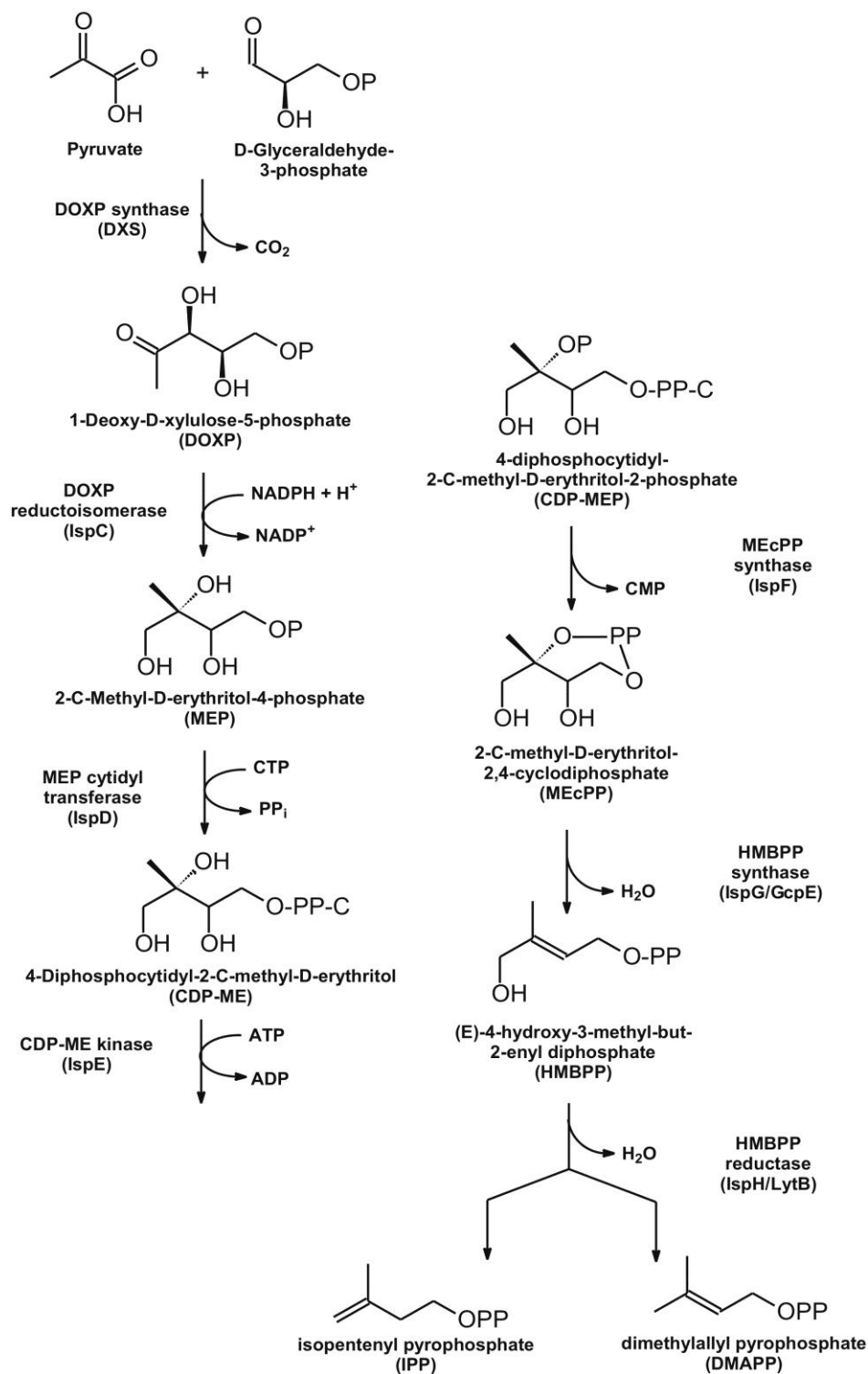


Figure 1.4 The DOXP pathway for isoprenoid biosynthesis

of CTP, which is catalyzed by MEP cytidyltransferase (also named IspD, EC 2.7.7.60).

- iv. The fourth step is catalyzed by CDP-ME kinase (also named IspE, EC 2.7.1.148), which introduces a phosphate residue into CDP-ME to yield a nucleotide derivative: 2-phospho-4-(cytidine 5'-diphospho)-2-C-methyl-D-erythritol (CDP-MEP) by using ATP as substrate.
- v. The fifth step is the elimination of CMP from CDP-MEP to generate 2-C-methyl-D-erythritol 2,4-cyclodiphosphate (MEcPP). It is catalyzed by MEcPP synthase (also named IspF, EC 4.6.1.12). MEcPP is a cyclic diphosphate compound containing the branched 5-carbon structure as well as the diphosphate group which is necessary for IPP and DMAPP.

So far, the crystal structures of IspC, IspD, IspE, and IspF proteins have been determined and the mechanisms for these enzymes have been elucidated. However, the last two steps have not yet been characterized.

- vi. The conversion of MEcPP into 1-hydroxy-2-methyl-2-(E)-butenyl 4-diphosphate (HMBPP) is achieved by the catalysis of (E)-4-hydroxy-3-methylbut-2-enyl diphosphate synthase (also named IspG or GcpE, EC 1.17.7.1). GcpE is an iron-sulfur protein with a [4Fe-4S] cluster which catalyzes the opening of the ring and concomitant two-electron reduction.

- vii. HMBPP is converted into IPP and DMAPP by the catalysis of (E)-4-hydroxy-3-methylbut-2-enyl diphosphate reductase (also named IspH or LytB, EC 1.17.1.2 which is another iron-sulfur protein that contains a [4Fe-4S] cluster.

1.3 Iron-Sulfur Proteins

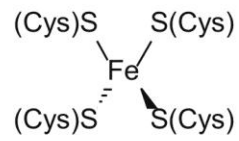
The research in this dissertation will focus on the two iron-sulfur-cluster containing proteins, GcpE and LytB. Therefore, this class of proteins will be described here. Numerous iron-sulfur proteins have been found in each of the three domains of living organisms, i.e. in Bacteria, Archaea and Eukarya. They are essential and form a major subset or class of the large and varied family of metalloenzymes. The iron-sulfur clusters consist of metal Fe ions along with various coordinating ligands. These include amino acid side chains, main chain peptide groups, cofactors, and/or relatively simple inorganic molecules or species like sulfide (S^{2-}), water (in the form of either H_2O or OH^-), carbon monoxide (CO), cyanide (CN^-) or substrate molecules, as well as some more complex molecules. Cysteine and histidine are the most common amino acid residues as protein ligands for metalloclusters, particularly for iron coordination. Commonly, the iron ions in iron-sulfur clusters are complexed with inorganic sulfide (S^{2-}) and cysteine thiols as ligands, where the cysteines provide the connection to the polypeptide chain of proteins. In contrast to most other cofactors, they are essentially of an inorganic nature consisting simply of iron cations (Fe^{2+} or Fe^{3+}) and inorganic sulfide anions (S^{2-}).

By the classification of International Union of Biochemistry (IUB), the iron-sulfur proteins are divided into two groups: simple and complex iron-sulfur proteins (23). Simple Fe-S proteins, which contain only iron-sulfur clusters, include rubredoxins, ferredoxins, hydrogenases, endonuclease III, and aconitase. Meanwhile, the complex ones have iron-sulfur clusters and other prosthetic groups, such as flavin, molybdopterin, and siroheme (24;25).

1.3.1 The Basic Structures of Iron-Sulfur Clusters

Four basic structures have been established for iron-sulfur proteins based on crystallographic structural analysis. They have been characterized both in model compounds and in naturally occurring proteins. As shown in Figure. 1.5, these basic chemical structures contain either one, two, three or four irons. Strictly speaking the single iron is not a cluster, but is normally included in this list. Rubredoxins, found in bacteria, contain a single Fe atom liganded to four Cys residues (A); the other forms are the rhombic two-iron-two-sulfur [2Fe-2S] clusters (B), the cuboidal three-iron-four-sulfur [3Fe-4S] clusters (C), and the cubane four-iron-four-sulfur [4Fe-4S] clusters (D). As mentioned above, the protein ligands are frequently Cys residues, but a number of other ligands have been found. For example, [2Fe-2S] clusters have also been found in which two His residues replace two of the thiol ligands. These clusters are called Rieske clusters.

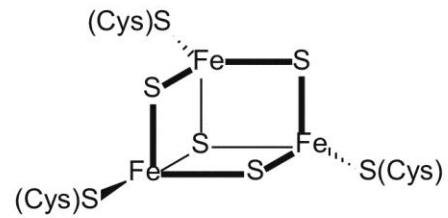
A: Single non-heme Iron



B: [2Fe-2S]



C: [3Fe-4S]



D: [4Fe-4S]

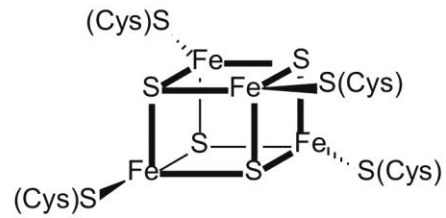


Figure 1.5 Basic types of iron-sulfur clusters

Multiple iron-containing clusters can be considered as higher-order derivatives of the basic core structures. External conditions, such as pH or the presence of oxidant or reductant may cause a number of interconversions or even destruction of the cluster type. These processes may introduce functional features relevant to catalytic activity, even some that are exotic or unexpected.

1.3.2 The Biological Functions of Iron-Sulfur Clusters

Iron-sulfur proteins are distinct in their biological functions as in electron transfer chains, reduction catalysis, photosynthesis, the respiratory chain and nitrogen fixation, due to the properties of iron-sulfur clusters (26).

Iron-sulfur clusters are some of the most ubiquitous and functionally versatile prosthetic groups in nature. Table 1.1 presents a summary of the biological functions and types of iron-sulfur clusters. In general, their functions can be classified into several groups.

Firstly, the iron-sulfur cluster functions as an electron carrier involved in electron transferring processes. Its primary biological role is to mediate electron transport in the photosynthetic and respiratory electron transport chains. This is achieved by the delocalization of electrons over both iron and sulfur atoms in iron-sulfur clusters. The redox potentials of iron-sulfur clusters have a range of over 1 volt. The 4Fe cluster in 7Fe-containing ferredoxins has a midpoint potential of -650 mV. On the other end of the continuum, high potential iron-sulfur proteins (HiPIPs), have potentials ranging from

Table 1.1 Biological functions and types of iron-sulfur clusters.

Adapted from (27)

Biological Functions	Cluster types	Examples
Electron transfer	[2Fe-2S]	Ferredoxins; Redox enzymes
	[3Fe-4S]	
Coupled electron/proton transfer	[4Fe-4S]	Rieske protein
	[2Fe-2S]	Nitrogenase
	[8Fe-7S]	(de)Hydratases
Substrate binding and activation	[4Fe-4S]	Radical SAM enzymes
	Ni-Ni-[4Fe-4S], [Ni-4Fe-5S]	Acetyl-CoA synthase
Fe or cluster storage	[4Fe-4S]	Sulfite reductase
	[4Fe-4S]	Ferredoxins
Structural	[4Fe-4S]	Polyferredoxins
	[4Fe-4S]	Endonuclease III
	[4Fe-4S]	MutY
	[2Fe-2S]	SoxR
Regulation of gene expression	[4Fe-4S] / [2Fe-2S]	FNR
	[4Fe-4S]	IRP
	[2Fe-2S]	IscR
Regulation of enzyme activity	[4Fe-4S]	Glutamine PRPP amidotransferase
	[2Fe-2S]	Ferrochelatase
Disulfide reduction	[4Fe-4S]	Ferredoxin:thioredoxin reductase
	[4Fe-4S]	Heterodisulfide reductase
Sulfur donor	[2Fe-2S]	Biotin synthase

+350 mV up to +450 mV. Others with 4Fe, 3Fe, 2Fe clusters, such as rubredoxins and Rieske clusters, have potentials in between.

Catalysis is another major biological function of iron-sulfur clusters in both redox and non-redox enzymes. The hydrolyases class and radical SAM families are prominent substrate binding examples. In the case of aconitase, the substrate citrate binds to the unique uncoordinated iron (28). For radical SAM (S-adenosyl-methionine) families, the reductive cleavage and generation of the 5'-deoxyadenosyl radical is facilitated by SAM binding *via* the amino and carboxylate groups of the methionine fragment (29;30). The detailed mechanisms of aconitase and radical SAM enzymes will be discussed in section 1.3.4. Recently, two more roles have emerged for iron-sulfur clusters: disulfide reduction and sulfur donation.

An iron-sulfur cluster has been discovered in some DNA repair proteins, including endonuclease III, MutY from *E. coli* and UV endonuclease from *Micrococcus luteus* (31). The iron-sulfur clusters play a structural role by stabilizing the protein's tertiary structure, but are not involved in the catalytic mechanism (32;33).

Iron-sulfur clusters have been implicated as sensors in transcriptional or translational regulation of gene expression in bacteria. In the regulation of enzyme activity, the iron-sulfur cluster functions as a "circuit breaker" by altering activity in response to external stimuli, such as presence or absence of oxygen. This is achieved by cluster assembly, repair, or interconversion. For instance, in the SoxR/SoxS system in *E. coli*, SoxR is a redox-responsive transcriptional activator containing a pair of [2Fe-2S] clusters.

The inactive SoxR with a $[2\text{Fe-2S}]^{1+}$ state is activated by oxidation to the $[2\text{Fe-2S}]^{2+}$ state by superoxide stress or nitric oxide. As a result of the oxidation, the transcriptional expression of SoxS is stimulated, which in turn results in the activation of the transcription of multiple enzymes active in the oxidative stress response (34-36). Another interesting example is the fumarate and nitrate reduction regulatory (FNR) protein, which is a bacterial transcription factor controlling the gene expression in both aerobic and anaerobic metabolism. The FNR dimer is transcriptionally active with a $[4\text{Fe-4S}]^{2+}$ bridged between the two subunits in the absence of oxygen. The presence of oxygen results in the dissociation of the active FNR dimer into an inactive monomeric, $[2\text{Fe-2S}]^{2+}$ -containing form (36).

1.3.3 Magnetic and Electronic Properties of Iron-Sulfur Proteins

The iron ions in iron-sulfur clusters show different magnetic and electronic properties due to differences in oxidation states, spin states, orbital contributions, and coordination numbers. The diamagnetic species with closed shells of electrons have no inherent magnetic properties. In contrast, paramagnetic ones, with unpaired electrons, respond to a magnetic field.

Different electronic structures are associated with certain iron-sulfur clusters (Fig. 1.6). The iron ion can be in the +2 or +3 oxidation states with high-spin configurations when coordinated by four cysteine sulfurs, so the ferric ions (d^5) give a spin $S = 5/2$ and the ferrous ions (d^6) give a spin $S = 2$ (37). The cluster oxidation states are calculated

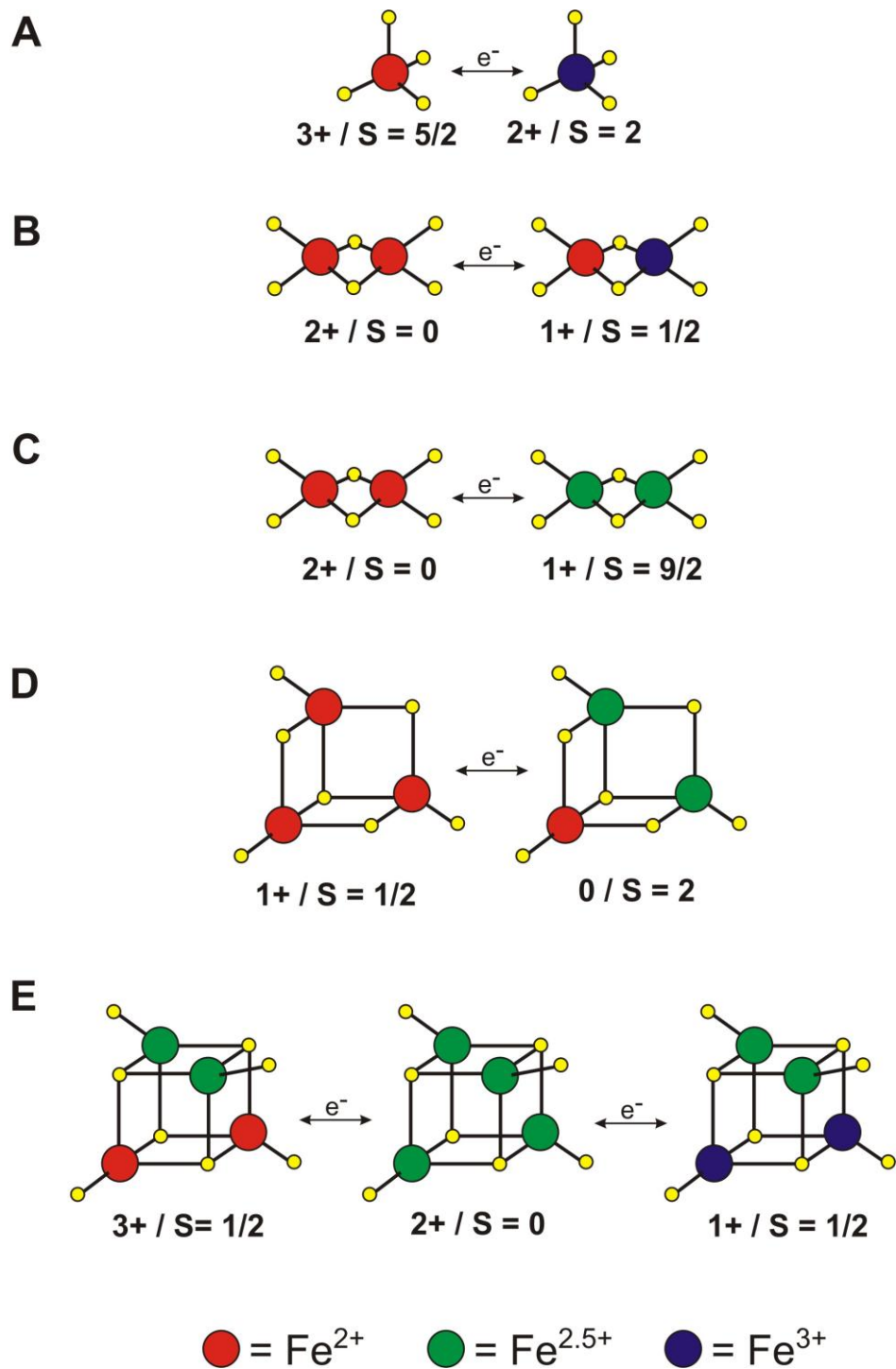


Figure 1.6 Magnetic Properties of iron-sulfur clusters. Adapted from (41)

from the iron and non-cysteine sulfur atoms present. The typical stable cluster oxidation states are +1 and +2 for the [2Fe-2S] clusters, 0 and +1 for the [3Fe-4S] clusters, +1 and +2 for ferredoxin-type [4Fe-4S] clusters, and +2 and +3 for HiPIP [4Fe-4S] clusters. Electrons can be delocalized so that the valences of individual iron atoms lie between ferrous and ferric forms. In multiple iron-containing clusters the iron atoms are magnetically coupled in pairs. The oxidized 2Fe cluster ([2Fe-2S]²⁺) has a spin of zero due to the antiferromagnetic coupling between two ferric ions. The reduced cluster ([2Fe-2S]¹⁺) has a spin of $S = 1/2$ due to antiferromagnetic coupling of high spin Fe²⁺ ($S = 2$) and high spin Fe³⁺ ($S = 5/2$) (38;39). The oxidized 3Fe cluster ([3Fe-4S]¹⁺) has a spin of $S = 1/2$ which results from the coupling of an intermediate spin $S = 2$ (or 3), yielded by the coupling of two ferric ions ($S = 5/2$), with the third ferric ion. The reduced cluster ([3Fe-4S]⁰) has a spin of $S = 2$. Here the ferromagnetic coupling of a ferric ion and a ferrous ion generates an intermediate spin $S = 9/2$, which is antiferromagnetic coupled to the third ferric ion ($S = 5/2$) (40). In the [4Fe-4S] clusters, four iron atoms form two pairs, each of which is coupled ferromagnetically, and then the spins of these two primary pairs are coupled antiparallel to give the total spin for the whole system. The ferric-ferric coupling yields spin $S = 5$, while spin S is equal to $9/2$ in the case of ferric-ferrous coupling and spin $S = 4$ for ferrous-ferrous coupling. The spin state $S = 1/2$ for [4Fe-4S]³⁺ is generated by the further coupling of the ferric-ferric pair with a ferric-ferrous pair, while the spin state $S = 0$ for [4Fe-4S]²⁺ is generated by the further coupling of two ferric-ferric pairs. Further coupling of a ferric-ferrous pair with a

ferrous-ferrous pair leads to the spin state $S = 1/2$ or $3/2$ for $[4\text{Fe-4S}]^{1+}$, and the coupling of two ferrous-ferrous pairs results in the spin state $S = 4$ for $[\text{Fe}_4\text{-S}_4]^0$. That has been observed in a very limited amount of proteins.

These specific magnetic and electronic molecules are derived from EPR, ENDOR, and Mössbauer spectroscopy studies. A great deal of valuable information can be supplied by these techniques about both the iron ions and their ligands. It is helpful in the investigation of iron-sulfur clusters and their function in iron-sulfur proteins.

1.3.4 Classes of [4Fe-4S] Clusters Involved in Catalysis

The [4Fe-4S] cluster is the most common and most representative form of the iron-sulfur clusters. Our target proteins, GcpE and LytB, are iron-sulfur proteins containing a [4Fe-4S] cluster in their active sites. Based on previous studies performed by our group, it has been proposed that the [4Fe-4S] cluster might be involved in substrate binding. So far, there are three classes of proteins that contain a 4Fe cluster which is directly involved in catalysis.

1.3.4.1 Hydrolyases

The first class is the hydrolyase class. Redox chemistry is not involved in the dehydration reactions which are catalyzed by this class of enzymes. Instead, substrates coordinate to a $[4\text{Fe-4S}]^{2+}$ cluster at the so-called unique iron site, which is not coordinated by the sulfur atom of a cysteine residue.

Aconitase (28;42) catalyzes the conversion of citrate into isocitrate via the intermediate *cis*-aconitate in the citric acid cycle (43) (Fig. 1.7). The [4Fe-4S]²⁺ cluster serves as a Lewis acid to facilitate a heterolytic C-O bond cleavage (28;42). The as-isolated aconitase is inactive and present in the oxidized form, a [3Fe-4S]¹⁺ cluster. The [3Fe-4S]¹⁺ cluster can be converted into a [4Fe-4S] cluster by the addition of iron during catalysis (44). This specific fourth iron position can be recovered after it was removed during the isolation. When the substrate citrate binds to this specific fourth iron atom, it is hexacoordinated. The ligands are three S²⁻ atoms of the cluster, a carboxyl oxygen and hydroxyl group of the substrate, and a solvent water molecule. Coordination of the hydroxyl group to the fourth iron atom of the cluster makes this hydroxyl group a better leaving group. Then, the dehydration reaction is facilitated to generate *cis*-aconitate. The *cis*-aconitate “flips” 180° within the active site about its carbon-carbon double bond. The isocitrate is produced by adding the hydroxyl group to the carbon of the double bond which is closer to the coordinated carboxyl group.

EPR analysis has indicated the direct interaction of the substrate with the [4Fe-4S]²⁺ cluster (45). Mössbauer spectroscopy and ¹H, ²H, ¹⁷O-ENDOR spectroscopy demonstrated that the substrate citrate is bound to the unique iron *via* one of the oxygen atoms from a carboxyl group and one oxygen atom from a hydroxyl group (28;45).

1.3.4.2 The Class of Radical SAM Proteins

The second class is formed by the recently discovered superfamily of Radical SAM

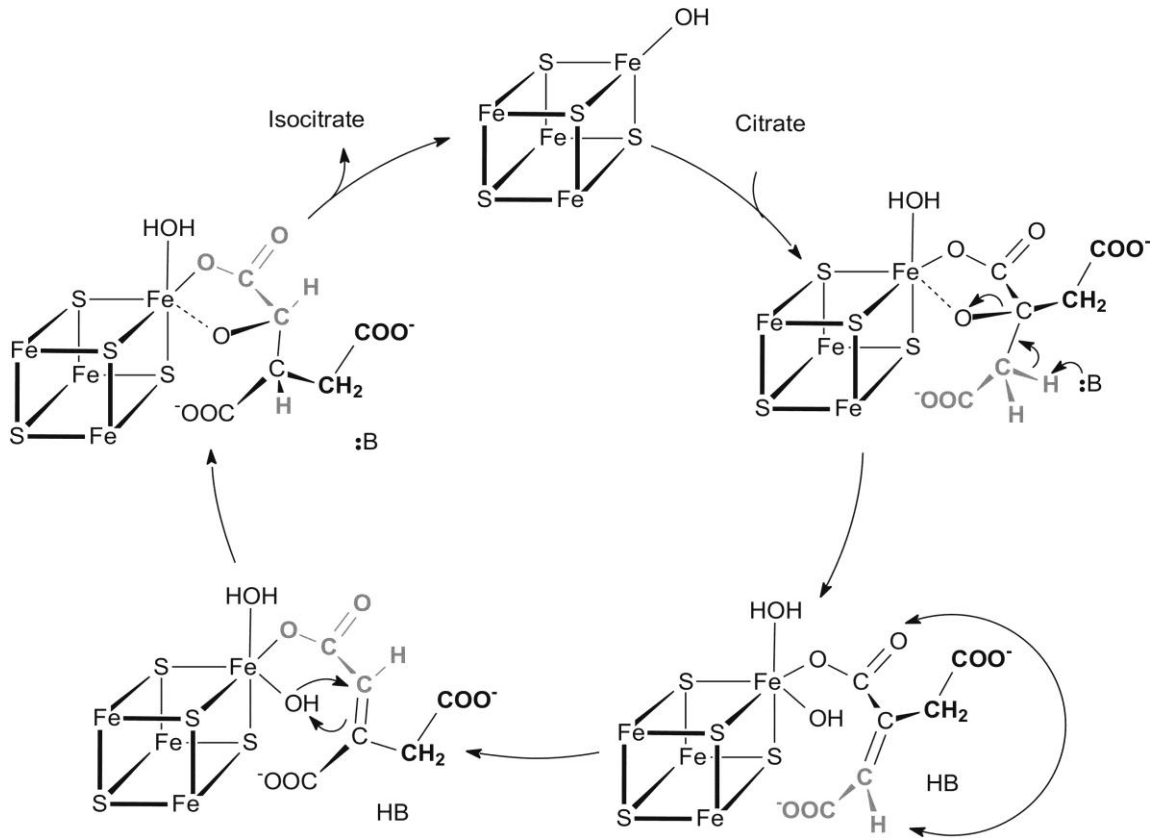


Figure 1.7 Reaction catalyzed by Aconitase

enzymes that function in DNA repair, and the biosynthesis of vitamins, coenzymes and antibiotics (46-49). Radical SAM enzymes are present in plants, bacteria and mammals, and catalyze a variety of reactions including methylations, sulfur insertion, isomerization, ring formation, anaerobic oxidation and protein radical formation.

Although they have diverse biological functions, radical SAM enzymes contain a [4Fe-4S] cluster coordinated by three cysteinyl residues. All radical SAM enzymes share a conserved “CxxxCxxC” motif (where C is cysteine and x is any amino acid), that is responsible for [4Fe-4S] cluster coordination. The fourth iron site (non-cysteine coordinated) is ligated during catalysis by SAM through its amino group and one carboxylate oxygen (Fig. 1.8 A) (50;51). This direct binding of SAM to the cluster was proven by ¹⁵N and ¹⁷O ENDOR spectroscopy for BioB, pyruvate formate lyase (PFL) activase and lysine 2,3-aminomutase (LAM) (51;52). The [4Fe-4S] cluster is utilized for the reductive cleavage of SAM to form a 5'-deoxyadenosyl radical (Fig. 1.8 B and C) (53-55).

SAM coordinates to the unique iron of the cluster *via* its amino and carboxylate groups (47-49;56). The cleavage can be reversible, as seen in lysine-2,3-aminomutase; or irreversible, as seen in the PFL system. The fates of the radical species can also be different. In the case of PFL the radical is generated on the PFL-activating enzyme and is subsequently transferred to PFL for the actual reaction, while in the case of biotin synthase the radical is generated on the 4Fe cluster present in one active site and is transferred to a second active site that contains a 2Fe cluster for the sulfur insertion step.

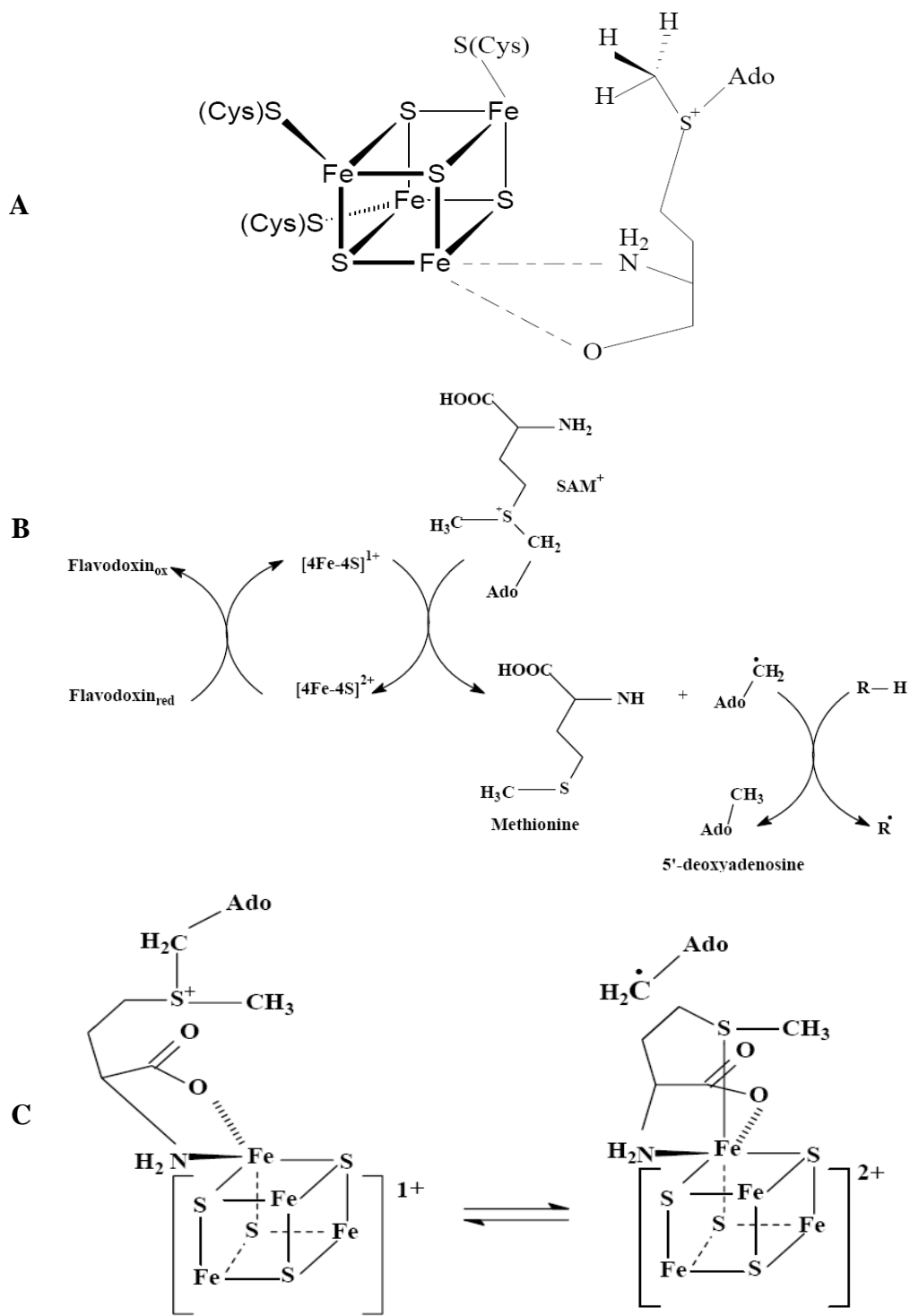


Figure 1.8 Binding of S-adenosyl methionine and reaction catalyzed by Radical SAM enzymes

The common thread in the function of these enzymes is that a powerful oxidizing agent, the 5'-deoxyadenosyl radical, is generated from SAM by using a low potential [4Fe-4S]²⁺ cluster as a strong reducing agent. The reduction of the [4Fe-4S]²⁺ cluster to the [4Fe-4S]⁺ cluster is achieved by different electron donors for different systems. Reduced flavodoxin is used by some radical SAM enzymes in *E. coli* (57-60). Adrenodoxin is used for plant biotin synthase (61-63). This reduction also can be achieved by an external electron donor like dithionite.

SAM is present as a co-substrate or cofactor near the [4Fe-4S] cluster. It is necessary for radical SAM enzymes to execute carbon based radical chemistry so that the electron can be transferred from the [4Fe-4S]⁺ cluster to the sulfonium atom of SAM. This electron transfer results in the break-down of SAM into methionine and a 5'-deoxyadenosyl radical. Then, the 5'-deoxyadenosyl radical takes a hydrogen atom away from an organic substrate to generate a substrate radical, or from an amino acid residue to form an amino acid radical.

1.3.4.3 Ferredoxin:thioredoxin Reductase (FTR) and Heterodisulfide Reductase (HDR)

The third class contains only two proteins: ferredoxin:thioredoxin reductase (FTR) and heterodisulfide reductase (HDR) (64-66). FTR catalyzes the reduction of a disulfide bond present on the substrate thioredoxin. It contains a [4Fe-4S] cluster as the prosthetic group. HDR catalyzes the reversible reduction of heterodisulfide (CoM-S-S-CoB) to the

thiol-coenzymes: coenzyme M (CoM-SH) and coenzyme B (CoB-SH). It contains a [4Fe-4S] cluster as well.

FTR uses yet another type of mechanism involving a 4Fe cluster. This enzyme functions as a switch, using single electrons donated by ferredoxin for a two electron reduction of a disulfide bond. The active site of FTR contains the unique combination of a [4Fe-4S] cluster in close proximity to an active-site disulfide bond (67). This [4Fe-4S] cluster mediates the electron transfer from reduced ferredoxin to the active site disulfide.

It has been proposed that in the first step, an electron from ferredoxin is used to break this disulfide bond, turning one cysteine sulfur into a thiyl radical and the other into a thiolate (Fig. 1.9). The thiolate sulfur is then free to interact with the disulfide bond on thioredoxin; thus, a new disulfide bond is formed between a cysteine residue of FTR and a cysteine residue of thioredoxin (68). The transfer of the second electron from the second ferredoxin results in the cleavage of the inter-protein disulfide bond, leaving two cysteine sulfhydryl groups on thioredoxin and regenerating the disulfide bond in the active site of FTR (69;70).

A key aspect of this mechanism is that the intermediate thiyl radical formed after the first electron transfer is stabilized through bonding with an iron atom of the 4Fe cluster. In this case, there is no unique iron ion, but one iron ends up with five sulfur ligands, three from the cluster and two from different cysteine residues. This thiyl-cluster complex is EPR-active and has unique electronic and magnetic properties (69;70). In particular, it has a more radical-type behavior, based on the fact that the EPR

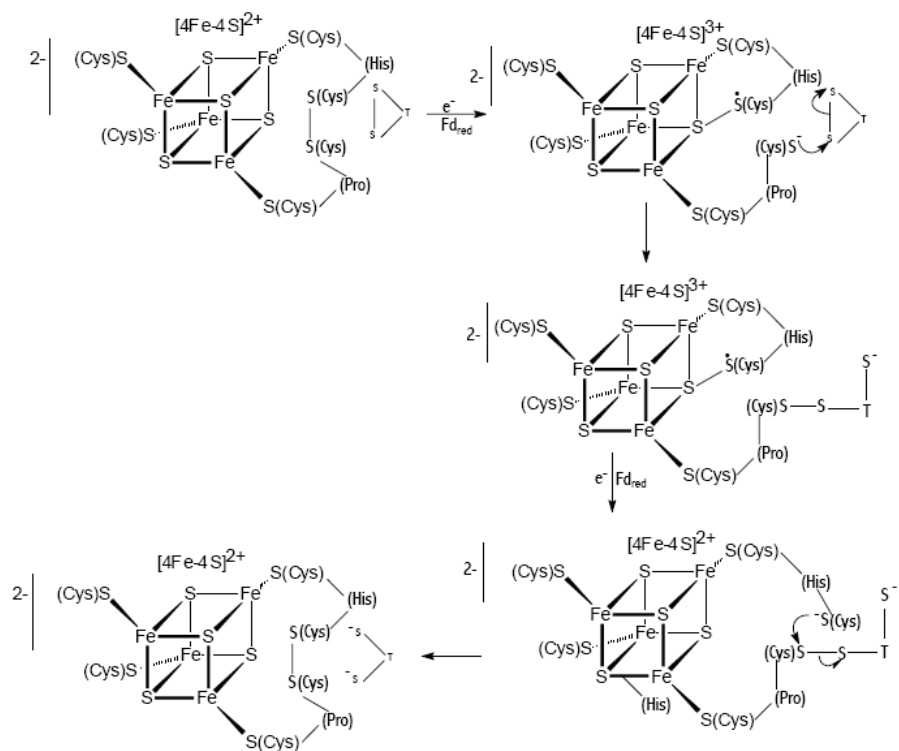


Figure 1.9 Proposed mechanism for FTR. Adapted from (71)

signal can be detected in EPR spectroscopy at much higher temperatures (up to 160 K) than any other type of 4Fe cluster.

HDR catalyzes a reversible heterodisulfide/dithiol cleavage by two one-electron reduction steps. It has been proposed that the first one-electron reduction breaks the heterodisulfide to form CoB-SH and a $[4\text{Fe-4S}]^{3+}$ cluster with CoM-S⁻ attached to a cluster sulfur (Fig. 1.10). Another proposed mechanism for this step is the cleavage of heterodisulfide generated CoB-SH and a transient intermediate. This transient intermediate is coordinated by CoM-S-S-Cys heterodisulfide; subsequently, the cleavage of this heterodisulfide forms Cys-S⁻ and CoM-S⁻ which are coordinated to the $[4\text{Fe-4S}]^{3+}$ cluster (Fig. 1.11). In the second electron reduction step, the $[4\text{Fe-4S}]^{3+}$ cluster is reduced back to $[4\text{Fe-4S}]^{2+}$ form with concomitant dissociation and protonation of CoM-S⁻ (65).

1.4 Physical Methods for Studying Metal Centers in Metalloproteins

Bioinorganic and/or biophysical techniques are making increasingly important contributions to a deeper and more thorough understanding of the enzymatic roles of metal-ion-containing cofactors. The striking features of metalloenzymes are the electronic and magnetic properties of their metal ions. The advantages and properties of the different techniques are summarized in Table 1.2. For instance, electron paramagnetic resonance spectroscopy (EPR) can be applied when the metal ion in a metal-enzyme system has an unpaired electron. While Mössbauer spectroscopy is mostly restricted to iron containing samples, electron-nuclear double resonance (ENDOR) is related to

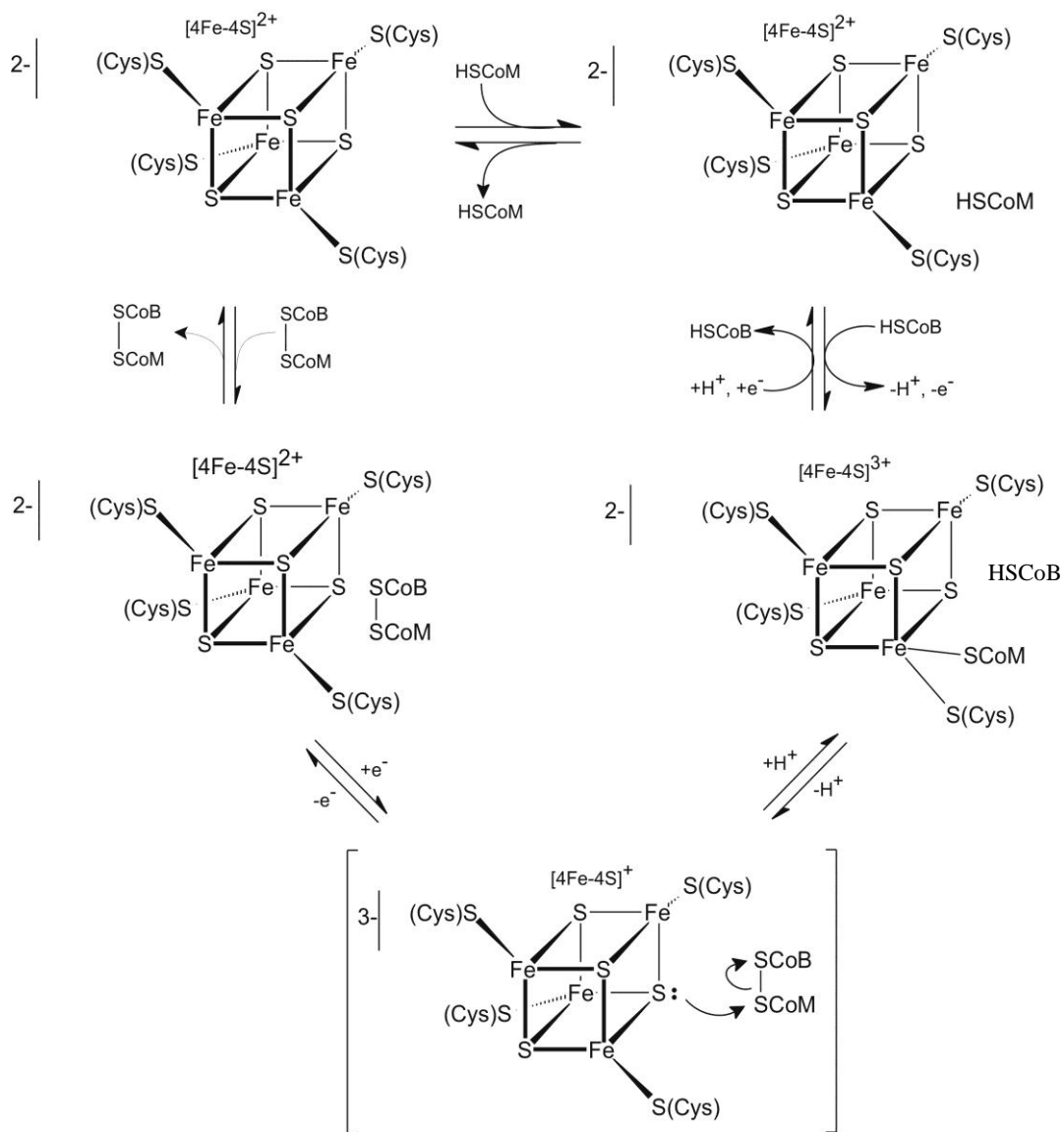


Figure 1.10 Proposed mechanism I for HDR. Adapted from (53)

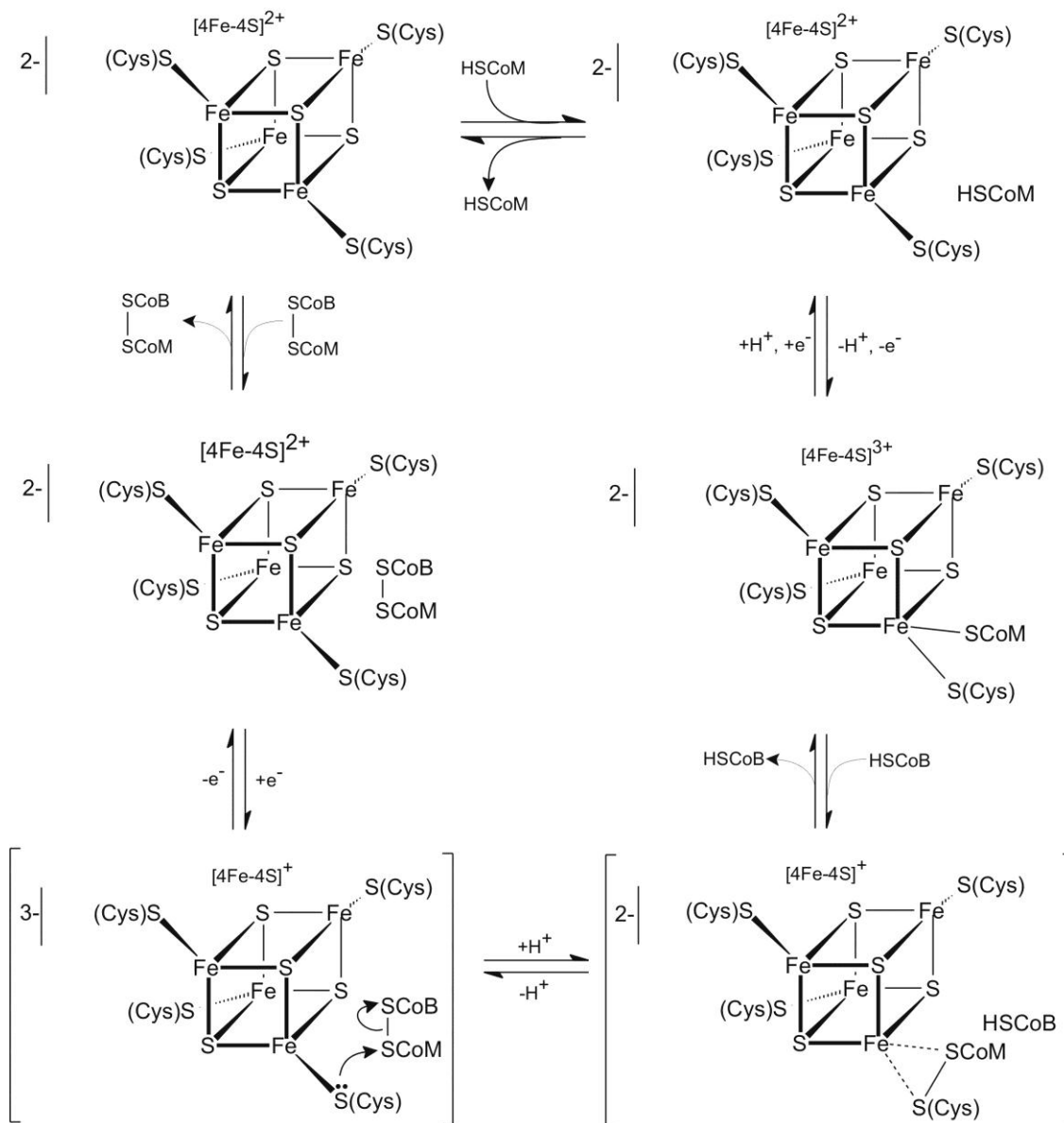


Figure 1.11 Proposed mechanism II for HDR. Adapted from (53)

Table 1.2 The advantages and properties of different techniques

methods	Advantageous	Parameters
Electronic absorption spectroscopy	Ligand-field; charge-transfer excited states	Energies, intensities, and band shapes
Vibrational spectroscopy	Identification of ligands coordinated to a metal center	Energies, intensities, and polarizations
Electron paramagnetic resonance (EPR)	Paramagnetic species	g-value, coupling constants, and relaxation time
Electron-nuclear double resonance (ENDOR)	Combine the high sensitivity of EPR and the high resolution of NMR	coupling constants, distance and angle of ligand binding
Mössbauer spectroscopy	Oxidation states, spin states, and chemical environment	Quadrupole coupling, isomer shift
Resonance Raman spectroscopy	Chromophoric active sites, and metal-ligand bonding	Intensity profiles, and depolarization ratios

the electron-nuclear spins interactions, circular dichroism (CD) is based on the asymmetric nature of the metal site, magnetic circular dichroism (MCD) and UV-visible absorption focus on the electronic transition. However, no unique spectroscopic method appears to satisfy all criteria, and thus, it is not expected that one single method will solve all questions about a particular enzyme. A combination of physical methods is required to probe the metal center in the metalloprotein, because each provides information on only certain properties of the metal ion.

1.4.1 Electron Paramagnetic Resonance Spectroscopy (EPR)

Since its development in 1944 by Zavoisky (72), electron paramagnetic resonance spectroscopy has become a popular, useful and necessary physical technique to investigate those species which contains one or more unpaired electrons. These include inorganic and organic free radicals, triplet states, and some systems of transition metal ions. Thus, metalloenzymes containing these species are ideal targets for EPR analyses. The main applications of EPR to metalloenzymes are: a) to probe electronic and magnetic properties and local environment of a paramagnetic center; b) to elucidate parts of the mechanism relevant to metal centers; c) incorporation experiments to investigate diamagnetic systems in combination with spin probes (73) or spin labels (74).

In addition, EPR has been regarded as an exceptional technique for insight into the structure of the paramagnetic cofactors in the free enzyme, intermediates, and product complexes (75). In fact, kinetic studies on those paramagnetic species involved in

catalysis can also be performed by EPR (76).

EPR is of particular interest in the study of iron-sulfur proteins. As described in Section 1.4.1, the different types of iron-sulfur clusters have different electronic and magnetic properties; therefore, those paramagnetic states should show typically distinct EPR spectra with specific peaks and patterns (Fig. 1.12). Thus, EPR spectroscopy is of great importance in gathering detailed information and to reveal properties about iron-sulfur proteins.

1.4.1.1 The Basic Principles of EPR

EPR spectroscopy is a technique emphasizing paramagnetic systems containing unpaired electrons. It is known that the electron can be either stabilized ($m_s = -1/2$) or destabilized ($m_s = +1/2$) when it is exposed to a magnetic field. The interaction of these magnetic moments with the magnetic field is called the Zeeman effect (Fig. 1.13). Based on the quantum concepts and equations, the electronic-Zeeman energies of spin state are

$$E = - \mu \cdot \mathbf{B} \quad (1)$$

$$\text{where } \mu = -g \cdot \beta \cdot \mathbf{S} \quad (2)$$

(μ is the magnitude of the magnetic moment of the electron which is related to the angular momentum, g is called the g factor or spectroscopic splitting factor, β is the Bohr magneton, \mathbf{S} is the symbol for the total spin associated with the electron, and \mathbf{B} is the external magnetic field). Thus, the magnitude of Zeeman effects varies linearly with the intensity of the magnetic field:

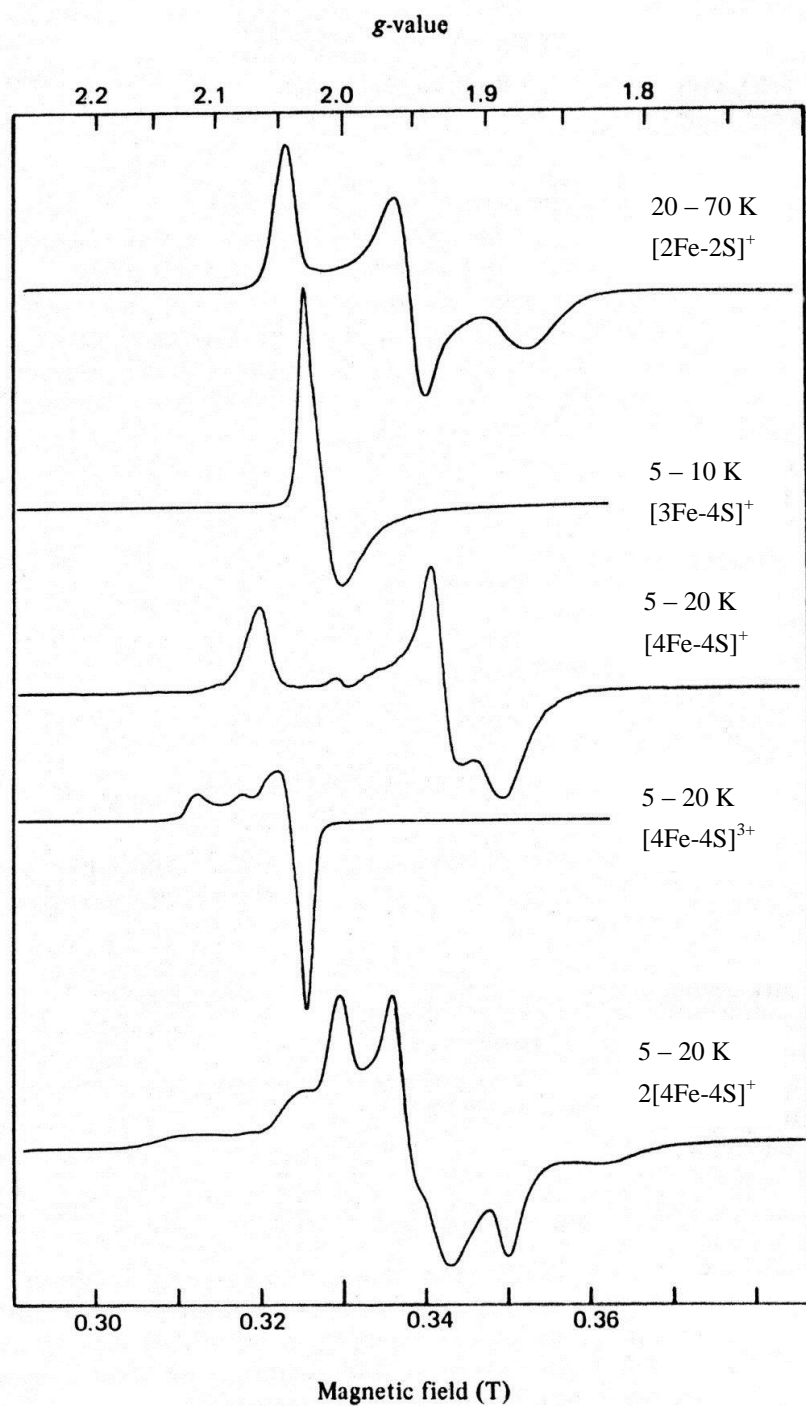


Figure 1.12 EPR spectra of iron-sulfur clusters. Adapted from (77;78)

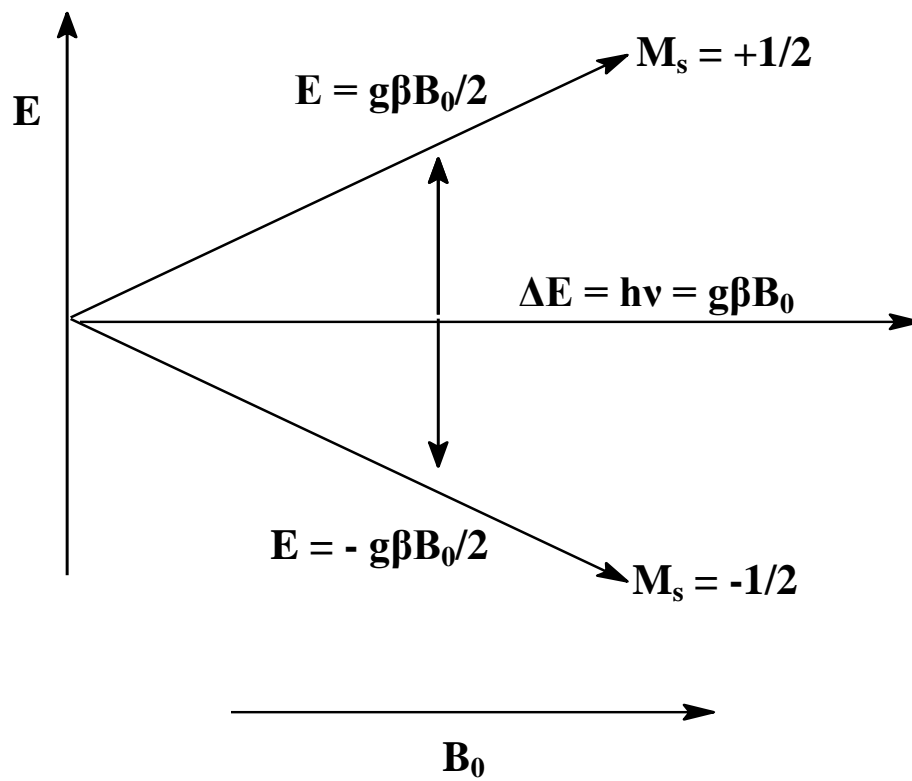


Figure 1.13 Zeeman effect

$$\Delta E = g \cdot \beta \cdot B_0 \quad (3)$$

The necessary requirement for EPR absorption is that the net population difference is big enough, which means that the number of transitions from the more-stable to the less-stable states must exceed those in the opposite direction. The resonance condition for “flipping the spin” is governed by Equation (4),

$$\Delta E = h\nu = g \cdot \beta \cdot B_0 \quad (4)$$

where h is Planck’s constant and ν is the microwave frequency. This resonance condition combines the electronic radiation ($h\nu$), the magnetic field (B_0), and the orbital behavior of the electron (g). The selection rule for an EPR transition is $\Delta M_s = \pm 1$ unit. The first derivative is generated by measuring the change of slope per increment in B_0 when the magnetic field is swept through the absorption envelope (79-81) (Fig. 1.14).

1.4.1.2 g-factor

The g factor, a tensor quantity, depends on the orientation of the molecules or ions in the applied magnetic field; therefore, the g factor is a key parameter of matter. Based on the equation (4), a g value can be calculated by the energy between the two spin levels as shown in equation (5).

$$g = h\nu/\beta B_0 = 0.714484 \nu \text{ (in MHz) } / B_0 \text{ (in Gauss)} \quad (5)$$

The g factor equals 2.00232 for a free electron, but it can vary due to interactions with the electrons and nuclei it resides on.

$$g = g + \Delta g \quad (6)$$

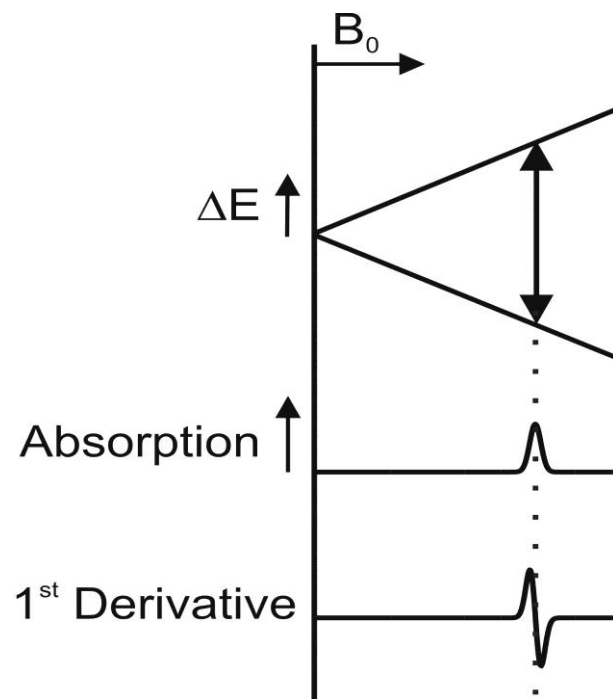


Figure 1.14 1st Derivative

The g-factor is anisotropic when the molecules are randomly oriented. The amount of g anisotropy is related to the degree of spin-orbit coupling. When the sample is in a low-viscosity solution, the anisotropic effect will be averaged to zero because the molecules are tumbling quickly. However, if the sample is in an immobilized orientation, the g factor will change according to the anisotropy. Typically, biological samples are prepared by freezing solutions for EPR analyses. As a result, the molecules are oriented randomly with respect to the applied magnetic field.

The g factors are designated as g_x , g_y , and g_z respectively according to the principal axis system (82-84). Figure 1.15 shows three possibilities of g anisotropy, the relevant EPR signal, and first derivative line shapes from the simplest example with spin $S = 1/2$. When $g_x = g_y = g_z$, it is designated as isotropic; when $g_x = g_y \neq g_z$, it is axial; and when $g_x \neq g_y \neq g_z$, it is rhombic (85;86).

1.4.1.3 The Magnetic Interactions

The electronic Zeeman interaction between the external magnetic field, B_0 , and the electron spin, S , is not the only determinant for the EPR peaks and patterns, although it will generate EPR spectra. Two other classes of interactions (Fig. 1.16), including electron-nuclear spin interactions and electron-electron spin interactions, are also present in biomolecular samples and have remarkable effects on EPR spectra.

Electron-nuclear spin interactions, including nuclear hyperfine and superhyperfine interactions (Fig. 1.17), exist when the paramagnetic electron of interest is within the

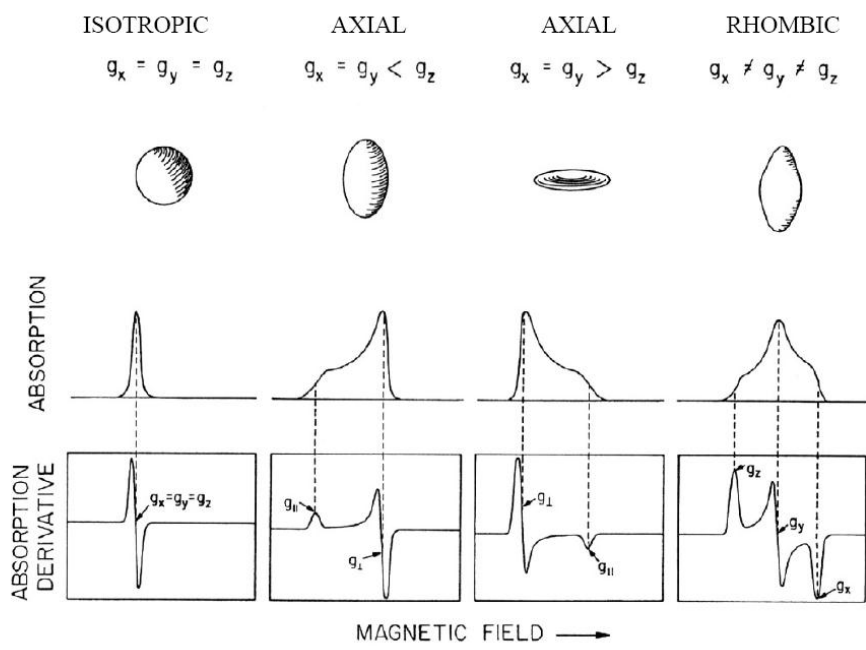
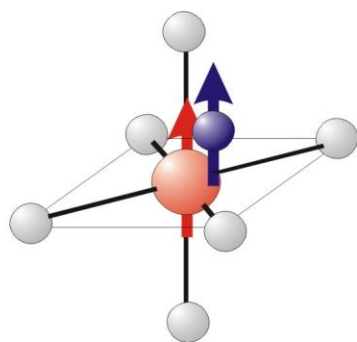
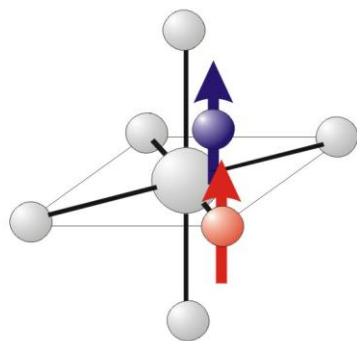


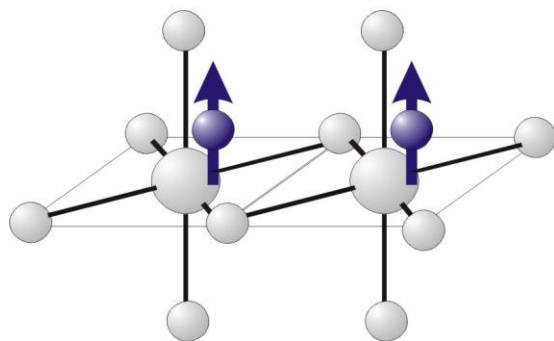
Figure 1.15 g-anisotropy. Taken with permission from (87). (Copyright University Science Books)



Hyperfine



Superhyperfine



Electron Spin-Spin

Figure 1.16 Interactions: electron-nuclear & electron-electron spin interactions

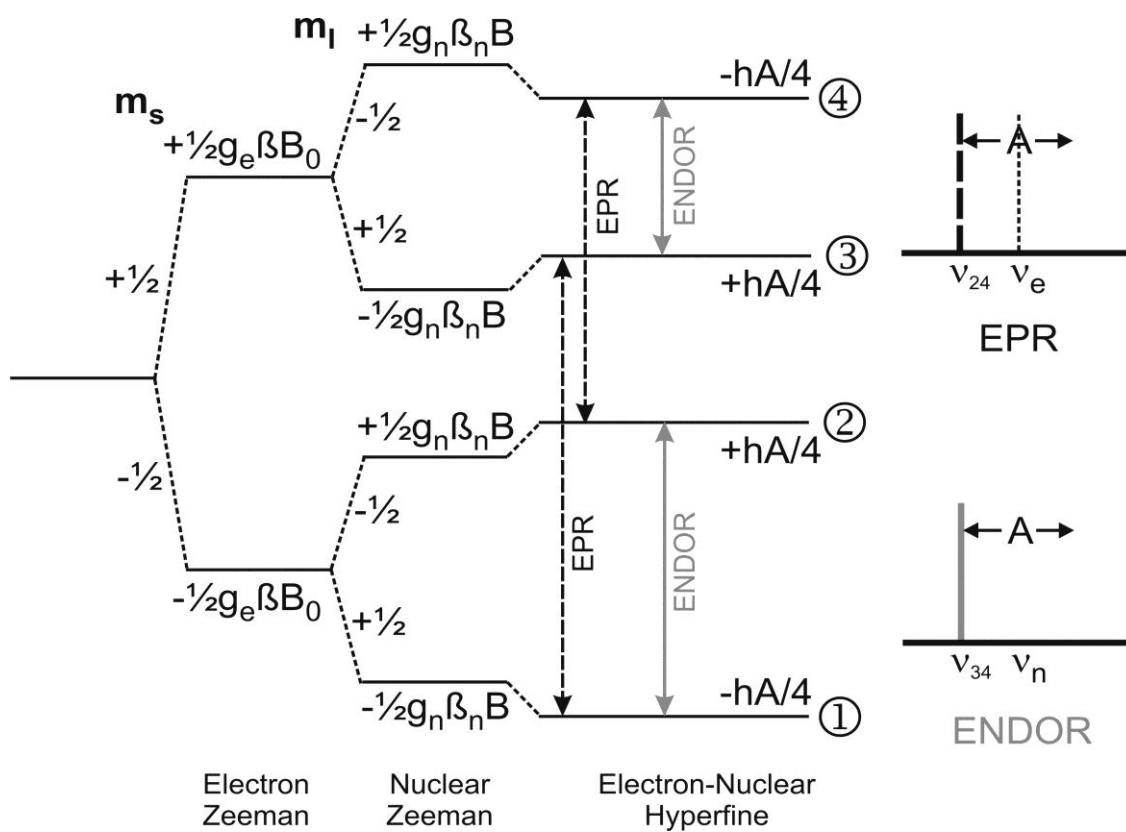


Figure 1.17 Hyperfine interaction

effect sphere of a nucleus that possesses a nuclei spin and consequently a nuclear magnetic moment. The hyperfine and superhyperfine interactions invariably perturb the EPR spectra, although they are weaker by one or more orders of magnitude than the electronic Zeeman interaction. The hyperfine interactions are very common because the relevant nucleus is part of the parent atom of the paramagnet. The electron interacts with its own nucleus. The superhyperfine interactions occur when the electron interacts with the relevant nucleus which belongs to a different part of the molecule. The most common case is the ligand to the metal. Table 1.3 and Table 1.4 summarize some properties of those nuclei which are of interest and often appear in bio-molecules. These nuclei can contribute to a magnetic field because they have a nuclear spin, charge, and a nuclear moment. The resulting nuclear hyperfine field can combine with the applied field to provide the magnetic field, satisfying the resonance condition.

Electron-electron interactions are induced when the paramagnetic electron of interest is close to a second paramagnetic one. Electron-electron interactions are either stronger or weaker than the electronic Zeeman interaction. They produce greater effects in the case of high-spin systems or exchange-coupled systems. Meanwhile, smaller effects are generated by the dipolar interactions when two or more paramagnetic clusters are present, including intermolecular or intramolecular dipolar interactions. The weaker effects occur with two paramagnets separated by distances greater than 10 \AA , often due to direct or ligand mediated bonding. In comparison, there is a profound effect on the EPR spectrum when two paramagnets are closer to each other than 10 \AA . This can be seen

Table 1.3 Ligand atom nuclear spins and their EPR superhyperfine patterns

Ligand	Isotope	Spin (abundance)	EPR lines
H	1, 2	$1/2 + 1$ (0.015%)	2 + 3
C	12, 13	$0 + 1/2$ (1.1%)	1 + 2
N	14, 15	$1 + 1/2$ (0.4%)	3 + 2
O	16, 17, 18	$0 + 5/2$ (0.04%)	1 + 6
F	19	$1/2$	2
P	31	$1/2$	2
S	32, 33, 34	$0 + 3/2$ (0.8%)	1 + 4
Cl	35, 37	$3/2$	4
As	75	$3/2$	4
Se	76, 77, 78, 80, 82	$0 + 1/2$ (7.6%)	1 + 4
Br	79, 81	$3/2$	4
I	127	$5/2$	6

Table 1.4 Transition metal nuclear spins

Metal	Valency	Isotope	Spin (abundance)	EPR lines
V	IV	51	7/2	8
Mn	II	55	5/2	6
Fe	III	54, 56, 57, 58	0 + 1/2 (2%)	1 + 2 (1%)
Co	II	59	7/2	8
Ni	III,I	58, 60, 61, 62, 64	0 + 3/2 (1%)	1 + 4 (0.25%)
Cu	II	63, 65	3/2	4
Mo	V	92, 94, 95, 96, 97, 98, 100	0 + 5/2 (25%)	1 + 6 (4%)
W	V	180, 182, 183, 184, 186	0 + 1/2 (14%)	1 + 2 (7%)

for example in Figure 1.12, bottom spectrum, where the interaction of two 4Fe cluster causes the appearance of a completely different EPR signal that also displays broad wings on each side of the main signal.

1.4.1.4 Frequency

Continuous wave (CW) spectrometry is commonly used for bioinorganic studies. The technique utilizes a fixed frequency and a variable magnetic field; thus, the abscissa is then proportional to reciprocal energy. CW at X-band microwave (mw) frequency (~9.5 GHz) was the main technique for EPR studies until the end of the 1980s. Thereafter, high-field EPR spectrometers equipped to irradiate much higher energies (so-called Q-band (mw frequency ~35 GHz) and W-band (mw frequency ~95 GHz) CW) were constructed and have become more and more popular for metalloprotein studies. Due to the EPR line widths' dependency on the magnetic field, different fixed frequencies can be utilized for different purposes. The lower frequency along with the narrow field range can be used to enhance the resolution of otherwise unresolved hyperfine structure, and the higher frequency along with the wide field range can be used to enhance the resolution associated with g anisotropy. This distinguishes the spectral features due to g anisotropy from those due to hyperfine and other interactions.

1.4.2 Electron-Nuclear Double Resonance (ENDOR)

Electron-nuclear double resonance (ENDOR) was introduced in 1956 by Feher (88)

and is another physical method widely used to obtain structural information about paramagnetic centers. In 1967, ENDOR was first used for the study of metalloproteins by Eisenberger and Pershan (89). The ENDOR spectrometer can be considered as consisting of a standard CW EPR spectrometer with an NMR radio frequency source and radio frequency coil within the microwave cavity.

Equation (10) shows the spin Hamiltonian for the simplest system, with effective electron spin $S=1/2$ and a single nucleus with $I = 1/2$:

$$H = g_e \beta_e B S - g_n \beta_n B I + S A I \quad (10)$$

(β_e and β_n are electronic and nuclear magnetons; g and g_n are the electronic and nuclear g tensors; A is the anisotropic hyperfine tensor)

The third term in equation (10) is present for the hyperfine interaction between the electronic and nuclear spins, which have been discussed in section 1.4.1.3. Normally, the energies obey the following order: electron Zeeman (~ 10 GHz) $>$ nuclear Zeeman ($1\sim 15$ MHz) \approx electron-nuclear hyperfine ($0\sim 10$ MHz). Consequently, the hyperfine interaction, which is generally too small to be resolved within the natural width of the EPR line, can be resolved with ENDOR.

In practice, the EPR signal at a given field is saturated initially by increasing microwave power, and then the radio frequency is modulated until it induces a nuclear transition. The number of ENDOR splitting lines that result from a nucleus with spin I , is governed by the $4 I$ rule. The basic parameters of the g factor, hyperfine coupling constant A , and quadrupole coupling constant are useful for ENDOR spectra analysis.

Though ENDOR spectroscopy is not capable of spin quantification, it offers fundamental advantages for cluster type identification, as well as structural and functional characterization. Magnetic nuclei like ^1H , ^2H , ^{13}C , ^{14}N , ^{15}N , ^{17}O , ^{31}P , and ^{33}S (as shown in Table 1.3) are very commonly and universally present as ligands to the transition metal clusters, which may contain another set of magnetic nuclei like V, Mn, Fe, Co, Ni, Cu, Mo, and W (as shown in Table 1.4). Consequently, those nuclei in the vicinity of the paramagnetic metal ion can be detected and identified by ENDOR. ENDOR studies confirmed that the Rieske cluster [2Fe-2S] of phthalate dioxygenase (90) was coordinated by the two imidazole nitrogens from histidine. Additionally, isotopic labeling experiments have additional applications in ENDOR spectroscopy. For instance, ^{57}Fe ($I = 1/2$) and ^{95}Mo ($I = 5/2$) have been used to introduce superhyperfine interaction into carbon monoxide dehydrogenase (91;92) and nitrogenase (92), respectively. Furthermore, ENDOR can be used to investigate the circumstances of direct ligand binding or ligand-mediated bonding when the ligand contains nuclei with nuclear spins. Not only can the presence of the particular ligand nucleus be identified, but also the distances and angles between the ligand and the paramagnetic centers can be determined by ENDOR. For iron-sulfur proteins, hydrogen binding to the clusters has also been investigated using ENDOR spectroscopy with ^2D substitution (93). Moreover, iron-sulfur clusters present in both the substrate free and bound forms have also been probed, as in the case of aconitase (28;94).

ENDOR has some advantages over both EPR and NMR. ENDOR resonance lines

are inherently narrower and sharper than those in EPR. The reasons are two-fold. Firstly, compared to EPR, most nuclei under ENDOR studies possess longer relaxation time; their spectral resolution is significantly enhanced by an order of a thousand or more in frequency. Another reason for the better spectral resolution of ENDOR is that the density of nuclear hyperfine lines is decreased; they are additive in ENDOR but multiplicative in EPR. In addition, unlike EPR, ENDOR is able to identify the interacting nucleus directly *via* the nuclear g_n factor with $I = 1/2$ and the nuclear quadrupole coupling constant for nuclei with $I > 1/2$. In comparison to NMR, the sensitivity of ENDOR is increased by orders of magnitude because of the large Boltzmann population difference of electron spin energy levels.

1.5 Significance of Research

All mammals use the mevalonate pathway for the synthesis of IPP and DMAPP, while an alternative pathway, the DOXP pathway, is the sole pathway in several pathogenic bacteria and apicomplexan parasites. Many of these microbes cause infections in hospitals and diseases like tuberculosis, plague, cholera, anthrax, malaria, gastro-intestinal ulcers, and venereal diseases (95). For instance, malaria caused by *Plasmodium falciparum* is a threat to human health, which is very common in most developing countries, and causes 1.5~2.7 million deaths among children and pregnant women annually (96). Table 1.5 summarizes some diseases related to organisms that use the DOXP pathway. Thus, the enzymes involved in the DOXP pathway are hot targets for

Table 1.5: Human bacterial pathogens that use the DOXP pathway

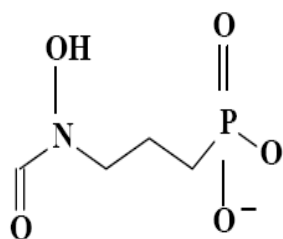
Microorganism	Examples of diseases
Gram-negative cocci	
<i>Neisseria meningitidis</i>	Meningitis, Waterhouse–Friderichsen syndrome
<i>N. gonorrhoea</i>	Gonorrhoea
Gram-positive non-spore-forming rods	
<i>Corynebacterium diphtheriae</i>	Diphtheria
<i>Listeria monocytogenes</i>	Listeriosis
<i>Actinomyces israelii</i>	Keratoactinomycosis
<i>Nocardia sp.</i>	Bronchopneumonia
Gram-positive spore-forming rods	
<i>Bacillus anthracis</i>	Anthrax
<i>Clostridium histolyticum</i>	Gas gangrene
<i>C. difficile</i>	Colititis
<i>C. botulinum</i>	Botulism
<i>C. tetani</i>	Tetanus
Gram-negative rods	
<i>E. coli</i>	Enterocolitis, urinary tract infection
<i>Salmonella typhi</i>	Typhus
<i>S. paratyphi</i>	Bacteraemia
<i>Shigella sonnei</i>	Typhus
<i>Yersinia enterocolitica</i>	Enterocolitis, diarrhoeal disease
<i>Y. pseudotuberculosis</i>	Gastroenteritis
<i>Y. pestis</i>	Plague
<i>Klebsiella pneumoniae</i>	Pneumonia
<i>K. ozaenae</i>	Ozena, atrophic rhinitis
<i>K. rhinoscleromatis</i>	Rhinoscleroma
<i>Serratia marcescens</i>	Wound infections, sepsis
<i>Proteus sp.</i>	Wound infections, sepsis
<i>Pseudomonas sp.</i>	Wound infections, sepsis
<i>Brucella abortus</i>	Morbus Bang
<i>B. melitensis</i>	Malta fever
<i>Francisella tularensis</i>	Tularaemia
<i>Haemophilus influenzae</i>	Pneumonia, meningitis
<i>H. ducreyi</i>	Ulcer molle
<i>Pasteurella sp.</i>	Wound infections, sepsis
<i>Bordetella pertussis</i>	Pertussis

Table 1.5: continuation

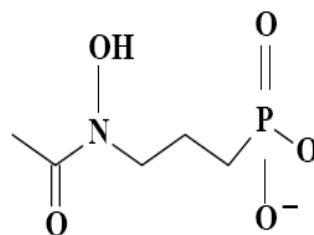
Microorganism	Examples of diseases
Gram-negative/spiral-shaped bacteria	
<i>Vibrio cholerae</i>	Cholera
<i>H. pylori</i>	Gastritis Type B
<i>Campylobacter jejuni</i>	Enterocolitis
Spirochaetal bacteria	
<i>Treponema pallidum</i>	Syphilis
<i>T. vincenti</i>	Necrotizing gingivitis
<i>Leptospira icterohaemorrhagica</i>	Morbus Weil
Acid-fast rods	
<i>M. tuberculosis</i>	Tuberculosis
<i>M. bovis</i>	Tuberculosis
<i>M. avium-intracellulare</i>	Tuberculosis, cervical adenitis
<i>M. leprae</i>	Leprosy (Morbus Hansen)
Obligate intracellular bacteria	
<i>Chlamydia psittaci</i>	Psittacosis
<i>C. trachomatis</i>	Chlamydia
<i>C. pneumoniae</i>	Pneumonia
<i>C. lymphogranulomatosis</i>	Lymphogranulomatosis
Wall-less bacteria	
<i>Mycoplasma penetrans</i>	Urogenital infections

researchers to develop new drugs or antibiotics.

Up to now, Fosmidomycin, an antibiotic isolated from *Streptomyces lavendulae*, is the only known drug to inhibit DOXP reductoisomerase (97-100), a key enzyme of the DOXP pathway (Fig. 1.18). Effectiveness of fosmidomycin and the derivative FR900098 against malaria was demonstrated in phase II clinical studies in Gabon and Thailand. This effect, however, was restricted by the reappearance of parasites in some of the patients during follow-up. This can be attributed to a low plasma half-life of the drugs, which shows the need for an improved drug or drug combination. Patients infected by acute uncomplicated *Plasmodium falciparum* could be treated with fosmidomycin, but an overall cure rate of 95% was achieved in clinical studies where fosmidomycin was tested in combination with clindamycin (97;98;101-103). Research efforts now focus on finding fosmidomycin analogs that can work as stand alone drugs (104-112), but also on finding inhibitors for the other enzymes in the DOXP pathway. These inhibitors are expected to show a pronounced synergistic increase in efficiency when used in combination with fosmidomycin. So, a full understanding of the pathway and the reaction mechanisms of the individual proteins could lead to new methods for killing these organisms. It is obvious that the knowledge of the function of GcpE and LytB in the DOXP pathway is necessary and urgent for the development of new drugs. Since many isoprenoids have biotechnological applications as drugs, flavors, pigments, perfumes and agrochemicals, the detailed knowledge of the mechanism of the enzymes and the



Fosmidomycin



FR90098

Figure 1.18 Fosmidomycin

regulation of the pathway might also benefit the biotechnological production of commercially interesting isoprenoids, such as carotenoids (113;114). Additionally, the DOXP pathway is present in the plastids of plants; thus, the development of novel herbicides that are less harmful to humans might be achieved by targeting this pathway (115;116).

Our target proteins: GcpE and LytB, are involved in the catalysis of the last two steps of the DOXP pathway. Previous studies by our group showed that both of them contain [4Fe-4S] clusters in their active sites. Several paramagnetic species have been detected by EPR spectroscopy and are considered to be involved in the reaction mechanism. The EPR analysis of these signals indicated that the [4Fe-4S] cluster might be involved in substrate binding and stabilization of reaction intermediates. ENDOR spectroscopy showed a very weak coupling from the phosphate group of substrate to the cluster. The reaction mechanisms cannot be illustrated clearly because the information we have now is not conclusive. Therefore, more measurements and analysis have to be performed in the future on these proteins to obtain more detailed information to clarify the reaction mechanisms of these two enzymes.

My research work is focusing on the spectroscopic characterization of the iron-sulfur clusters present at the active sites, the identification of new paramagnetic species trapped by EPR during the reactions, the investigation of binding models, and the clarification of the reaction mechanisms for GcpE and LytB. For GcpE, the reduction of iron-sulfur cluster is studied and different midpoint potentials for two separate electron

transfer steps are discovered. For LytB, site-directed mutagenesis is applied to several totally conserved residues for spectroscopic analysis. Based on all data, new mechanisms are proposed.

Chapter 2: (E)-4-hydroxy-3-methylbut-2-enyl Diphosphate Synthase

2.1 Introduction

(E)-4-hydroxy-3-methylbut-2-enyl diphosphate synthase (also named GcpE or IspG) is an iron-sulfur-cluster-containing protein. It catalyzes the conversion of 2-C-methyl-D-erythritol-2,4-cyclodiphosphate (MEcPP) into (E)-4-hydroxy-3-methylbut-2-enyl diphosphate (HMBPP), in the penultimate step of the DOXP pathway (5;117-120).

Previous research showed that the protein from *Thermus thermophilus* contains a single [4Fe-4S] cluster (121). Although the 410 nm band in the UV-visible absorbance spectra of as-isolated protein indicated the presence of [3Fe-4S]⁺ or [4Fe-4S]²⁺ clusters in the protein, further EPR and Resonance Raman spectroscopy studies confirmed the presence of only a [4Fe-4S]²⁺ cluster (121). This is in contrast to the work by other groups that also indicated the presence of other types of iron-sulfur clusters, including [2Fe-2S] and [3Fe-4S] clusters in GcpE from the same and different sources (122;123). Determination of iron content in both as-isolated enzyme (121;122;124) or reconstituted enzyme, showed the presence of 3.9 to 4.4 iron ions per enzyme molecule (125). Thus, only one cluster is coordinated by the protein. The other cluster types detected are

probably artifacts from exposure of the 4Fe cluster to oxygen or inherent instability of the cluster itself.

Comparison of the amino acid sequence of the GcpE enzyme from different sources show that there are three highly conserved cysteine residues present (Fig. 2.1). The thiol groups of the Cys residues are likely involved in coordinating the cluster. It is not known what the fourth ligand to the cluster is. Analysis of GcpE from *E. coli* and *Arabidopsis thaliana* by Mössbauer spectroscopy showed the presence of a $[4\text{Fe-4S}]^{2+}$ cluster containing three tetrahedrally sulfur-coordinated $\text{Fe}^{2.5+}$ and one tetrahedrally coordinated $\text{Fe}^{2.5+}$ with three sulfur ligands and one non-sulfur ligand (122).

One complication in the study of GcpE is that the cluster is not easily reduced. Generally, a $[4\text{Fe-4S}]^{1+}$ cluster can be generated from a $[4\text{Fe-4S}]^{2+}$ cluster under strong reducing conditions. This reduction of the cluster is indicated by bleaching of the typical 410 nm band in absorption spectroscopy. However, the UV-visible absorption of the incubated solution of as-isolated GcpE protein with dithionite does not show this bleaching of the 410 nm band (Fig. 2.2). Moreover, the EPR spectrum of the solution does not show a $[4\text{Fe-4S}]^{1+}$ signal either. These two observations suggest that this protein is not reduced by dithionite alone.

In the presence of dithionite and the substrate MEcPP, paramagnetic species can be detected. Figure 2.3 shows the EPR spectra of samples prepared with the freeze-quench method. From 28 ms to 0.5 s an isotropic signal with $g = 2.005$ can be detected. When the incubation time was increased to 1.2 s, a second, more rhombic signal ($g_{xyz} =$

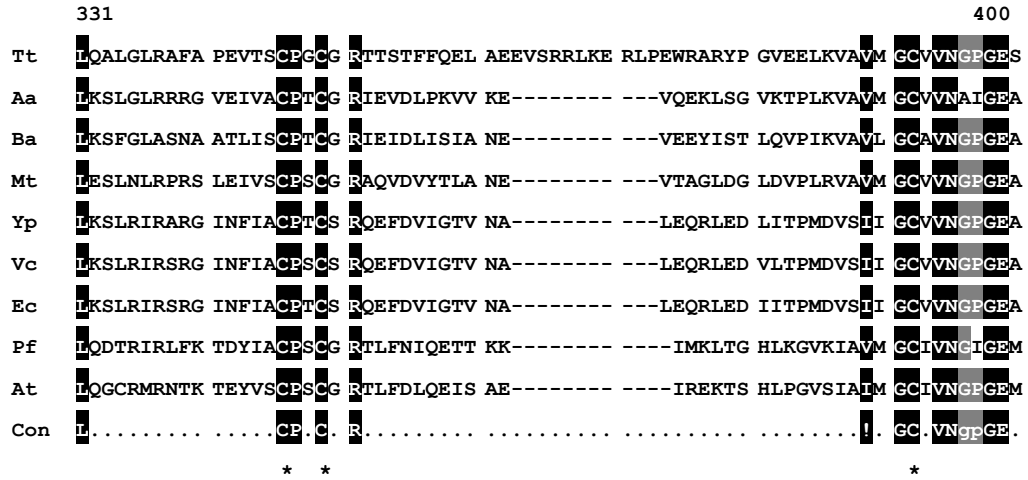


Figure 2.1: The alignment of GcpE sequences. The consensus sequence is based on alignment (Blosum62-12-2) of 63 unique sequences. For clarity only 9 are shown. Black background, 100% conserved; gray background, 80% conserved. Asterisks indicate the position of the conserved Cys residues. Abbreviations: Tt, *Thermus thermophilus* HB27; Aa, *Aquifex aeolicus*; Ba, *Bacillus anthracis* A2012; Mt, *Mycobacterium tuberculosis* H37Rv; Yp, *Yersinia pestis*; Vc, *Vibrio cholerae*; Ec, *Escherichia coli* K12; Pf, *Plasmodium falciparum* 3D7; At, *Arabidopsis thaliana*.

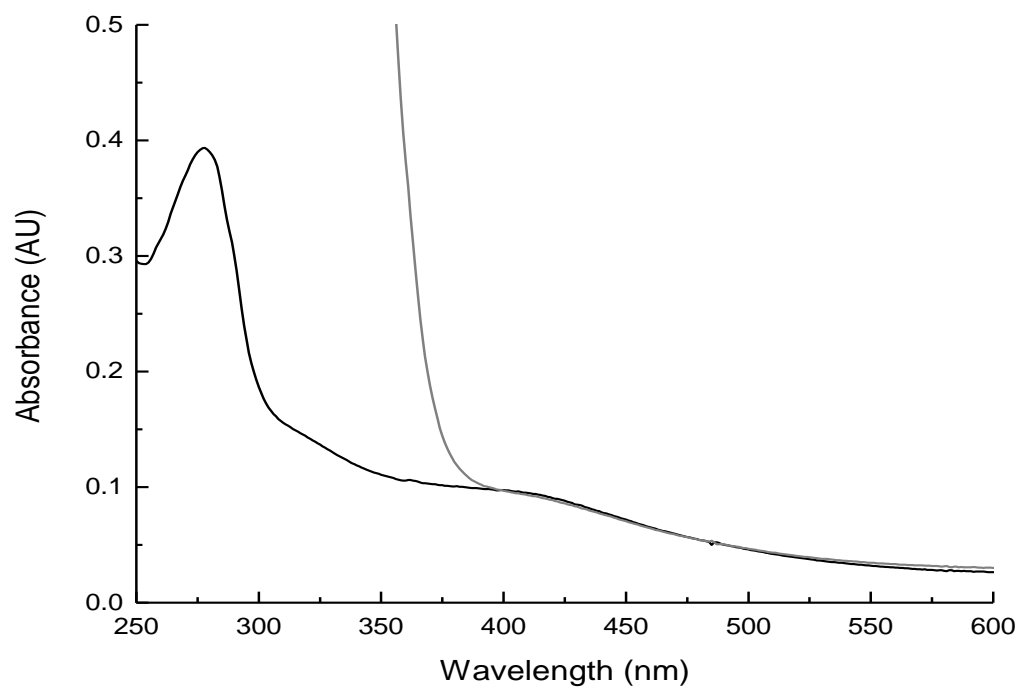


Figure 2.2: Absorption spectra for GcpE. Black line: as-isolated sample. Gray line: enzyme in the presence of 1 mM dithionite. GcpE concentration was 14.5 μ M.

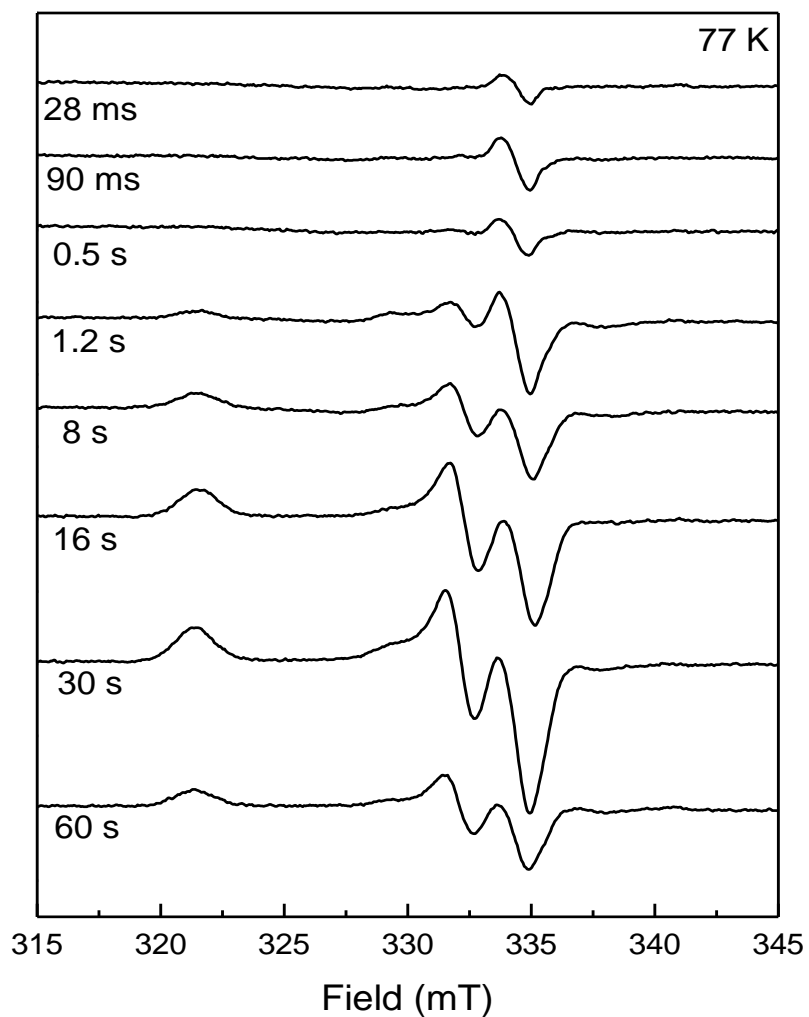


Figure 2.3: Electron paramagnetic resonance data for samples obtained with the freeze-quench technique in the presence of dithionite. After mixing each sample contained 0.4 mM GcpE, 5.5 mM MEcPP, and 25 mM dithionite in 100 mM TrisHCl, pH 8.0. Samples were mixed and incubated at RT. Data collected by Dolapo Adedeji.

2.000, 2.019, and 2.087), started to appear. A clearer spectrum of this species is shown in the overview in Figure 2.4 (trace A). The signal is remarkably similar to a signal detected in ferredoxin:thioredoxin reductase (FTR) (70). The signals in both GcpE and FTR show some resemblance to the EPR signals detected in so-called high-potential iron-sulfur proteins (HiPIPs) that have the 4Fe cluster in the 3+ oxidation state. Typically, however, HiPIPs are observed under highly oxidizing conditions and can only be detected in EPR spectroscopy at temperatures below 20 K. However, the signals in GcpE and FTR, cannot be measured below 20 K without saturation and are actually detectable up to 150 K. In both GcpE and FTR, the signals were detected under reducing conditions. For the discussion here, this signal is called FeS_A. The signal in FTR represents a cluster-bound reaction intermediate. Due to the transient behavior of the FeS_A species it was proposed that it represents a similar species in the GcpE reaction mechanism (117).

The intensity of the FeS_A signal reached maximum intensity after 30 s of incubation time, and clearly decreased after 60 s (Fig. 2.3). The maximal intensity reached is, in general, 0.1 to 0.3 spin. Measurements at different temperatures indicated that only the FeS_A species is present in these samples. No reduced clusters like [4Fe-4S]⁺ or [3Fe-4S]⁰ were detected using either perpendicular or parallel mode EPR spectroscopy.

The 30 s and 60 s samples in Figure 2.3, however, showed small amounts of other paramagnetic species. These can be more clearly detected in a different set of EPR spectra (Fig. 2.5). This set of data was prepared by incubating the samples at 55 °C instead of RT. The samples were flash frozen in liquid ethanol (200 K) at the indicated

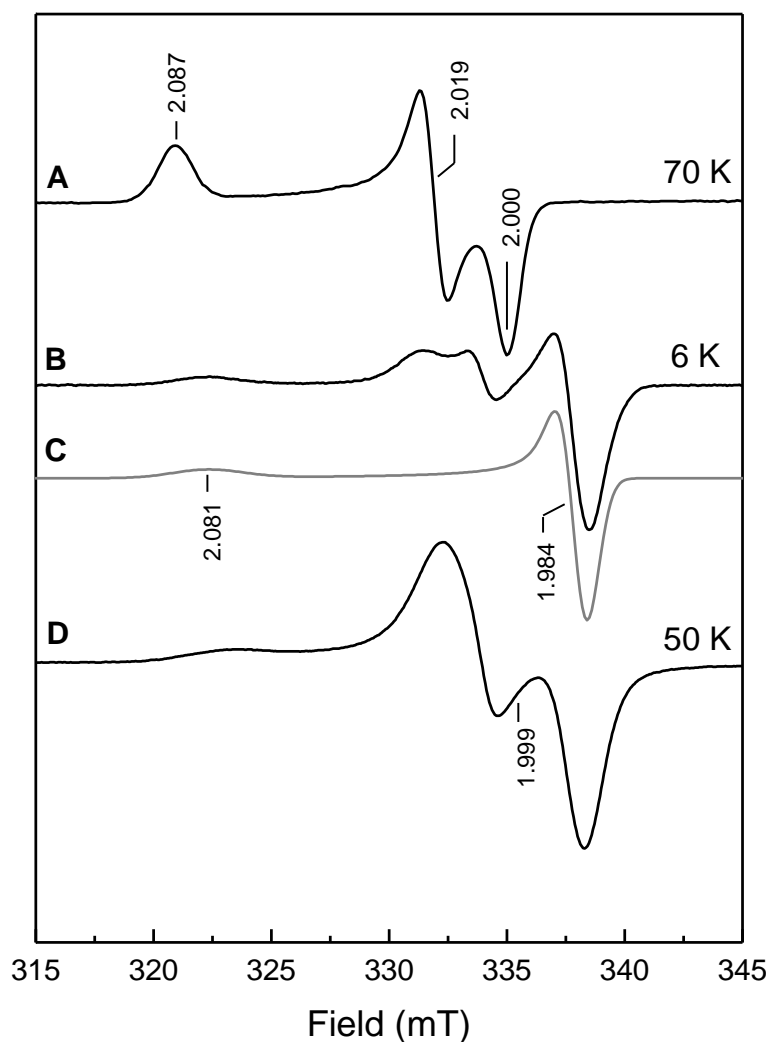


Figure 2.4: Overview of paramagnetic species detected in GcpE during turn-over experiments. A: FeS_A signal: 0.10 mM GcpE, 4.0 mM MEcPP, and 4.7 mM dithionite, incubated at 55°C for 20 s. **B:** FeS_B: as A, incubated at 55°C for 4 min and 7 s. Microwave power incident to the cavity, 2.0 mW. **C:** Simulation of the axial component of B. **D:** Same as B but measured at 50 K, microwave power incident to the cavity, 2.0 mW. Data collected by Dolapo Adedeji.

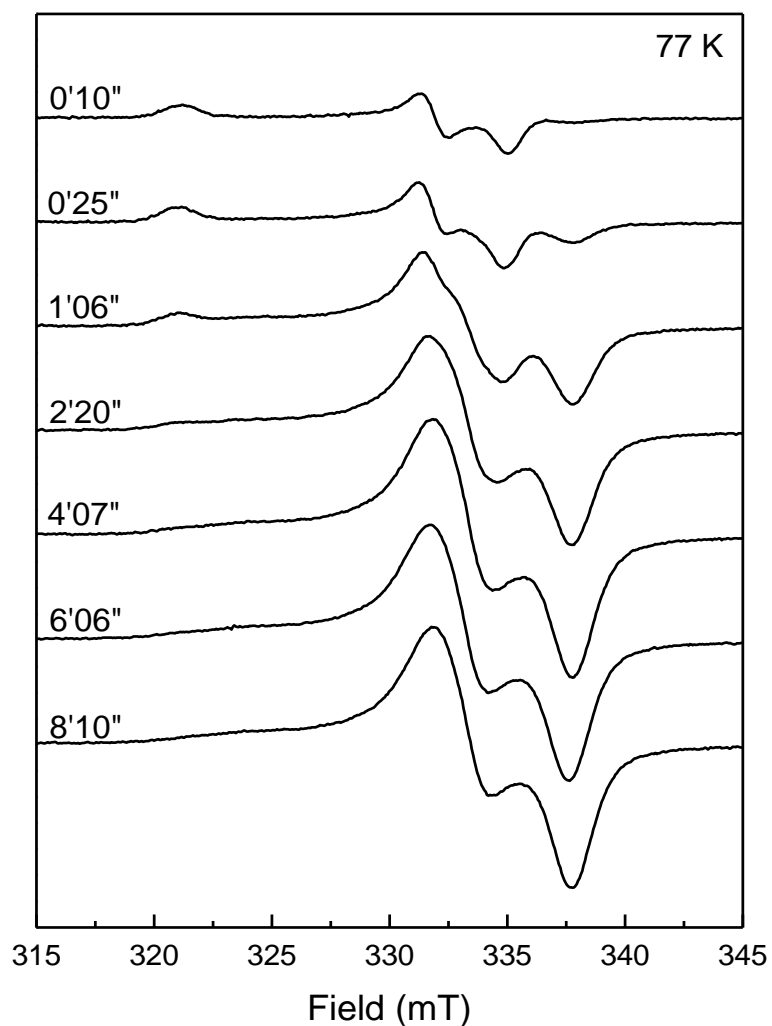


Figure 2.5: Electron paramagnetic resonance data for samples which were hand-mixed and flash frozen in the presence of dithionite. Samples were pre-incubated, mixed and incubated at 55 °C. After mixing each sample contained 0.10 mM GcpE, 4.0 mM MEcPP, and 15 mM dithionite in 100 mM TrisHCl, pH 8.0. Data collected by Dolapo Adedeji.

incubation times. This set of EPR data showed a very similar behavior as the FeS_A species. Again the maximal intensity of the EPR signal is reached at around 25 s after which it disappears again. A second signal can now be detected in the 25 s sample. This signal (FeS_B) reached its maximal intensity at 4 min and 7 s and this intensity stayed that high for the rest of the measuring period (16 min). The maximal intensity of this signal was about 0.7 spin. This behavior indicated that it is not a transient species. Temperature studies showed that the FeS_B signal represents at least two paramagnetic species. For these studies the 4'07" sample was used (Fig. 2.6). At 6 K the most dominant species present has an axial EPR signal. This spectrum is also shown in Figure 2.4 (trace B). Trace C in the same figure shows a simulation of the axial species (simulation parameters: $g_{\parallel} = 2.081$ and $g_{\perp} = 1.984$; $W_{\parallel} = 2.50$ mT and $W_{\perp} = 1.20$ mT). As the temperature increased, the axial signal started to broaden until it was broadened beyond detection at 50 K. At this temperature the remaining EPR spectrum resembled a two-fold split isotropic species, but the low-field peak at 320-325 mT still appears to be part of this signal. The whole set of peaks can be detected without broadening up to 80 K. At higher temperatures the signal starts to broaden too. From these studies it can be concluded that there are at least two species present that make up the FeS_B signal. The signals detected at 6 K in addition to the axial species could be due to the second species detected at higher temperature. It is also possible, however, that there is a third species present.

The most important conclusion from this earlier work is that the [4Fe-4S] cluster in GcpE is probably directly involved in the mechanism by binding the substrate and the

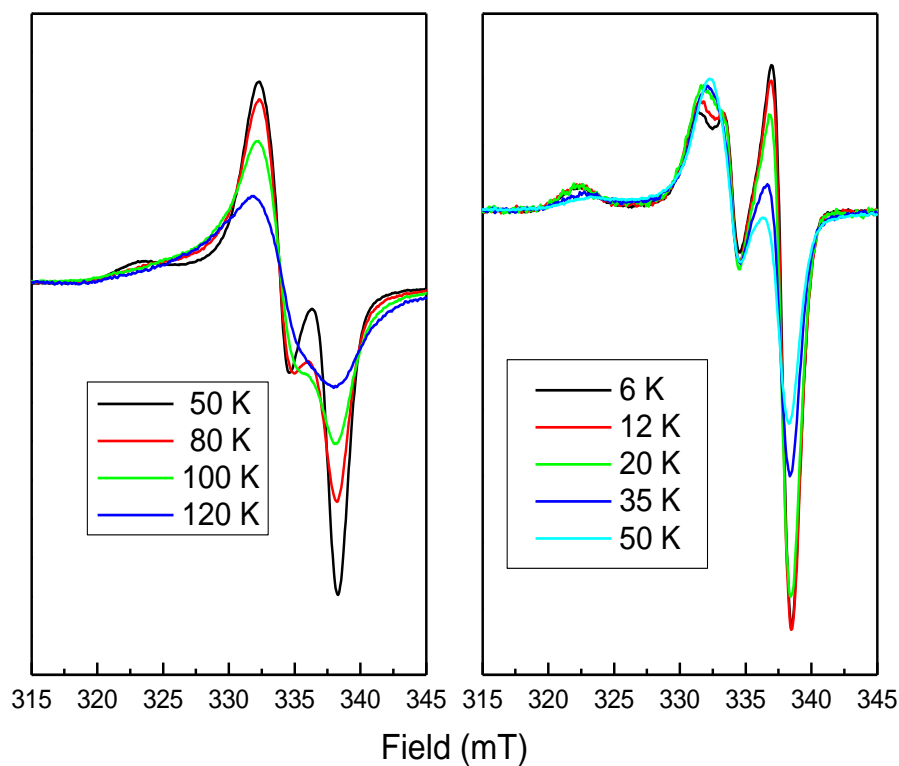


Figure 2.6: Temperature behavior for the different paramagnetic species detected in a GcpE sample that was hand-mixed with dithionite and MEcPP and flash frozen at 4 min and 20 s. After mixing the sample contained 0.10 mM GcpE, 4.0 mM MEcPP, and 15 mM dithionite in 100 mM TrisHCl, pH 8.0. The signal amplitudes of the EPR spectra were corrected for differences in receiver gain, microwave power and sample temperature (see section 2.2.6). Data collected by Dolapo Adedeji.

reaction intermediates.

2.1.1 Statement of Research

To seek inhibitors as potential drugs, it is important to gain more information by the exploration of the reaction mechanism of GcpE. So far, however, many details remain unclear.

The assignment of the FeS_A species to a cluster-bound reaction intermediate is only based on the similarities of the EPR features with the EPR signal detected in FTR. One of the first things that have to be tested is whether this signal and the FeS_B signal are due to the iron-sulfur center. This will be tested by a Fe-isotope experiment with ⁵⁷Fe-enriched protein. Broadening effects due to electron spin/nuclear spin interactions will be introduced into the EPR spectra of both the FeS_A and FeS_B species if they are iron-sulfur-cluster based.

Based on the fact that incubation of GcpE with dithionite and MEcPP resulted in the formation of the substrate HMBPP (5) it seems logical to propose that the paramagnetic species detected in Figures 2.3 and 2.5 are somehow related to the reaction mechanism. To confirm the specific role attributed to the FeS_A species, it is important to establish whether this is a kinetically competent species.

If the FeS_A species indeed represents a cluster-bound reaction intermediate, it would be interesting how the reaction intermediate is bound to the iron-sulfur cluster. Consulting the binding modes in other catalytic [4Fe-4S]-cluster-containing enzymes, discussed in

Chapter 1, section 1.3.4, we propose that two functional groups present in the substrate MEcPP, the hydroxyl group and the diphosphate groups, are considered most likely to bind to the cluster. Isotopic labeling of atoms in these functional groups in combination with ENDOR analysis will be helpful in understanding the mode of binding of the substrate or reaction intermediates to the cluster.

In addition the FeS_B EPR signal might represent two or even three paramagnetic species. High frequency EPR in combination with ENDOR experiments are needed to determine the amount of species present and to learn more about their individual properties.

The role of reductants on both the formation of reduced cluster and the paramagnetic reaction intermediates will be investigated. As will be shown below, different specific activities can be determined for GcpE, dependent on the reductant used. It will be investigated if the redox potential has an effect on the different steps in the reaction mechanism and the formation of the different paramagnetic species.

2.2 Experiments and Materials

Anaerobic conditions are required for all experiments. This was achieved by performing all purification steps, sample handling and experiments in a glove box (Coy Laboratory Products, Inc., Grass Lake, USA) filled with a gas mixture consisting of 95% N₂ and 5% H₂. All buffers and solutions used in the procedures were degassed by boiling them under a nitrogen atmosphere and subsequent cooling down under vacuum for 2 to

12 hours. The solutions were equilibrated in the tent by stirring overnight before use.

Elemental ^{57}Fe (95 % enrichment) was from WEB Research Co. $^{57}\text{FeCl}_3$ was prepared by reacting solid ^{57}Fe in 37% HCl. After all iron reacted the pH was adjusted to 4-5 with NaOH. Titanium(III) citrate (200 mM) was prepared from TiCl_3 (Fluka) in 250 mM sodium citrate under strictly anaerobic conditions. The pH of the solution was adjusted to 7.0 with sodium hydrogen carbonate. The substrate MEcPP was isolated from *Corynebacterium ammoniagenes* and was provided by the group of Hassan Jomaa from the Justus-Liebig University at Giessen, Germany. HMBPP was synthesized by this same group. Dithionite was from Fisher Scientific, Methyl viologen was from Aldrich. All gases and gas mixtures were from Airgas.

2.2.1 Expression and Purification

To be able to overexpress the *gcpE* gene from *T. thermophilus*, a synthetic gene (Eurofins Medigenomix GmbH, Martinsried, Germany) was used to compensate for the difference in CG content with the host *E. coli* and was inserted into a pQE-60 vector (Qiagen). The expression of the *gcpE* gene is controlled by the *lac* promoter. The plasmid was prepared and the C-terminal His-tag was removed by the group of Hassan Jomaa (5). At Auburn the plasmid was used to transform *E. coli* XL-1 blue competent cells (Stratagene). The cell cultures were started with a single colony from an LB-Amp plate (LB-agar plate supplemented with 100 mg/L ampicillin). It was transferred into SOC medium (20.0 g tryptone, 5.0 g yeast extract, 0.5 g NaCl, 10 mL 1 M MgCl_2 , 10 mL 1 M

MgSO₄, and 20 mL 20% (w/v) glucose per liter) containing 100 mg/L ampicillin and 100 μM FeCl₃. For the isotope-enriched protein ⁵⁷FeCl₃ was used. The cultures were incubated at 37°C with constant shaking.

Isopropyl-β-D-thiogalactoside (IPTG) was added to 1 L cell cultures to a final concentration of 0.4 mM as inducer when the optical density at 600nm (OD₆₀₀) of the cell culture reached 0.4-0.6. The cells were harvested by centrifugation at 5,500 rpm for 30 minutes (Sorvall RC-5B Refrigerated Superspeed Centrifuge, Sorvall GS-3 Rotor, Du Pont Instrument) when the OD₆₀₀ of the cell culture reached 4.5-5.0. The cell pellets were used directly or stored at -80°C until needed.

The cell pellets were resuspended in 20 mM Tris-HCl, pH 8.0. The cells were lysed by sonication followed by centrifugation at 16,000 rpm for 20 minutes (Beckman XL-70 Ultracentrifuge, YPE 45 Ti Rotor, Beckman Coulter, Inc.). The supernatant was subjected to a heat treatment by incubation in a 65 °C water-bath for 30 minutes to denature non-target proteins. The supernatant after a second centrifugation step at 30,000 rpm for 30 minutes (Beckman XL-70 Ultracentrifuge, YPE 45 Ti Rotor, Beckman Coulter, Inc.) was filtered with a 0.2 μM filter unit, then loaded onto the first column, diethylaminoethyl (DEAE) Sepharose (GE Health Care). The protein was eluted with a NaCl gradient in 20 mM TrisHCl, pH 8.0. GcpE eluted at a concentration of 0.5-0.7 mM NaCl. The main fractions as determined by SDS-PAGE (sodium dodecyl sulfate polyacrylamide gel electrophoresis) or the brown color of the enzyme, were collected and washed in an Amicon concentration unit with 20 mM TrisHCl, pH 8.0. A Mono Q column

(GE Health Care) was used for the next purification step. The same gradient was applied to this column and fractions were pooled based on SPS-PAGE or the brown color. GcpE eluted at a concentration of 0.2 mM NaCl. The protein solution could be used directly or stored in the refrigerator until use. Purity of the protein was checked by SDS-PAGE with Coomassie blue staining. All experiments and assays were performed in 20 mM Tris-HCl, pH 8.0

2.2.2 Protein Determination

The enzyme concentration was determined by the Bradford method (126) or directly based on the absorbance at 280 nm depending on Tyr and Trp content ($\epsilon = 26930 \text{ M}^{-1}\text{cm}^{-1}$).

2.2.3 Iron Determination

The iron determination was carried out with a rapid ferrozine-based colorimetric method (127). Protein samples used for the iron determination were run over a Chelex column (Bio-Rad) to remove adventitiously bound iron. All containers and pipette tips used for this determination were repeatedly soaked in boiling 1 M HCl and washed with ultra pure water. The iron standards (0, 10, 20, 30, 40, 50 μM) were made by dissolving ferrous ethylenediammonium sulfate in 0.01 M HCl. Iron releasing reagent (0.5 ml – containing equal amounts of 0.6 M HCl and 0.142 M potassium permanganate) was added to both the iron standard samples and the protein samples (1 ml). The solutions

were incubation at 60 °C for 2 hrs. The samples were centrifuged to remove precipitated protein. The iron chelating and reducing reagent was added to the samples (0.1 mL - containing 6.5 M ferrozine, 13.1 mM neocuprine, 2 M ascorbic acid, and 5 M ammonium acetate), which were incubated for at least another 30 minutes. The absorbance at 562 nm was recorded for creation of the standard curve and determination of the iron concentration in the protein samples.

2.2.4 Sulfur Determination

The sulfur determination was carried out with a colorimetric method (adapted from (128)). The sulfur reagent had to be made fresh for each determination: 0.1 g N,N-dimethyl-p-phenylenediamine sulfate and 0.15 g ferric chloride ($\text{FeCl}_3 \cdot 6\text{H}_2\text{O}$) were dissolved in 12.5 mL 6 M HCl, followed with dilution by a factor of 4 with 6 M HCl. The sulfur standards (0, 10, 20, 30, 40, and 50 μM) were prepared by dissolving $\text{Na}_2\text{S} \cdot 9\text{H}_2\text{O}$ in water. The sulfur reagent (83.4 μL) was added to the sulfur standards and protein samples (1 ml), which were subsequently incubated for 30 minutes. The absorbance at 670 nm was recorded for creation of the standard curve and determination of the sulfur concentration in the protein samples.

2.2.5 Kinetic Studies

A colorimetric assay was used to obtain kinetic parameters. The starting solution contained GcpE, dithionite, and the redox dye methyl viologen, which has a blue color

when reduced. The activity was determined by measuring the absorbance change at 603 nm ($\epsilon = 1.36 \times 10^4 \text{ M}^{-1}\text{cm}^{-1}$) as a function of time.

In some of the EPR-detected experiments, dithionite-reduced methyl viologen was used. This was prepared by adding a half equivalent of dithionite to the methyl viologen solution before use in the experiment.

2.2.6 Electronic and Magnetic Characterizations

The UV-vis absorption spectra of the protein samples were achieved under anaerobic conditions by using the Ocean Optics USB 2000 miniature fiber optic spectrometer inside the glove box or using stoppered cuvettes in a HP 8451A UV-visible Spectrophotometer or an Agilent 8453 UV-visible Spectrophotometer.

CW EPR spectra were measured at X-band (9 GHz) frequency on a Bruker EMX spectrometer, fitted with the ER-4119-HS high sensitivity perpendicular-mode cavity. General EPR conditions were: microwave frequency, 9.385 GHz; microwave power incident to the cavity, 0.20 mW; field modulation frequency, 100 kHz; microwave amplitude, 0.6 mT.

The Oxford Instrument ESR 900 flow cryostat in combination with the ITC4 temperature controller was used for measurements in the 4 K to 300 K range using a helium flow. Measurements at 77 K were performed by fitting the cavity with a liquid nitrogen finger Dewar.

Samples for EPR were prepared in quartz tubes that were sealed with a closed off

rubber tube. The samples were either frozen using liquid nitrogen or cold ethanol (200K). The last method provides an immediately frozen sample.

A copper perchlorate standard (10 mM CuSO₄, 2 mM NaClO₄, 10 mM HCl) was used for spin quantifications on spectra measured under non-saturating conditions by comparison of the double integral of the signal from the samples with that from the standard. Signal intensities are presented as amount of spin which is the fraction of the amount of EPR signal detected over the amount of [4Fe-4S] cluster present in the sample.

The software package developed by S. P. J. Albracht was used for computer simulations of the EPR signals (129).

Pulsed EPR and ENDOR data at X-band and Q-band (35 GHz) frequency were collected by Nicholas Lees in the group of Brian Hoffman at Northwestern University, Evanston, IL. Samples were prepared in Auburn, stored in liquid nitrogen and transported in a nitrogen dry-shipper (Taylor-Wharton).

An important method for understanding the temperature behavior of EPR signals is to create Curie plots where the normalized signal intensity is plotted against the sample temperature. A signal that is not saturated at low temperatures or temperature broadened at higher temperature should display a horizontal line in a Curie plot.

The Normalized Signal Intensity (I_n) was calculated according to:

$$I_n = \frac{(I_0 \cdot T \cdot 10^{\text{dB}/20})}{(\text{gain})}$$

With: I_0 , observed intensity; T, absolute temperature in K; dB, reading of the attenuator;

gain, gain.

For comparison of the spectra at different temperatures, the signal intensity as obtained *via* double integration can be used as I_0 . When more than one signal is present, the individual species will have to be simulated and subtracted or the intensity of an isolated peak can be used. The normalized spectra can be compared in overlaid or stacked plots.

2.3 Results

2.3.1 Expression and Purification

The GcpE gene was expressed successfully in *E. coli* XL-1 Blue cells. The GcpE protein was purified using two sequential ion-exchange columns, a DEAE sepharose column (Fig. 2.7) and a Mono Q column (Fig. 2.8). The protein was considered pure (>95%) as judged by SDS-PAGE (Fig. 2.9) with a little impure proteins present as shown in the line 6 (the oversize spot was due to the overloading of protein). The third gel filtration column was used only when the purer protein samples were needed for measurements. In general the cluster content is 100 ± 3 % based on the iron and sulfur determination.

2.3.2 Basic Absorption and EPR spectroscopy

As previously shown, a band around 410 nm was observed in the

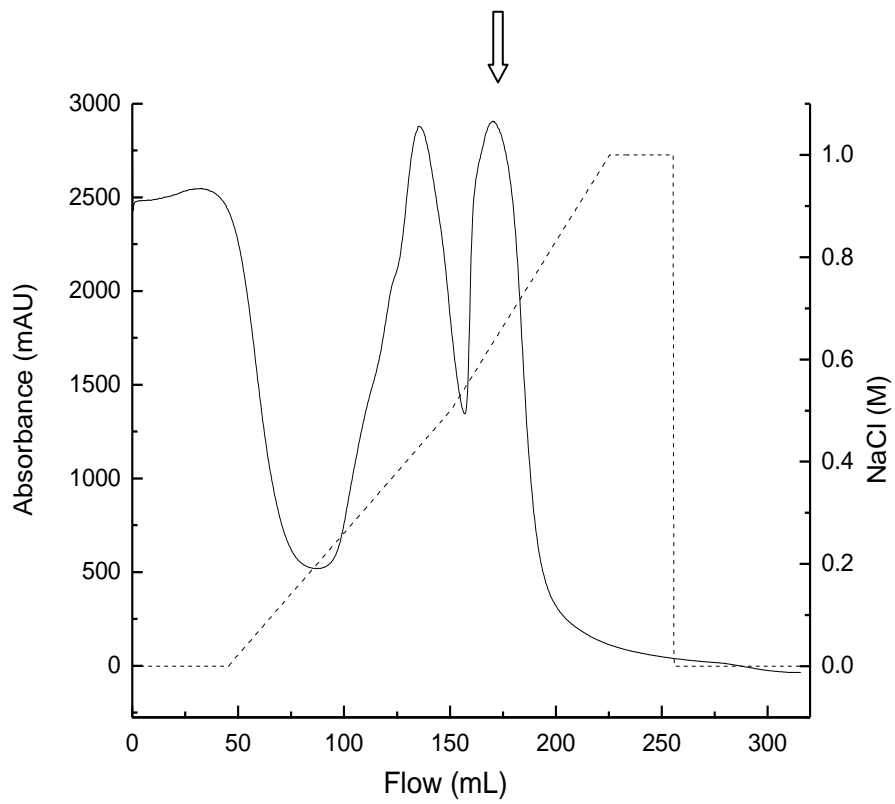


Figure 2.7: FPLC profile of DEAE sepharose column

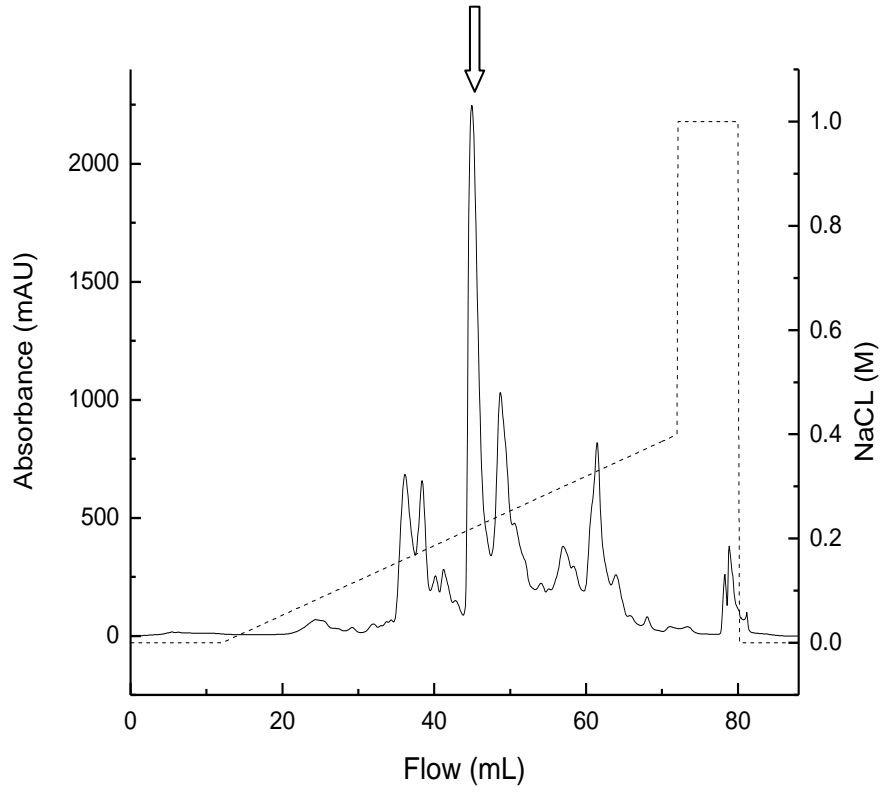


Figure 2.8: FPLC profile of Mono Q column

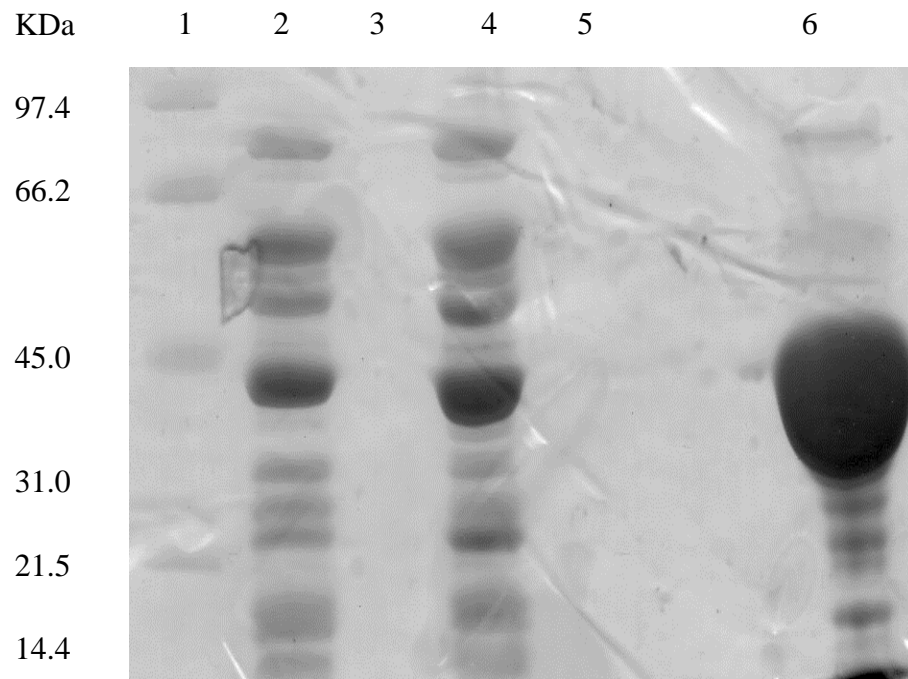


Figure 2.9: SDS-PAGE showing the progress in the purification of GcpE. Lane 1, marker; lane 2, cell extract; lane 3, flow through of the DEAE sepharose chromatography column; lane 4, elute enzyme after DEAE sepharose chromatography; line 5, flow through of MONO Q chromatography; line 6, elute enzyme after MONO Q chromatography.

UV-Visible absorbance spectrum for the as-isolated GcpE protein. No $[3\text{Fe-4S}]^{1+}$ EPR signal was detected, indicating the presence of only a $[4\text{Fe-4S}]^{2+}$ cluster. Upon addition of dithionite minimal bleaching of the 410 nm band was observed, but no EPR signals were detected (not shown). Nevertheless, The FeS_A and FeS_B signals can be generated with properties and patterns as detected before, by the incubation of protein with dithionite and MEcPP.

2.3.3 The FeS_A Species and FeS_B Species are Iron-Sulfur Based

The effects of introducing the ^{57}Fe -isotope ($I = 1/2$) into the $[4\text{Fe-4S}]$ cluster of GcpE are shown in Figure 2.10. Comparison of the EPR spectra of the ^{57}Fe -enriched samples with the spectra obtained with GcpE containing the natural abundance isotope shows a clearly detectable broadening of the EPR spectra for all species: FeS_A (Fig. 2.10, panel A) and FeS_B at 7 K and 50 K (Fig. 2.10, panel B and C). This result indicates that all observed EPR signals originate completely or in part on the iron-sulfur cluster in the active site of GcpE.

2.3.4 Kinetic studies

The kinetic parameters were obtained in the colorimetric assay in the presence of methyl viologen. Based on Michaelis-Menten and Lineweaver-Burk plots (Fig. 2.11), the kinetic parameters determined for GcpE are: $K_M \sim 8.0 \mu\text{M}$, $V_{\text{max}} \sim 0.13 \mu\text{M}\cdot\text{s}^{-1}$, and $k_{\text{cat}} \sim 0.09 \text{ s}^{-1}$ at RT in TrisHCl, pH 8.0. The specific activity is $0.124 \mu\text{mol}\cdot\text{mg}^{-1}\cdot\text{min}^{-1}$.

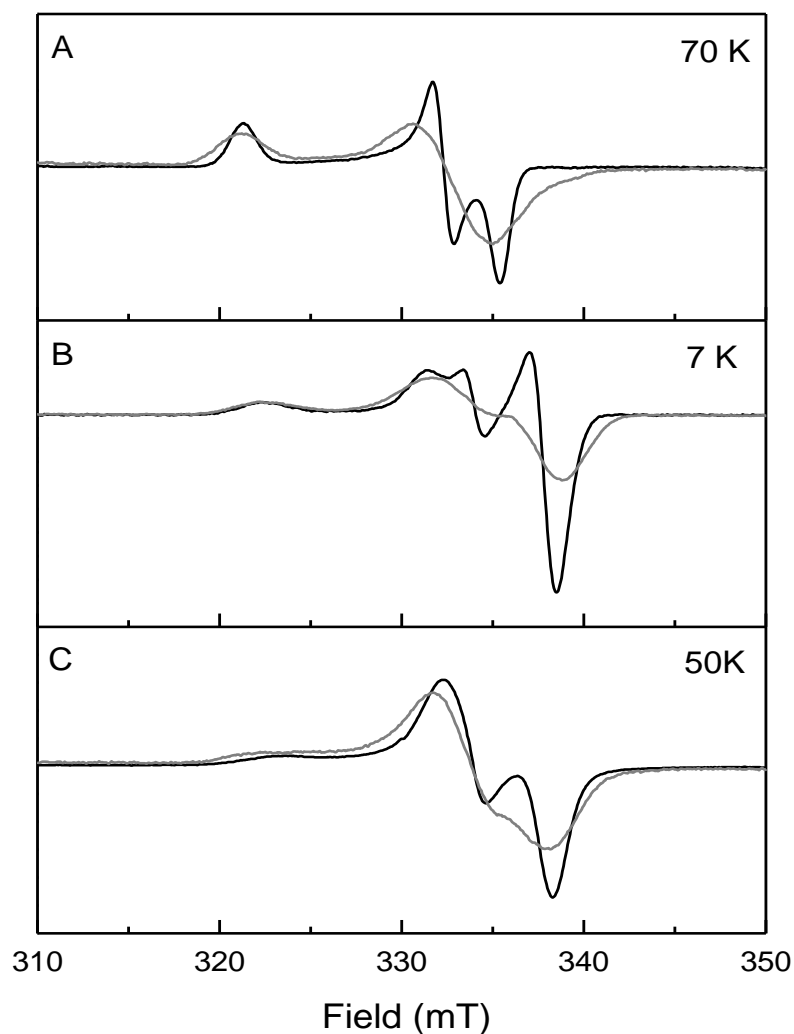


Figure 2.10: Overlay of the spectra from Figure 2.4 (black lines) with similar samples prepared with ^{57}Fe -enriched enzyme (gray lines). Signal amplitudes were corrected for differences in sample concentration. **A:** FeS_A signal present in a sample incubated at RT and frozen after 20 s of incubation time. **B:** FeS_B signal present in a sample incubated at RT and frozen after 5 min of incubation time. **C:** Same as B but measured at 50 K. For other EPR conditions see legend of Figure 2.4.

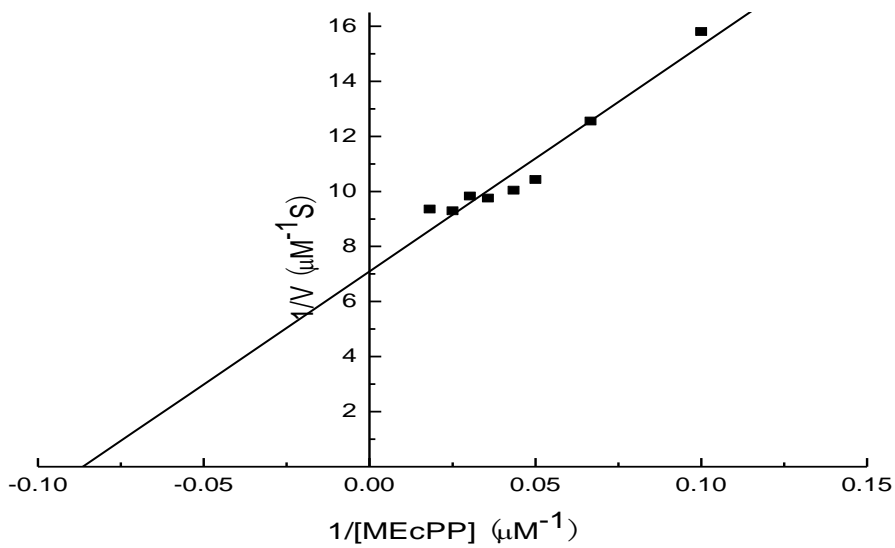
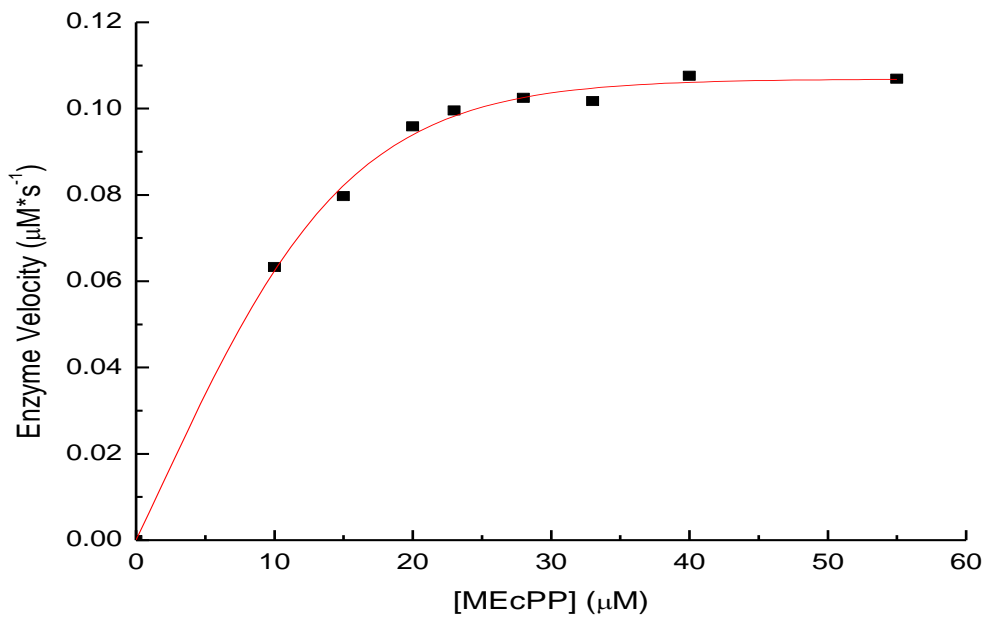


Figure 2.11: Michaelis-Menten and Lineweaver-Burk plots for GcpE. The assay was performed with 1.5 μM GcpE, 30 μM dithionite and 100 μM methyl viologen.

There is a discrepancy between the parameters obtained with the colorimetric assay and kinetic data obtained from the Freeze-quench experiment performed by Dolapo. The colorimetric assay with methyl viologen indicates a turnover-number of about 11 s. The Freeze-quench data, however, shows the development and disappearance of the FeS_A species in the first 60 s of the reaction (Fig. 2.3). Figure 2.12, shows additional RT kinetic data where the whole process was followed by freezing selected samples for EPR spectroscopy. The FeS_A signal develops first and reaches its maximal intensity within 10 to 20 s. In this case, it very slowly disappears over the rest of the measuring time, with the biggest decrease in between 20 and 30 min. The FeS_B species can be detected after 1 min. Its intensity keeps increasing during the whole 120 min, but a plateau is reached towards the end of the incubation time. This is different than the data obtained with the freeze-quench method (Fig. 2.3). It appears that the sample temperature must have been higher in the latter technique which would have affected the reaction speed significantly.

Irrespective of the differences, both the RT freeze-quench data and the other RT data, would indicate that none of the detected species in EPR are kinetically competent, but below we will show that the presence of methyl viologen greatly speeds up the reaction rate and the data obtained with both methods (EPR-detected or colorimetric assay) cannot be compared directly.

Ideally, the enzymatic assay could be changed by leaving out the methyl viologen and following the change in absorbance of the 330 nm peak associated with reduced dithionite. Alternatively, methyl viologen could be used in the EPR-detected assay.

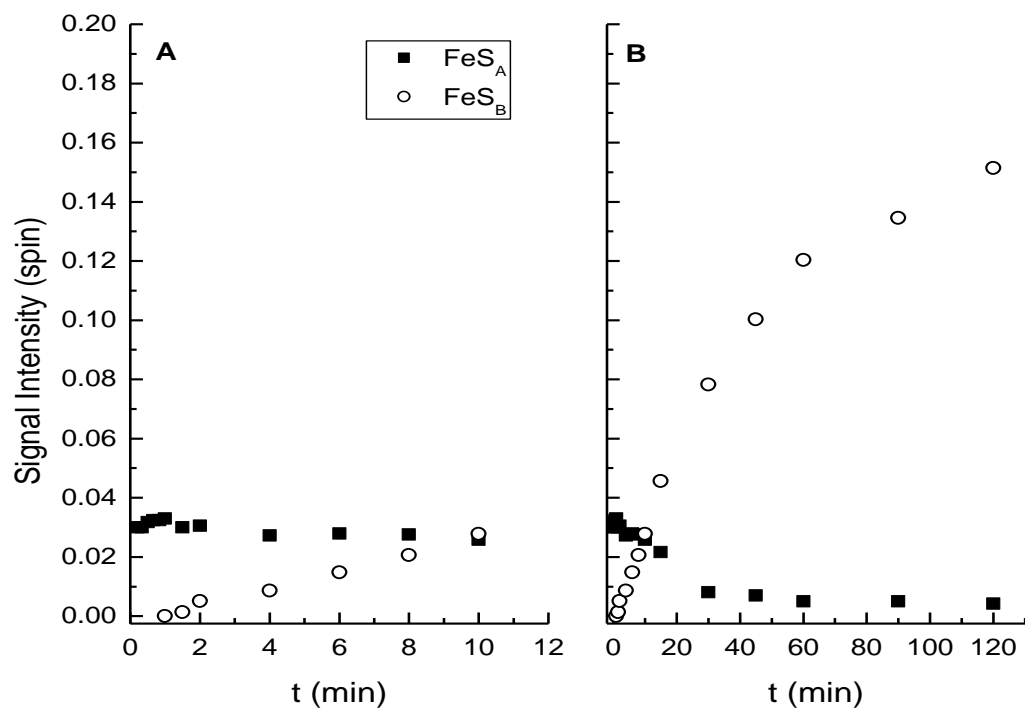


Figure 2.12: Time dependency of the development of the FeS_A and FeS_B species in GcpE. Concentration: GcpE, 250 μ M; MEcPP, 5 mM; dithionite, 20 mM. Samples incubated at RT. The EPR signals detected at 70 K have been used to determine the signal intensities used in this plot.

However, both options are problematic.

The continuation of the reaction catalyzed by GcpE seems to be dependent on the amount of dithionite present. Figure 2.13 shows the intensity of the FeS_A EPR signal measured after an incubation time of 30 s. The highest intensity is found for dithionite concentrations at 5 mM or lower. At these concentrations the FeS_A signal is not a transient species but accumulates over time. It appears that not only the dithionite concentration is important but that also the associated redox potential might play a role. The first step of the reaction, the reductive formation of the FeS_A species seems to have a higher potential than the second step, the reductive formation of a diamagnetic intermediate. When a certain threshold value is reached the FeS_A signal becomes a transient signal again. As a result the maximal intensity reached is also lower. The same intensity is reached with dithionite concentrations of 15 mM or higher. This means that in our kinetics assay we need at least 15 mM dithionite, which is such an excess that besides from the impossibility to even measure this in regular absorption spectroscopy, the actual change in concentration during the assay will be too small to be detectable.

Alternatively, methyl viologen could be used in the EPR assay and although this can be done, the methyl viologen is EPR-active and its EPR signal shows overlap with the GcpE signal. Due to the relative high intensity of the methyl viologen EPR signal it is not possible to directly observe the GcpE signal. However, reasonable data were obtained when the methyl viologen signal were subtracted out (see below).

In the following part, data will be presented where different reaction conditions were

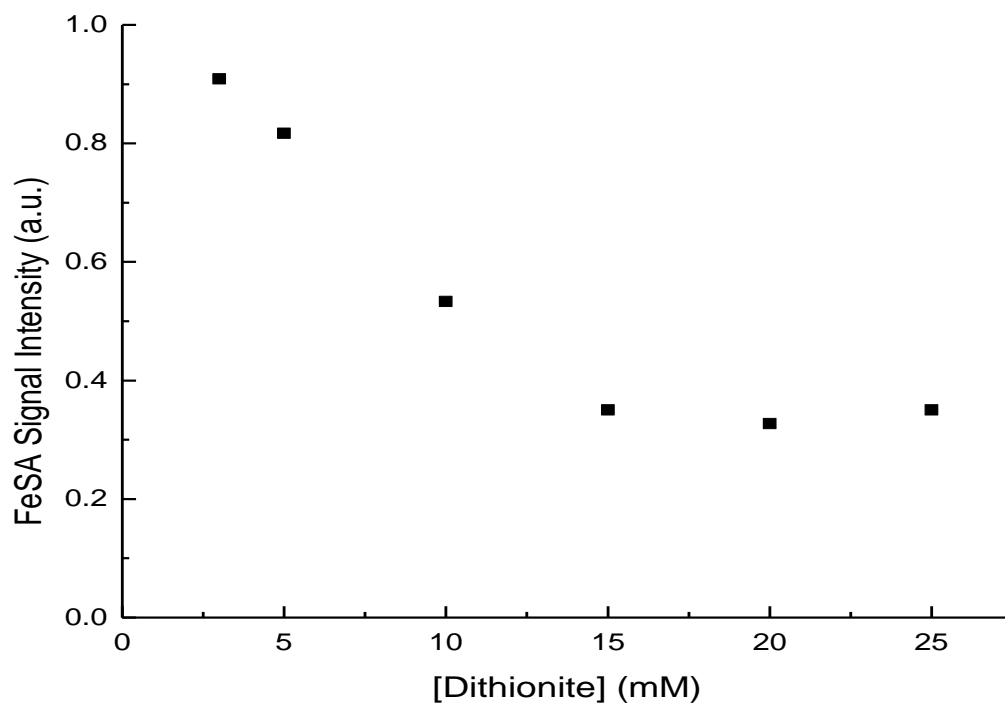


Figure 2.13: Dependency of the FeS_A EPR signal intensity on the concentration of dithionite. Samples were frozen after 30 s of incubation. Concentration of GcpE, 100 μ M; MEcPP, 0.5 mM.

tested. The aim was to investigate the role of both MEcPP and different reductants on the development and intensity of the EPR-active species in GcpE. In part this was done to understand the effect of different redox potentials on the mechanism and the development of the different species, but it was also important to increase the signal intensity of the FeS_A species to be able to perform ENDOR and Mössbauer studies. Both techniques require much higher concentrations than regular EPR spectroscopy, and in the case of the latter technique there is a need for a higher partial intensity of the FeS_A species since all forms of the 4Fe cluster present in the protein sample will be detectable.

2.3.4.1 Effect of MEcPP on the Signal Intensity of the FeS_A Species

Time dependency analyses by EPR spectroscopy were executed for two series of samples with different MEcPP concentrations: 0.5 mM and 3.0 mM. Although both of them showed similar signal patterns and trends of signal development, there is a clear difference in signal intensity (Fig. 2.14). The signal accumulation appears to level off after 30 s of incubation for the 0.5 mM series and after 60 s of incubation for the 3.0 mM series.

Figure 2.15 shows the signal intensity of the FeS_A species after incubation of the samples with different amount of MEcPP for 30 s. Again the signals were identical in shape (no FeS_B present) but the intensities changed with varying substrate amounts. Below a concentration of 3 mM MEcPP, the intensity appears to be increasing with higher amount of substrate. The intensity is constant at concentrations of 3 mM

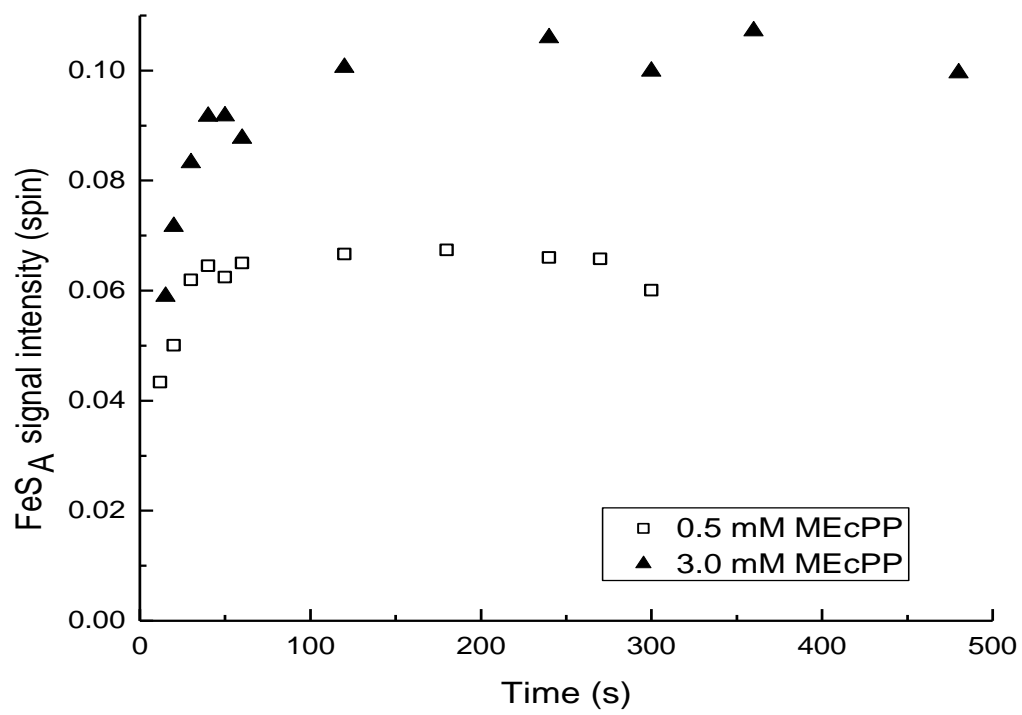


Figure 2.14: FeS_A EPR signal intensity as a function of the concentration of MEcPP and as a function of time. Concentration of GcpE, 100 μ M; Dithionite, 3.0 mM.

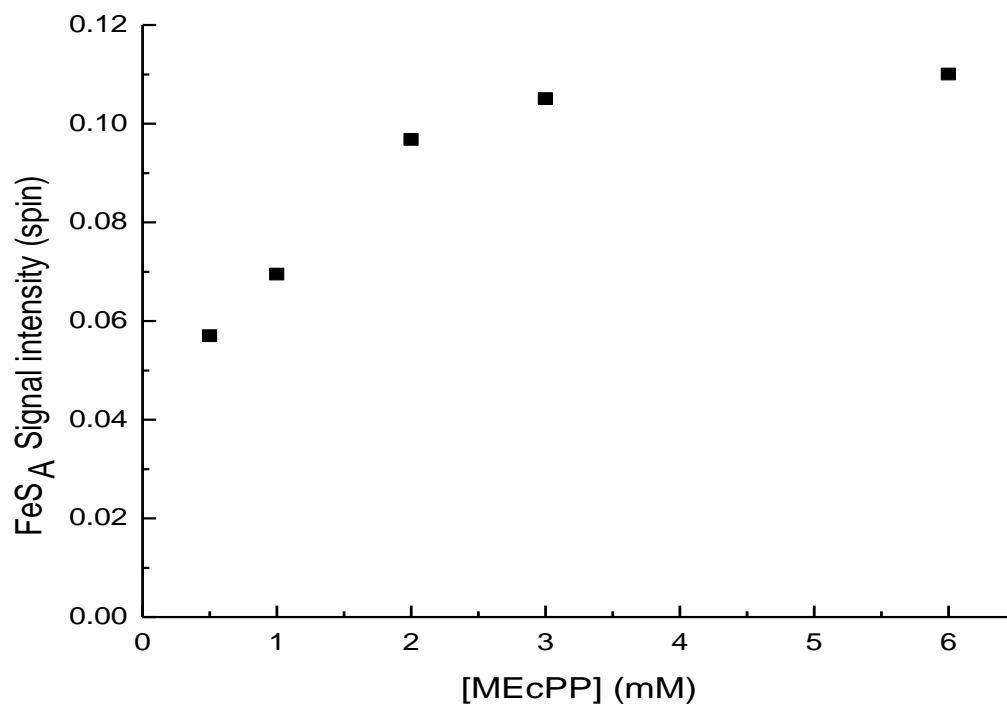


Figure 2.15: Dependency of FeS_A EPR signal intensity on the concentration of MEcPP. Samples were frozen after 30 s of incubation. Concentration of GcpE, 100 μ M; Dithionite, 3.0 mM.

or higher. It shows that the optimal concentration of MEcPP is 3 mM or higher for the EPR assay to obtain intense signals as high as possible.

2.3.4.2 Detection of FeS_A and FeS_B Species in Single-Turnover Experiments

In the EPR-detected kinetic experiments presented up until now there was always an excess of MEcPP and dithionite present which allowed for the several reaction cycles to take place. This approach worked well since the high concentration of both compounds caused an increase in the intensity of the FeS_A species. Due to the uncertainty about the speed of the reaction in the absence of methyl viologen it is not clear what part of the data represents pre-steady-state or steady-state conditions and where the reaction runs out of substrate. To get a better idea about the pre-steady-state conditions, single turnover experiments were performed. The data in Figure 2.16 show almost identical trends of formation and breakdown of the different paramagnetic species as detected before (see Fig. 2.2 and Fig. 2.4). However the signal intensity of the first HiPIP-like FeS_A species reached its maximal value within 10'' at RT, and represented only about 0.05 to 0.1 spin. The FeS_B started to developed after about min of incubation and accumulated over time.

2.3.4.3 Effect of Methyl Viologen on the Signal Intensity of the FeS_A Species

The presence of the methyl viologen resulted in an isotropic signal in the EPR spectrum, which made the detection of the GcpE signals difficult to follow. Figure 2.17, trace A, shows the EPR spectrum of a sample with a limiting amount of methyl viologen

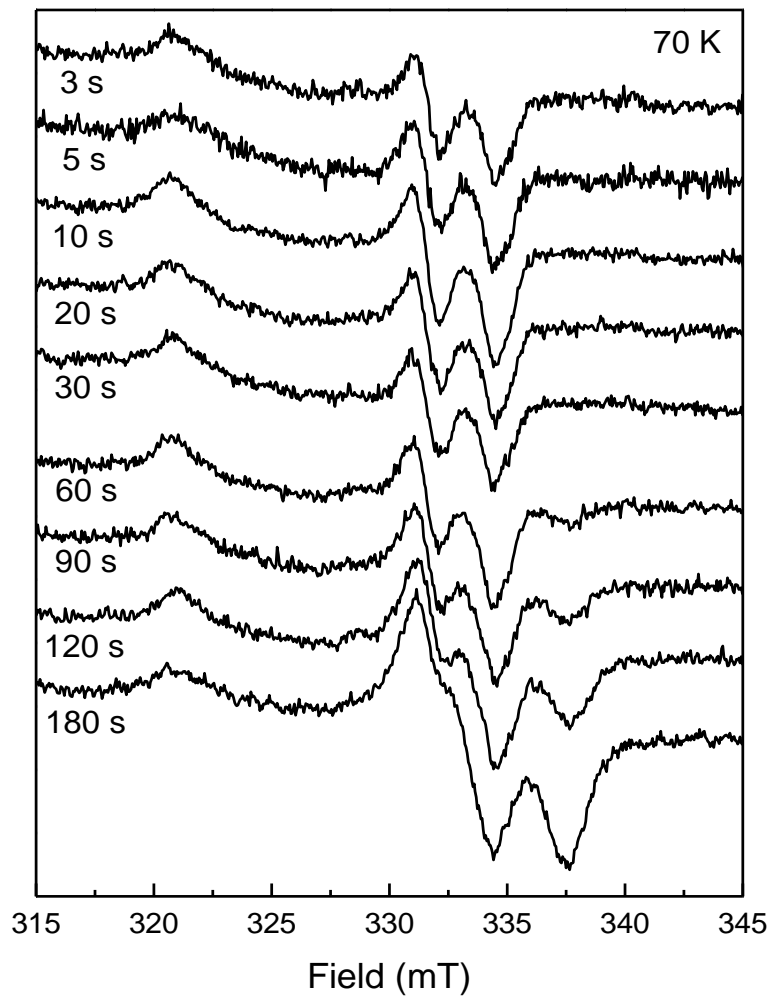


Figure 2.16: Single turn-over experiment. Samples were pre-incubated, mixed and incubated at RT. After mixing each sample contained 0.2 mM GcpE, 0.2 mM MEcPP.

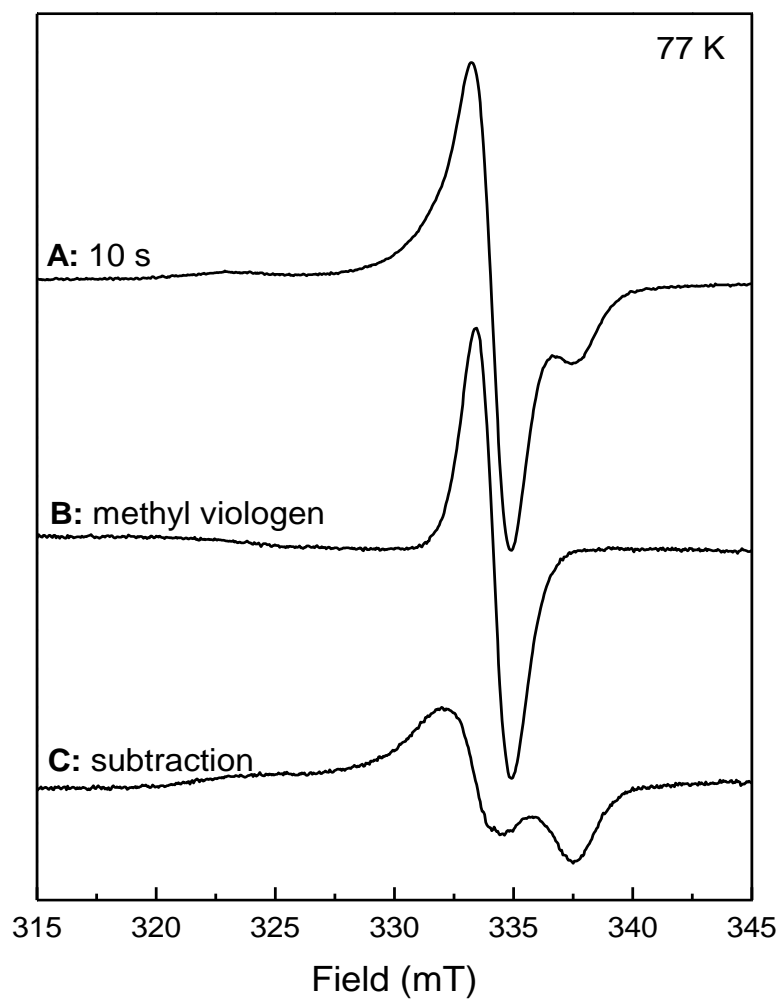


Figure 2.17: Electron paramagnetic resonance spectrum for a 10 s sample that was prepared in the presence of methyl viologen. Sample was pre-incubated, mixed and incubated at RT. After mixing, the sample contained 1.1 mM GcpE, 10 mM MEcPP, and 5 mM dithionite-reduced methyl viologen.

after a 10 s incubation time at RT. Figure 2.17, trace B, is the isotropic signal of pure methyl viologen. The subtraction of spectrum B from spectrum A generates a spectrum (Fig. 2.17, trace C) that is identical to that of the FeS_B species as shown in Figures 2.4 and 2.5. Under these conditions the FeS_B signal is formed within 10 s, which is in line with the k_{cat} values of 0.09 s^{-1} . This data would indicate that the FeS_B species is formed within the time to do one turnover and is therefore related to the reaction cycle. That would mean that this is probably also true for the FeS_A species. Under the used conditions, however, the FeS_A signal is not detectable. On the other hand, the FeS_A species is formed within 10 s under single-turn-over conditions. This would indicate that the presence of methyl viologen mainly changes the kinetics of the second step, the disappearance of the FeS_A species.

2.3.4.4. Effect of Titanium(III) Citrate on the Signal Intensity of the FeS_A Species

Another reductant that was investigated was titanium(III) citrate. This is a much stronger reductant than dithionite ($E_m = -560 \text{ mV versus SHE at pH 8.0}$) (130). As will be shown below, exposure of GcpE to this compound resulted in cluster breakdown. However, it can be used in equimolar amounts or slightly higher amounts in the presence of substrate. This seemed a promising approach to induce the FeS_A signal in much higher quantities. The FeS_A species is induced when GcpE is incubated with both titanium(III) citrate and MEcPP. The data in Figure 2.18, show the accumulation of the FeS_A species when a half-equivalent of titanium(III) citrate was used (Panel A) and when an equivalent

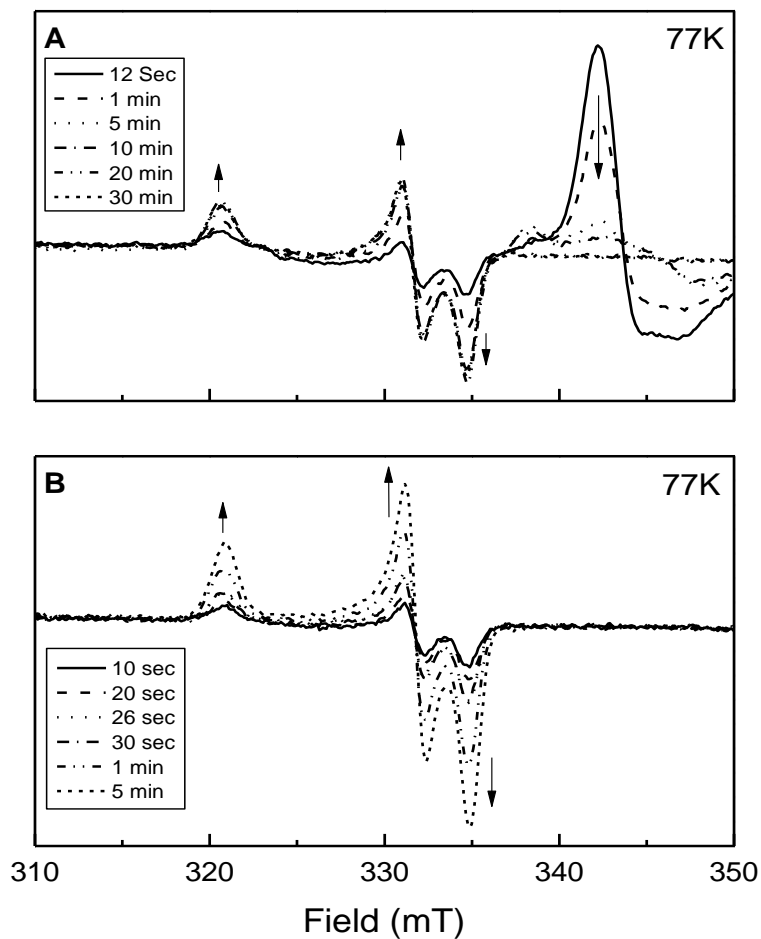


Figure 2.18: FeS_A EPR signal intensity as a function of the concentration of titanium(III) citrate and as a function of time. Panel A with concentration of GcpE = 96 μM; Titanium(III) citrate = 48 μM; MEcPP = 960 μM. Panel B with concentration of GcpE: 386 μM; Titanium(III) citrate = 386 μM; MEcPP = 3.86 mM

was used (Panel B). Surprisingly, the FeS_A species takes much longer to develop, up to 20 min when a half-equivalent was used and doesn't even appear to be at a maximum value after 5 min when an equivalent of titanium(III) citrate is used. The maximal intensities reached are 0.085 spin when a half-equivalent of titanium(III) citrate was used and 0.05 spin when an equivalent was used. Besides the much slower development of the FeS_A species, the experiments are in line with the fact that only 1 electron is needed to induce the FeS_A species.

It was tested if longer incubation times and/or higher amount of titanium(III) citrate would lead to the formation of higher amounts of the FeS_A species. Figure 2.19 shows the formation of the FeS_A species as a function of the titanium(III) citrate concentration and as a function of time. The data show that in the case of a 1 equivalent of titanium(III) citrate the longer incubation time does not improve the signal intensity of the FeS_A species. Increasing the amount of titanium(III) citrate 2-fold or 5-fold resulted in an overall lower amount of EPR signal in comparison to 0.5 and 1-fold amounts of titanium(III) citrate. In the case of a 5-fold amount the FeS_B species also starts to develop (not shown). With a 10-fold amount of titanium(III) citrate (Fig. 2.20) the FeS_A signal could be detected in the 30 s and 1 min samples, but did not appear in the 2 min sample. Instead, a strong FeS_B was detected in the 2 min spectra. Surprisingly, the FeS_B signal became weaker in the 4 min spectra, which was accompanied by the reappearance of the FeS_A species. This mixture stayed detectable up to 96 min. This would indicate that under these conditions the FeS_B species is also a transient species. However, as will be shown

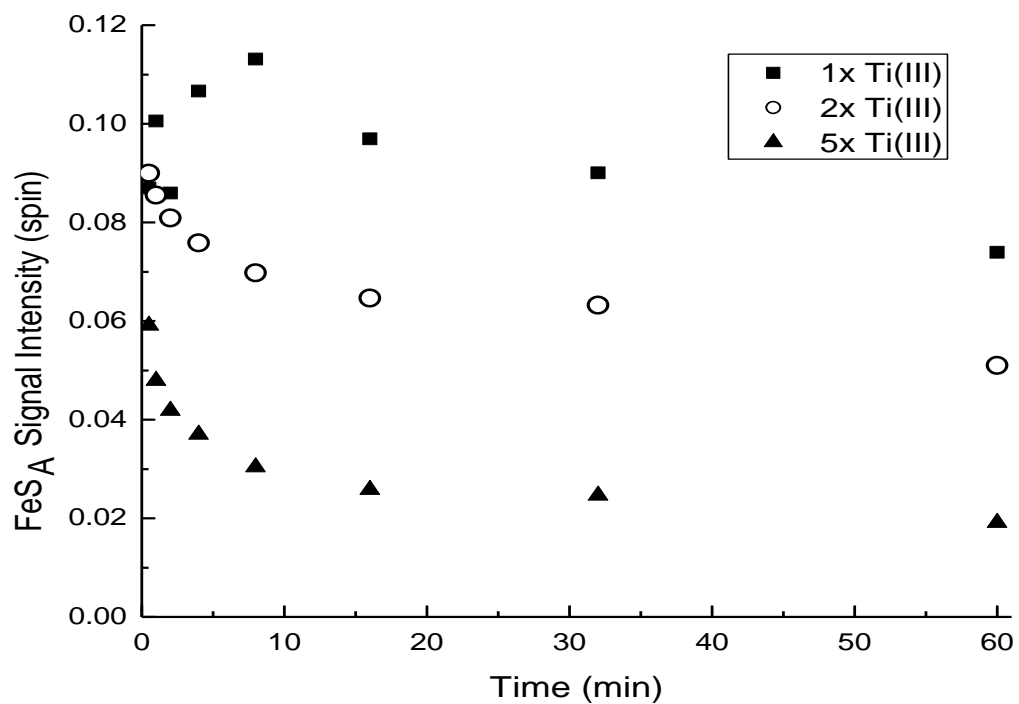


Figure 2.19: FeS_A EPR signal intensity as a function of the concentration of titanium(III) citrate and as a function of time. Concentration of GcpE, 273 μ M; MEcPP, 2 mM; titanium(III) citrate, 273 μ M (■), 546 μ M (○), and 1365 μ M (▲).

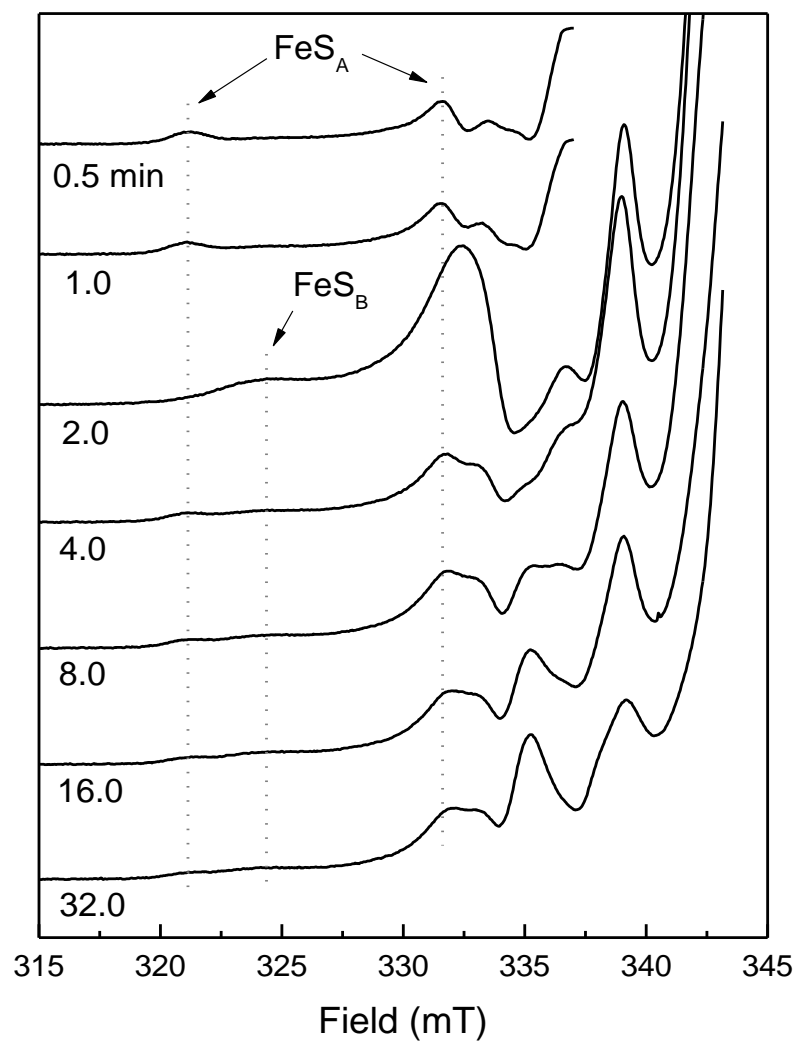


Figure 2.20: FeS_A EPR signal intensity as a function of the concentration of titanium(III) citrate and as a function of time. Concentration of GcpE, 273 μ M; MEcPP, 2 mM; titanium(III) citrate, 2730 μ M (10 equivalent).

below, the disappearance of the signal is probably due to cluster breakdown.

2.3.5 Spectroscopic Properties of the FeS_A Species

A property that sets aside the FeS_A species from other iron-sulfur-cluster based signals, except from the ones found in FTR and LytB, is the unique temperature behavior. This is highlighted by the Curie plot shown in Figure 2.21. The EPR signal cannot be measured below 20 K without saturation. It starts to broaden above 100 K and is broadened beyond detection at 160 K. From 20 K to 100 K, the signal can be measured without saturation. This temperature behavior of the FeS_A signal is very similar to that of the signal detected in FTR.

The data on ⁵⁷Fe-enriched enzyme (Fig. 2.10) confirmed that just like in FTR the FeS_A signal is in part iron-sulfur-cluster based and probably represent a cluster-bound reaction intermediate. The question that remains is how this reaction intermediate is bound to the cluster. There are several functional groups in the MEcPP structure that could be involved in binding to the cluster. Based on the chemistry observed in aconitase the leaving hydroxyl group, and maybe also the other hydroxyl group could bind to the unique iron in the 4Fe cluster. The phosphate groups would be less likely candidates, but a bond from a phosphate oxygen to an heme-iron ion is observed in sulfite reductase (131).

To prove the binding of the hydroxyl groups, isotopic-labeling studies were performed. The phosphorous atoms present in MEcPP, however, have a nuclear spin

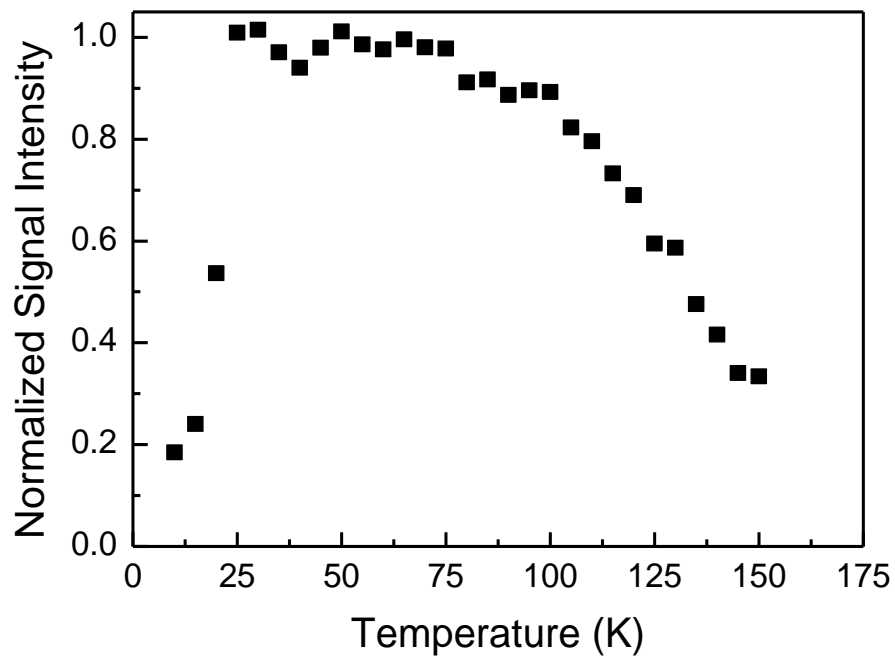


Figure 2.21: Curie Plot of the FeS_A EPR signal.

$I = \frac{1}{2}$. Therefore ^{31}P -pulsed ENDOR studies were performed to test for hyperfine coupling to the cluster spin. Figure 2.22 shows the ^{31}P -Mims ENDOR data for an EPR sample that was quenched at 10 sec and only showed the transient FeS_A signal (Fig. 2.22, panel A). The spectra in Figure 2.22, panel B, show a doublet centered at the ^{31}P Larmor frequency with a maximum splitting of about 0.2 MHz at g_1 , clearly demonstrating the presence of a single ^{31}P nucleus in proximity to the cluster spin. The data can be simulated using either a dipolar ([0.22, -0.11, -0.09] MHz, Fig. 2.23, panel A) or isotropic ([0.21, 0.09, 0.05] MHz, Fig. 2.23, panel B) dominated tensor, but regardless of the model, the small size of the coupling indicates that the phosphate groups of MEcPP, although nearby to the cluster associated with the FeS_A signal, are not directly bound to the cluster. The couplings are in fact smaller than observed for the distant, non-bonding phosphate in an intermediate of the enzyme lysine 2,3-aminomutase (132). Using the same simple point dipole calculation detailed in the previous reference, and treating the iron sulfur cluster as a point source minimum of unit electron spin density, the maximum dipolar tensor above gives a distance of the phosphorus nucleus from the unique iron of 6.6 Å.

2.3.6 Reduction of the [4Fe-4S] cluster

In an attempt to get the $[\text{4Fe-4S}]^+$ form of the cluster in GcpE, as-isolated enzyme was incubated with either a mixture of dithionite and methyl viologen, or titanium(III) citrate.

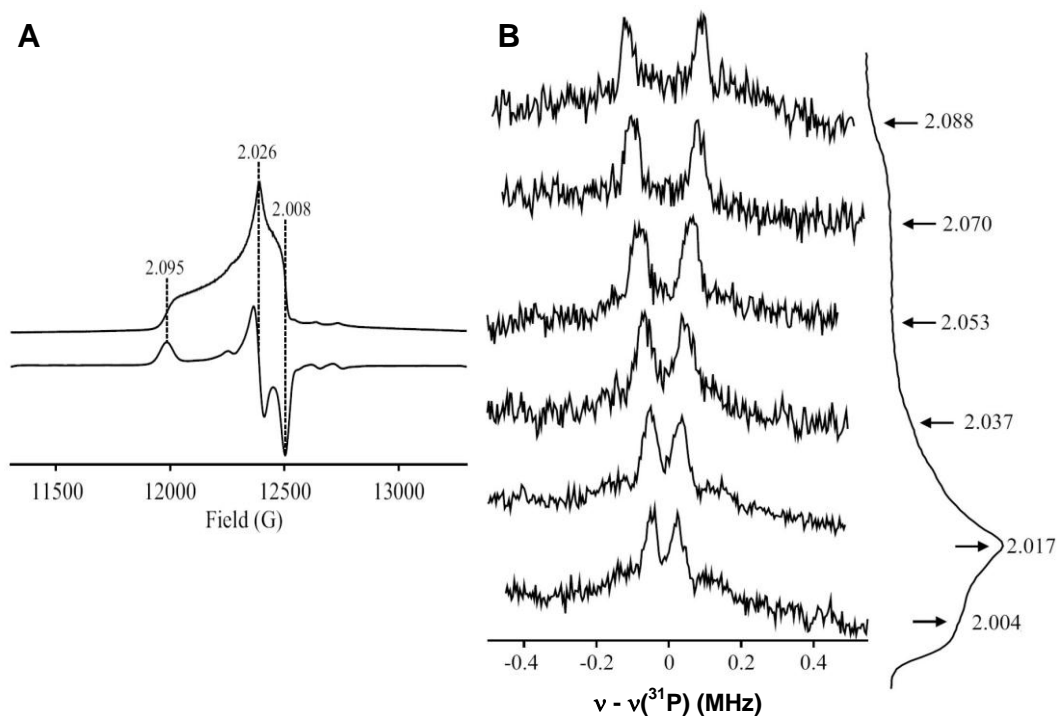


Figure 2.22: 35 GHz CW EPR and pulsed ENDOR spectra of the FeS_A species. A: CW EPR spectra of a sample incubated at 55 °C and frozen after 10 s. Derivative spectra were generated through post-processing. EPR conditions: microwave frequency, 35.140 GHz; temperature 2 K. **B:** Pulsed ³¹P ENDOR spectra. Spectra were collected at the g values indicated, and are shown alongside the respective pulse-echo detected EPR spectra. ENDOR spectra are normalized to a fixed intensity for clarity. Conditions: Mims pulse sequence: microwave pulse length 30 ns, RF pulse length 20 μs, repetition rate 20 ms, τ = 800 ns, microwave frequency 34.876 GHz (EPR); 34.871 GHz (ENDOR). Data collected by Nicholas Lees.

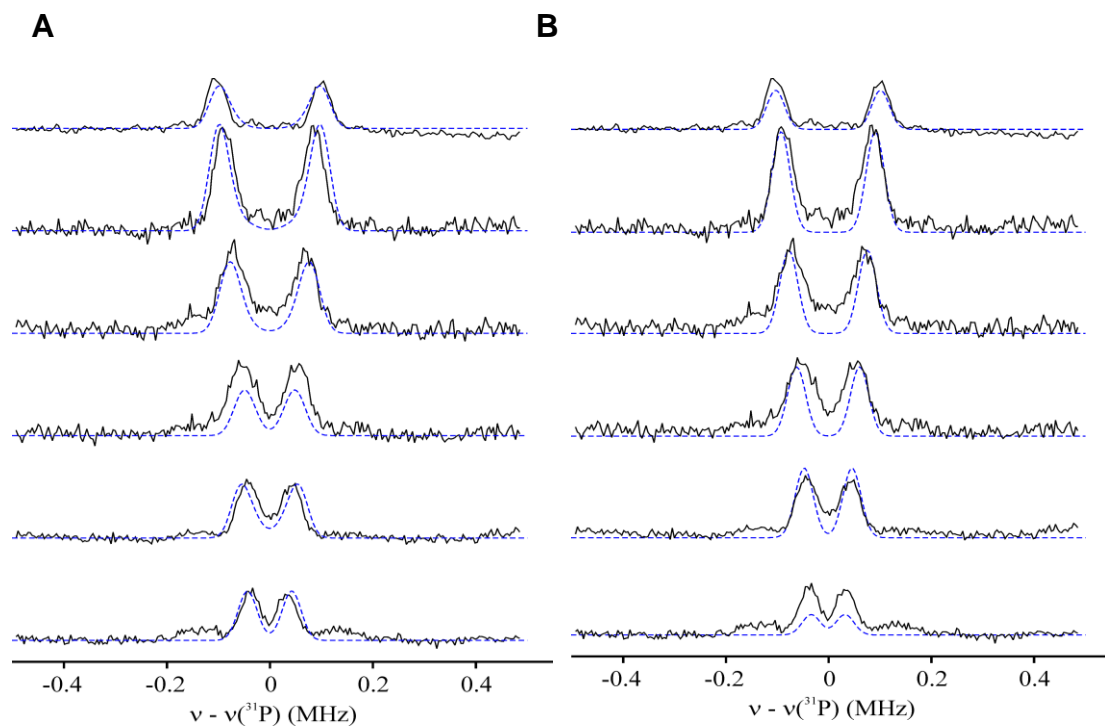


Figure 2.23: 35 GHz pulsed ^{31}P ENDOR spectra (black line) and spectral simulations (blue line). A: Dipolar dominated simulation. EPR conditions as in Fig. 2.22, with $\tau = 600$ ns. Simulation parameters: $A = [0.22, -0.11, -0.09]$ MHz, $\gamma = 20^\circ$. **B:** Isotropic dominated simulations. Simulation parameters: $A = [0.21, 0.09, 0.05]$ MHz. Simulations performed by Nicholas Lees.

Figure 2.24 shows the effect of different concentrations of dithionite-reduced methyl viologen. The large off-scale peak is due to reduced methyl viologen. The small positive feature at 320 mT and the derivative feature at 350 mT are due to a $[4\text{Fe-4S}]^+$ cluster. The data show that the 4Fe cluster in GcpE can be reduced by reduced methyl viologen. However, this signal is not very intense in comparison to the protein concentration. In general, the signal intensity was in the range of 0.01 – 0.05 spin.

A clean $[4\text{Fe-4S}]^+$ signal can be obtained when the excess methyl viologen is removed by running the sample over a PD10 desalting column. Figure 2.25 trace A, shows the EPR signal obtained with this method. This signal is a typical $[4\text{Fe-4S}]^+$ EPR signal.

Note in Figure 2.24 that the amount of reduced cluster actually decreased when the concentration of reduced methyl viologen was increased. This would indicate that the reduced cluster is not stable and falls apart under high reducing conditions. This was further proven by an experiment where GcpE was incubated with an excess of titanium citrate. The UV-visible absorbance spectra (Fig. 2.26) showed a bleaching of band at 410 nm after incubation with titanium citrate. This could indicate either the reduction or the breakdown of the iron-sulfur cluster. Parallel EPR measurements did show reduction of the cluster, but the amount of reduced cluster detected was much less than what would have been expected based on the absorption data. Extensive washing of the sample, to remove the excess titanium(III) citrate caused the loss of all EPR signals but did not return the 410 nm band indicating the loss of the 4Fe cluster or possibly the conversion

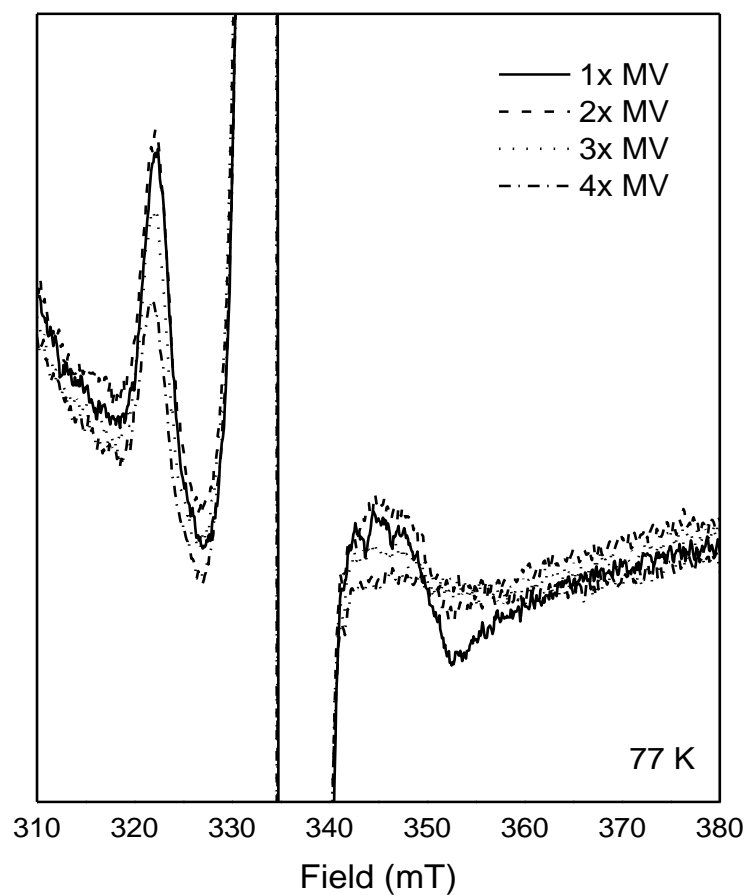


Figure 2.24: Incubation of as-isolated GcpE with dithionite-reduced methyl viologen. The samples contained 0.356 mM GcpE, and either 0.356 mM (solid line), 0.712 mM (dash line), 1.068 mM (dot line) or 1.424 mM methyl viologen (dash-dot line).

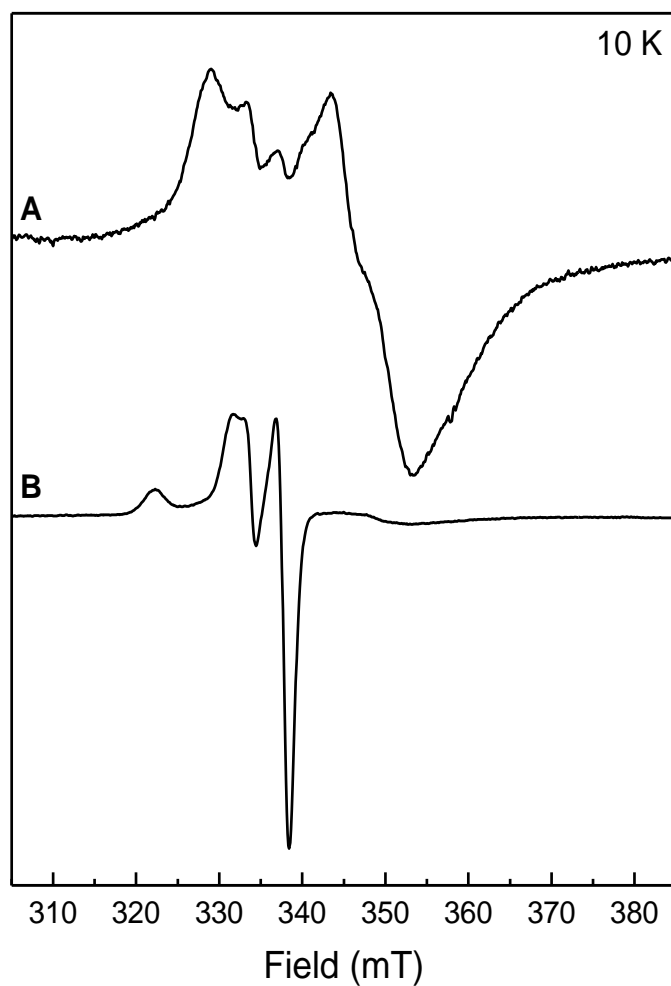


Figure 2.25: Electron paramagnetic resonance data for reduced GcpE samples.

A: Sample contained 1.3 mM GcpE and 10 mM dithionite. Signal intensity is 0.01 spin. **B:** Sample with adventitiously bound HMBPP. The sample contained 0.5 mM GcpE and 10 mM dithionite. Signal intensity is 0.02 spin.

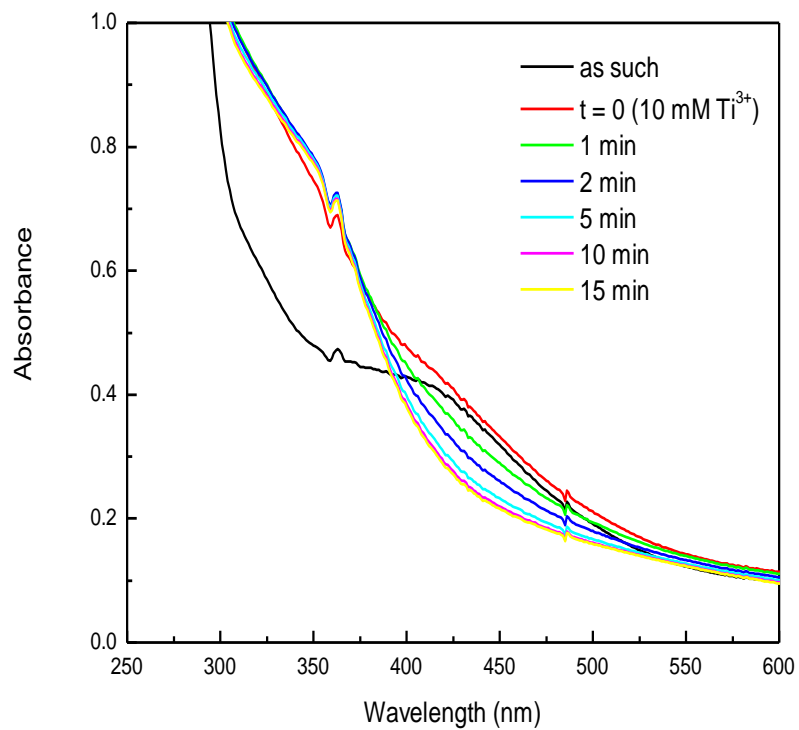


Figure 2.26: UV-visible absorption of GcpE treated with titanium(III) citrate.

The concentration of GcpE is 90 μ M and the concentration of Ti(III) citrate is 1 mM.

into a 3Fe cluster. However, exposure to air did not return any of the 410 nm absorption indicating the complete loss of the cluster.

The most common function of iron-sulfur-containing proteins is electron-transfer. The fact that only very low amounts of reduced cluster can be detected in GcpE could indicate that the cluster is only involved in substrate binding and not in electron transfer. The absence of a $[4\text{Fe-4S}]^+$ EPR signal in GcpE during turn-over experiments seems to be in line with this. It is hard to imagine, on the other hand, how electrons could get to the substrate if not somehow *via* the cluster. To check if the reduced cluster could transfer electrons to the substrate, protein was reduced with dithionite-reduced methyl viologen. The methyl viologen was removed by running the sample over a PD10 desalting column. Figure 2.27, trace A shows the EPR signal for this sample, measured at 10 K. Upon addition of MEcPP to the sample and incubation for 30 s before freezing, the EPR signal of the reduced cluster disappeared and a new signal appeared (Fig. 2.27, trace B). This signal is due to the FeS_A species, but at 10 K the signal is highly saturated and not recognizable as such. By increasing the measuring temperature to 70 K the unsaturated FeS_A signal can be detected (Fig. 2.27, trace C).

2.3.7 Origin of the FeS_B Species

Some of the reduced protein samples showed a different EPR signal upon reduction (Fig. 2.25, trace B) or a mixture of the two signals shown in Figure 2.25. This signal is identical to the FeS_B signal detected in the kinetic studies. It turned out that this FeS_B -like

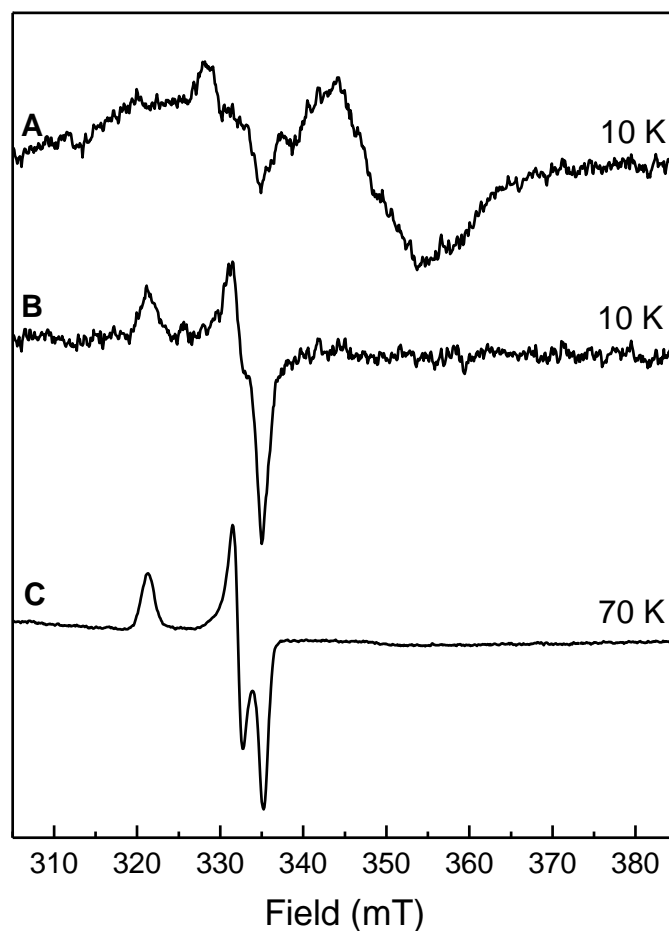


Figure 2.27: Electron transfer from reduced GcpE to MEcPP. The protein sample was pre-incubated with 0.5 mM dithionite-reduced methyl viologen. The methyl viologen was removed by running the sample over a desalting column (PD10). **A:** GcpE after desalting step. **B:** As A after addition of 10 mM MEcPP and incubation for 30 sec before freezing. **C:** Same as B, measured at 70 K. The enzyme concentration is 53 μM in all samples.

signal could only be detected in reduced GcpE samples if the enzyme was purified with a DEAE-Sepharose column that was used in several rounds of purification. With a freshly regenerated column only a regular $[4\text{Fe-4S}]^+$ spectrum is detected in the enzyme. Clearly something is bound to the enzyme causing the appearance of the FeS_B -like signal. Enzyme preparations showing this FeS_B -like signal (Fig. 2.28, trace A) can be converted into enzyme showing more of the regular $[4\text{Fe-4S}]^+$ signal by running the enzyme solution over a desalting PD10 column (Fig. 2.28, trace B). The compound that is removed is probably the reaction product HMBPP since adding this compound to enzyme preparations that only showed the $[4\text{Fe-4S}]^+$ signal (Fig. 2.28, trace C) converted most of this into the FeS_B -like signal (Fig. 2.28, trace D). Therefore it can be concluded that the FeS_B species is due to reduced enzyme with HMBPP bound.

The conversion of the enzyme sample showing mainly the FeS_B signal into a sample mainly showing the $[4\text{Fe-4S}]^+$ signal by running the protein sample of the PD10 column appears to increase the total amount of spins significantly (Fig. 2.28, traces A and B). It is not clear what is causing this effect since it indicates an increase in reduced species. The ‘larger’ intensity observed after the conversion of a $[4\text{Fe-4S}]^+$ signal into the FeS_B signal upon addition of HMBPP (Fig. 2.28, traces C and D) is due to the fact that the signal intensity of the $[4\text{Fe-4S}]^+$ signal is spread out over a much wider range than the intensity of the FeS_B signal. Double integration of both EPR signals show an almost equal amount of signal intensity lost and gained in the conversion of the two species.

To further prove that the FeS_B species does not represent a dead-end product, GcpE

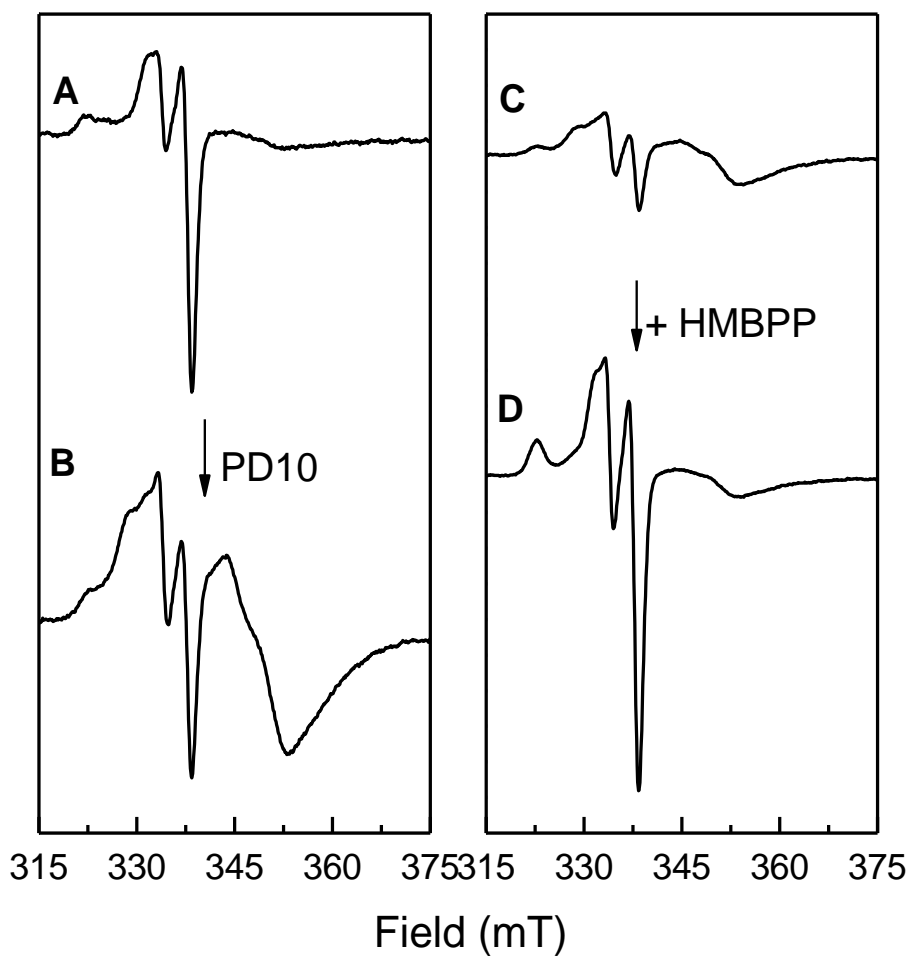


Figure 2.28: FeS_B species from reduced GcpE with HMBPP bound. **A:** GcpE incubated with 13.3 mM dithionite; **B:** As A after running over a desalting column (PD10); **C:** Same as B; **D:** As C after addition of 10 mM HMBPP. The enzyme concentration is 0.5 mM in all samples. All samples were measured at 10 K, 20dB.

was incubated with both dithionite and MEcPP and at different time intervals a sample was tested for activity in the colorimetric assay with methyl viologen and in parallel a sample was taken that was frozen for examination in EPR spectroscopy (Fig. 2.29). All samples displayed the same specific activity (not shown) indicating that the accumulation of the FeS_B signals is not accompanied by a significant loss of activity. This is in line with the assignment of a reduced enzyme with possibly bound reaction product. The fact that much more 'reduced' cluster, up to 0.5 spin for the FeS_B species vs. 0.05 spin for the [4Fe-4S]⁺ signal, can be detected under turn-over conditions could be due to the fact that direct binding of HMBPP to the cluster has a significant effect on the midpoint potential of the cluster itself as seen in other enzymes. Under these conditions the substrate MEcPP would have to compete with the bound HMBPP which would indicate that HMBPP is a competitive inhibitor of GcpE.

Due to the limited amount of HMBPP available a K₁ has not been determined yet for HMBPP. The fact that all species in Figure 2.29 show identical activities indicates that MEcPP must easily outcompete HMBPP. This was further shown in an experiment where as-isolated protein was first incubated with substrate and excess dithionite. To make sure no changes were taking place anymore in the signal intensity of the FeS_B species, the sample was incubated for 32 min (Fig. 2.30. panel A). Following the incubation more MEcPP was added to the enzyme solution (t = 0) and the sample was incubated for another 32 min (Fig. 2.30. panel B). At first glance there does not seem to be a change in the EPR spectrum of the enzyme sample during this time interval. However, when

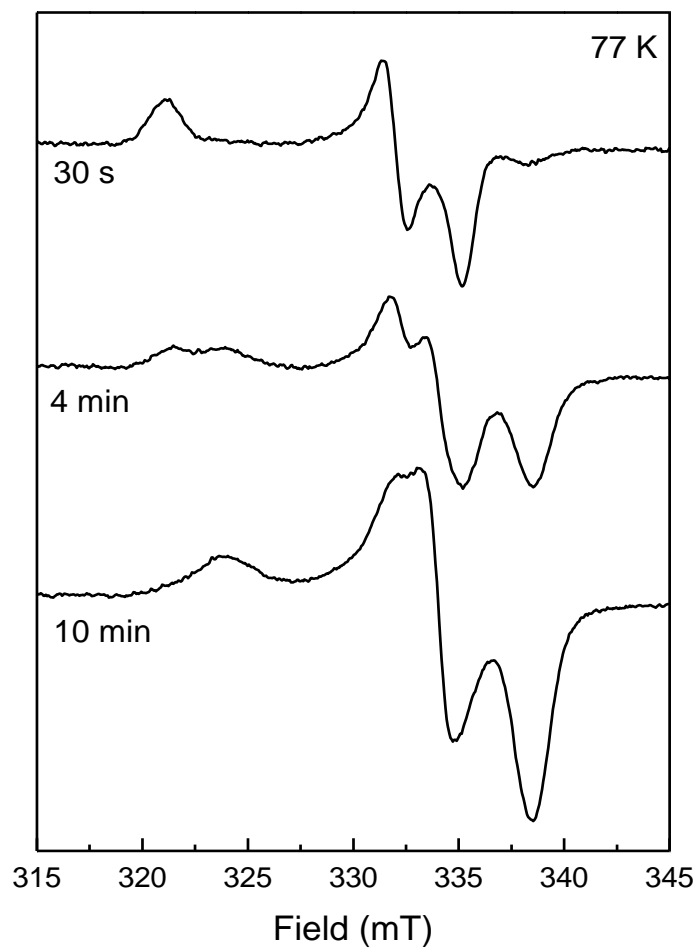


Figure 2.29: EPR signals of GcpE samples that were tested for activity. Samples contained 120 μ M GcpE, 5 mM dithionite and 4 mM MEcPP and were incubated for the indicated times at RT.

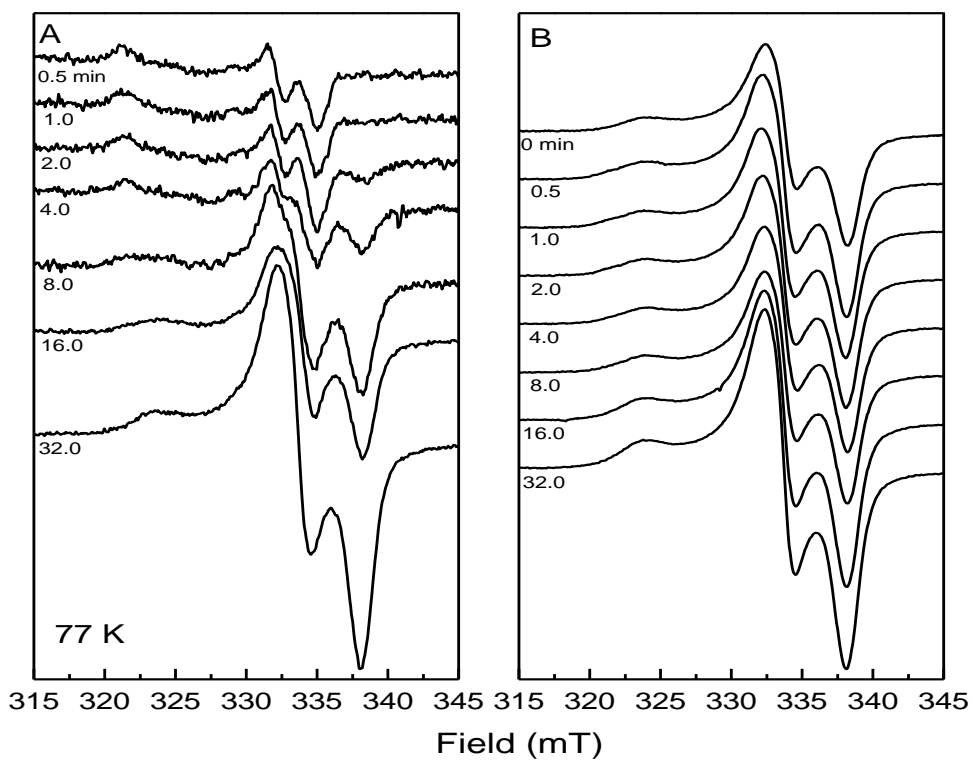


Figure 2.30: Addition of MEcPP to the FeS_B form. **A:** Sample contains 200 μM GcpE, 200 μM MEcPP and 30 mM dithionite. Sample were frozen at the indicated times. **B:** After the first round of incubation another 200 μM MEcPP was added. Sample were frozen at the indicated times.

a subtraction is made of the EPR signal of the sample after 30 s of incubation and the EPR signal of the sample at $t = 0$ s, a difference spectrum is obtained that resembles the FeS_A EPR signal (Fig. 2.31).

2.3.7.1 Spectroscopic Properties of the FeS_B Species

Temperature studies (Fig. 2.6) showed that the FeS_B EPR signal could be due to 2 or even 3 different magnetic species. All these species have their origin on the iron-sulfur cluster as proven by the broadening of the EPR signal over the whole signal range by the introduction of the nuclear spin isotope ^{57}Fe . This was also confirmed by the fact that the ^{57}Fe -coupling was equal over the whole signal envelope as determined by ^{57}Fe -ENDOR (not shown). Of course we also looked at the ^{31}P -ENDOR spectra for the FeS_B species.

Shown as an overlay in Figure 2.32 (Panel B, blue spectra) are the ^{31}P -ENDOR data for a sample that was frozen after 5 min of incubation displaying the mixture of FeS_B signals (Fig. 2.32, panel A). The black spectra in Figure 2.32, panel B, are the ones determined for the FeS_A species. At g_1 , a single pair of peaks is observed centered about the ^{31}P Larmor frequency, also with a small coupling, $A \sim 0.4$ MHz, although larger than that observed for the 10 s FeS_A sample. Thus the FeS_B centers also have a phosphate group, probably from HMBPP, nearby to the cluster, but again the coupling is too small for direct binding of phosphate to the cluster. Above ~ 12300 G, three different ^{31}P features are visible. None correspond to those observed for the 10s sample, indicating that there is no EPR signal from the FeS_A center in this sample.

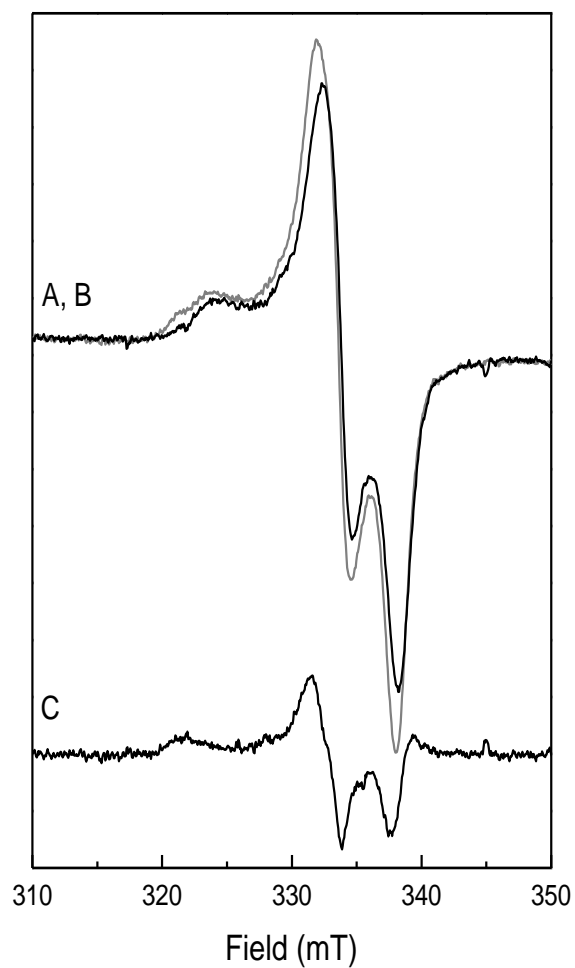


Figure 2.31: Comparison of the ‘0 min’ and the ‘0.5 min’ traces from Figure 2.30, panel B. The ‘0 min’ sample is trace A (black). The ‘0.5 min’ sample is trace B (gray). The difference spectrum is trace C.

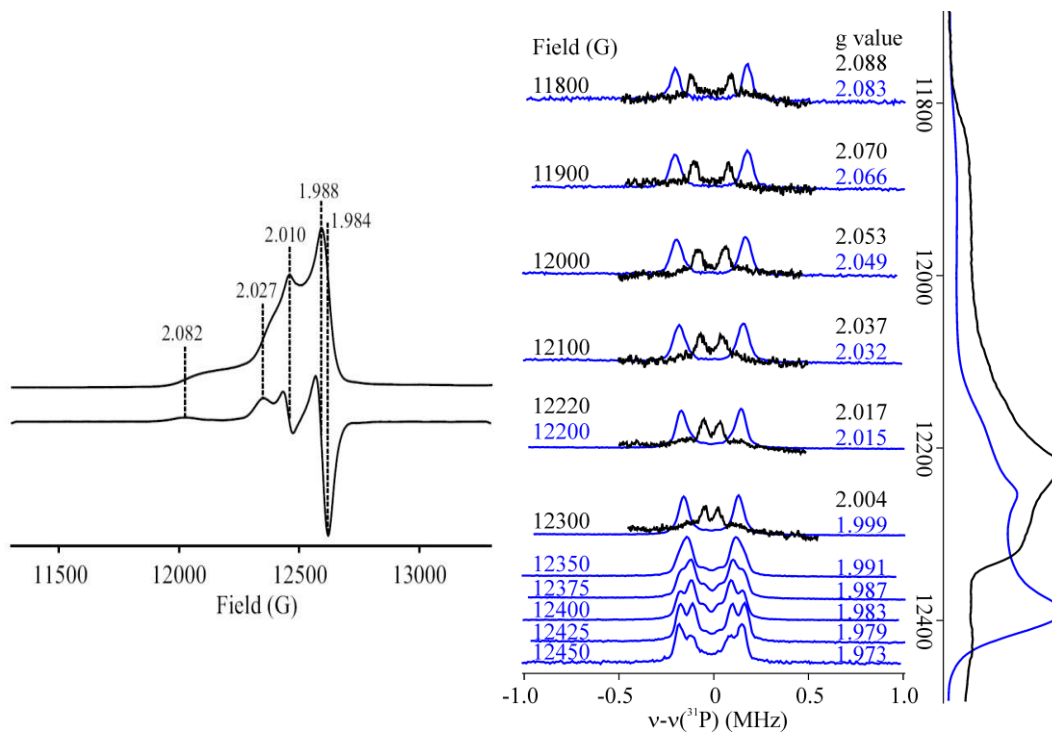


Figure 2.32: 35 GHz pulsed ^{31}P ENDOR spectra of a GcpE samples flash frozen after 5 min (blue line) incubation time (the FeS_A species). A: CW EPR spectra. Derivative spectra were generated through post-processing. **B:** ^{31}P ENDOR spectra. Spectra were collected at the fields and g values indicated. ENDOR spectra are normalized to a fixed intensity for clarity. Conditions: Mims pulse sequence, microwave pulse length 30 ns, RF pulse length 20 μs , repetition rate 20 ms, $\tau = 500$ ns (EPR); 600 ns (ENDOR), microwave frequency 34.857 GHz. Data collected by Nicholas Lees.

Analysis of the multiple ^{31}P features at fields above 12300 G must take into account the observation, described above, that the EPR spectrum of the 5 min sample shows multiple features due to different species. The bulk of the EPR intensity appears to be due to an axial species with $g_{\parallel} = 2.08$, $g_{\perp} = 1.98$, while additional features are seen within this range at g values of 2.03 and 2.01 (Fig. 2.4, traces B and C). It is not certain whether these features belong to the same EPR species, but their relative intensities remain identical under a range of experimental conditions. While there are no resolved ^{31}P ENDOR features that appear to correspond to the EPR intensity at the latter g values, the overall intensity of the ^{31}P ENDOR does increase in approximate proportion to the increase in EPR intensity, indicating that all of the EPR species present (at least two) show ^{31}P ENDOR due to interaction with the product HMBPP. Furthermore, analysis of a second sample (not shown) showed a significantly different intensity ratio for one of the three ENDOR peaks compared to the other two, ruling out the possibility that all three of the ENDOR peaks could arise from the two phosphorus atoms of the substrate and a single EPR species.

Given the uncertainty surrounding the number of EPR species, their g values and the number of contributing ^{31}P nuclei, no definitive fit for the data from FeS_B can be obtained. However, we can account for all the data with any one of the three simplest models.

There is a single pair of peaks at the low field edge of the EPR spectrum that can be followed across the entire EPR envelope, which we assume in all models to belong to the axial EPR species as described earlier, designated here as B_1 (Fig. 2.4, traces B and C).

However, it is unclear whether that pair becomes the middle or outer pair at the high field edge. Since the inner pair of peaks has an invariant intensity ratio relative to the middle pair in the two samples, we assume that both the middle and inner pair arise from the same EPR species, and could potentially represent either one or two phosphorus nuclei. The third pair of peaks must arise from a different EPR species (B_2). As the overall ENDOR intensity rises sharply at the g_1 -like feature at $g = 2.03$, we can assume that this is the edge of the EPR envelope for B_2 , and the ENDOR coupling coincidentally matches that of B_1 , therefore only one peak is observed. If we assume that there are only two EPR species present in total, then the $g = 2.01$ feature is g_2 of B_2 , and g_3 must be very close to g_3 of B_1 , as the ENDOR signals from both occur in the same field region on the high field side.

A full description of these models and simulations for FeS_B will be published elsewhere (paper submitted to JACS). While the line shapes generated in these simulations are good, all of the simulations suffer from problems with the relative intensities of peaks both at the same g value, and across the EPR envelope, suggesting that the assumptions about the number of EPR species and their g values may not be entirely correct. Regardless of the model, the maximum observed ^{31}P hyperfine coupling is ~ 0.4 MHz, precluding the possibility of direct binding of phosphate to the cluster.

2.4 Discussion and Conclusion

2.4.1 Reduction of the [4Fe-4S] Cluster in GcpE

The [4Fe-4S] cluster in GcpE was attributed with the unusual property that it can not be reduced by dithionite alone, although this compound is widely used as an artificial electron donor. Methyl viologen has been used as a redox mediator in enzymatic redox titrations, due to its powerful strength of electron transferring to a metal center in a protein. Reduced methyl viologen can reduce the [4Fe-4S]²⁺ cluster in GcpE to the [4Fe-4S]¹⁺ cluster as shown in Figure 2.24. Titanium(III) citrate is a stronger reductant than dithionite and has been used in enzyme studies. It has the same drawback as methyl viologen that it is paramagnetic and its EPR signal overlaps with and overshadows the EPR signals displayed by GcpE. The incubation of GcpE with titanium(III) citrate alone, destroyed the [4Fe-4S]²⁺ cluster. Only a small [3Fe-4S]⁺ signal could be detected in EPR spectroscopy. In the presence of substrate, however, titanium(III) citrate does not destroy the cluster, but forms the transient FeS_A EPR signal. This datum is in line with recent work by Xiao et al. (133). In this work, GcpE was incubated with several different reductants. GcpE was highly active in a small redox potential window with values at around -446 mV (vs. NHE), a value close to the midpoint potential of methyl viologen. At both higher and lower redox values the GcpE activity was reduced.

The observation was made that the cluster can be reduced by dithionite, if the sample is first incubated with dithionite and is subsequently run over a PD10 desalting

column (Fig. 2.28, panel A). Under turn-over conditions, relative high amounts of the HMBPP-[4Fe-4S]⁺ species accumulate. In this case it appears that the binding of HMBPP to the cluster causes a change in the midpoint potential of the cluster. We hypothesize that in the case of the increased reduction rate of the cluster after PD10 treatment there also might be a ligand present on the cluster that is removed by this treatment and caused a change in the midpoint potential of the cluster. In a future experiment the midpoint potential of the cluster should be determined in the presence and absence of different ligands.

It is not immediately clear why methyl viologen can reduce the cluster and dithionite by itself cannot. The midpoint potential of methyl viologen is higher than that of dithionite. Methyl viologen, however, is generally used as a redox dye since it facilitates fast electron transfer to the target proteins. The fact that reduced methyl viologen is positively charged and dithionite is negatively charged could explain the difference in interaction of these compounds with the enzyme and/or cluster. It could also be a problem with dithionite having access to the cluster (see below).

2.4.2 The FeS_A Species

The presence of the substrate MEcPP accompanied by reductants (including dithionite, reduced methyl viologen, and Titanium(III) citrate) generated the paramagnetic species FeS_A and FeS_B. The two species were detected in all cases showing the same trend: first the formation and slow disappearance of the FeS_A species, followed

by the accumulation of the FeS_B species in time dependent studies.

The EPR signal of the FeS_A species shows high resemblance in shape, and temperature behavior to a signal detected in FTR. Initially, this signal was proposed to be due to a radical-type intermediate that was stabilized by binding to a 4Fe cluster (70). This could explain the unusual combination of an iron-sulfur-cluster-based signal that was detectable up to 150 K, a property more commonly found for radical-type species. Later work, however, showed that it was a pure [4Fe-4S]³⁺ species and the unusual temperature behavior is probably the result of the changed cluster properties due to the additional sulfur ligand present on the 'unique' iron in the cluster (71).

The assignment of the FeS_A species to a reaction intermediate bound to the iron-sulfur cluster was mainly based on the similarities of its EPR properties to those of the signal detected in FTR (121). Additionally, comparison of the FeS_A signal detected in GcpE grown on natural abundance iron and GcpE enriched in ⁵⁷Fe-isotope showed that a considerable broadening was introduced by the nuclear spin of ⁵⁷Fe, indicating that the signals are iron-sulfur based.

As mentioned before, MEcPP has two functional groups that may potentially be used for binding to the 4Fe cluster in GcpE, the hydroxyl group and the diphosphate group. In the case of aconitase, the leaving hydroxyl group of citrate (or iso-citrate) binds to the iron-sulfur cluster. Meanwhile, in the crystal structure of sulfite reductase a phosphate molecule is present that is bound to the heme-iron via one of the oxygen atoms (134). Based on the fact that a hydroxyl group is lost in the formation of HMBPP, this

hydroxyl group is the most likely candidate to coordinate to the iron-sulfur cluster. To prove the binding of the hydroxyl group, labeling studies of either the hydroxyl oxygen or the carbon atom the group is attached to will be needed. This is planned for the near future. An experiment that is currently under way is to look for the possible exchange of the hydrogen of the hydroxyl group with deuterium in D₂O and a possible measurable effect in ¹H-ENDOR. Due to the presence of phosphorous atoms with a nuclear spin $I = 1/2$, it was possible to already perform ³¹P-ENDOR measurement. Although the ³¹P-ENDOR spectra of both the FeS_A and FeS_B species show ³¹P superhyperfine coupling, these couplings are weak, which indicate that the phosphate groups of MEcPP or HMBPP are not directly bound to the cluster in any of these forms. For the FeS_A species a distance of 6.6 Å could be estimated for the distance of the phosphorus atom to the unique iron in the cluster. Thus, these data at least imply that the substrate and product are in close proximity to the iron-sulfur cluster.

2.4.3 The FeS_B Species

The FeS_B species turns out to hide some surprises. First of all, there appears to be at least two and possibly three species associates with this signal. At 6 K an axial species can be recognized (Fig. 2.4, traces B and C) while a separate species can be detected at 50 K (Fig. 2.4, trace D). Additional species can be detected at 6 K that might or might not be a third species. In all studies, however, these species always develop together and from a functional point of view they behave like one species. Surprisingly, ⁵⁷Fe-enrichment of

the cluster in GcpE showed a broadening of the EPR signal over the whole spectrum at both low and high temperature indicating that all species present originate on the 4Fe cluster (Fig. 2.10).

The accumulation of the FeS_B species in kinetic experiments could indicate a dead-end path that is not related to the reaction mechanism of GcpE. However, activity measurements on samples taken at different points during an EPR-detected kinetic experiment (Fig. 2.29) showed that the accumulation of FeS_B species was not accompanied with a significant loss of activity. It indicates that the FeS_B species might be a possible resting state of the enzyme instead of being dead-end products. Figure 2.31 shows that the addition of substrate to a sample showing the FeS_B EPR signal generated the FeS_A signal just as protein that showed no signal.

Although the FeS_A species could be due to an [4Fe-4S]¹⁺ form or [4Fe-4S]³⁺ form of the cluster, it is established that FeS_B is in a [4Fe-4S]¹⁺ form. Moreover, the data in Figure 2.28 showed that this [4Fe-4S]¹⁺ form is bound by product HMBPP. As a result, FeS_B is understood as being generated by product binding to the [4Fe-4S]¹⁺ cluster.

Additional CW and pulsed high frequency EPR measurements to delineate the different FeS_B species did not give a clear answer. W-band and Q-band EPR analysis (not shown) were expected to give more detailed information about the signal. However, data obtained at these frequencies only showed similar overall signals as detected by X-band EPR. The W-band spectra also had very low signal-to-noise ratios. Thus, they did not help in the separation of the different signal or discovery of the origins of them.

2.4.4 Reaction Conditions: Temperature, Substrate Concentration, Reduction System

First, the temperature is indicated as a big factor for the enzyme activity of GcpE by the results obtained from EPR experiments performed with dithionite at RT and 55 °C (Fig. 2.12). It is consistent with higher specific activity of $0.6 \mu\text{mol}\cdot\text{mg}^{-1}\cdot\text{min}^{-1}$ at 55 °C (5) and lower specific activity of $0.124 \mu\text{mol}\cdot\text{mg}^{-1}\cdot\text{min}^{-1}$ at RT.

As well, the reduction system and the substrate concentration are factors of influence for this reaction. Based on the previous freeze-quench result, the reaction seems to take about 1 min for one cycle. An excess of dithionite and substrate are necessarily needed for detection of the reaction intermediate under steady-state conditions. However, the activity assay performed by the colorimetric method coupled with methyl viologen at RT gave a k_{cat} of $\sim 0.09 \text{ s}^{-1}$ which means one cycle should only take about 11 sec to finish. Additionally, the single-turnover experiment showed the similar inconsistency for the kinetic parameters. These differences are due to the different reaction conditions. It implies a different midpoint potential dependency for the formation of the FeS_A and FeS_B species. The appearance and subsequent disappearance of FeS_A species as well as the formation and accumulation of FeS_B species represent independent redox processes.

Titration with substrate showed that the speed of the formation of the intermediate species is not influenced by the substrate concentration. However, the signal intensity of FeS_A is highly dependent on the concentration of MEcPP.

The different midpoint potentials for the two separate electron-transfer steps were

further investigated in titration experiments with dithionite, reduced methyl viologen, and Titanium(III) citrate. EPR spectra confirm that the reaction is significantly faster in the presence of methyl viologen than when only dithionite present as electron donor. The spectrum C in Figure 2.17 indicates that only 10^{-7} s is need for one full reaction cycle in the presence of methyl viologen, and also that the breakdown of the FeS_A species is not the rate limiting step, which is the case when only dithionite functions as electron donor. Apparently, methyl viologen functions better and more efficiently than dithionite as electron donor for this reaction. With titanium(III) citrate, it seems that the FeS_B signal also behaves like a transient species. Since titanium(III) citrate can also damage the cluster, the ‘transient’ character could be due to just that.

2.4.5 Proposed Mechanisms

It is known that these reductive processes involve the overall transfer of two electrons and result in the cleavage of a C-O(H) bond. An intermediate radical species is expected to be involved in this reduction process, because the [4Fe-4S] cluster in GcpE can only transfer one electron at a time. Several hypothetical radical-type mechanisms were reported in the literature.

Figure 2.33 (5) shows a mechanism without the direct involvement of the iron-sulfur cluster. The ring opening of cyclodiphosphate initiates the reaction to form a tertiary carbocation. This relatively stable carbocation can be reduced by two consecutive one-electron transfers. The hydroxyl group of substrate MEcPP will be eliminated as

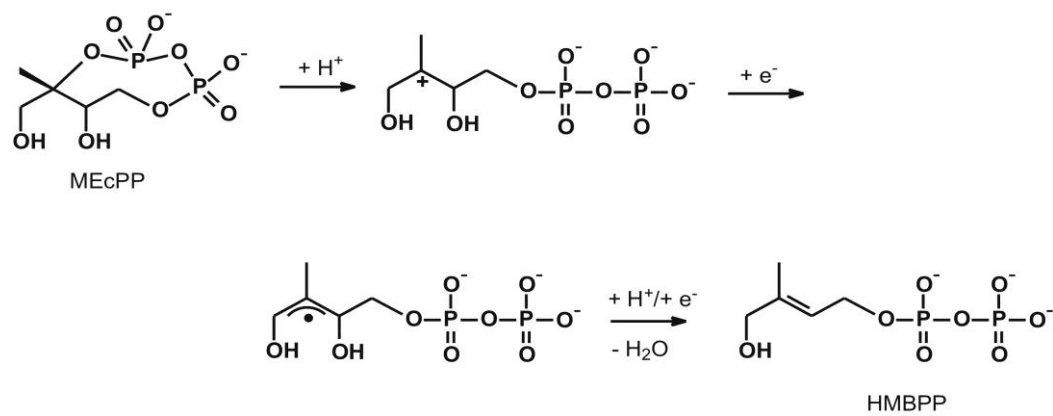


Figure 2.33: Hypothetical mechanism I

water to yield the product HMBPP.

In an alternative model (Fig. 2.34) the hydroxyl group was proposed to become a better leaving group by transfer to the enzyme before its release as H₂O (125).

In a third proposed mechanism, the binding of the iron-sulfur cluster to the reaction intermediate is directly involved in the elimination of the hydroxyl group (Fig. 2.35). The proposed binding, release and rebinding, however, does not seem to be a logic series of steps. Additionally, it invokes the formation of a transient epoxy species directly after the ring opening. The epoxy species has been shown to be a substrate, but it is not clear if such a species is actually formed during the mechanism.

Although all mechanistic details are not investigated clearly so far, it still indicates that the reaction mechanism has to be completely different from ones previously proposed. The 28ms — 0.5s spectra in Figure 2.3 could be due to the carbon radical, but the rest of the signals cannot be explained based on these mechanisms.

Therefore, based on the knowledge of GcpE, an alternative mechanism is proposed as shown in Figure 2.36. The reaction starts with the binding of MEcPP to the [4Fe-4S]²⁺ cluster, which results in a change in midpoint potential of the cluster and the reduction of the 4Fe cluster by electron transfer from dithionite, or in the cell by the natural electron donor. This species is one of candidates for the origin of the FeS_A signal ([4Fe-4S]¹⁺ form). The subsequent protonation of MEcPP results in ring opening and the formation of a carbocation. Internal electron transfer from the cluster to the substrate results in the formation of a carbon radical. There are several possibilities of how the cluster

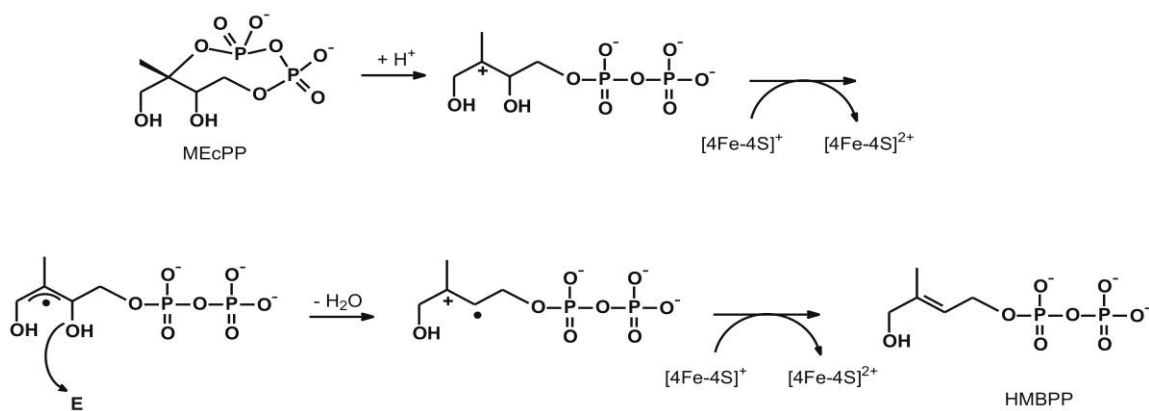


Figure 2.34: Hypothetical mechanism II

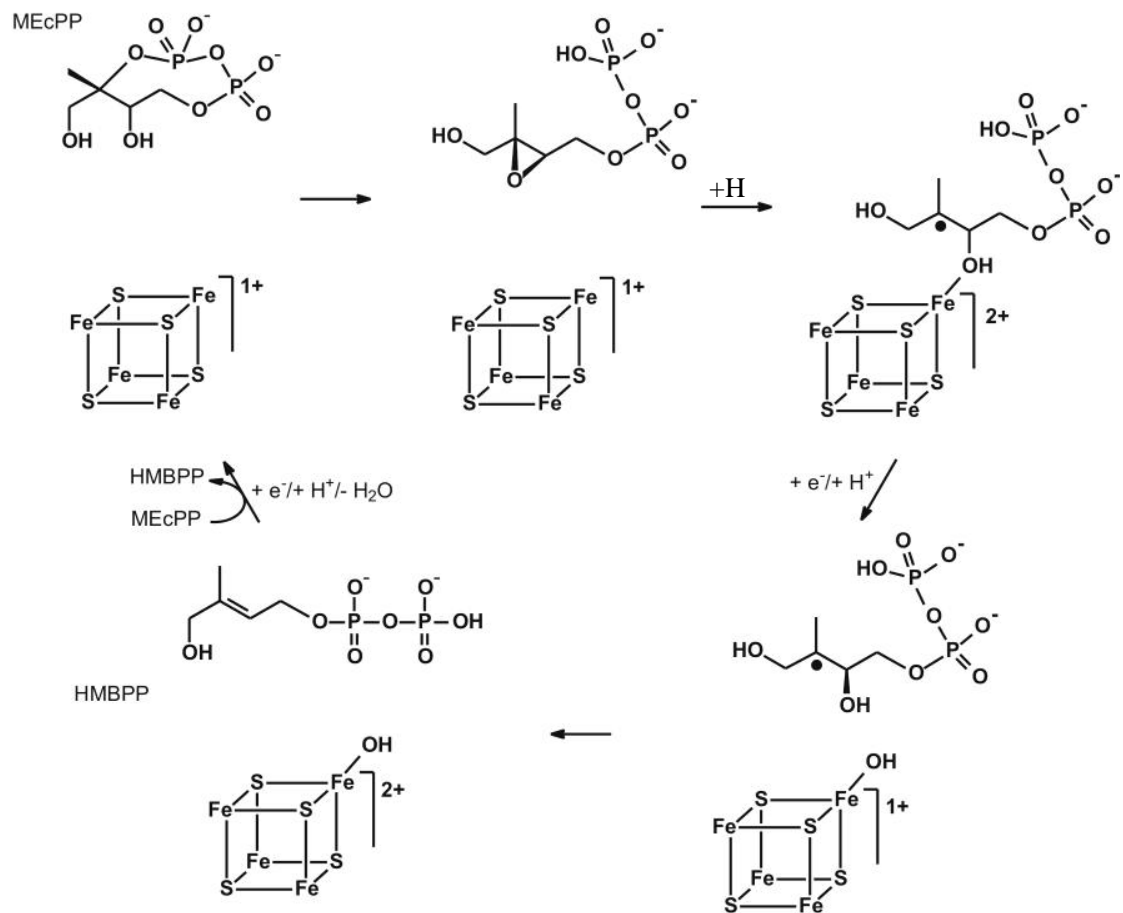


Figure 2.35: Hypothetical mechanism III (12)

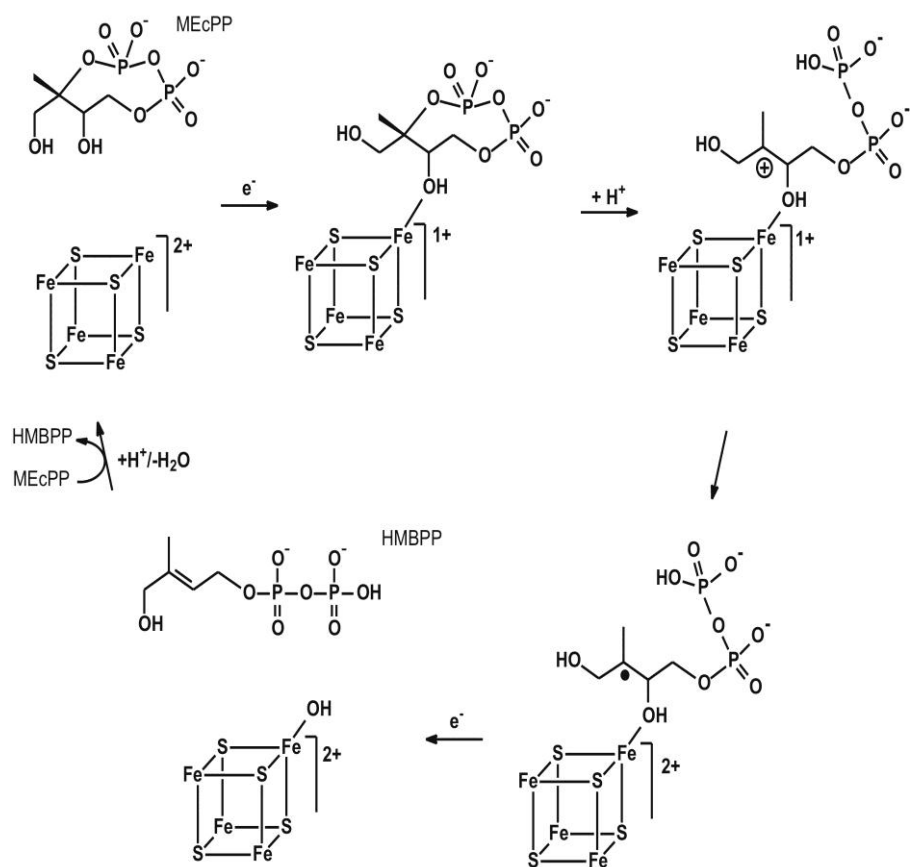


Figure 2.36: Hypothetical mechanism IV

can stabilize this radical species. One option would be the transfer of an additional electron, making the cluster formally 3+. However, this would create a carbon anion species that could be very reactive. However, formation of a η -type complex would provide the needed stabilization of either the radical or an anion species. Such a species would be the second candidate for the origin of the FeS_A species ([4Fe-4S]¹⁺ form). Labeling studies with ¹³C-isotope will be needed to prove such a type of bonding. Transfer of a second electron from the outside electron donor to the active-site cluster results in the release of the hydroxyl group and double bond formation. The hydroxyl group can stay bound to the cluster and comes off later since it is probably only weakly bound as shown for example for aconitase. This is a simple model that explains the formation of the FeS_A species. The formation of the FeS_B signals would be due to the adventitious binding of the reaction product HMBPP to the reduced cluster, probably via the remaining hydroxyl group on HMBPP. To fully understand the iron-sulfur-based signals described here, ENDOR and Mössbauer studies with ⁵⁷Fe-isotope-labeled enzyme are needed.

Chapter 3: (E)-4-hydroxy-3-methylbut-2-enyl Diphosphate Reductase

3.1 Introduction

3.1.1 Function of LytB in the Cell

The (E)-4-hydroxy-3-methylbut-2-enyl diphosphate reductase (IspH or LytB) catalyses the terminal step of the DOXP pathway, the conversion of (E)-4-hydroxy-3-methyl-but-2-enyl diphosphate (HMBPP) into two products: isopentenyl diphosphate (IPP) and dimethylallyl diphosphate (DMAPP) (135-141).

The ratio of IPP and DMAPP *in vivo* or *in vitro* can be anywhere between 4:1 and 6:1, depending on the origin of the enzyme (*E. coli*, *Aquifex aeolicus*, or *Plasmodium falciparum*), or enzyme type (as-isolated or reconstituted). Electrons can be donated by the natural flavodoxin/flavodoxin reductase/NADH system, or by artificial donors including photoactivated deazaflavin and dithionite.

Different specific activities have been published for this enzyme in the literature. The LytB protein from *E. coli* fused to maltose-binding protein had a specific activity of 3 nmol·min⁻¹·mg⁻¹ using flavodoxin/flavodoxin reductase/NADH and a specific activity of 0.4 μmol·min⁻¹·mg⁻¹ with photoactivated deazaflavin (135). The specific activity of

LytB protein from *A. aeolicus* when performed at 60 °C was $6.6 \pm 0.3 \mu\text{mol}\cdot\text{min}^{-1}\cdot\text{mg}^{-1}$ with reduced methyl viologen as electron donor (137). The highest activity was reported for LytB from *P. falciparum*, approximately $2.1 \mu\text{mol}\cdot\text{min}^{-1}\cdot\text{mg}^{-1}$ with reduced methyl viologen at 30 °C (142).

3.1.2 Characterization of the Iron-Sulfur Cluster of LytB

The exact nature of the iron-sulfur cluster of LytB remains a matter of debate: being either a [3Fe-4S] or [4Fe-4S] cluster. Amino acid sequence alignments of LytB showed only three absolutely conserved cysteine residues (Fig. 3.1) (143;144). Mutation of these three Cys residues into Ser residues, caused a loss in activity (140). The absorption spectrum of as-purified LytB protein displayed a band at 410 nm and a shoulder at 320 nm, which are characteristic for both types of iron-sulfur clusters. Gräwert et al. reported a pulsed EPR signal (X-band) at 345 mT with $g_{\parallel} = 2.032$ and $g_{\perp} = 2.003$ at 5.5 K (140), indicating the presence of a [3Fe-4S]¹⁺ cluster in the LytB enzyme from *E. coli*. However, the authors did not present data on the reduced enzyme. As a result, the possibility of the presence of a 4Fe cluster cannot be ruled out, since the [4Fe-4S]²⁺ cluster is a diamagnetic species and is EPR silent under the conditions used in the paper. In contrast, a typical EPR signal of a [4Fe-4S]¹⁺ cluster was detected by Wolff *et al.* (136) in reconstituted LytB protein from *E. coli* after reduction with dithionite.

Mössbauer spectroscopy showed the presence of a [4Fe-4S]²⁺ cluster with an unusual coordination sphere in the LytB protein from *E. coli* (145). It was shown to

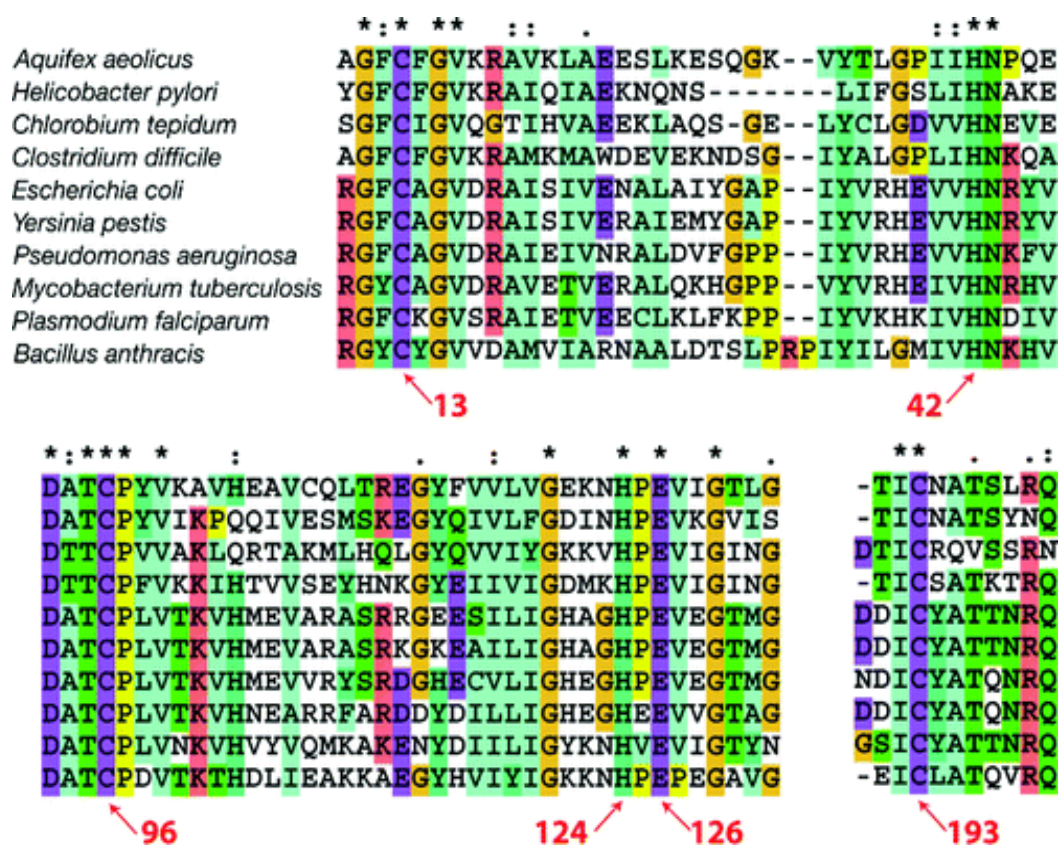


Figure 3.1. Amino acid sequence alignment of LytB proteins showing conserved residues of interest. Taken with permission from (77). (Copyright American Chemical Society)

contain one pair of iron ions with a delocalized electron (“Fe^{2.5+}-Fe^{2.5+}”) and one valence-trapped pair (“Fe³⁺-Fe²⁺”). The addition of HMBPP decreased the isomer shift of the iron with the unusual coordination sphere, which was indicative for coordination of HMBPP to the iron-sulfur cluster.

3.1.3 Crystal Structures of LytB

The enzyme crystal structure should supply the most convincing information about the iron-sulfur cluster type. However, the discussion about the nature of the iron-sulfur cluster of LytB did not end there. The crystal structures of LytB proteins from *A. aeolicus* and *E. coli* were solved recently. Both of them showed a [3Fe-4S] cluster present in the center of the protein.

The LytB protein from *A. aeolicus*, a thermophilic eubacterium, was overexpressed and purified in *E. coli*. The crystal structure of this protein was solved at 1.65 Å resolution (77). The structure (Fig. 3.2) showed that each protein monomer has a cloverleaf structure built up of α/β domains which are surrounding a central [3Fe-4S] cluster. There is a pronounced cavity with ca. 10 Å x 20 Å located at the front side, even though the overall structure is quite flat. This pronounced cavity might be available for substrate access/product egress. The [3Fe-4S] cluster is found at the bottom of the crevice. The backside of this protein does not show any possible route for substrate access.

The presence of a 3Fe cluster was surprising since data by our group clearly

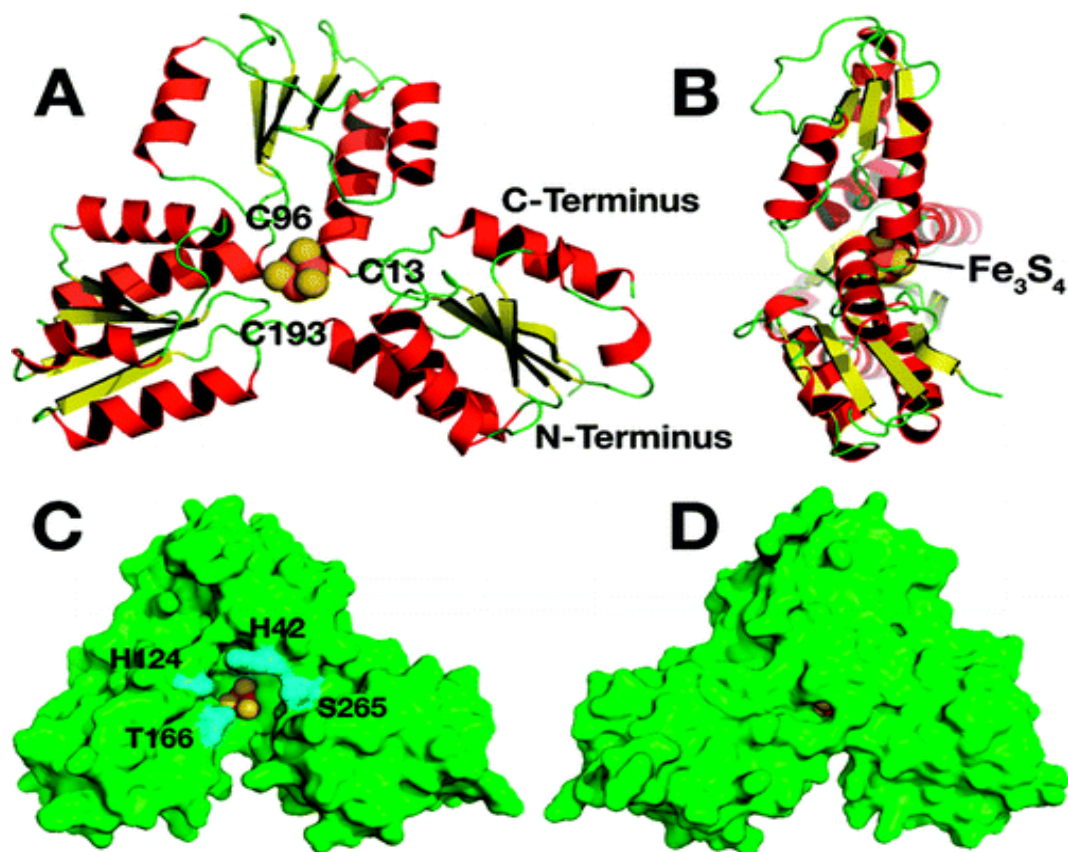


Figure 3.2. Structure of LytB from *A. aeolicus* (PDB [3DNF](#)). (A) monomer showing a cloverleaf structure consisting of three lobes surrounding a central [3Fe-4S] cluster; (B) side view; (C) front view of protein (as in panel A), illustrating the proposed substrate entry route to the [3Fe-4S] cluster. The four residues in blue (H42, H124, T166, and S265) are very highly conserved over 224 species. The [3Fe-4S] cluster is shown in yellow/brown and is essentially inaccessible from the rear face of the protein (D). Taken with permission from (77). (Copyright American Chemical Society)

showed that active enzyme contained a 4Fe cluster (see below). Therefore, the 4Fe cluster was computationally reconstituted. Figure 3.3 shows a simulation of the active site with both the cluster present and the substrate HMBPP. These studies showed that His42 and His124 are probably involved in the coordination of the diphosphate group. The only highly conserved amino acid present in the active site that can participate in acid-base chemistry is Glu126. This amino acid is proposed to play a role as a proton donor to C2 or C4 of HMBPP. The model also indicated a possible interaction of the hydroxyl group of HMBPP with the unique iron of the active-site cluster.

Gräwert *et al.* published a structure for LytB from *E. coli* that also contained a [3Fe-4S] cluster (146). The overall structure is very similar to that of the *A. aeolicus* structure. Surprisingly, the [3Fe-4S] cluster was proposed to be the catalytic competent cofactor based on activity studies.

3.1.4 Proposed Reaction Mechanisms

The LytB enzyme catalyzes a similar reaction as the GcpE enzyme. The two-electron reduction of HMBPP is achieved by two successive one-electron steps, resulting in the cleavage of a C-O bond. The iron-sulfur cluster is proposed to be directly involved in substrate binding and catalysis. Similar functions have only been found in a very small group of iron-sulfur-cluster-containing proteins, including hydrolyases, radical SAM enzymes, and FTR/HDR. However, LytB and GcpE do not fall into any of these groups.

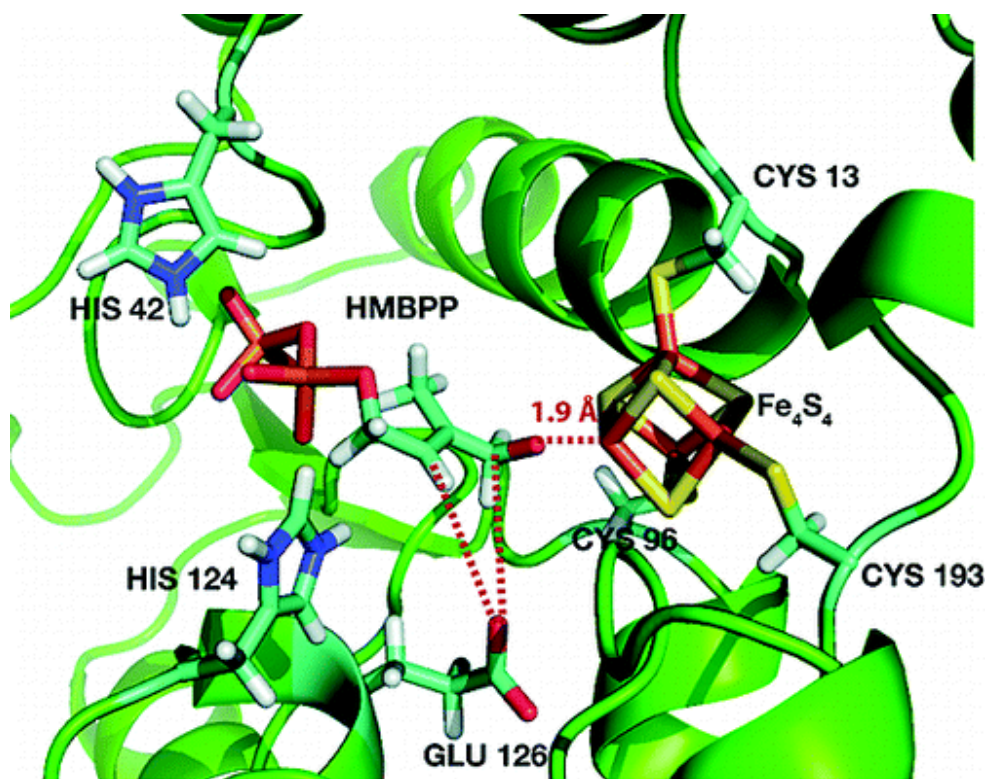


Figure 3.3. Proposed ligand docking to LytB. The model shows the location of HMBPP in the central cavity, the possible electrostatic interactions of HMBPP with His42, His124, and the location of Glu126, a possible proton donor in the reaction mechanism. Taken with permission from (77). (Copyright American Chemical Society)

A radical mechanism for LytB (*135-137;147*) has to be proposed if it is assumed that the $[4\text{Fe-4S}]^{2+/1+}$ center can only function as a one-electron donor. Figure 3.4 (*135*) shows a representative model for this type of reaction mechanism. The first electron transfer causes the elimination of the hydroxyl group at the C4 position and the formation of an allylic radical. This is reduced to an allylic anion by the second electron transfer from the iron-sulfur cluster, which is followed by the protonation at either the C2 or C4 position. A problem with any radical-type mechanism is that the diphosphate group at the C1 position is a better leaving group than the hydroxyl group at the C4 position. This can be solved, however, by proposing the binding of the hydroxyl group to an iron ion of the $[4\text{Fe-4S}]$ cluster.

Figure 3.5 shows another mechanism based on the $[3\text{Fe-4S}]$ center as the prosthetic group of LytB (*146*). The substrate HMBPP is assumed to bind in a quasi-cyclic conformation stabilized by the hydrogen bond formed between the acidic proton of the diphosphate group and the oxygen atom of the hydroxyl group. Transfer of the first electron generates a $[\text{HMBPP}(\text{H}^+)]^{3-}$ radical which represents the first intermediate. In this case, the hydroxyl group is bound by the enzyme. Transfer of the second electron creates the allylic anionic intermediate followed by the protonation step. A problem with this mechanism is that the redox potentials of 3Fe clusters are too high to be able to transfer an electron to HMBPP or any of the intermediates. The model can also not explain why the hydroxyl group is split off and not the diphosphate moiety.

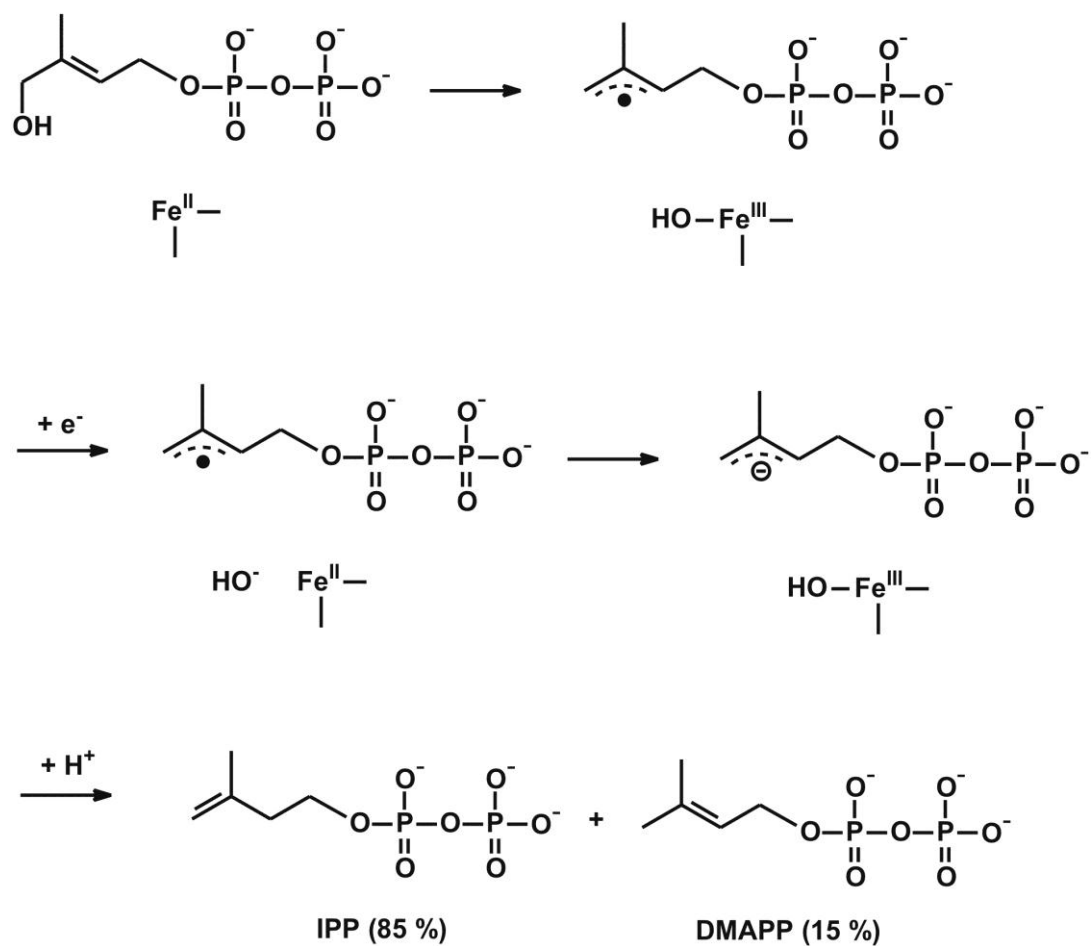


Figure 3.4. Hypothetical mechanism I. Adapted from (135)

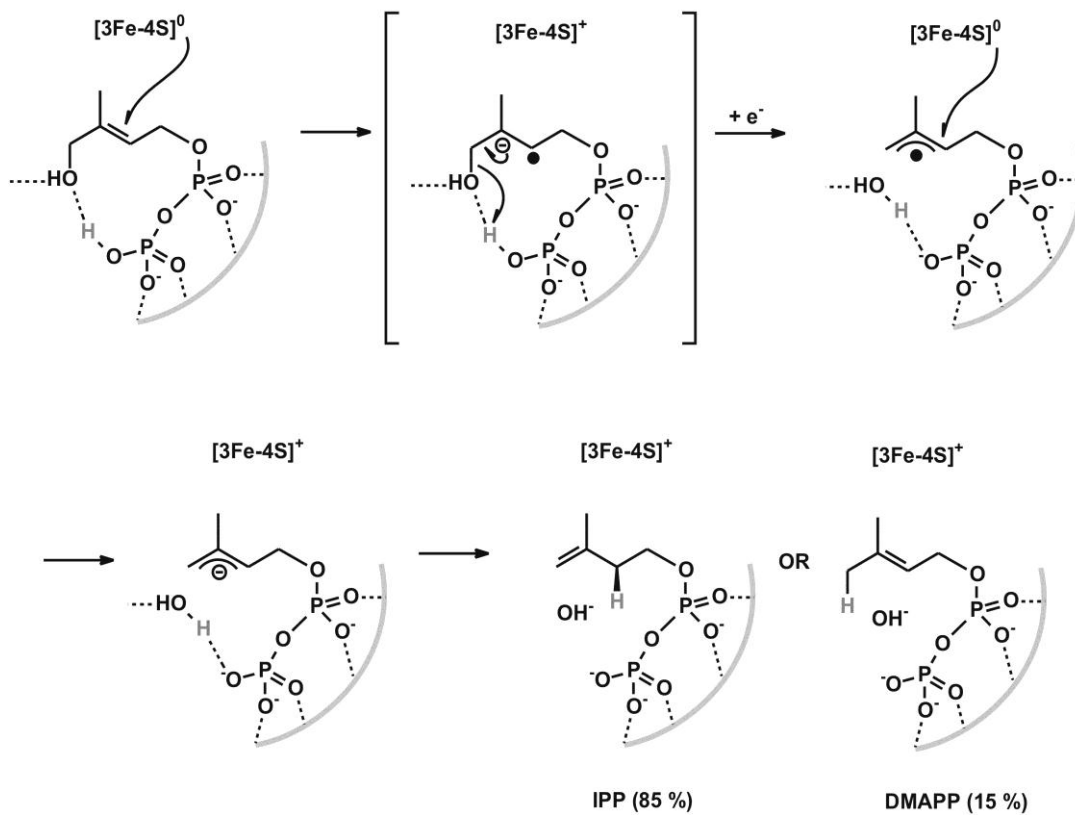


Figure 3.5. Hypothetical Mechanism II. The gray line indicates the rim of the cavity containing the active site. Adapted from (146)

3.1.5 Statement of Research on LytB

In the research presented here several questions related to the function of LytB will be addressed.

- I. The LytB protein has been purified from different sources, such as *E. coli*, *A. aeolicus*, and *P. falciparum*. It is clear now that it is an iron-sulfur-cluster containing enzyme, but it is not established whether the [3Fe-4S] form or the [4Fe-4S] form is the active form.
- II. A typical problem with [4Fe-4S] clusters is their sensitivity to oxygen. Exposure to oxygen can result in loss of an iron ion and formation of a 3Fe-4S cluster. One way to avoid this would be to perform all purification steps under exclusion of oxygen. If this is not sufficient, reconstitution procedures will be tested. In either case, the activities of pure 3Fe-containing enzyme or pure 4Fe-containing enzyme will be measured and compared.
- III. Different radical intermediates have been postulated for this reaction. Is it possible to trap any of these using different methods, including the use of substrate analogs, quench methods, or site-directed mutagenesis?
- IV. In addition, can we find evidence for the direct involvement of the iron-sulfur cluster using labeling studies in combination with ENDOR spectroscopy?
- V. The crystal structure of the LytB protein from *A. aeolicus* implied a role for several amino acid residues in catalysis. His42 and His124 might be involved in diphosphate binding. Glu126 could be a proton donor for C2 or C4. Site-directed

mutagenesis of these residues will be used to test this.

3.2 Experiments and Materials

3.2.1 Expressions Vectors for Wild-Type LytB and Mutants

The expression plasmids for LytB from *A. aeolicus* and *P. falciparum* were provided by the group of Dr. Hassam Jomaa at the Justus-Liebig University at Giessen, Germany. The plasmids with site-directed mutants of LytB from *A. aeolicus* were provided by the group of Dr. Oldfield at the University of Illinois, Urbana-Champaign, IL.

3.2.2 Expression and Purification

The different plasmids were used to transform *E. coli* XL-1 blue cells (Stratagene). The cell cultures were started with a single colony from an LB-Amp plate that was transferred into SOC medium containing 100 mg/L ampicillin and 300 μ M FeCl₃. The cultures were incubated at 37 ° C under shaking. For ⁵⁷Fe-isotope-enriched protein, ⁵⁷Fe Cl₃ was used (see section 2.2 in Chapter 2).

For LytB from *A. aeolicus* (both wild type and mutants) and *P. falciparum*, anhydrotetracycline with 0.2 mg·L⁻¹ was used as inducer. The cells were harvested by centrifugation at 5,500 rpm for 30 minutes (Sorvall RC-5B Refrigerated Superspeed Centrifuge, Sorvall GS-3 Rotor, Du Pont Instrument). The cell pellets were stored at -80 ° C until needed.

The purification and subsequent sample handling steps were performed in the Coy box using dioxygen free buffers. Buffer containing 50 mM Tris-HCl, 100 mM NaCl, pH 8.0, was used to re-suspend the cell pellets. The cells were disintegrated by sonication, followed by centrifugation at 35,000 rpm for 30 minutes (Beckman XL-70 Ultracentrifuge, YPE 45 Ti Rotor, Beckman Coulter, Inc.). In the case of *P. falciparum* enzyme, the supernatant was loaded onto a HisTrap Affinity column (Pharmacia, GE Healthcare). In the case of *A. aeolicus* enzyme, the supernatant after the sonication and centrifugation steps was first incubated at 65 ° C in a water bath for 30 minutes. This was followed by a second centrifugation step after which the supernatant was loaded on the HisTrap Affinity column. In all cases, protein was eluted with increasing amounts of imidazole in 50 mM Tris-HCl and 100 mM NaCl, pH 8.0. Enzyme eluted at an imidazole concentration of 250 mM. The main fractions were collected and used freshly. Unless indicated, all experiments were performed in 50 mM Tris-HCl, 100 mM NaCl, pH 8.0

3.2.3 Characterization of the Purified Enzymes

Protein determination, iron determination, and sulfur determination followed the same procedures as described for the GcpE protein (see Sections 2.2.1, 2.2.2, 2.2.3 in Chapter 2). For the protein determination using the 280 nm absorption an extinction coefficient of $26,930 \text{ M}^{-1}\text{cm}^{-1}$ was used. For the iron determination, protein samples were pretreated by running the protein solution over a regenerated and equilibrated Chelex 100 column (Bio-Rad) to remove adventitiously bound iron ions.

3.2.4 Reconstitution

Most of the LytB samples showed substoichiometric amounts of the active-site [4Fe-4S] cluster. Reconstitution of the cluster was achieved using a method modified from the literature (127). All solutions were anaerobic. Enzyme was incubated for 3 hours with dithiothreitol (at least 5 mM), FeCl₃ (5x protein concentration), and Na₂S (5x protein concentration) in 50 mM TrisHCl, pH 8.0. The samples were centrifuged in an Eppendorf centrifuge (4500 rpm for 5 min) to remove black iron-containing precipitate. The supernatant was desalted by running it over PD 10 column. The eluted protein was used directly.

3.2.5 Enzyme Activity Assay

UV-vis absorption spectra were obtained under anaerobic conditions using the Ocean Optics USB 2000 miniature fiber optic spectrometer inside the glove box or using stoppered cuvettes in a HP 8451A UV-visible Spectrophotometer or an Agilent 8453 UV-visible Spectrophotometer.

Enzyme activity assay was performed using the same method as described for GcpE (section 2.2.5). The kinetic studies for WT and mutant LytB were performed at RT with the reaction mixture containing dithionite, methyl viologen, and substrate. The activity of LytB was determined by monitoring the oxidation of dithionite-reduced methyl viologen at 732 nm ($\epsilon_{732} = 2200 \text{ M}^{-1}\text{cm}^{-1}$) or at 603 nm ($\epsilon_{603} = 1.36 \times 10^4 \text{ M}^{-1}\text{cm}^{-1}$). The concentration of substrate HMBPP was varied from 0 μM to 500 μM .

3.2.6. Circular Dichroism (CD) Spectroscopy

CD spectroscopy was carried out to check proper folding of the mutant enzymes. As-isolated enzyme was washed with 5 mM phosphate buffer (pH 8.0) to remove both imidazole and the Tris buffer. An aliquot was transferred into a 0.1 mm cuvette which was capped inside the glove box. All CD data were collected on the J-810 Spectropolarimeter (Jasco).

3.2.7. EPR Spectroscopy

In the case of LytB, the cluster is easily reduced by the addition of dithionite. Incubation with both dithionite and the substrate HMBPP does not result in the detection of an intermediate signal under the conditions used. An ‘intermediate signal’ was induced by incubation the enzyme with an excess of dithionite and subsequently removing the excess by running the sample over a desalting PD10 column. The cluster stays reduced after this procedure and this represents the ‘one-electron-reduced’ form of the enzyme. Addition of HMBPP to this form induced the disappearance of the cluster signal and the formation of the ‘intermediate’ species, which for convenience is called FeS_I.

CW EPR spectra were measured at X-band (9 GHz) frequency on a Bruker EMX spectrometer, fitted with the ER-4119-HS high sensitivity perpendicular-mode cavity. General EPR conditions were: microwave frequency, 9.385 GHz; microwave power incident to the cavity, 0.20 mW; field modulation frequency, 100 kHz; microwave amplitude, 0.6 mT.

The Oxford Instrument ESR 900 flow cryostat in combination with the ITC4 temperature controller was used for measurements in the 4 K to 300 K range using a helium flow. Measurements at 77 K were performed by fitting the cavity with a liquid nitrogen finger Dewar.

A copper perchlorate standard (10 mM CuSO₄, 2 mM NaClO₄, 10 mM HCl) was used for spin quantifications on spectra measured under non-saturating conditions by comparison of the double integral of the signal from the samples with that from the standard. Signal intensities are presented as amount of spin which is the fraction of the amount of EPR signal detected over the amount of [4Fe-4S] cluster present in the sample. Curie plots were made as described in section 2.2.6.

Pulsed EPR and ENDOR data at X-band and Q-band (35 GHz) frequency were collected by Nicholas Lees in the group of Dr. Brian Hoffman at Northwestern University, Evanston, IL. Samples were prepared in Auburn, stored in liquid nitrogen and transported in a nitrogen dry-shipper.

3.3 Results

3.3.1 Expression and Purification

Wild-type LytB protein (from *P. falciparum* and *A. aeolicus*) and mutated LytB proteins from *A. aeolicus* were overexpressed successfully in *E. coli* X-L1 blue cells.

All LytB proteins contained a His₆-tag and were purified by immobilized nickel

affinity chromatography (Fig. 3.6). The protein samples were judged to be pure (> 95%) based on SDS-Page (Fig. 3.7).

3.3.2 Wild-Type Enzyme

3.3.2.1 Cluster Type Present in Wild-Type LytB Enzymes

Figure 3.8 shows the absorption spectra of the LytB protein from *P. falciparum*. As-isolated LytB has a band at 410 nm and a shoulder around 320 nm (Fig. 3.8, solid line). The band at 410 nm is indicative for the presence of [3Fe-4S]¹⁺ or [4Fe-4S]²⁺ clusters. The band at 320 nm could be due to bound single iron ions. The reduction of the iron-sulfur clusters was achieved by the addition of dithionite, indicated by the bleaching of the 410 nm band (Fig. 3.8, dashed line). The iron-sulfur cluster can be destroyed by exposure to oxygen which also resulted in inactivation of LytB protein. Similar spectra of as-isolated and reduced proteins were obtained for LytB enzyme from *A. aeolicus* (Fig. 3.9).

Figure 3.10 shows the EPR spectra for the different forms of the *A. aeolicus* enzyme. The as-isolated enzyme showed an EPR signal that is typical for a [3Fe-4S]¹⁺ cluster at 345 mT (0.002 spin) (Fig. 3.10, trace A). Figure 3.10, spectrum B shows the EPR signal for dithionite-reduced enzyme. Two features are detectable at round 100-150 mT and

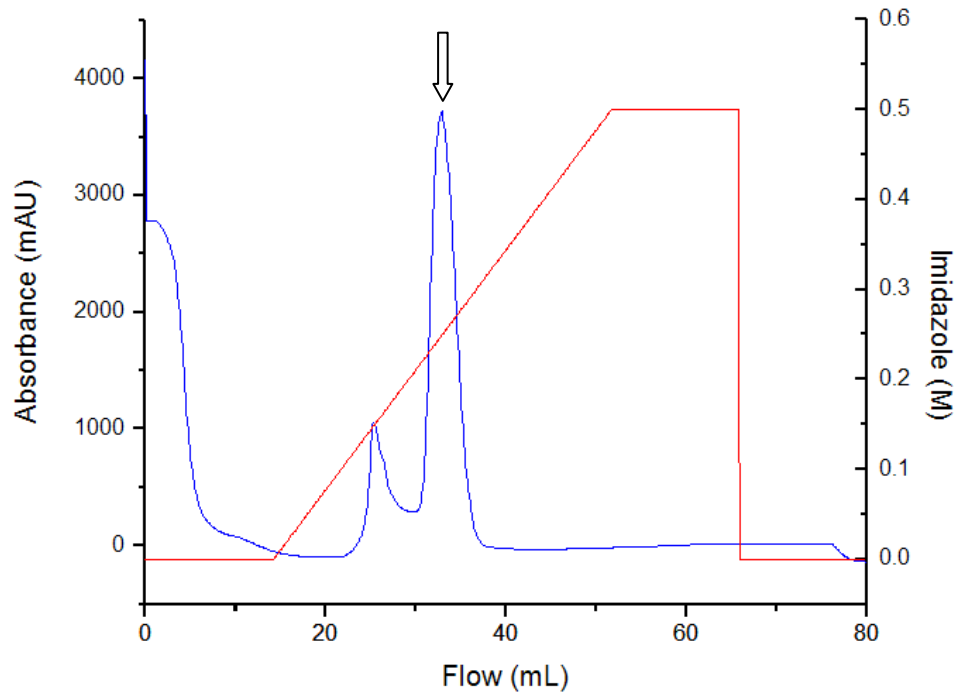


Figure 3.6. FPLC profile for purification of the *P. falciparum* enzyme on an immobilized nickel affinity chromatography column.

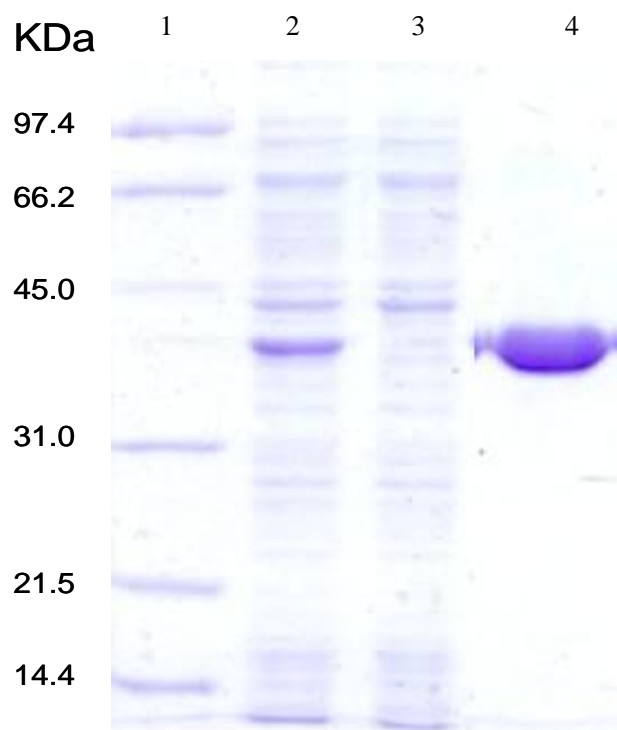


Figure 3.7. SDS-PAGE showing the progress in the purification of the *P. falciparum* enzyme. Lane 1, marker; lane 2, cell extract; lane 3, flow through of the immobilized nickel affinity chromatography column; lane 4, 10 µg elute enzyme.

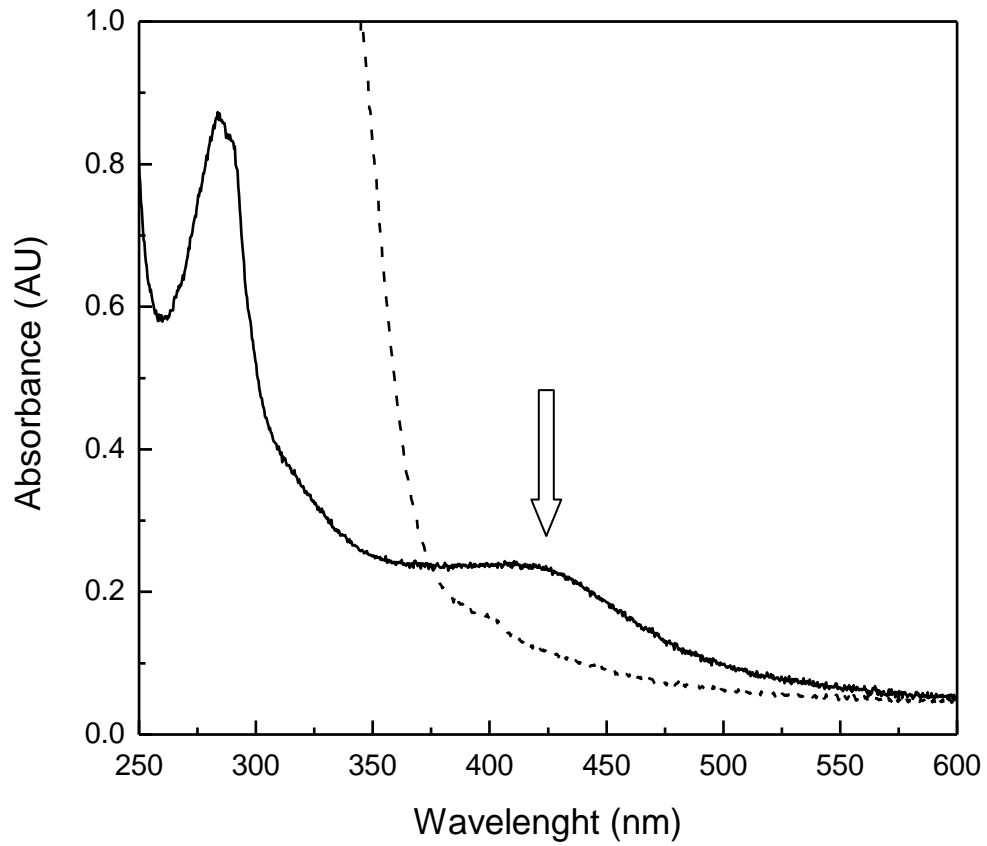


Figure 3.8. UV-visible absorption of as-isolated (—) and dithionite-reduced (---) LytB protein from *P. falciparum*. The peak at 330 nm is due to dithionite.

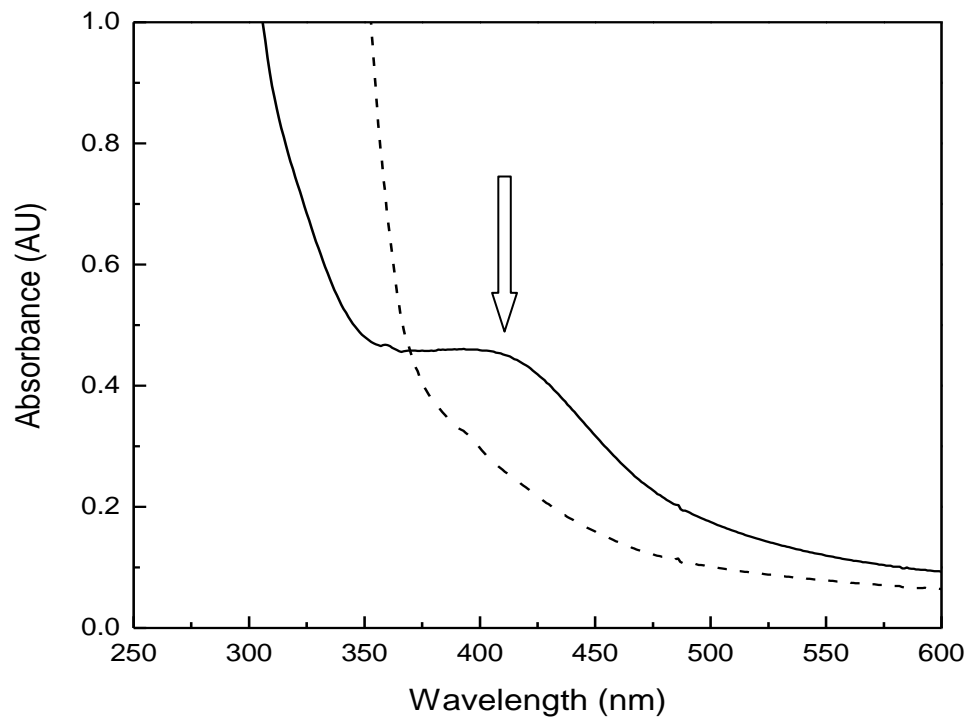


Figure 3.9. UV-visible absorption of as-isolated (—) and dithionite-reduced (---)

LytB protein from *A. aeolicus*. The peak at 330 nm is due to dithionite.

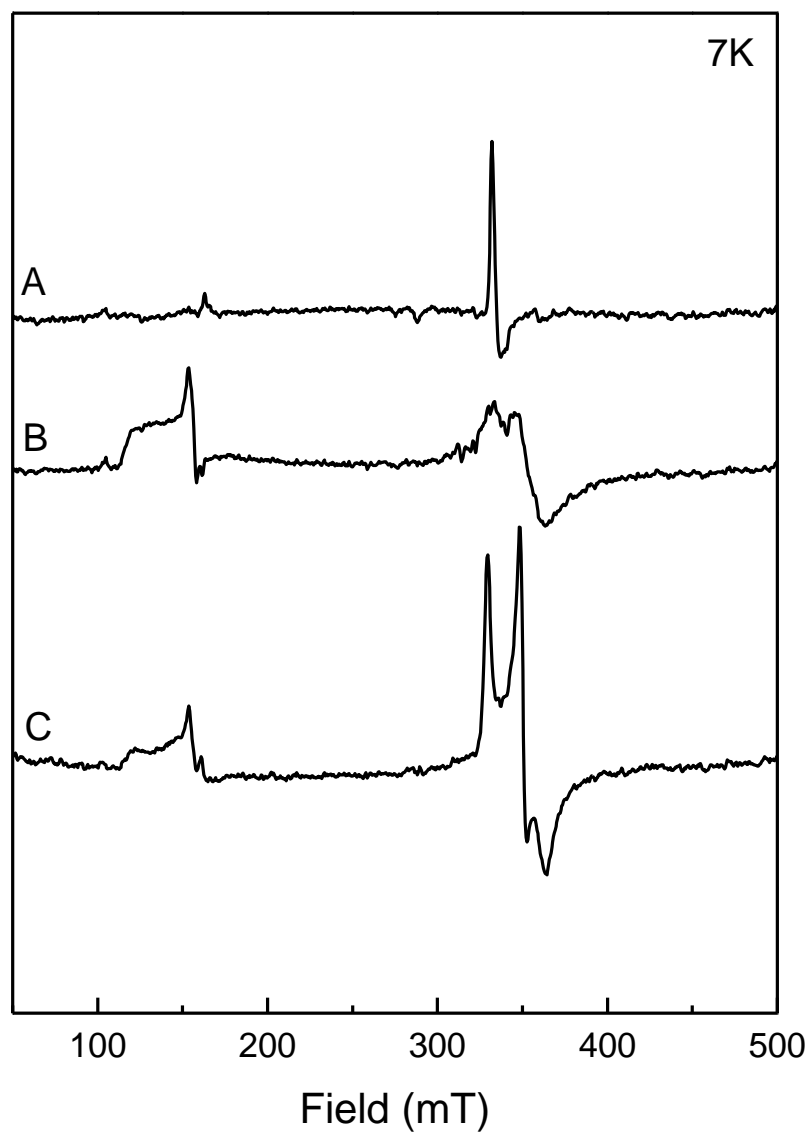


Figure 3.10. EPR spectra of LytB protein from *A. aeolicus*. (A) As-isolated; (B) Reduced by excess dithionite; (C) Reduced by excess dithionite in the presence of 20% ethylene glycol. LytB concentration was 0.36 mM, dithionite was 2 mM.

300-350 mT. Both features can be attributed to a $[4\text{Fe-4S}]^{1+}$ species with a spin $S = 3/2$. The peaks at around 100-150 mT are due to the $[S = \pm 3/2]$ doublet of the system while the peaks at around 300-350 mT are due to the $[S = \pm 1/2]$ doublet (0.018 spin). Addition of ethylene glycol converts part of the $S = 3/2$ system into a pure $S = 1/2$ system. This can be observed by the appearance of a new well defined EPR signal with $g_{x,y,z} = 2.0349$, 1.914, and 1.844 in Figure 3.10, trace C (0.083 spin).

The EPR spectrum of as-isolated LytB protein from *P. falciparum* did not show the presence of a $[3\text{Fe-4S}]^{1+}$ cluster (Fig. 3.11, trace A). Incubation under air, however, induced the 3Fe EPR signal, due to degradation of the $[4\text{Fe-4S}]^{2+}$ clusters. An EPR signal due to a $[4\text{Fe-4S}]^{1+}$ cluster with spin $S = 1/2$ was detected after addition of dithionite (Fig. 3.11, trace B). $S = 3/2$ species were not detected (not shown).

The temperature behavior for the $[4\text{Fe-4S}]^{1+}$ species in *A. aeolicus* is shown in Figure 3.12, panel A. The plot shows a representative pattern for $[4\text{Fe-4S}]^{1+}$ clusters: a very narrow temperature range (10 – 20 K) is available for measuring this signal. Below 10 K, the signal is saturated; above 20 K, the signal starts to broaden.

Based on the EPR data it appears that the native enzyme contains a 4Fe cluster and the 3Fe cluster is a breakdown product due to exposure to oxygen. This was further proven by comparing the 4Fe cluster content with enzymatic activity (see below).

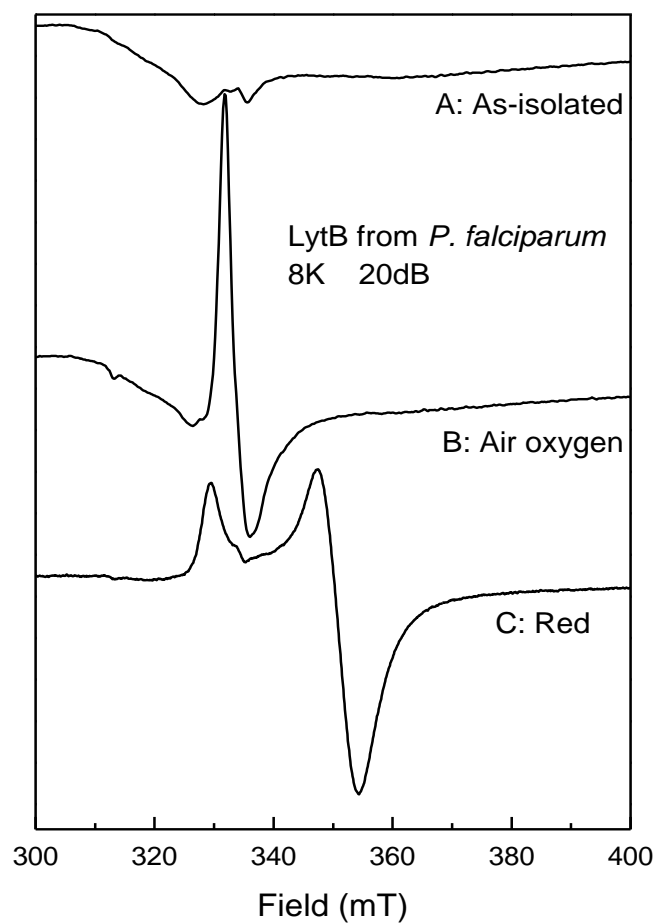


Figure 3.11. EPR spectra of LytB protein from *P. falciparum*. (A) As-isolated; (B) Exposed to air oxygen; (C) Reduced by excess dithionite. LytB concentration was 129 μM , dithionite was 5 mM.

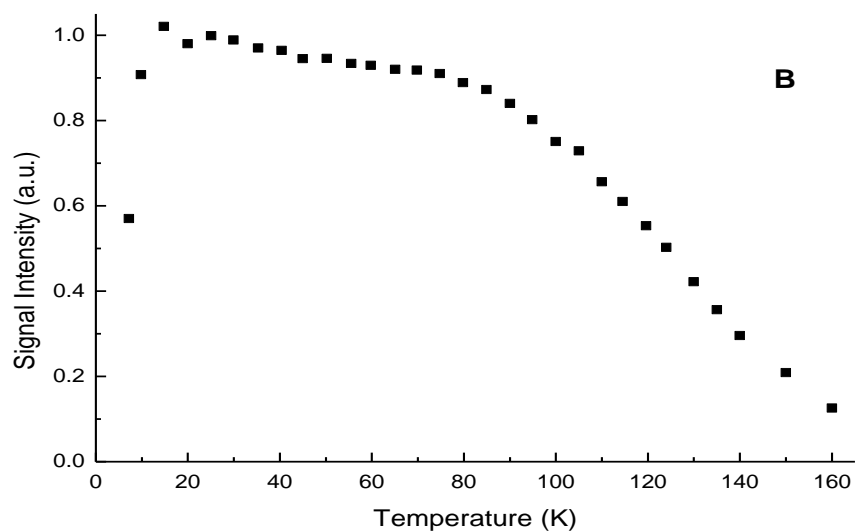
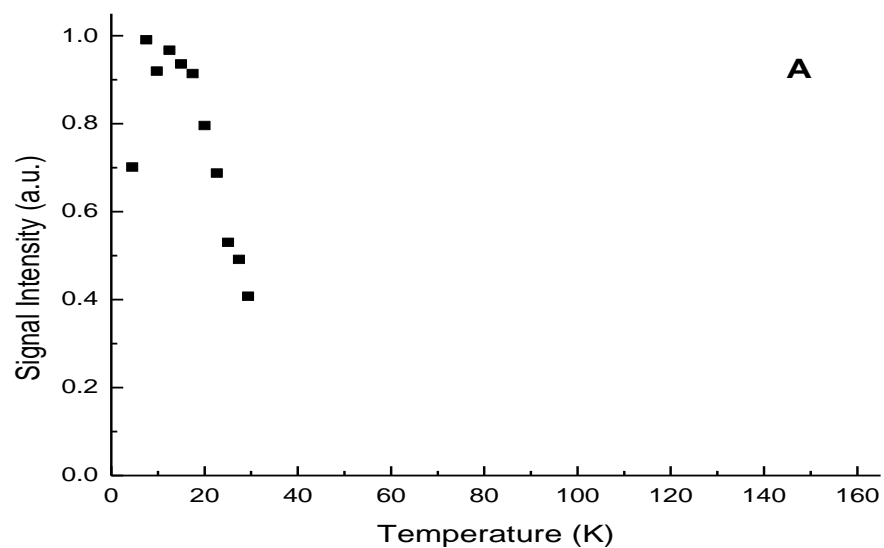


Figure 3.12. Curie plots for the EPR signal in LytB from *A. aeolicus*. (A) The $[4\text{Fe-4S}]^{1+}$ cluster ($S = 1/2$). (B) The paramagnetic species induced after incubation of one-electron reduced enzyme with HMBPP.

3.3.2.2 Cluster Content Related to Activity

The relationship between cluster content and enzymatic activity was measured with as-isolated protein, protein after treatment with Chelex 100 resin, reconstituted protein, and protein after exposure to oxygen. Figure 3.13 shows that, at least in the case of WT enzyme, the cluster is not affected by the Chelex treatment. Table 3.1 gives an overview of the different samples from different purifications (Purification I, II and III), their cluster content and the observed parameters. The cluster content was calculated based on the iron determination. Additionally, the sulfur determination was performed for cluster content, but always only half amounts of clusters were given by this method. It is not clear why the numbers from the sulfur determination are only half of those from the iron determination. In Figure 3.14, $V_{\max}/[E]$ is plotted against cluster content. It proves that the enzyme activity is proportional to the iron content in all samples. Since only 4Fe clusters were detected in EPR spectroscopy, it proves that the enzyme activity is directly correlated to the [4Fe-4S] cluster content and not the presence of a 3Fe cluster.

It is important to note that values obtained in activity assay should always be compared with, or corrected for cluster content.

3.3.2.3 Kinetic Studies

The enzymatic characterization of *P. falciparum* LytB was performed with reduced methyl viologen. The kinetic parameters were determined at RT with different HMBPP concentrations (Fig. 3.15). The K_M was calculated to be approximately 19 μM based on

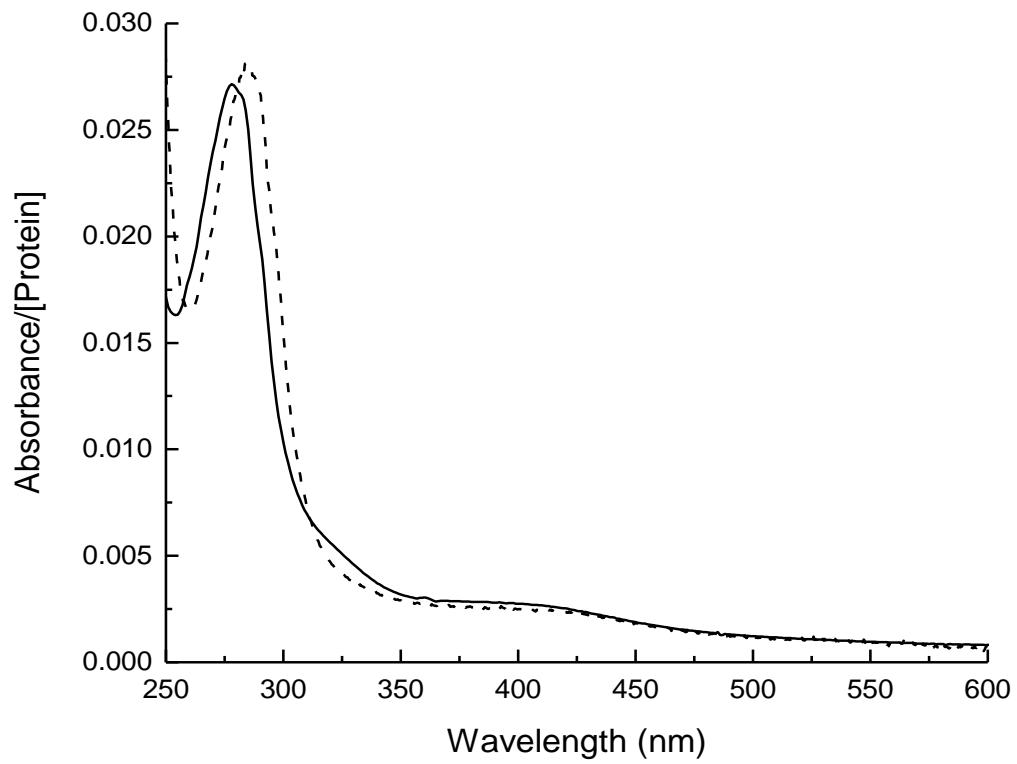


Figure 3.13. Absorption spectra of LytB protein from *A. aeolicus* before the treatment with Chelex Resin (—) and after the treatment with Chelex Resin (---).

Table 3.1 V_{\max} , cluster content and corrected specific activity for the LytB samples from *A. aeolicus*

I. WT

	Cluster Content %	V_{\max} ($\mu\text{M}\cdot\text{S}^{-1}$)	Specific Activity ($\mu\text{mol}\cdot\text{min}^{-1}\cdot\text{mg}^{-1}$)	Specific Activity after Correction with cluster content
Before Chelex	12.9(Fe)	0.412	0.246	1.907(Fe)
After Chelex	11.6(Fe)	0.327	0.194	1.672(Fe)
Reconstitution	85.6(Fe)	2.647	1.552	1.813(Fe)

II. WT

	Cluster Content %	V_{\max} ($\mu\text{M}\cdot\text{S}^{-1}$)	Specific Activity ($\mu\text{mol}\cdot\text{min}^{-1}\cdot\text{mg}^{-1}$)	Specific Activity after Correction with cluster content
Before Chelex	16.1(Fe)	0.257	0.229	1.422(Fe)
After Chelex	14.9(Fe)	0.272	0.239	1.604(Fe)
Reconstitution	56.3(Fe)	0.854	0.750	1.332(Fe)

III. WT

	Cluster Content %	V_{\max} ($\mu\text{M}\cdot\text{S}^{-1}$)	Specific Activity ($\mu\text{mol}\cdot\text{min}^{-1}\cdot\text{mg}^{-1}$)	Specific Activity after Correction with cluster content
Purification with O_2	0(Fe)	0.05	0.0	N/A

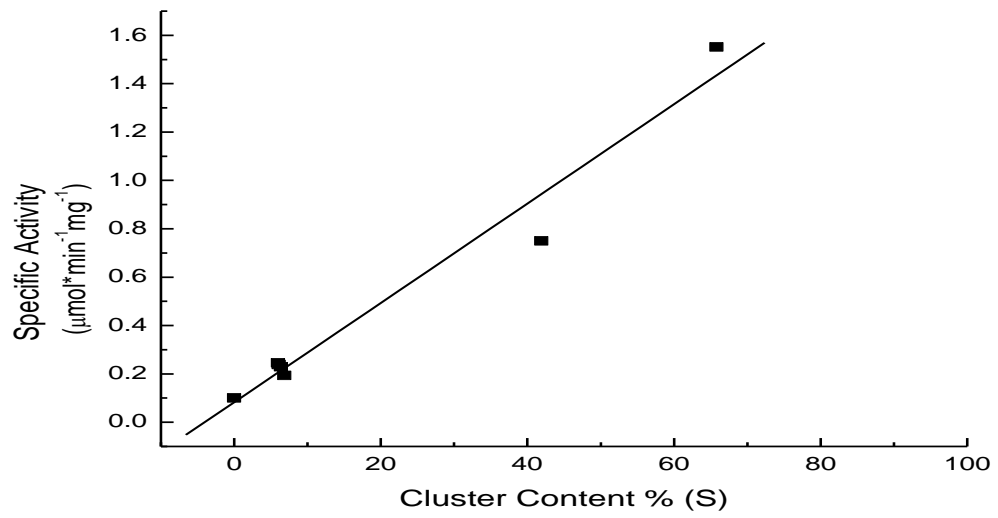
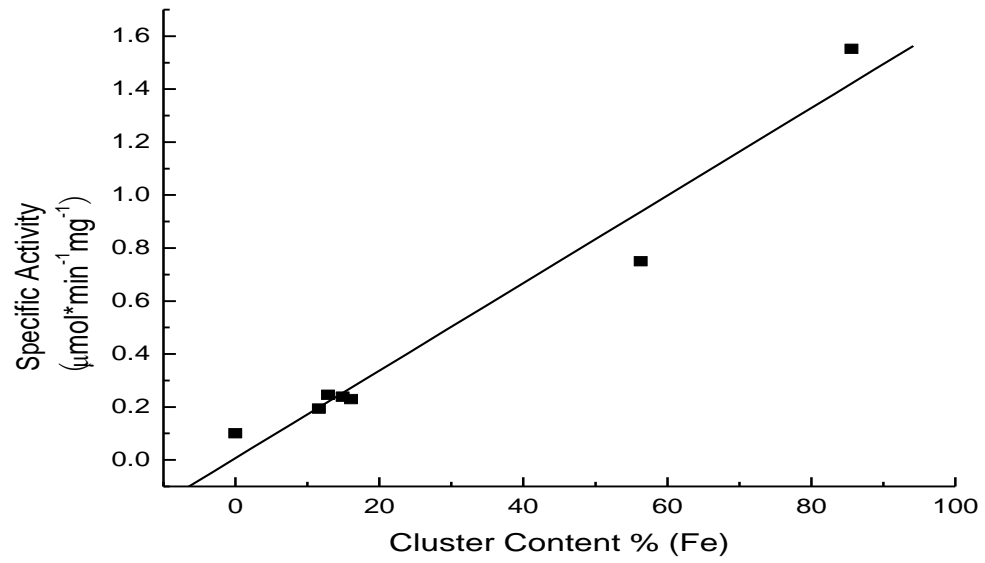


Figure 3.14. Relationship of enzyme activity on cluster content. Cluster content was determined by iron content (**A**) or by acid-labile-sulfur content (**B**).

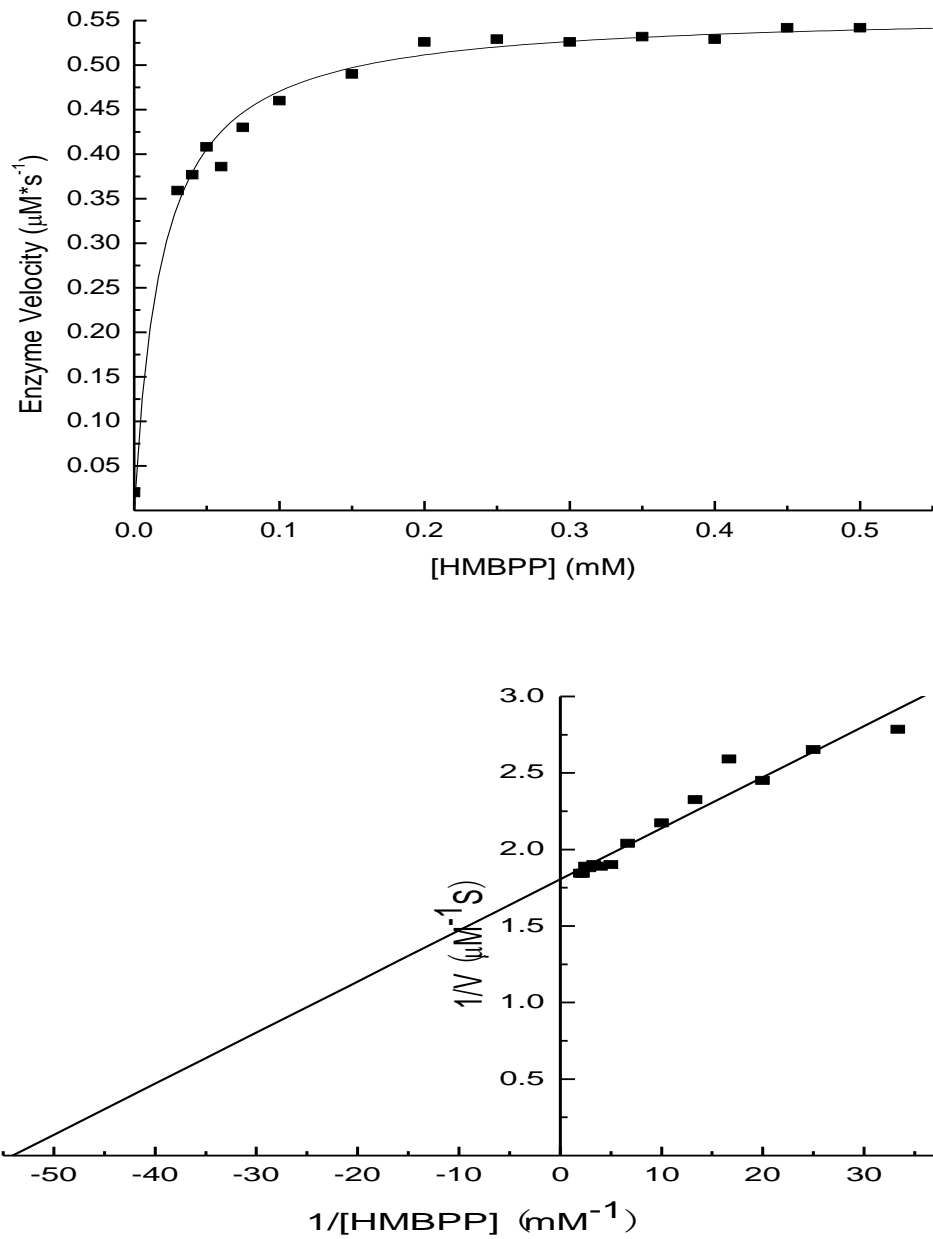


Figure 3.15 Michaelis-Menten and Lineweaver-Burk plots. The assay was performed with 10 μM *P. falciparum* LytB, 75 μM dithionite and 300 μM methyl viologen.

Michaelis-Menten and Lineweaver-Burk plots. The specific activity was $2.91 \mu\text{mol}\cdot\text{min}^{-1}\cdot\text{mg}^{-1}$, corresponding to a k_{cat} of 0.34 s^{-1} . The kinetic parameters are in agreement with those determined by previous studies (142).

The incubation of reduced enzyme in the presence of HMBPP and an excess dithionite did not generate a new paramagnetic species as observed in GcpE (Fig. 3.16, Trace B). Incubation for shorter or longer times did not induce a new signal either. Disappearance of the $[\text{4Fe-4S}]^{1+}$ signal indicated that the enzyme was being oxidized by the addition of substrate. We interpret this data that unlike GcpE, with two different midpoint potentials for the two separate one-electron transfers, LytB does not have this problem. It appears that, unlike the reaction in GcpE, the first step in the LytB catalyzed reaction is rate-limiting. The reaction is also significantly faster in LytB which has a K_{cat} of 0.34 s^{-1} vs. 0.09 s^{-1} for GcpE.

To investigate the formation of any paramagnetic intermediate freeze-quench studies will be needed. Since the cluster in the LytB enzymes can be reduced, it is possible to create a situation where only one electron is available which automatically stalls the reaction.

3.3.2.4 Characterization of the HMBPP Induced Signal, FeS_I

The “one-electron-reduced” protein can be obtained by incubating LytB with dithionite and removing the excess dithionite with a PD 10 desalting column. UV-visible spectroscopy was used to examine that this procedure worked. Figure 3.17 shows the

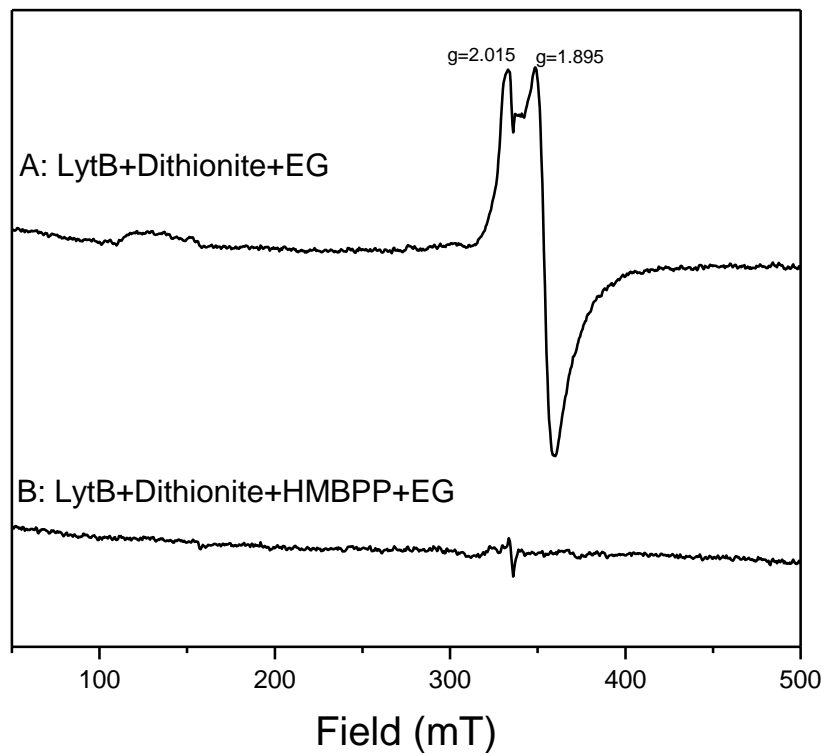


Figure 3.16. EPR spectra of the LytB protein from *P. falciparum* before and after addition of HMBPP. (A) Reduced with an excess dithionite; (B) Reduced with an excess dithionite and subsequent incubation with HMBPP for 12 s. LytB concentration was 234 μ M, dithionite was 4.55 mM. HMBPP was 4.55 mM.

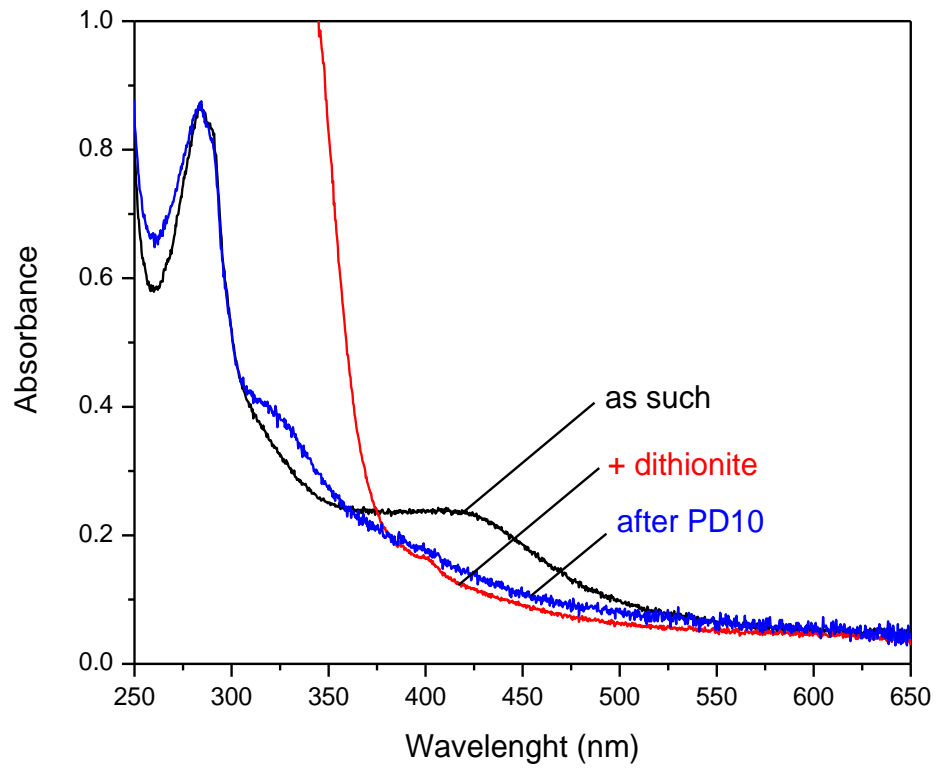


Figure 3.17. The effect of reduction of the cluster with dithionite and subsequent application to a PD 10 desalting column, on the absorption spectra of the LytB enzyme from *P. falciparum*.

spectrum for as-isolated LytB displaying the typical 410 nm band. The reduction of the 4Fe cluster was achieved by incubation with excess dithionite which was indicated by bleaching of the 410 nm band. The excess dithionite was detectable as a large absorption band at around 330 nm. The reduced LytB protein sample was run over a PD 10 column to remove the excess dithionite. The UV-visible absorption spectrum after this procedure only showed a minimal increase in intensity of the 410 nm band and very little of the 330 nm band is left behind, indicating that almost all dithionite was removed and the cluster was still present in the $[4\text{Fe-4S}]^{1+}$ form as checked by EPR spectroscopy (Fig. 3.18, trace A).

The incubation of HMBPP with one-electron-reduced protein resulted in the formation of a new paramagnetic species (Fig. 3.18, trace B) which is very similar to the FeS_A EPR signal detected in GcpE. For the discussion here we will call this signal FeS_I . The temperature plots were obtained for both the $[4\text{Fe-4S}]^{1+}$ signal and the new paramagnetic species (Fig. 3.12, panel B). They behave fully different from each. The reduced $[4\text{Fe-4S}]^{1+}$ signal can only be detected in a very narrow temperature range, as described above. Conversely, the FeS_I signal has an incredibly wide temperature range (20 K to 75 K) where it can be measured without saturation or broadening.

^{57}Fe -enriched samples were prepared for comparison with enzyme containing natural abundance isotope. The ^{57}Fe -enriched LytB protein behaves similar to regular LytB protein. No paramagnetic species was detected in as-isolated protein. The reduction of $[4\text{Fe-4S}]^{2+}$ cluster into $[4\text{Fe-4S}]^{1+}$ form was achieved by incubation with dithionite,

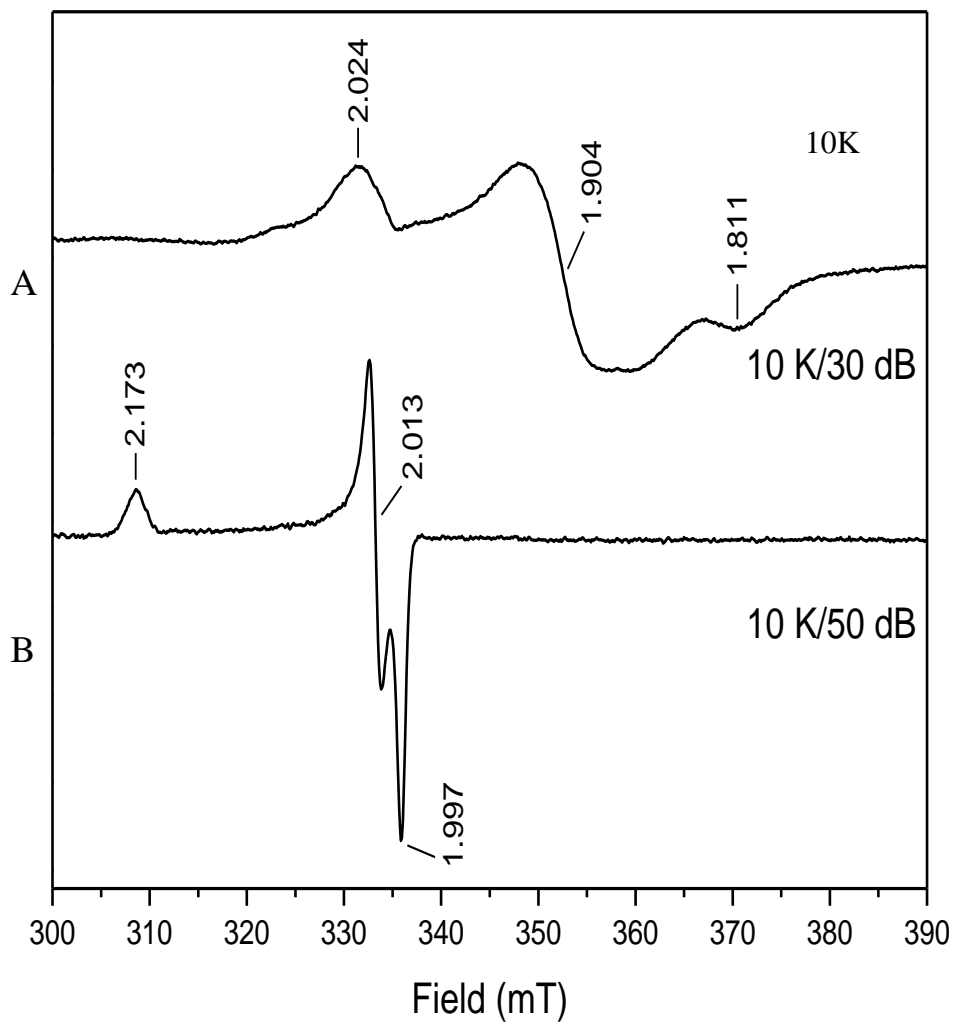


Figure 3.18. EPR spectra of LytB Protein from *P. falciparum*. The upper spectrum is reduced signal after incubation with dithionite; the bottom spectrum is the intermediate species generated by “one-electron-reduced” protein after incubation with substrate.

and either a $[4\text{Fe-4S}]^{1+}$ with $S = 1/2$ or $S = 3/2$ was detected in the presence or absence of ethylene glycol. The FeS_I signal was detected in “one-electron-reduced” ^{57}Fe -enriched protein after addition of HMBPP and subsequent incubation for 30 seconds before freezing the sample (Fig. 3.19). The observable broadening effects resulted from the nuclear spin of ^{57}Fe , showing that the signal is iron-sulfur based.

3.3.2.5 ENDOR Spectroscopy

Samples were prepared for ENDOR measurements to probe the mode of binding of the reaction intermediate to the 4Fe cluster. Several samples were made including samples with ^{57}Fe -labeled enzyme and D-labeled HMBPP. The goal of the first set of samples, was to detect the ^{13}P coupling due to the two phosphate groups in HMBPP. Figure 3.20, panel A, shows the ^{31}P -Mims ENDOR data for sample I. As with the data obtained for the FeS_A signal in GcpE, the spectra show a doublet centered at the ^{31}P Larmor frequency with a maximum splitting of about 0.2 MHz at g_1 , indicative for the presence of a single ^{31}P -nucleus in proximity to the cluster spin. Also in this case the minimum distance of the phosphorus nucleus from the unique iron was estimated to be 6.6 Å.

Not all samples showed these clear peaks. An example of this, sample II, is shown in Figure 3.20, panel B. In this sample the weak ^{31}P signal is not detectable but is overshadowed by a broader peak that has a much higher relative intensity. Although the band does represent a very diffuse ^{31}P -coupling pattern, the origin of this peak was not

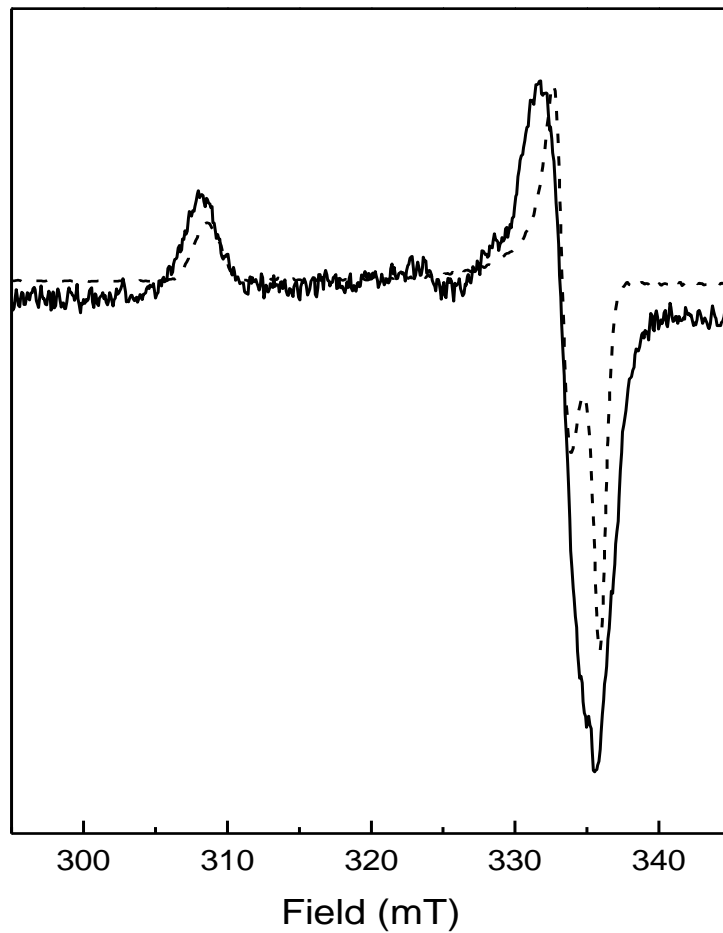


Figure 3.19. Comparison of EPR signal of the ‘intermediate’ species obtained with *A. aeolicus* enzyme from cell grown on natural abundance iron containing medium (---) and from cell grown on ^{57}Fe -enriched medium (—). Sample contained 115 μM “one-electron reduced” protein, 20% ethylene glycol and 20 mM HMBPP. Sample was incubation for 30 seconds before freezing.

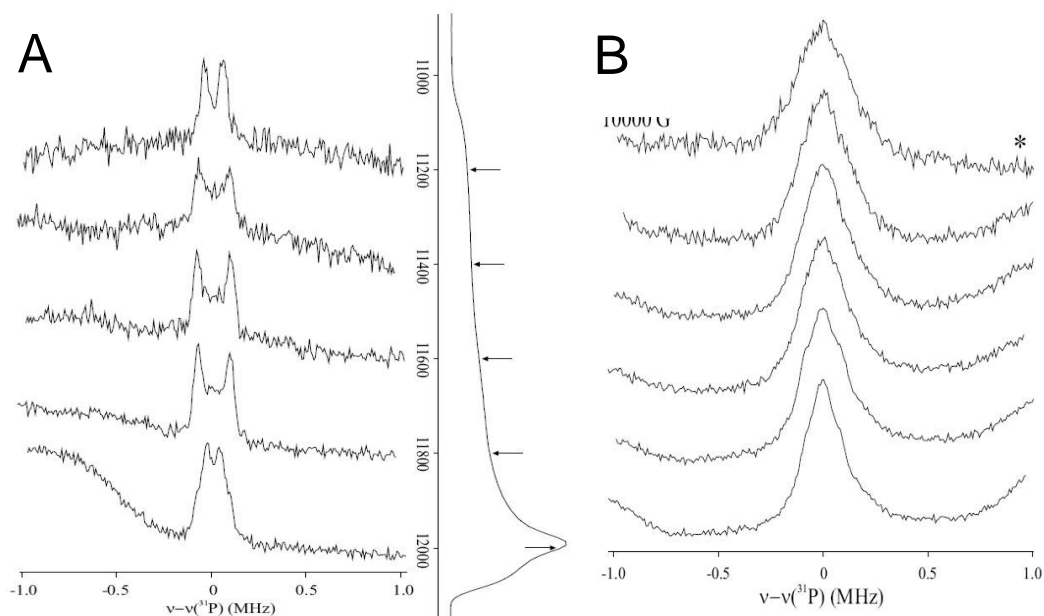


Figure 3.20: 35 GHz CW EPR and pulsed ENDOR spectra of the FeS_I species. A: Pulsed ³¹P ENDOR spectra. Spectra were collected at the positions indicated on the pulse-echo detected EPR spectra shown on the right of the panel. ENDOR spectra are normalized to a fixed intensity for clarity. Sample contained 1.7 mM one electron-reduced LytB from *P. falciparum*, 33 mM HMBPP. Sample was incubated for 25 s at RT before freezing. Conditions: Mims pulse sequence: microwave pulse length 30 ns, RF pulse length 20 μs, repetition rate 20 ms, τ = 800 n, microwave frequency 34.871 GHz, temperature 2 K. **B:** Pulsed ³¹P ENDOR spectra on a sample showing a broad S = 3/2 signal in addition to the FeS_I species. EPR and samples conditions are the same. Data collected by Nicholas Lees.

clear. It was also noticed that this coupling extended beyond the boundaries of the FeS_1 signal, as shown by the spectrum obtained at the 10,000 G field position. A thorough investigation of samples I and II showed that in sample II there is a very broad paramagnetic species present (Fig. 3.21, trace B, arrows) that is absent in sample I (Fig. 3.21, trace A). Re-examination of this sample at Auburn showed that this signal is due to the $[\text{4Fe-4S}]^+$ cluster with spin $S=3/2$ (not shown). Due to the high similarity in the shape of the EPR signal with that of the $[\text{4Fe-4S}]^+$ EPR signal detected in enzyme treated with dithionite only, the best interpretation of the signal is that of a reduced cluster with substrate bound.

Figure 3.22, shows the data obtained for reduced enzyme incubated with HMBPP labeled with deuterium at the C4 position. Labeled compound was synthesized as a racemate mixture. The data show the presence of ^2H -coupling over the whole signal envelope. Two different couplings are clearly detectable which would be due to the two positions the deuterium label can occupy in HMBPP. At the g3 position, however, a third coupling can be detected, which could indicate a possible variation in the binding of HMBPP to the cluster. A rough estimate can be made for the distance of the ^2H atom to the cluster: 4.4 Å.

A ^{57}Fe -labeled sample was also prepared to determine the oxidation state of the cluster. This sample is still under investigation.

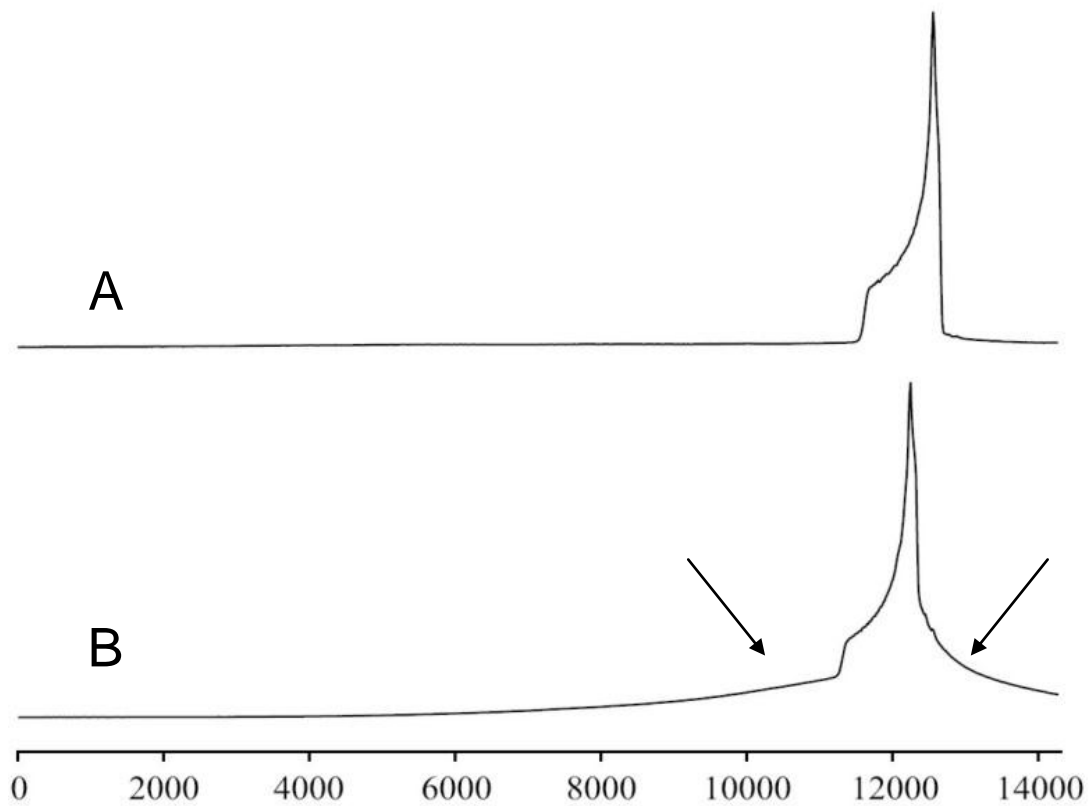


Figure 3.21: EPR data showing the absorption spectra for the EPR/ENDOR samples used in Figure 3.20

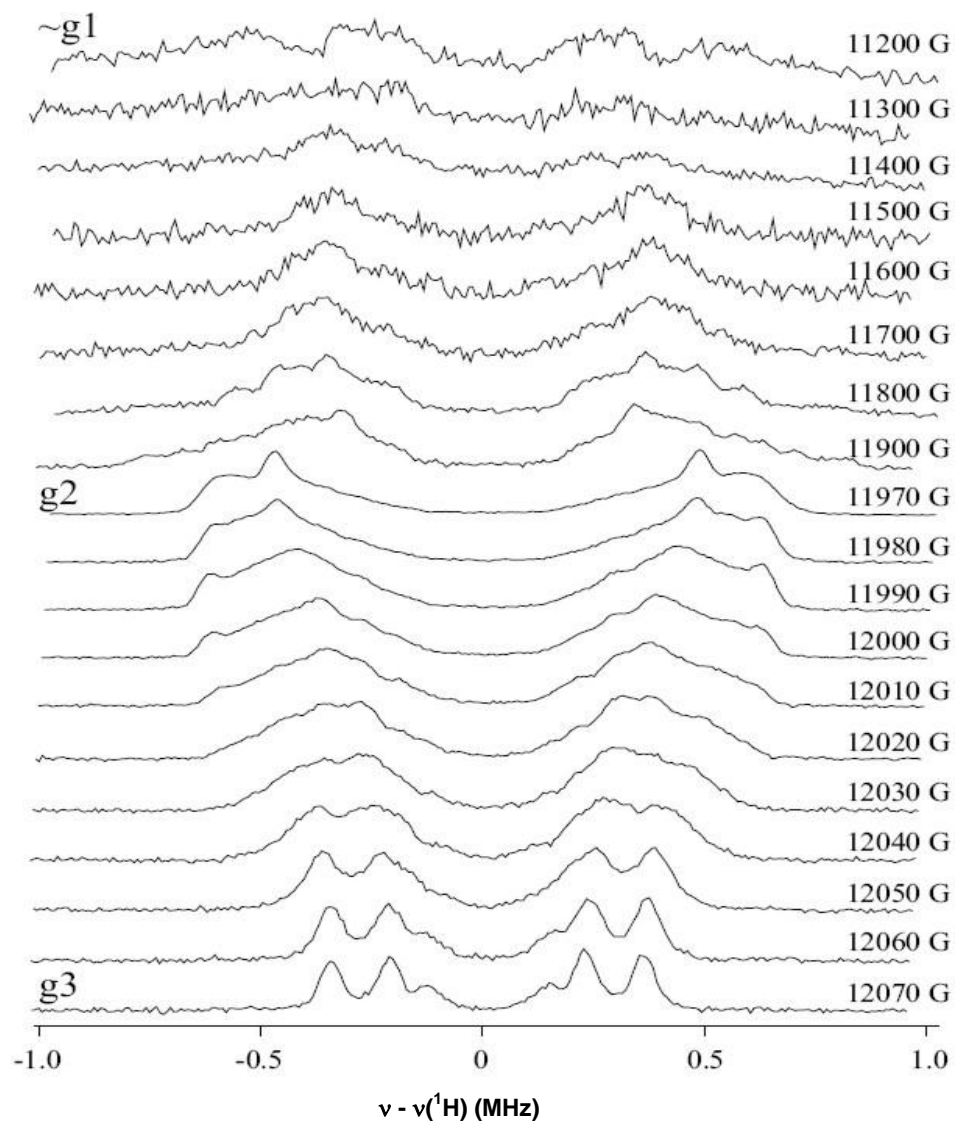


Figure 3.22. Pulsed ^2H -ENDOR spectra of the FeS_I species. Spectra were collected at the field positions indicated. Sample contained 1.2 mM one-electron-reduced LytB from *P. falciparum*, 33 mM D-HMBPP. Sample was incubated for 25 s at RT before freezing. Conditions: Mims pulse sequence: microwave pulse length 30 ns, RF pulse length 20 μs , repetition rate 20 ms, $\tau = 800$ n, microwave frequency 34.871 GHz, temperature 2 K. Data collected by Nicholas Lees.

3.3.2.6 CD Spectroscopy

The ENDOR data on the $S = 3/2$ species would indicate that substrate can bind to the cluster without being converted immediately. This could be due to the spin state of the cluster since there is no evidence for cluster with a $S = 1/2$ spin to show this behavior. Moreover, it could indicate that substrate would bind to the oxidized 4Fe cluster. This was investigated using circular dichroism spectroscopy. The CD spectra of reconstituted protein from *A. aeolicus* did not display a spectrum representative for iron-sulfur-cluster-containing proteins (Fig. 3.23, solid line). The addition of HMBPP induced a spectrum typical for 4Fe cluster (Fig. 3.23, dashed line), indicating the probable binding of HMBPP to the cluster. HMBPP was added in 1, 2, 4 and 8 protein equivalents. In each case the same amount of change was observed.

3.3.3 Mutated Enzymes

The crystal structures of LytB protein from *E. coli* and *A. aeolicus* were determined recently. Both of them exhibit a [3Fe-4S] cluster positioned in the central cavity. The structure of LytB protein from *A. aeolicus* (77) displays a pronounced ca. 10 Å x 20 Å cavity at the front side with the iron-sulfur cluster located at the bottom of the cavity. Modeling studies indicated that the substrate HMBPP binds to His42 and His124 with its diphosphate oxygens while the oxygen atom at C4 position of HMBPP is located ~1.9 Å from the unique Fe atom site. The structure also indicated a role for Glu126. The

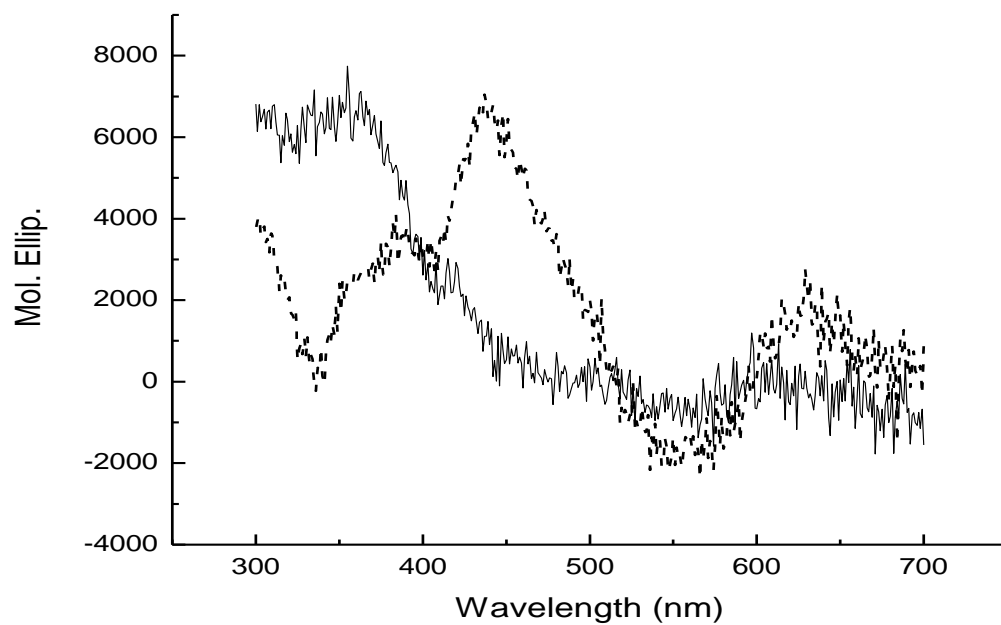


Figure 3.23: Circular dichroism spectra of Reconstituted LytB from *A. aeolicus*.

Solid line: as-isolated enzyme. Dashed line: enzyme in the presence of HMBPP. LytB concentration was 0.6 mM. HMBPP concentration was 4.76 mM.

carboxyl group of Glu126 is ~ 4 Å from C2 of HMBPP, which would be only ~ 2 Å from its final position in the product as proposed in the computational model. Note that this is the only totally conserved acidic residue. Accordingly, this close proximity suggests and supports a protonation role of Glu126 to C2 of the allylic species.

Based on these considerations, His42, His124, and Glu126 (*A. aeolicus* numbering) are predicted to have important roles in the reaction. To test this, site-directed mutants were made: H42A, H42F, H124A, H124F, E126A, and E126Q.

3.3.3.1 Mutants Characterization

All LytB mutants were expressed with similar level as seen in WT. They were analyzed with UV-visible absorption, EPR, and CD spectroscopy. Figure 3.24 display the UV-visible absorption spectra of all mutants. Although all of them displayed the 410 nm band and the 320 nm band, these bands had different ratios in the different mutants. The difference in intensity of 410 nm indicates variable [4Fe-4S] cluster content. Running the samples over a Chelex column greatly reduced the intensity of the 320 nm band (Fig. 3.25), indicating that this band is probably due to adventitiously bound iron or single iron ions present in the cluster site. The mutant E126A had a more intense 320 nm band, and the H124F mutant appeared to contain more iron-sulfur cluster than the other mutants.

EPR measurements of as-isolated and reduced mutant proteins were performed. Figure 3.26, panel A, exhibits EPR spectra of as-isolated mutated proteins, which suggested no or very small amounts of $[3\text{Fe-4S}]^{1+}$ cluster present. All mutants showed

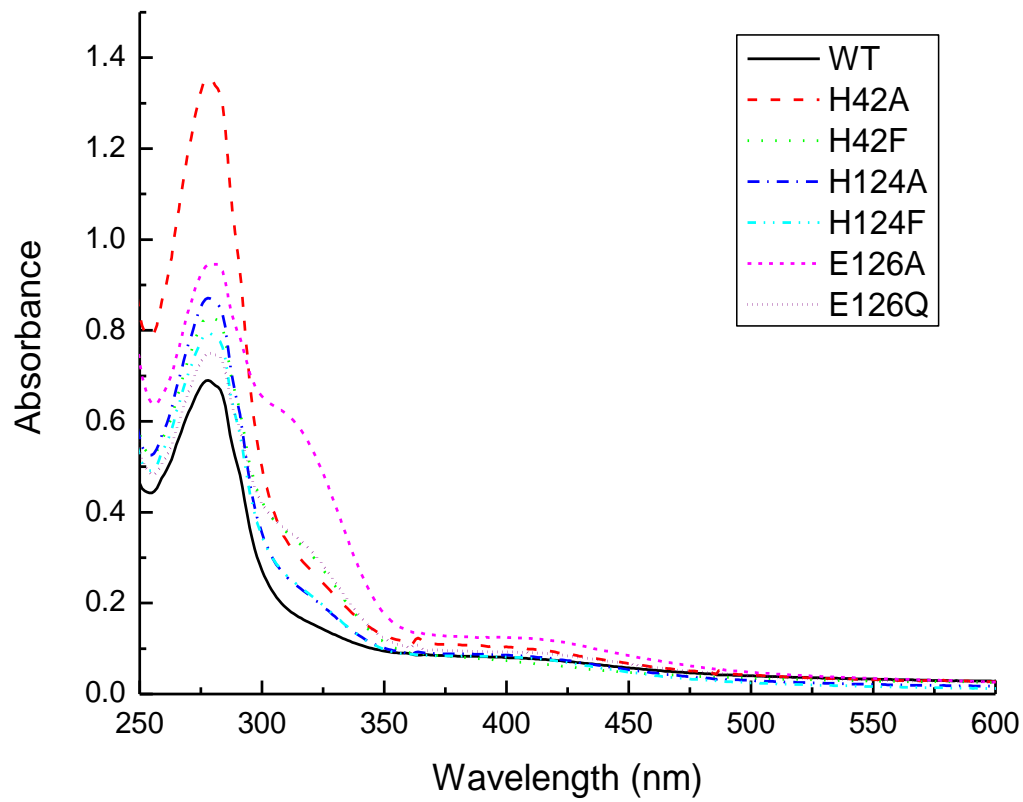


Figure 3.24. Absorption spectra for WT and mutant LytB proteins from *A. aeolicus*. Here, in order to achieve similar iron-sulfur cluster content for comparison, different amounts of proteins were used for measurements.

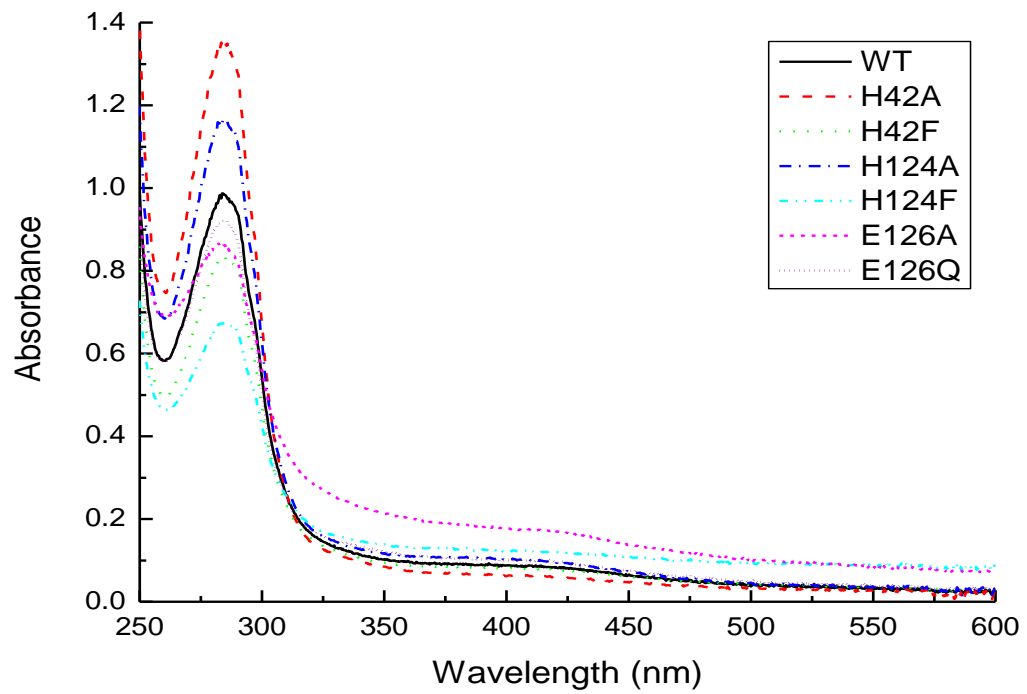


Figure 3.25. Absorption spectra for WT and mutant LytB proteins from *A. aeolicus* after Chelex treatment.

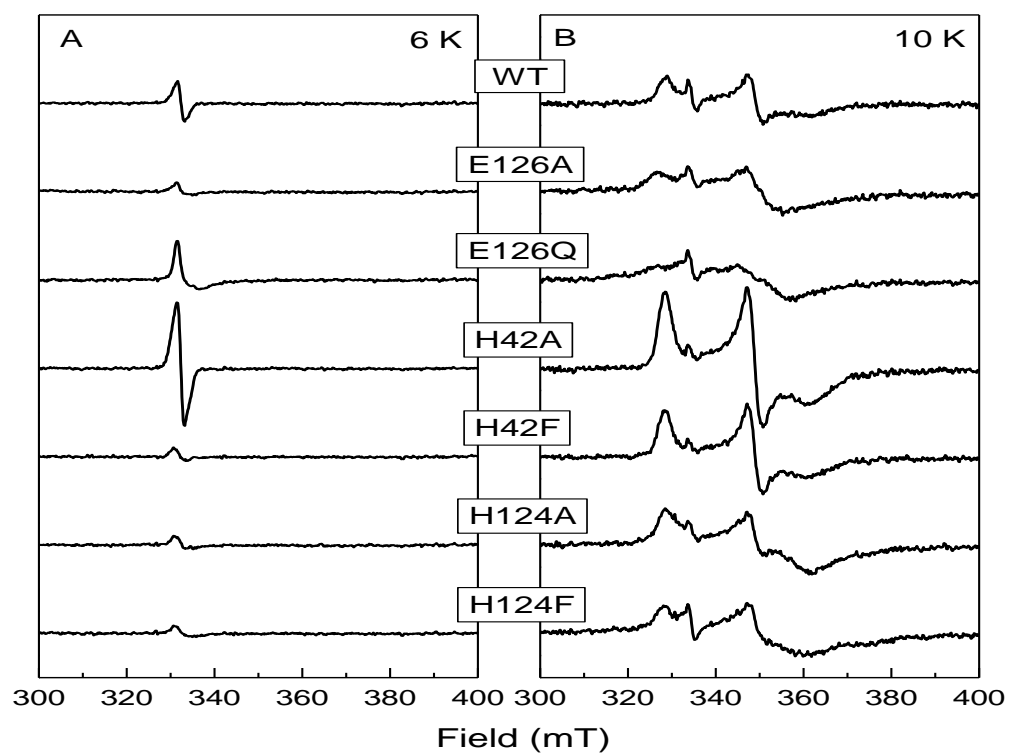


Figure 3.26. EPR spectra of WT and mutant LytB proteins from *A. aeolicus*. (A) Enzyme as isolated. (B) Enzyme in the presence of dithionite.

low 4Fe cluster content, which could have been the result of cluster breakdown, and could result in the presence of high amounts of 3Fe clusters. For WT and H42A, the signals detected are due to the radical species, not 3Fe clusters. This is not the case, however, indicating that the 3Fe cluster is also not stable, or only a low amount of 4Fe cluster was inserted in the first place.

After addition of dithionite to the mutant proteins, the $[4\text{Fe-4S}]^{1+}$ cluster EPR signal was detected in all mutants (Fig. 3.26, panel B). The ratio of $S = 1/2$ and $S = 3/2$ species is different for the different mutants. In case of the Glu126 mutants no conversion to the $S = 1/2$ form was observed upon addition of ethylene glycol. The intensity of the reduced signals is much higher than the intensity of the $[3\text{Fe-4S}]$ signals. Hence, it can be concluded that again the main cluster type present is the $[4\text{Fe-4S}]$ cluster.

The low cluster content and the broad $S = 3/2$ EPR signal made it very difficult to obtain EPR spectra with a high signal-to-noise ratio. Therefore, the cluster reconstitution procedure was applied to all mutant protein. Figure 3.27 shows the EPR spectra for reconstituted WT and mutant enzymes. In this case, the H42A, H42F and E126A mutants show a regular $[4\text{Fe-4S}]^{1+}$ $S = 1/2$ signal. However, the H124A and H124F mutants present an unusual signal with different g values. Both the E126A and E126Q mutants appear to display a mixture of the regular $S = 1/2$ species and the unusual signal found in the case of the H124A and H124F mutants. But they contain different ratios of those two species, where E126A has more regular species than the unusual species and E126Q has about equal amounts of them.

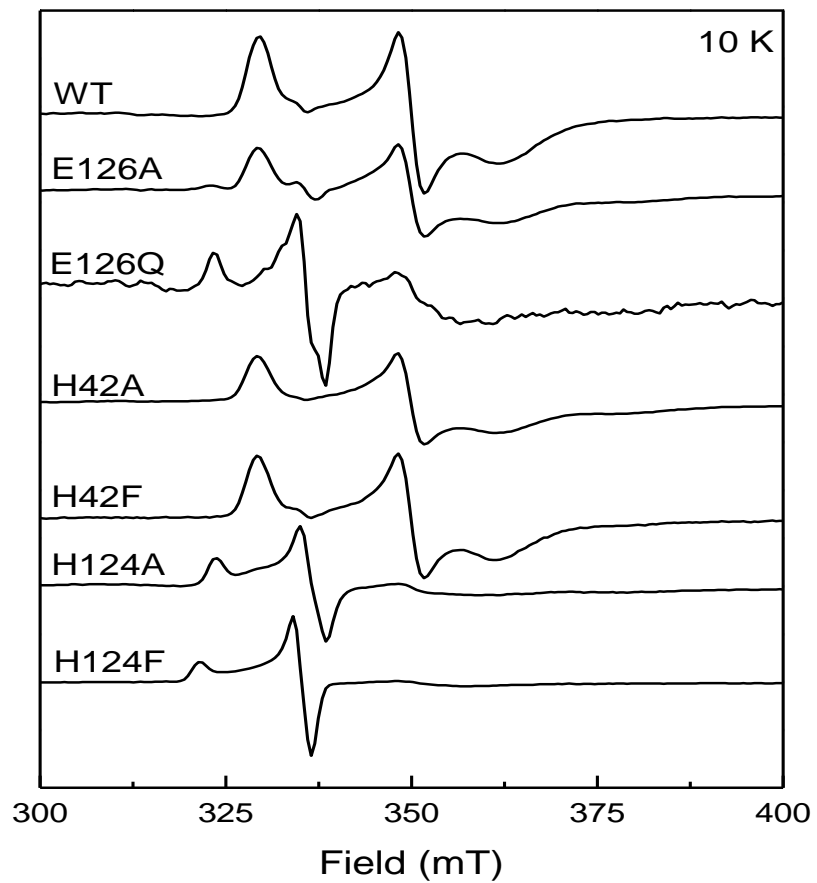


Figure 3.27. EPR spectra of reduced WT and mutant LytB proteins from *A. aeolicus* after cluster reconstitution. Enzymes were reduced with excess dithionite.

To check if all the mutants were properly folded, circular dichroism spectra were measured for WT and mutant protein (Fig. 3.28). The data show that all protein samples have very similar spectra, indicating that the proteins are folded properly. The spectrum for the H124F mutant is more intense, but the overall shape of the spectrum is similar to that of the other protein samples.

3.3.3.2 Activity

Activity assays were performed for all six mutated proteins. Table 3.2 shows the overall comparison with each other and to wild-type protein. The H42F mutant is the only one that showed measurable activity (after correction for protein concentration and cluster content). Note that reconstitution in *A. aeolicus* enzyme does not give the same amount of cluster as found for *P. falciparum* enzyme.

3.3.3.3 Incubation of One-Electron-Reduced Mutant LytB with HMBPP

One-electron-reduced enzyme was produced for all mutant enzymes, which were subsequently incubated with HMBPP. Figure 3.29 shows the overview of the detectable EPR signals acquired at 70K. The H42A and H42F mutants did not display any paramagnetic species. The H124A and H124F mutants exhibited a species with $g_{x,y,z} = 2.015, 2.033, 2.040$. The E126A and E126Q mutants showed a mixture of signals, but the main species has g values of 2.120, 2.002, and 1.965.

Due to the low cluster content of the enzyme samples, the same experiments

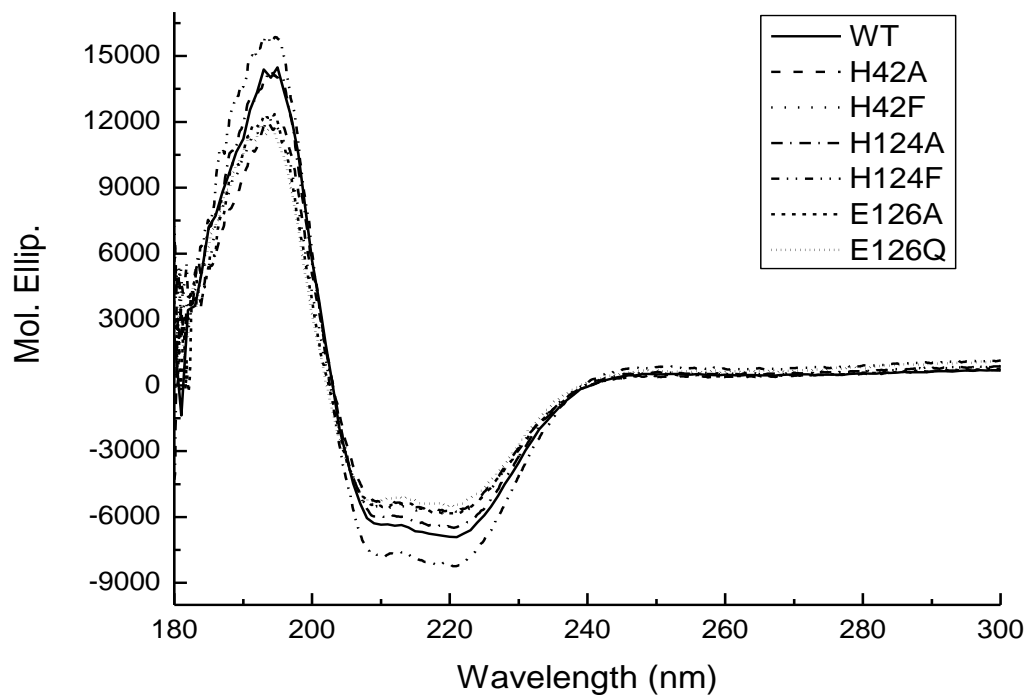


Figure 3.28. Circular dichroism spectra of WT and mutant LytB proteins from *A. aeolicus*.

Table 3.2 Enzymatic activity of WT and mutant enzymes from *A. aeolicus*

Reconstituted Enzyme	Cluster Content (%)	Specific Activity ($\mu\text{mol}\cdot\text{min}^{-1}\cdot\text{mg}^{-1}$)	Specific Activity after Correction with Cluster Content	K_M (μM)
WT	42.9	0.838	1.95	45
H42A	29.9	0.054	0.2	n.d.
H42F	45.9	0.498	1.085	166
H124A	33.2	0.046	0.138	n.d.
H124F	35.6	0.070	0.197	n.d.
E126A	41	0.076	0.185	n.d.
E126Q	29.6	0.058	0.196	n.d.

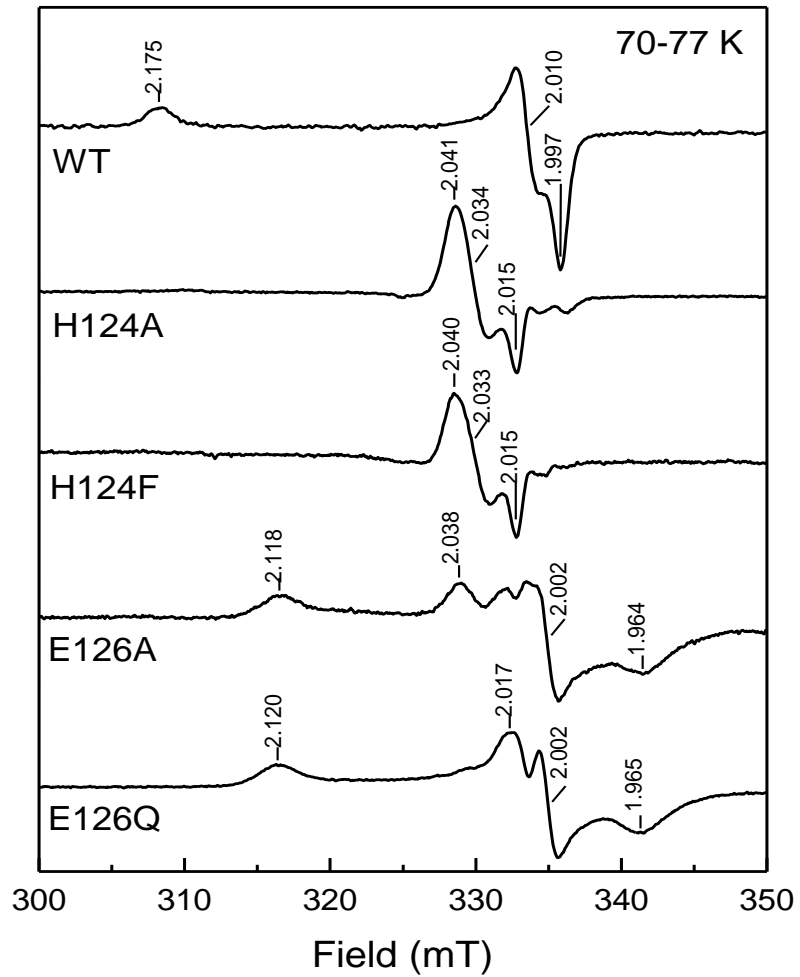


Figure 3.29. ‘FeS_I’ EPR signals detected in WT and mutant enzymes from *A. aeolicus*. Protein was the as-isolated protein.

were performed with the reconstituted proteins. Several new signals were detected in these studies, some were like the FeS_I species, but showed different temperature behavior. A selection of spectra taken at different temperatures is shown for the different mutants in Figure 3.30. All spectra are corrected for differences in gain, temperature and power, using the formula in section 2.2.6.

Figure 3.30, panel A, shows the temperature data obtained for the H42A mutant. At 10-20 K an EPR signal due to the $[\text{4Fe-4S}]^{1+}$ can be detected. At higher temperatures the FeS_I species can be detected but the signal intensity is very low. It can be concluded that the majority of the protein stayed reduced after the addition of substrate. The signal represents 0.03 spin. Together with the fact that this mutant is not active (Table 3.2) this would indicate that the mutation of replacement of His42 with Ala affects the binding of HMBPP.

Figure 3.30, panel B shows the temperature data obtained for the H42F mutant. At lower temperatures (from 5 K to 20 K) a mixture of the $[\text{4Fe-4S}]^+$ signal and the FeS_I signal is present. At 50 K only the FeS_I signal is detectable. When the temperature is increased from 50K to 70K, the intensity of this signal decreases. This behavior is different with that displayed by the intermediate signal in wild-type protein that has a very wide temperature range for detection. The detection of this species, however, is in line with the 50% WT activity detected for this mutant (Table 3.2).

Figure 3.30, panel C, shows the temperature data obtained for the H124A mutant. The sample does not show an EPR signal due to the $[\text{4Fe-4S}]^+$ cluster which could

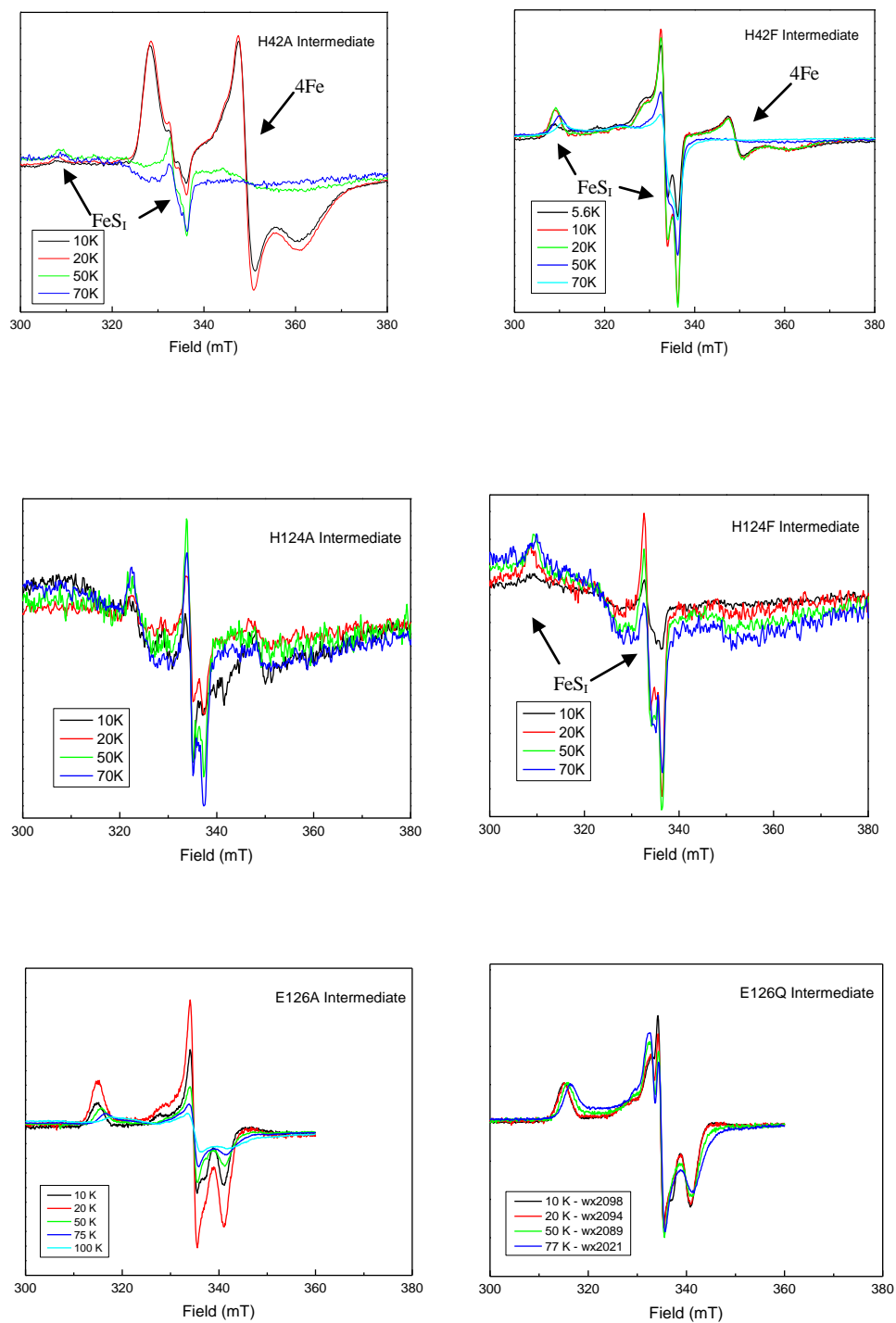


Figure 3.30 Temperature behavior studies of FeS_I with reconstituted mutant enzymes from *A. aeolicus*.

indicate that the cluster does get oxidized upon addition of substrate. A new paramagnetic species can be detected that does not share any EPR properties with that of the $[4\text{Fe-4S}]^{1+}$ cluster but is somewhat similar to the FeS_I species detected in WT protein. It needs to be tested whether the new signal is iron-sulfur based or not. If it is iron-sulfur based, it could be the result from substrate binding. The overall signal intensity of this new signal is very low (0.015 spin) which is in line with the very low activity found in the activity studies (Table 3.2). Assuming this represents a cluster-bound reaction intermediate, it appears that the H124A mutation has an effect on the amount of species formed and possibly on the way the substrate is bound since the new species has different g-values.

The data obtained for the H124F mutant is very similar to that of the H124A mutant (Fig. 3.30, panel D), but in this case a low-intense WT-like FeS_I signal is detectable. Also this species showed temperature broadening at 70 K, unlike the WT signal. The signal intensity is again very low (0.008 spin).

Figure 3.30, panel E, shows the data obtained for the E126A mutant. Yet, another new species is detected in this sample. This is the same species detected in the as-isolated mutant enzyme without the cluster reconstitution (Fig. 3.29). The signal intensity appears to be comparable in between 10 K and 20 K, but broadening of the signal is detected at higher temperatures. Studies with excess dithionite showed that this species is not a transient species but accumulated over time.

Figure 3.30, panel F, shows the data obtained for the E126Q mutant. This mutant shows the same species as the E126A mutant. At around 332 mT, however, there appears

to be an additional species present. It was not possible to obtain an EPR signal for this species by subtraction since the main species in these samples shows additional temperature broadening in each spectrum, which induced additional features in the difference spectra. As for the E126A, mutant this species accumulates over time in experiments with excess dithionite, showing it is not an intermediate species. Since both mutants are not active this would imply a role for Glu126 in a step of the reaction mechanism after the formation of a reaction intermediate, which is in principle trapped in this mutant. The mutation, however, seems to have a strong effect on the EPR properties of the trapped species since its EPR spectrum is different from that of the FeS_I species. Figure 3.31 shows an overview of the three main type signals detected: The FeS_I species in WT, H42F and H124F enzyme. The [4Fe-4S]⁺ in H42A enzyme and the new signal in the Glu126 mutants.

3.4 Discussion and Conclusion

3.4.1 Type of Cluster Present at Active Site

Overexpression and purification of recombinant LytB protein was accomplished for proteins from *A. aeolicus* and *P. falciparum*. The type of iron-sulfur cluster was determined to be a single [4Fe-4S] cluster. It was confirmed that the enzymatic activity is related to the amount of [4Fe-4S] cluster present. The fact that two crystal structures were published (146;77) where the protein contained a 3Fe cluster is probably due to an

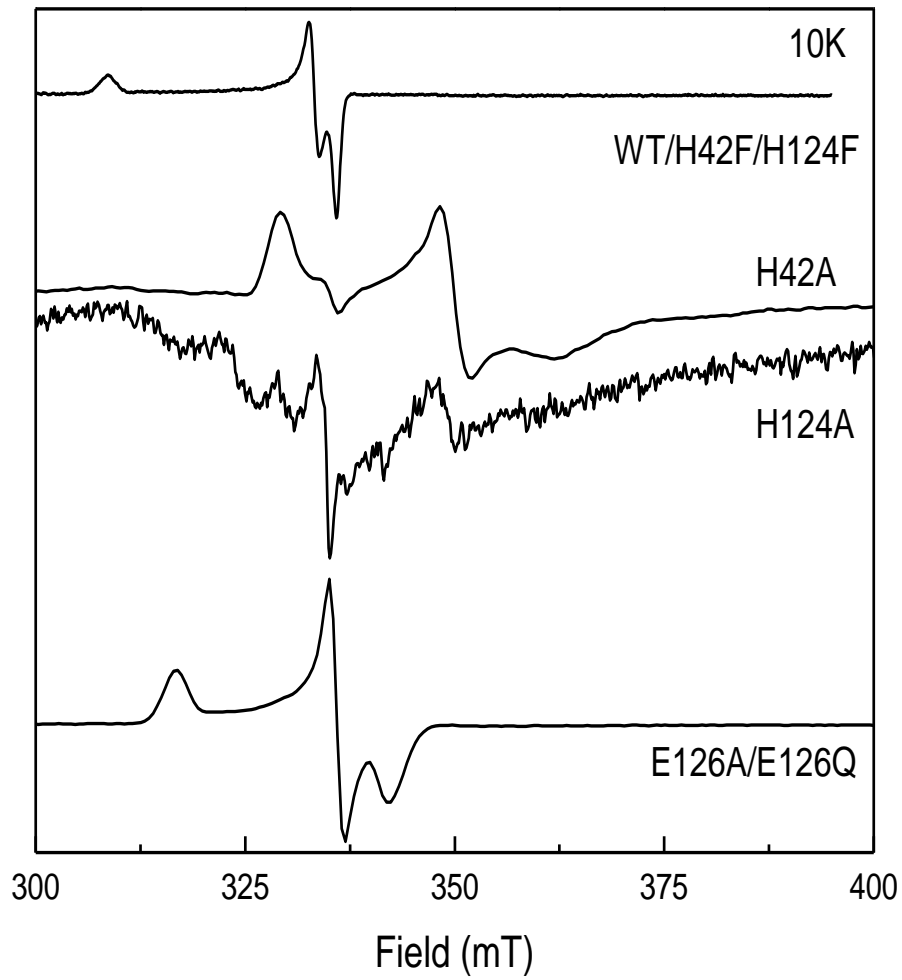


Figure 3.31. Overview of the signals detected in one-electron reduced WT and mutant enzymes after incubation with HMBPP for 30 s.

inherent instability of the 4Fe cluster or instability caused by the crystallization conditions. In a very recent paper a structure was presented where the enzyme was crystallized in the presence of the substrate HMBPP. In this case a 4Fe cluster was present in the structure (Fig. 3.32) (148).

3.4.2 Reduction of the [4Fe-4S] cluster

LytB catalyzes the conversion of HMBPP into IPP and DMAPP, which is the last step in the DOXP pathway for isoprenoid biosynthesis. The iron-sulfur cluster can accept a single electron from natural electron donors or appropriate external sources and transfers them stepwise for reduction. Under these conditions, however, no paramagnetic intermediate species can be trapped and detected in EPR spectrometry. Freeze-quench experiment should be performed to look for paramagnetic species at a faster time scale than used here. When the enzyme is supplied with only one electron, the second electron transfer step is terminated by deficiency of electrons. In this case, a paramagnetic species is obtained after addition of HMBPP with similar properties as the FeS_A signal detected in GcpE. This species was named FeS_I. The FeS_I EPR signal is also iron-sulfur based, and it was proposed to be due to a cluster-bound substrate or reaction intermediate.

3.4.3 Substrate Binding

The structure of the substrate HMBPP contains a hydroxyl group at the C4 position and a diphosphate group at the C1 position that could function as attachment points.

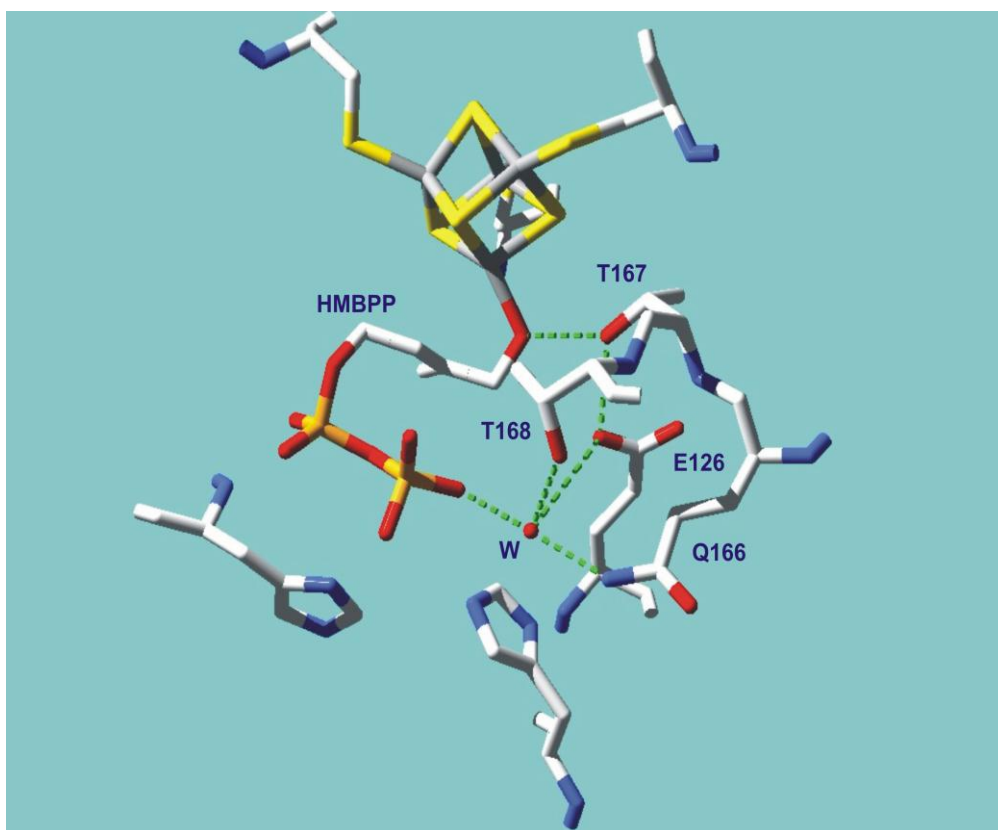


Figure 3.32 Detail of the active site of LytB protein crystallized in the presence of HMBPP. PDB ID 3KE8 (148).

ENDOR analysis implies a weak coupling from ^{31}P of the diphosphate group. It indicates that the phosphate group is in close proximity to the cluster, but not directly bound. Thus, the hydroxyl group is the most likely point of attachment. The ENDOR studies using HMBPP labeled with deuterium at the C4 position show the presence of ^2H -coupling over the whole signal envelope. The distance was estimated as 4.4 Å from the deuterium at the C4 position to the iron-sulfur cluster.

Our model was recently confirmed by Mössbauer studies and the crystal structure of a LytB:HMBPP complex. Gräwert et al. reported five crystal structures of recombinant *E. coli* LytB protein in complex with substrate, converted substrate, products and PPI (148). In the structure with HMBPP the hydroxyl group at the C4 position is coordinated to the unique iron of the 4Fe cluster (Fig. 3.32).

The structure of the complex with substrate shows that the oxygen at the C4 position is involved in a network of hydrogen binding with Thr167, Glu126, a water molecule and the phosphate group of HMBPP. It is proposed that Thr167 may act as a proton relay and Glu126 is the ultimate proton donor inside the network.

It was proposed that His124 might play an important role in substrate docking. Most amino acid residues which coordinate to the diphosphate group are structurally rearranged when the conformation changes between a closed and opened conformation (Fig. 3.33). However, His124 is not one of them.

3.4.4 Mutants Studies

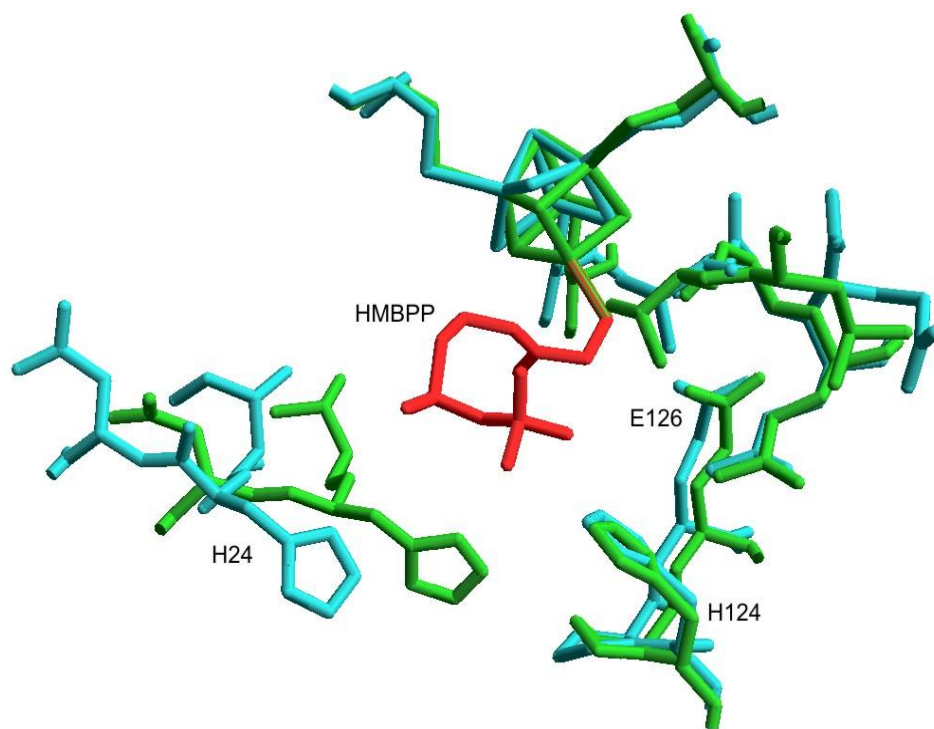


Figure 3.33 Overlay of the open form detected in LytB from *A. aeolicus* (blue - PDB ID 3DNF) and the closed form detected in LytB from *E. coli* (green - PDB ID 3KE8). HMBPP is in red.

Based on the earlier crystal structures of LytB protein from *A. aeolicus* and *E. coli*, mutants were prepared, including H42A, H42F, H124A, H124F, E126A and E126Q. The enzymatic activity was analyzed and showed that only the H42F mutant is active. Absorption, CD, and EPR measurements show that the mutant proteins are properly folded and contain 4Fe clusters. Since the cluster content was low, reconstitution of the clusters was performed. In this case, however, the H124A, H124F and E126Q mutants show a different EPR signal for the 4Fe cluster.

The His42 was proposed to participate in the interaction with one of the diphosphate oxygens of HMBPP. The mutation of His42 with Ala caused loss of most of the activity. The incubation of one-electron-reduced H42A with substrate does not result in the formation of a new paramagnetic species, at least not in significant amount. The mutation of His42 into Phe resulted in an enzyme that still showed partial activity and formed the FeS_I species. The observed V_{\max} is about half of that of WT enzyme. From this data it can be concluded that His42 is important for binding but that the replacement of this residue causes large conformational changes in the active site channel. Maybe the transition of the open to the closed conformation is affected by this mutation.

The involvement of His124 in hydrogen bonding with one of the diphosphate oxygens of HMBPP is indicated by the loss of most activity after mutation of His124 to Ala or Phe. The incubation of reconstituted enzymes (both H124A and H124F) with dithionite generates a paramagnetic species with different properties than the WT enzyme. This might be due to an incorrect insertion of cluster after reconstitution because the

reconstitution may lead to the cluster not being coordinated properly. However, the non-reconstituted samples do not show this effect. Therefore, it cannot explain that for H124A and H124F, neither non-reconstituted enzymes nor the reconstituted enzymes are active. The EPR studies show that the reduced clusters of both H124A and H124F mutant enzymes can be oxidized when incubated with substrate. Only low amounts of the 'FeS_I' species were detected, with similar in H124F, or different in H124A, EPR properties than the WT species. The oxidation of the cluster indicates that substrate binding occurs but this binding might not be in the same way as in the WT enzyme. It is in line with the important role of His124 for substrate docking indicated by the crystal structure of enzyme in the complex with substrate. However it could also indicate a role in the protonation process through the hydrogen bond interaction with other amino acid side groups and the water molecule in the active site. The wrong docking could result in the formation of a radical species on HMBPP that is not stabilized by the cluster. Interestingly a radical-type signal was detected in the non-reconstituted one-electron-reduced samples after addition of HMBPP. Why the same signal was not detected in the reconstituted samples is not clear. Studies at different time intervals will be needed to address this.

The absence of activity in the Glu126 mutants showed that this residue is important for the catalytic conversion of HMBPP into IPP and DMAPP. The incubation of non-reconstituted and reconstituted enzymes (both E126A and E126Q) with dithionite generates the same [Fe-4S]¹⁺ signal as in WT enzyme. However, the new paramagnetic

species detected after addition of dithionite and substrate has different EPR properties in comparison with the WT FeS₁ signal. This new E126A/Q species accumulated over time. In a recent paper by Oldfield and coworkers, broadening of this signal was shown when the protein was labeled with ⁵⁷Fe-isotope (149). This also indicates that this species is due to the iron-sulfur cluster and that it must represent a form of the cluster with bound substrate, a reaction intermediate, or a dead-end reaction product. The exact origin of this species needs to be determined. The data are in line with an important function of the Glu126 in the reaction mechanism, either directly or through the hydrogen bonded water molecule.

The work presented here is in line with the proposed roles of the three residues, His42, His124, and Glu126, in the binding of substrate and catalysis. The work also shows that the mutations can have a large effect on the conformation of the active site and electronic properties of the 4Fe cluster. This is the first time that these effects are described in more detail. In several recent papers (146;149) changing amino acid residues in or close to the active site are mentioned without presenting data of the cluster properties and cluster content. This is not correct since in some cases the observed absence of activity might be due to loss of cluster which can be wrongly interpreted as an important role of the mutated residue in the reaction mechanism.

There is another interesting amino acid residue, Thr167, which is proposed to be involved in hydrogen binding and might play a role as a proton relay. Mutation of this residue should be done to investigate this. Moreover, the origins of the paramagnetic

species which were detected for the H124 and E126 mutants need to be clarified using spectroscopy techniques and isotopic labeling experiments. The freeze-quench technique can be used to study the formation of these signals in more details.

3.4.5 Proposed Mechanism

Recently, the crystal structure of the LytB:HMBPP complex was resolved, and a new mechanism was proposed (Fig. 3.34) which now included a role for the [4Fe-4S] cluster (148). It was suggested that Lewis-acid activation and proton coupled electron transfer takes place in this mechanism. HMBPP docks to the oxidized cluster via the hydroxyl group. Subsequently the cluster is reduced after which the first electron is transferred into the allyl system accompanied with a proton transfer to the hydroxyl group at the C4 of HMBPP. Thus, the C-O bond is cleaved, the hydroxyl is abstracted as a water molecule and an allyl radical intermediate is generated. After re-reduction of the cluster, the second electron transfer occurs to the allyl radical and an allyl anion is formed. This species is protonated at either C2, yielding DMAPP, or C4, yielding IPP. The protons can come from either the adjacent β -phosphate moiety or the released water molecule.

A second mechanism was proposed by Oldfield's group (Fig. 3.35) (149). Initially, substrate binds the iron-sulfur cluster through the oxygen of the hydroxyl group at the C4 position. Then the first electron transfer results in the formation of a π (or π/σ) complex. The subsequent deoxygenation of substrate generates a water molecule and an η^1 -allyl complex by protonation *via* Glu126 (and His124) to the reduced complex. The second

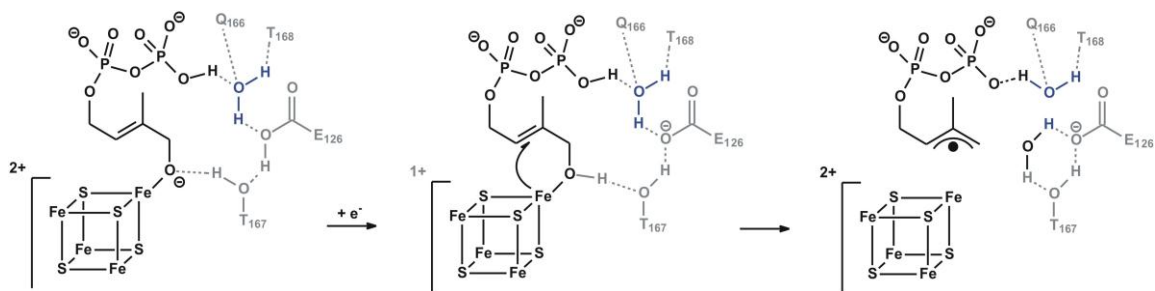


Figure 3.34 Hypothetical Mechanism I. Adapted from (148).

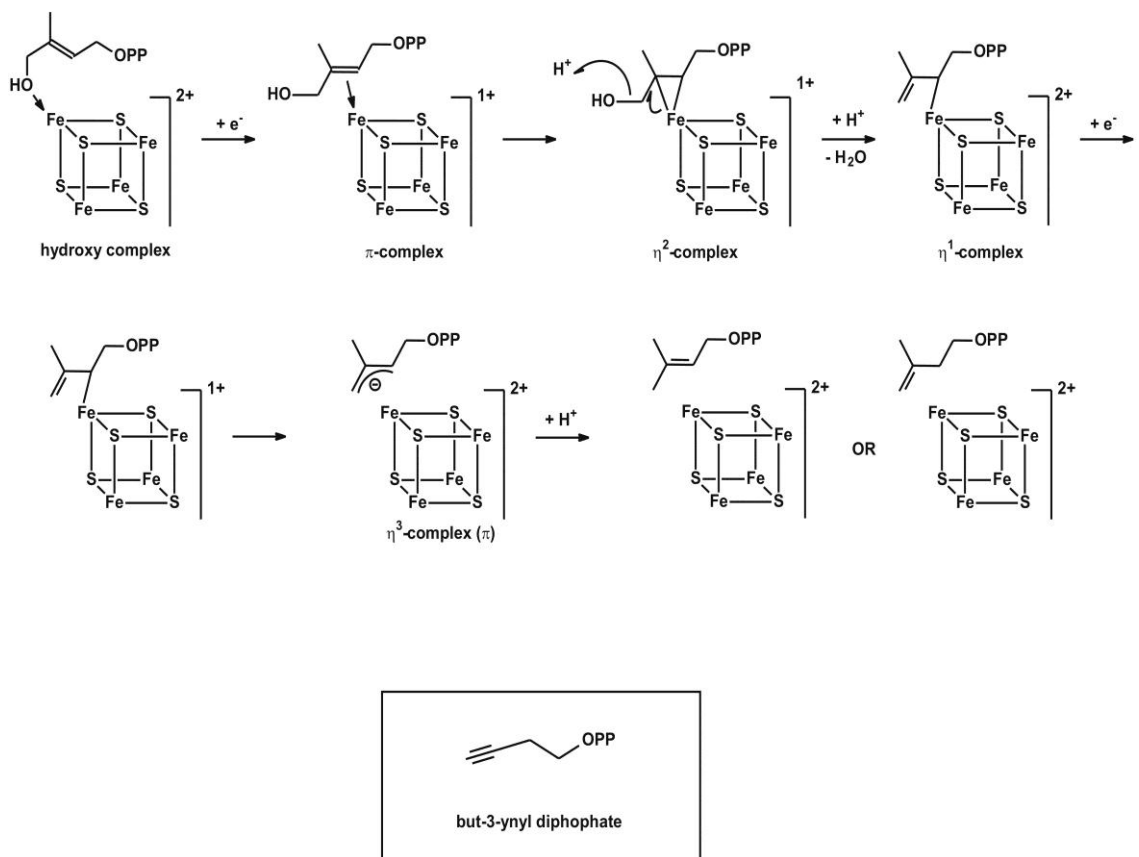


Figure 3.35 Hypothetical Mechanism II. Adapted from (149).

electron transfer yields a η^3 -allyl complex. The final products are yielded by protonation. The model is based on the E126A signal that was also found by our group. ^{13}C -ENDOR studies with $u\text{-}^{13}\text{C}$ -HMBPP showed the presence of two pairs of peaks which were attributed to two different carbon atoms. The other three carbon atoms were not detected. Due to the high coupling constants it was proposed that this was due to side-on binding of the double bond of HMBPP to the unique iron in LytB. A problem with this interpretation is that stronger couplings have been found for carbon atoms that are not directly coordinated to a metal ions (Brian Hoffman, personal communication). Our ^2H -ENDOR studies (Fig. 3.22), with the same enzyme showed that HMBPP could be bound in two different ways. This would mean that the two pairs of signals detected in the ^{13}C -ENDOR could be due to the same carbon atom. Unfortunately, a full set of data was not presented in these studies to exclude this possibility.

Based on this assumption, however, acetylenic diphosphate compounds were proposed and shown to be very strong inhibitors of LytB, $\text{IC}_{50} = 0.45 \mu\text{M}$ for but-3-ynyl diphosphate (Figure 3.35, insert). Addition of this latter compound to the reduced enzyme induced a new EPR signal that resembled that of the FeS_I species: $g_{zyx} = 2.087, 2.012,$ and 1.992.

Figure 3.36 shows a very basic mechanism that we use as our working model. Currently we do not have the ^{57}Fe -ENDOR data for the FeS_I species, but based on the similarities with the FeS_A signal in GcpE and the work done by Oldfields group, it seems reasonable to assume that the cluster in the FeS_I form is in the 1+ oxidation state. That

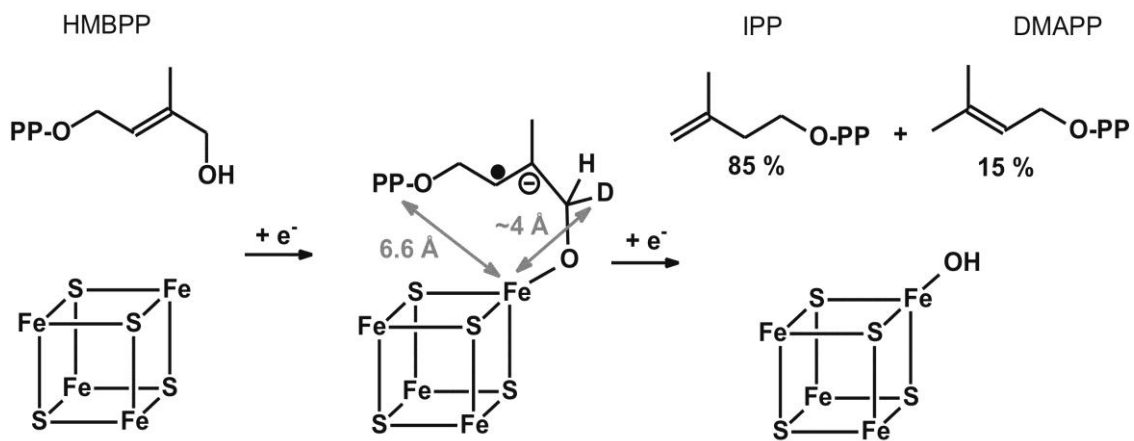


Figure 3.36 Hypothetical Mechanism III.

would also mean that the FeS_I species just represents the initial binding of HMBPP to the cluster. It is not clear, however, why such a species should be a low energy point in the reaction pathway. In both hypothetical reaction mechanisms I and II the enzyme should get trapped in a 2+ oxidation state and should therefore be EPR silent. Of course we do not know if the FeS_I species is a real intermediate and not a dead end product. This should be tested just like we did for the FeS_B signal in GcpE. If it is a true intermediate, however, adding a second electron, which presumably is donated via the 4Fe cluster would transiently induce a $[\text{4Fe-4S}]^0$ oxidation state. This form was found for example in the nitrogenase Fe-protein. An alternative explanation would be that there is an internal electron transfer to the substrate, either bound via the hydroxyl group or via a π/η complex, but that the electron is delocalized over the whole substrate-cluster complex which could be the reason for the unique properties of the FeS_I species. Freeze quench studies have to be performed to see if the FeS_I species can be detected as a transient species.

Chapter 4 Conclusions and Future Work

This work focused on two iron-sulfur proteins, GcpE and LytB, which are involved in the DOXP pathway for isoprenoid biosynthesis. GcpE converts MEcPP into HMBPP in the second to the last step of the DOXP pathway. LytB catalyzes the last step by converting of HMBPP into IPP and DMAPP. Both of them contain a [4Fe-4S] cluster in the active site. Here we presented a full spectroscopic characterization of these iron-sulfur clusters using absorption, EPR and ENDOR spectroscopies. In addition several cluster-associated reaction intermediates were described that were found in EPR-detected kinetic studies.

4.1 GcpE

The iron-sulfur cluster in GcpE appeared to have the unique property of not being able to be reduced or stay reduced for extended periods. The reduction of this protein was tested with different reductants, including dithionite, dithionite reduced methyl viologen, and titanium(III) citrate. The results indicated that the iron-sulfur cluster in GcpE can only be reduced in a very narrow redox potential range. Optimal reduction, although still at low levels, was detected with equimolar amounts of methyl viologen. The use of

excess amounts of methyl viologen or the stronger reductant titanium(III) citrate resulted in partial reduction and at the same time cluster breakdown. The amount of reduction appears to be affected by the binding of either product or substrate to the cluster. In the latter case the FeS_B signal was induced. The addition of HMBPP can reversibly convert the [4Fe-4S]⁺ EPR signal into the FeS_B signal. Addition of MEcPP causes the appearance of the FeS_A signal. It is not clear at this point whether the FeS_A species just represents the substrate-bound species or a more advanced reaction intermediate. The induction of both signals, however, indicates that the binding of compounds might change the midpoint potential of the iron-sulfur cluster, resulting in a higher reduction level in the presence of an appropriate reductant. In future experiments, this change in midpoint potential of the iron-sulfur cluster in the presence and absence of different ligands can be determined in EPR-detected redox titrations.

The data presented here showed that both the FeS_A and FeS_B species are kinetically competent. However, this was done in a very indirect way and very different reaction conditions. The new freeze-quench setup should allow for the direct measurement of the rates of the different reaction steps: the appearance and disappearance of the FeS_A species and the appearance of the FeS_B species. An important experiment will be to do kinetic experiments in the presence of dithionite and an equivalent amount of methyl viologen. This would allow the comparison of the EPR-based data with that obtained with the colorimetric assay. It is expected that the low amount of methylviologen would still provide the fast kinetics as observed in the colorimetric assay but will also allow the

detection of the other paramagnetic species after subtraction of the radical signal due to reduced methyl viologen.

The origin of the FeS_A species was not identified now, but there are two possible candidates as shown in our proposed mechanism (Fig. 2.36). The first possibility is the $[\text{4Fe-4S}]$ cluster in the 1+ oxidation state bound by substrate, and the second one is the cluster in 3+ oxidation state bound by a reaction intermediate. Mössbauer spectroscopy will be necessary to determine which oxidation state is present. To be able to get good data, the signal concentration should at least be 2 mM for Mössbauer experiments. Although we can make very concentrated samples, up to 6-8 mM, that would have enough of the FeS_A species present it is important to keep looking for conditions that can increase the relative amount of signal present since it will greatly simplify the Mössbauer experiments and simplify the interpretation of the data.

There are two potential groups of the substrate MEcPP that could be involved in the binding to the 4Fe cluster: the diphosphate group and the hydroxyl group. The ^{31}P -ENDOR analysis ruled out the possibility of the diphosphate group, leaving the hydroxyl group as the only candidate. The most direct way to prove this would be to use ^{18}O labeling. Due to the high expenses, however, we will be labeling several of the carbon atoms positions with ^{13}C and analyze the samples with bound ^{13}C -MEcPP with ENDOR spectroscopy.

As mentioned, the FeS_B species is the result of the product HMBPP binding to the reduced $[\text{4Fe-4S}]^{1+}$ cluster. As with the FeS_A species, the exact binding model is unclear,

so isotopic labeling experiments coupled with ENDOR spectroscopy and Mössbauer analysis will be performed to work this out. Furthermore, it is mentioned that the FeS_B species is a mixture of at least two species, maybe more. High frequency EPR (W-band) was used to separate the different signals, but failed due to low signal-to-noise ratios. Samples with higher concentrations have to be made and this experiment repeated.

4.2 LytB

Our data clearly showed that the 4Fe cluster is the active form of LytB. The enzymatic activity is proportional to the 4Fe cluster content. LytB can be reduced by dithionite alone and the overall reaction can be finished in 12 second, maybe shorter. In this case the midpoint potential of dithionite is sufficient to provide electrons for both steps in the two-electron-mechanism without the formation of paramagnetic species (at least on a 's' time scale). Only one new paramagnetic species, FeS_I , was trapped after incubation of one-electron-reduced protein with dithionite and substrate. In the near future, the freeze-quench technique will be used to analyze the overall reaction on a faster (ms) time scale. It is important to show that the FeS_I species is on the reaction path and not a dead end product.

The new paramagnetic species FeS_I is similar to the FeS_A species detected in GcpE. It was also proposed to be a 4Fe species with either substrate or a reaction intermediate bound through the diphosphate group or the hydroxyl group. The broadening effect shown in ^{57}Fe -EPR spectrum tells that it is iron-sulfur cluster based. The ^{31}P -ENDOR

data exclude the possibility of the direct binding from the diphosphate group. HMBPP labeled with deuterium at the C4 position was used for ENDOR analysis. The observed coupling was in line with the direct binding of the hydroxyl group to the cluster. The recent 3D structures (*148*) show HMBPP bound to the cluster via its hydroxyl group. For the reaction intermediate however, different types of bonding have been proposed. This needs be confirmed by ENDOR measurements in combination with ¹³C-isotopic labeling experiments. In particular our data indicate that HMBPP might be bound in different orientations which would make the π -bonding model less likely (*149*). Mössbauer experiments will be needed to determine the redox state of the 4Fe cluster.

Six mutant proteins including H42A, H42F, H124A, H124F, E126A, and E126Q were prepared for LytB, according to the fact that these three residues are totally conserved and the crystal structure indicated a possible role in the reaction mechanism.

The His42 mutants confirmed a role in the docking of the diphosphate of HMBPP. However, the decrease in activity cannot be overcome by increased substrate concentrations which might indicate that the mutations cause a change in the active site conformation that affects more than just the binding of HMBPP. In the case of the His124 mutants most activity was lost after mutation of His124 to Ala or Phe. A mixture of the regular 4Fe EPR signal and a new signal were detected upon incubation with dithionite. These signals disappeared upon addition of HMBPP. In the non-reconstituted enzyme an additional radical-type signal was detected. This data indicate that the binding of HMBPP is affected in such a way that although it can still be reduced by the cluster, a radical

species is induced that is not stabilized by the cluster and upon further reaction appears to inactivate LytB. This reaction has to be studied in more detail using the freeze-quench setup. With the help of NMR and probably mass spectrometry the products of this 'reaction' have to be identified. The Glu126 mutants are also dead, but in this case addition of HMBPP to the reduced enzyme causes the formation of a new stable paramagnetic species, based on the spread in g-values that is probably an FeS-based species. The same type of ENDOR and Mössbauer experiments as proposed for FeS_A and FeS_I have to be performed here to understand the origin of this species.

The most important conclusion of these mutations is that the effects of these are much more complex and that previous work where the importance of a residue was mainly based on the absence of activity is highly inadequate and possibly wrong since mutations further away from the cluster still seem to have an effect on the cluster properties and therefore the reaction. Based on the most recent crystal structure studies (148), Thr167 is an additional residue that seems to play an important role in the enzyme. It was proposed to be involved in a hydrogen binding network, keeping an essential water molecule in place, and also to function as a proton relay. Therefore, mutations of this residue have to be made and their effect on the cluster properties and activity measured.

References

1. Sacchettini, J. C. and Poulter, C. D. (1997) *Science* 277, 1788-1789.
2. Croteau, R. K. T. M. a. L. N. G. (2008) *Biochemistry and Molecular Biology of Plants ASPD*.
3. Goldstein, J. L. a. B. M. S. (1990) *Nature* 342, 425-430.
4. McGarvey, D. J. and Croteau, R. (1995) *Plant Cell* 7, 1026.
5. Kollas, A.-K., Duin, E. C., Eberl, M., Altincicek, B., Hintz, M., Reichenberg, A., Henschker, D., Henne, A., Steinbrecher, I., Ostrovsky, D. N., Hedderich, R., Beck, E., Jomaa, H., and Wiesner, J. (2002) *FEBS Lett.* 532, 432-436.
6. Andersson, D. I. (2003) *Current Opini. Microbiol.* 6, 452-456.
7. Kleinig, K. (1989) *Annu. Rev. Plant Physiol.* 40, 39-59.
8. Chappel, J. (1995) *Annu. Rev. Plant Physiol.* 46, 521-547.
9. Bach, T. J. (1995) *Lipids* 30, 191-202.
10. Treharne, K. J., Mercer, E. I., and Goodwin, T. W. (1966) *Biochem. J.* 99, 239-245.
11. Banthorpe, D. V., Charlwood, B. V., and Francis, M. J. O. (1972) *Chem. Rev.* 72, 115-155.
12. Bach, T. J. and Lichtenthaler, H. K. (1987) *Am. Chem. Soc. Symp. Series* 325, 109.
13. Bach, T. J., Weber, T., and Motel, A. (1990) *Rec. Adv. Phytochem.* 24, 1.
14. Zhou, D. and White, R. H. (1991) *Biochem. J.* 273, 627-634.
15. Kreuz, K. and Kleinig, H. (1981) *Planta* 153, 578-581.
16. Kreuz, K. and Kleinig, H. (1984) *Eur. J. Biochem.* 141, 531-535.
17. Rohmer, M. The discovery of a mevalonate-independent pathway for isoprenoid biosynthesis in bacteria, algae and higher plants. *Nat.Prod.Rep.* 16, 565-574. 1999.

18. Rohmer, M., Seemann, M., Horbach, S., Bringer-Meyer, S., and Sahm, H. (1996) *J. Am. Chem. Soc.* *118*, 2564-2566.
19. White, R. H. (1978) *Biochemistry* *17*, 3833-3840.
20. David, S., Esteamareix, B., Fischer, J. C., and Therisod, M. (1981) *J. AM. CHEM. SOC.* *103*, 7341-7342.
21. Kennedy, I. A., Hill, R. E., Pauloski, R. M., Sayer, B. G., and Spenser, I. D. (1995) *J. AM. CHEM. SOC.* *117*, 1661-1662.
22. Kojo H., Shigi Y, and Nishida M. (1980) *J. Antibiot.* *33*, 44-48.
23. Palmer, G. and Reedijk, J. (1991) *Eur. J. Biochem.* *200*, 599-611.
24. Cammack, R. (1992) *Adv. Inorg. Chem.* *38*, 281-322.
25. Kennedy, M. C. and Stout, C. D. (1992) *Adv. Inorg. Chem.* *38*, 323-339.
26. Mouseca, J. M. and Lamotte, B. (1998) *Coordination Chemistry Reviews* *178-180*, 1573-1614.
27. Johnson, D. C., Dean, D. R., Smith, A. D., and Johnson, M. K. Structure, Function, and Formation of Biological Iron-Sulfur Clusters. (2005) *Annu.Rev.Biochem.* *74*, 247-281.
28. Beinert, H., Kennedy, M. C., and Stout, C. D. (1996) *Chem. Rev.* *96*, 2335-2374.
29. Jarrett, J. T. (2003) *Curr. Opin. Chem. Biol.* *7*, 174-182.
30. Cheek, J. and Broderick, J. B. (2001) *J. Biol. Inorg. Chem.* *6*, 209-226.
31. Henderson, R. A. (2005) *Chem. Rev.* *105*, 2365-2437.
32. Fu, W., O'Handley, S., Cunningham, R. P., and Johnson, M. K. (1992) *J. Biol. Chem.* *267*, 16135-16137.
33. Lukianova, O. A. and David, S. S. (2005) *Curr. Opin. Chem. Biol.* *9*, 145-151.
34. Demple, B., Ding, H., and Jorgensten, M. (2002) *Methods in Enzymology*.
35. Grandu, P. and Weiss, B. (1996) *Proc. Natl. Acad. Sci. USA* *93*, 10094-10098.
36. Killey, P. J. and Beinert, H. (2003) *Current Opini. Microbiol.* *6*, 181-182.
37. Rafik, G. L. (2002) *EPR in Biochemistry and Medicine*.
38. Berg, J. M. and Holm, R. H. (1982) pp 1-66, Wiley Interscience, New York.

39. Gutlick, P., Link, R., and Trautwein, A. (1978) *Mossbauer Spectroscopy and Transition Metal Chemistry* Springer Verlag, Berlin.
40. Sands, R. H. and Dunham, W. R. (1974) *Quarterly Reviews of Biophysics* 7, 443-504.
41. Beinert, H. (2000) *J. Biol. Inorg. Chem.* 5, 2-15.
42. Flint, D. H. and Allen, R. M. (1996) *Chem. Rev.* 96, 2315-2334.
43. Glusker, J. P. (1971) *The Enzymes* Academic Press, New York.
44. Kent, T. A., Dreyer, J.-L., Kennedy, M. C., Huynh, B. H., Emptage, M. H., Beinert, H., and Munck, E. (1982) *Proc. Natl. Acad. Sci. USA.* 79, 1096-1100.
45. Emptage, M. H., Kent, T. A., Kennedy, M. C., Beinert, H., and Munck, E. (1983) *Proc. Natl. Acad. Sci. USA.* 80, 4674-4678.
46. Sofia, H. J., Chen, G., Hetzler, B. G., Reyes-Spindola, J. F., and Miller, N. E. (2001) *Nucleic Acid Res.* 29, 1097-1106.
47. Layer, G., Heinz, D. W., Jahn, D., and Schubert, W.-D. (2004) *Curr. Opin. Chem. Biol.* 8, 468-476.
48. Marsh, E. N. G., Patwardhan, A., and Huhta, M. S. (2004) *Bioorg. Chem.* 32, 326-340.
49. Wang, S. C. and Frey, P. A. (2007) *Trends Biochem. Sci.* 32, 101-110.
50. Walsby, C. J., Hong, W., Broerick, W. E., Cheek, J., Ortillo, D., Broderick, J. B., and Hoffman, B. M. (2002) *J. Am. Chem. Soc.* 124, 3143-3151.
51. Walsby, C. J., Ortillo, D., Broerick, W. E., Broderick, J. B., and Hoffman, B. M. (2002) *J. Am. Chem. Soc.* 124, 11270-11271.
52. Cosper, M. M., Jameson, G. N. L., Davydov, R., Eidsness, M. K., Hoffman, B. M., Huynh, B., and Johnson, M. K. (2002) *J. Am. Chem. Soc.* 124, 14006-14007.
53. Cheek, J. and Broderick, J. B. (2001) *J. Biol. Inorg. Chem.* 6, 209-226.
54. Kulzer, R., Pits, T., Kappi, R., Hutterman, J., and Knappe, J. (1998) *J. Biol. Chem.* 273, 4897-4903.
55. Tamarit, J., Gerezc, C., Meler, C., Mulliez, E., Trautwein, A., and Fontecave, M. (2000) *J. Biol. Chem.* 275, 15669-15675.
56. Berkovitch, F., Nicolet, Y., Wan, J. T., Jarrett, J. T., and Drennan, C. L. (2004) *Science* 303, 76-79.
57. Liu, A. and Grälund, A. (2000) *J. Biol. Chem.* 275, 12367-12373.

58. Ollagnier, S., Meier, C., Mulliez, E., Gaillard, J., Schuenemann, V., Trautwein, A., Mattioli, T., Lutz, M., and Fontecave, M. (1999) *J. Am. Chem. Soc.* 121, 6344-6350.
59. Krebs, C., Henshaw, T. F., Cheek, J., Huynh, B. H., and Broderick, J. B. (2000) *J. Am. Chem. Soc.* 122, 12497-12506.
60. Broderick, J. B., Henshaw, T. F., Cheek, J., Wojtuszewski, K., Smith, S. R., Trojan, M. R., McGhan, R. M., Kopf, A., Kibbey, M., and Broderick, W. E. (2000) *Biochem. Biophys. Res. Com.* 269, 451-456.
61. Wagner, A. F. V., Frey, M., Neugebauer, F. A., Schafer, W., and Knappe, J. (1992) *Proc. Natl. Acad. Sci. USA* 89, 996-1000.
62. Bianchi, V., Eliasson, R., Fontecave, M., Mulliez, E., Hoover, D. M., Matthews, R. G., and Reichard, P. (1993) *Biochem. Biophys. Res. Com.* 197, 792-797.
63. Picclocchi, A., Douce, R., and Alban, C. (2003) *J. Biol. Chem.* 278, 24966-24975.
64. Madadi-Kahkesh, S., Duin, E. C., Heim, S., Albracht, S. P. J., Johnson, M. K., and Hedderich, R. (2001) *Eur. J. Biochem.* 268, 2566-2577.
65. Duin, E. C., Madadi-Kahkesh, S., Hedderich, R., Clay, M. D., and Johnson, M. K. (2002) *FEBS Lett.* 512, 263-268.
66. Duin, E. C., Bauer, C., Jaun, B., and Hedderich, R. (2003) *FEBS Lett.* 538, 81-84.
67. Dai, S., Saarinen, M., Ramaswamy, S., Meyer, Y., Jacquot, J.-P., and Eklund, H. (1996) *J. Mol. Biol.* 264, 1044-1057.
68. Dai, S. D., Friemann, R., Glauser, D. A., Bourquin, F., Manieri, W., Schürmann, P., and Eklund, H. (2007) *Nature* 448, 92-96.
69. Jameson, G. N. L., Walters, E. M., Manieri, W., Schümann, P., Johnson, M. K., and Huynh, B. H. (2003) *J. Am. Chem. Soc.* 125, 1146-1147.
70. Walters, E. M., Garcia-Serres, R., Jameson, G. N. L., Glauser, D. A., Bourquin, F., Manieri, W., Schümann, P., Johnson, M. K., and Huynh, B.-H. (2005) *J. Am. Chem. Soc.* 127, 9612-9624.
71. Staples, C. R., Gaymard, E., Stritt-Etter, A.-L., Telser, J., Hoffman, B. M., Schümann, P., Knaff, D. B., and Johnson, M. K. (1998) *Biochemistry* 37, 4612-4620.
72. Zavoisky, E. (1945) *J. Phys. USSR* 9, 211-245.
73. Sutcliffe, L. H. (1998) *Phys. Med. Biol.* 43, 1987.

74. Hubbell, W. L., Gross, A., Langen, R., and Lietzow, M. A. (1998) *Curr. Opin. Struct. Biol.* 8, 649.
75. Pilbrow, J. R. and Hanson, G. R. (1993) *Meth. Enzymol.* 227, 330-353.
76. Brudvig, G. W. (1995) *Meth. Enzymol.* 246, 536-554.
77. Rekkittke, I., Wiesner, J., Rörich, R., Demmer, U., Warkentin, E., Xu, W., Troschke, K., Hintz, M., No, J. H., Duin, E. C., Oldfield, E., Jomma, H., and Ermler, U. (2008) *J. Am. Chem. Soc.* 130, 17206-17207.
78. Cammack, R., Patil, D. S., and Fernandez, V. M. (1985) *Biochem. Soc. Trans.* 13, 572-578.
79. Ingram, D. J. E. (1969) *Biological and Biochemical Applications of Electron Spin Resonance* Hilger, London.
80. Alger, R. (1968) in *EPR Techniques and Applications*, Wiley Interscience, New York.
81. Poole, C. P. (1983) in *A comprehensive Treatise on Experimental Techniques*, Wiley, New York.
82. Carrington, A. (1967) *Introduction to Magnetic Resonance*, New York.
83. Weil, J. A., Bolton, J. R., and Wertz, J. E. (1994) *Electron paramagnetic resonance*, John Wiley & Sons, Inc., New York.
84. Gordy, E. (1980) *Theory and Applications of Electron Spin Resonance*, New York.
85. Bell, J. E. (1982) CRC Press, Inc., Boca Racon, Florida.
86. Sarifut-Denov, R. G. and Larina, L. I. (2001) Kluwer, New York.
87. Palmer, G. and Que, L., Jr. (2002) in *Physical Methods in Bioinorganic Chemistry* pp 132, University Science Books, Mill Valley, California.
88. Feher, G. (1956) *Phys. Rev.* 834-835.
89. Eisenberger, P. and Pershan, P. S. (1967) *J. Chem. Phys.* 47, 3327-3334.
90. Gubriel, R. J., Batie, C. J., Sivaraja, M., True, A. E., Fee, J. A., Hoffman, B. M., and Ballou, D. P. (1989) *Biochemistry* 28, 4861-4871.
91. Fan, C., Gorst, C. M., Ragsdale, S. W., and Hoffman, B. M. (1991) *Biochemistry* 30, 431-435.
92. True, A. E., Nelson, M. J., Venters, R. A., Orme-Johnson, W. H., and Hoffman, B. M. (1988) *J. Am. Chem. Soc.* 110, 1935-1943.
93. Hoffman, B. M., DeRose, V. J., Gubriel, R. J., Houseman, L. P., Doun, P. E., and Elser, J. (1993) in

Biological Magnetic Resonance (Berliner, L. J. and Reuben, J., Eds.) Plenum Press, New York.

94. Beinert, H., Gruel, M. J., Guest, J. R., and Thomson, A. J. (1995) *Eur. J. Biochem.* 233, 317-326.
95. Rohdich, F., Bacher, A., and Eisenreich, W. (2005) *Biochem. Soc. Trans.* 33, 785-791.
96. Phillips, R. (2001) *Clin. Microbiol. Rev.* 14, 208-226.
97. Kuzuyama, T., Shimizu, T., Takahashi, S., and Seto, H. (1998) *Tetrahedron Lett.* 39, 7913-7916.
98. Zeidler, J., Schwender, J., Muller, C., Wiesner, J., Weidemeyer, C., Beck, E., Jomaa, H., and Lichtenthaler, H. K. (1998) *Z. Naturforsch.* 53c, 980-986.
99. Jomaa, H., Wiesner, J., Sanderbrand, S., Altincicek, B., Weidemeyer, C., Hintz, M., Turbachova, I., Eberl, M., Zeidler, J., Lichtenthaler, H. K., Soldati, D., and Beck, E. (1999) *Science* 285, 1573-1576.
100. Koppisch, A. T., Fox, D. T., Blagg, B. S. J., and Poulter, D. C. (2002) *Biochemistry* 41, 236-243.
101. Missinou, M. A., Borrmann, S., Schindler, A., Issifou, S., Adegnika, A. A., Matsiegui, P.-B., Binder, R., Lell, B., Wiesner, J., Baranek, T., Jomaa, H., and Kreamsner, P. G. (2002) *The Lancet* 360, 1941-1942.
102. Lell, B., Ruangweerayut, R., Wiesner, J., Missinou, M. A., Schindler, A., Baranek, T., Hintz, M., Hutchinson, D., Jomaa, H., and Kreamsner, P. G. (2003) *Antimicrobial Agents and Chemotherapy* 47, 735-738.
103. Borrmann, S., Issifou, S., Esser, G., Adegnika, A. A., Ramharter, M., Matsiegui, P. B., Oyakhrome, S., Mawili-Mboumba, D. P., Missinou, M. A., Kun, J. F. J., Jomaa, H., and Kreamsner, P. G. (2004) *Journal of Infectious Diseases* 190, 1534-1540.
104. Giessmann, D., Heidler, P., Haemers, T., Van Calenbergh, S., Reichenberg, A., Jomaa, H., Weidemeyer, C., Sanderbrand, S., Wiesner, J., and Link, A. (2008) *Chemistry & Biodiversity* 5, 643-656.
105. Haemers, T., Wiesner, J., Giessmann, D., Verbrugghen, T., Hillaert, U., Ortmann, R., Jomaa, H., Link, A., Schlitzer, M., and Van Calenbergh, S. (2008) *Bioorganic & Medicinal Chemistry* 16, 3361-3371.
106. Wiesner, J., Ortmann, R., Jomaa, H., and Schlitzer, M. (2007) *Archiv der Pharmazie* 340, 667-669.
107. Ortmann, R., Wiesner, J., Silber, K., Klebe, G., Jomaa, H., and Schlitzer, M. (2007) *Archiv der Pharmazie* 340, 483-490.
108. Devreux, V., Wiesner, J., Jomaa, H., Van der Eycken, J., and Van Calenbergh, S. (2007) *Bioorganic*

& *Medicinal Chemistry Letters* 17, 4920-4923.

109. Devreux, V., Wiesner, J., Jomaa, H., Rozenski, J., Van der Eycken, J., and Van Calenbergh, S. (2007) *Journal of Organic Chemistry* 72, 3783-3789.
110. Haemers, T., Wiesner, J., Busson, R., Jomaa, H., and Van Calenbergh, S. (2006) *European Journal of Organic Chemistry* 3856-3863.
111. Devreux, V., Wiesner, J., Goeman, J. L., Van der Eycken, J., Jomaa, H., and Van Calenbergh, S. (2006) *Journal of Medicinal Chemistry* 49, 2656-2660.
112. Haemers, T., Wiesner, J., Van Poecke, S., Goeman, J., Henschker, D., Beck, E., Jomaa, H., and Van Calenbergh, S. (2006) *Bioorganic & Medicinal Chemistry Letters* 16, 1888-1891.
113. Matthews, P. D. and Wurtzel, E. T. (2000) *Appl. Microbiol. Biotechnol.* 53, 396-400.
114. Rodríguez-Concepción, M., Querol, J., Lois, L. M., Imperial, S., and Boronat, A. (2003) *Planta* 217, 476-482.
115. Lichtenthaler, H. K., Zeidler, J., Schwender, J., and Müller, C. (2000) *Zeitschrift für Naturforschung C-A Journal of Biosciences* 55, 305-313.
116. Fellermeier, M., Kis, K., Sagner, S., Maier, U., Bacher, A., and Zenk, M. H. (1999) *Tetrahedron Letters* 40, 2743-2746.
117. Hecht, S., Eisenreich, W., Adam, P., Amslinger, S., Kis, K., Bacher, A., Arigoni, D., and Rohdich, F. (2001) *Proc. Natl. Acad. Sci. USA* 98, 14837-14842.
118. Wolff, M., Seemann, M., Grosdemange-Billiard, C., Tritsch, D., Campos, N., Rodrigue-Concepcion, M., Boronat, A., and Rohmer, M. (2002) *Tetrahedron* 43, 2555-2559.
119. Seemann, M., Campos, N., Rodrigue-Concepcion, M., Ibanez, E., Duvold, T., Tritsch, D., Boronat, A., and Rohmer, M. (2002) *Tetrahedron* 43, 1413-1415.
120. Rohdich, F., Zepeck, F., Adam, P., Hecht, S., Kaiser, J., Laupitz, R., Grawert, T., Amslinger, S., Eisenreich, W., Bacher, A., and Arigoni, D. (2003) *Proc. Natl. Acad. Sci. USA* 100, 1586-1591.
121. Adediji, D., Hernandez, H., Wiesner, J., Köler, U., Jomaa, H., and Duin, E. C. (2007) *FEBS Lett.* 581, 279-283.
122. Seemann, M., Wegner, P., Schüemann, V., Tse Sum Bui, B., Wolff, M., Marquet, A., Trautwein, A., and Rohmer, M. (2005) *J. Biol. Inorg. Chem.* 10, 131-137.
123. Okada, K. and Hase, T. (2005) *J. Biol. Chem.* 280, 20672-20679.

124. Altincicek, B., Kollas, A.-K., Sanderbrand, S., Wiesner, J., Hintz, M., Beck, E., and Jomaa, H. (2001) *J. Bacteriol.* 183, 2411-2416.
125. Seemann, M., Bui, B. T. S., Wolff, M., Tritsch, D., Campos, N., Boronat, A., Marquet, A., and Rohmer, M. (2002) *Angew. Chem. Int. Ed.* 41, 4337-4339.
126. Bradford, M. M. (1976) *Anal. Biochem.* 72, 248-254.
127. Fish, W. W. (1988) *Meth. Enzymol.* 158, 357-364.
128. Cline, J. D. (1969) *Limnol. Oceanogr.* 14, 454-458.
129. Beinert, H. and Albracht, S. P. J. (1982) *Biochim. Biophys. Acta* 683, 245-277.
130. Watt, G. D. and McDonald, J. W. (1985) *Biochemistry* 24, 7226-7231.
131. Stroupe (2001) Handbook of *Metalloproteins*.
132. Lees, N. S., Chen, D., Walsby, C. J., Behshad, E., Frey, P. A., and Hoffman, B. M. (2006) *J. Am. Chem. Soc.* 128, 10145-10154.
133. Xiao, Y., Zahariou, G., Sanakis, Y., and Liu, P. (2009) *Biochemistry* 48, 10483-10485.
134. Stroupe, M. E. and Getzoff, E. D. (2001) in Handbook of *Metalloproteins* (Messerschmidt, A., Huber, R., Poulos, T., and Wieghardt, K., Eds.) pp 471-485, John Wiley & Sons, Ltd, Chichester.
135. Rohdich, F., Zepeck, F., Adam, P., Hecht, S., Kaiser, J., Laupitz, R., Gräwert, T., Amslinger, S., Eisenreich, W., Bacher, A., and Arigoni, D. (2003) *Proc. Natl. Acad. Sci. USA* 100, 1586-1591.
136. Wolff, M., Seemann, M., Bui, B. T. S., Frapart, Y., Tritsch, D., Estrabot, A. G., Rodrigue-Concepcion, M., Boronat, A., marquet, A., and Rohmer, M. (2003) *FEBS Lett.* 541, 115-120.
137. Altincicek, B., Duin, E. C., Reichenberg, A., Hedderich, R., Kollas, A.-K., Hintz, M., Wagner, S., Wiesner, J., Beck, E., and Jomma, H. (2002) *FEBS Lett.* 532, 437-440.
138. Xiao, Y., Zhao, Z. K., and Liu, P. (2008) *J. Am. Chem. Soc.* 130, 2164-2165.
139. Rohdich, F., Hecht, S., Gätner, K., Adam, P., Krieger, C., Amslinger, S., Arigoni, D., Bacher, A., and Eisenreich, W. (2002) *Proc. Natl. Acad. Sci. USA* 99, 1158-1163.
140. Gräwert, T., Kaiser, J., Zepeck, F., Laupitz, R., Hecht, S., Amslinger, S., Schramek, N., Schleicher, E., Weber, S., Haslbeck, M., Buchner, J., Rieder, C., Arigoni, D., Bacher, A., Eisenreich, W., and Rohdich, F. (2004) *J. Am. Chem. Soc.* 126, 12847-12855.
141. Xiao, Y. and Liu, P. (2008) *Angew. Chem. Int. Ed.* 47, 9722-9725.

142. Röhrich, R. C., Englert, N., Troschke, k., Reichenberg, A., Hintz, M., Seeber, F., Balconi, E., Aliverti, A., Zanetti, G., Köler, U., Pfeiffer, M., Beck, E., Jomma, H., and Wiesner, J. (2005) *FEBS Lett.* 579, 6433-6438.
143. Cuff, J. A., Clamp, M. E., Siddiqui, A. S., Finlay, M., and Barton, G. J. (1998) *Bioinformatics* 14, 892-893.
144. Thompson, J. D., Gibson, T. J., Plewniak, F., Jeanmougin, F., and Higgins, D. G. (1997) *Nucleic Acid Res.* 25, 4876-4882.
145. Seemann, M., Janthawornpong, K., Schweizer, J., Böttger, L. H., Janoschka, A., Ahrens-Botzong, A., Tambou, E. N., Rotthaus, O., Trautwein, A. X., Rohmer, M., and Schüemann, V. (2009) *J. Am. Chem. Soc.* 131, 13184-13185.
146. Gräwert, T., Rohdich, F., Span, I., Bacher, A., Eisenreich, W., Eppinger, J., and Groll, M. (2009) *Angew. Chem. Int. Ed.* 48, 1-5.
147. Adam, P., Hecht, S., Eisenreich, W., Kaiser, J., Gräwert, T., Arigoni, D., Bacher, A., and Rohdich, F. (2002) *Proc. Natl. Acad. Sci. USA* 99, 12108-12113.
148. Gräwert, T., Span, I., Eisenreich, W., Rohdich, F., Eppinger, J., Bacher, A., and Groll, M. (2010) *Proc. Natl. Acad. Sci. USA* 107, 1077-1081.
149. Wang, W., Wang, K., Liu, Y., No, J.-H., Li, J., Nilges, M. J., and Oldfield, E. (2010) *Proc. Natl. Acad. Sci. USA* 107, 4522-4527.